



저작자표시-비영리-변경금지 2.0 대한민국

이용자는 아래의 조건을 따르는 경우에 한하여 자유롭게

- 이 저작물을 복제, 배포, 전송, 전시, 공연 및 방송할 수 있습니다.

다음과 같은 조건을 따라야 합니다:



저작자표시. 귀하는 원저작자를 표시하여야 합니다.



비영리. 귀하는 이 저작물을 영리 목적으로 이용할 수 없습니다.



변경금지. 귀하는 이 저작물을 개작, 변형 또는 가공할 수 없습니다.

- 귀하는, 이 저작물의 재이용이나 배포의 경우, 이 저작물에 적용된 이용허락조건을 명확하게 나타내어야 합니다.
- 저작권자로부터 별도의 허가를 받으면 이러한 조건들은 적용되지 않습니다.

저작권법에 따른 이용자의 권리는 위의 내용에 의하여 영향을 받지 않습니다.

이것은 [이용허락규약\(Legal Code\)](#)을 이해하기 쉽게 요약한 것입니다.

[Disclaimer](#)

Doctoral Thesis

Multifunctional and Highly Sensitive Electronic  
Skins Based on Micro/Nanostructured Composite  
Materials

Jonghwa Park

Department of Energy Engineering

Graduate School of UNIST

2019

# Multifunctional and Highly Sensitive Electronic Skins Based on Micro/Nanostructured Composite Materials

Jonghwa Park

Department of Energy Engineering

Graduate School of UNIST

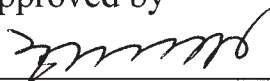
# Multifunctional and Highly Sensitive Electronic Skins Based on Micro/Nanostructured Composite Materials

A thesis/dissertation  
submitted to the Graduate School of UNIST  
in partial fulfillment of the  
requirements for the degree of  
Doctor of Philosophy

Jonghwa Park

01. 14. 2019

Approved by



---

Advisor

Hyunhyub Ko

# Multifunctional and Highly Sensitive Electronic Skins Based on Micro/Nanostructured Composite Materials

Jonghwa Park

This certifies that the thesis/dissertation of Jonghwa Park is approved.

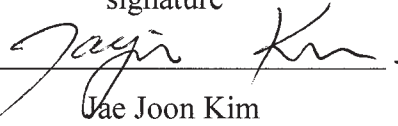
01. 14. 2019

signature



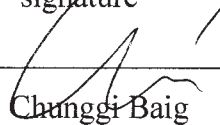
Advisor: Hyunhyub Ko

signature



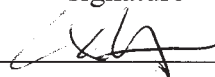
Jae Joon Kim

signature



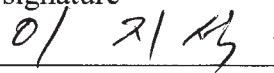
Chunggi Baig

signature



Chang Young Lee

signature



Jiseok Lee



## Abstract

Electronic skins (e-skins) enabling to detect various mechanical/chemical stimuli and environmental conditions by converting into various electrical and optical signals have attracted much attentions for various fields including wearable electronics, intelligent/medical robotics, healthcare monitoring devices, and haptic interfaces. Conventional e-skins have been widely used for the realization of these applications, however it is still considered that new e-skins with enhanced sensor performances (i.e. sensitivity, flexibility, multifunctionality, etc.) should be developed. In accordance with these demands, two approaches to explore novel functional materials or to modify device architectures have been introduced for enhancing sensor performance and acquiring multifunctional sensing capabilities. Firstly, a synthesis of multifunctional materials combined with conductive fillers (carbon nanotube, graphene oxide) and functional polymer matrix (i.e. ferroelectric polymer, elastomer) can provide the multimodal sensing capability of various stimuli and stretchability. Secondly, controlling design of device structures into various micro/nanostructures enables a significant improvement on sensing capabilities of e-skins with sensitivity and multidirectional force sensing, resulting from structural advantages such as large surface area, effective stress propagation, and anisotropic deformation. Therefore, a demonstration of e-skin combined with the functional composites and uniquely designed microstructures can offer a powerful platform to realize ideal sensor systems for next generation applications such as wearable electronics, healthcare devices, acoustic sensor, and haptic interface devices.

In this thesis, we introduce the novel multifunctional and high performance electronic skins combined with various types of composite materials and nature-inspired 3D microstructures. Firstly, Chapter 1 briefly introduces various types of e-skins and the latest research trends of microstructured e-skins and summarizes the key components for their promising application fields. In chapters 2 and 3, mimicked by interlocking system between epidermal and dermal layers in human skin, we demonstrate the piezoresistive e-skins based on CNT/PDMS composite materials with interlocked microdome arrays for great pressure sensitivity and multidirectional force sensing capabilities. In chapter 4, we conduct in-depth study on giant tunneling piezoresistance in interlocking system and investigate systematically on the geometrical effect of microstructures on multidirectional force sensitivity and selectivity in interlocking sensor systems. In chapter 5, we demonstrate the ferroelectric e-skin that can detect and discriminate the static/dynamic touches and temperature inspired by multi-stimuli detection of various mechanoreceptors in human skin. Using the multifunctional sensing capabilities, we demonstrated our e-skin to the temperature-dependent pressure monitoring of artery vessel, high-precision acoustic sound detection, and surface texture recognition of various surfaces. In chapter 6, we demonstrate the linear and wide range pressure sensor with multilayered composite films having interlocked microdomes. In

chapter 7, we present a new-concept of e-skin based on mechanochromic polymer and porous structures for overcoming limitations in conventional mechanochromic systems with low mechanochromic performances and limited stretchability. In addition, our mechanochromic e-skins enable the dual-mode detection of static and dynamic forces without any external power. Our e-skins based on functional composites and uniquely designed microstructures can provide a solid platform for next generation e-skin in wearable electronics, humanoid robotics, flexible sensors, and wearable medical diagnostic systems





## Contents

Abstract .....	1
Contents .....	4
List of Figures .....	6
List of Tables .....	25
Nomenclature .....	26
Chapter 1. Introduction .....	27
1.1 Electronic skin .....	30
1.2 Limitation of conventional electronic skins .....	31
1.3 Working principles of various electronic skins .....	34
1.4 Microstructured electronic skins .....	37
- Bio-inspired microstructure for electronic skins .....	39
- 2D and 3D microstructure for electronic skins .....	41
1.5 Application of electronic skins .....	43
- Flexible electronics & sensors .....	43
- Prosthetics and robotics .....	45
- Biomedical devices .....	47
Chapter 2. Piezoresistive composite elastomers with interlocked microdome arrays for ultrasensitive and multimodal electronic skins .....	48
2.1 Introduction .....	48
2.2 Experimental Details .....	49
2.3 Results and Discussion .....	51
2.4 Conclusions .....	72
Chapter 3. Piezoresistive composite elastomers with interlocked microdome arrays with multi-directional force sensing capability .....	73
3.1 Introduction .....	73
3.2 Experimental Details .....	75
3.3 Results and Discussion .....	76
3.4 Conclusions .....	92
Chapter 4. Microstructure engineering of multidirectional electronic skins for tailoring force sensitivity	

and selectivity -----	93
4.1 Introduction -----	93
4.2 Experimental Details -----	95
4.3 Results and Discussion -----	97
4.4 Conclusions -----	127
Chapter 5. Fingertip skin-inspired microstructured ferroelectric skins with multi-stimuli detection capability -----	128
5.1 Introduction -----	128
5.2 Experimental Details -----	131
5.3 Results and Discussion -----	136
5.4 Conclusions -----	165
Chapter 6. Multilayered ferroelectric electronic skins with ultrahigh pressure sensitivity and linear response over exceptionally broad pressure range -----	166
6.1 Introduction -----	166
6.2 Experimental Details -----	168
6.3 Results and Discussion -----	170
6.4 Conclusions -----	190
Chapter 7. Mechanochromic electronic skins for the visualization of mechanical stimuli -----	191
7.1 Introduction -----	191
7.2 Experimental Details -----	193
7.3 Results and Discussion -----	195
7.4 Conclusions -----	228
Chapter 8. Summary and Future perspective -----	229
References -----	232
Appendix A: List of Achievements -----	254
Acknowledgements -----	258

## List of Figures

**Figure 1.1.** Wearable devices and sensors with self-powered systems and multifunctional abilities. (left) Self-powered wearable electronic skins based on piezoelectric, triboelectric, and thermoelectric harvest mechanical and thermal energy from the human body. Through the physical movements of various body parts (shoulders, elbows, knees, ankles, etc.) and the heat dissipation from the body, high power of several to tens of watts are generated. (right) Multifunctional electronic skins based on resistive, capacitive, triboelectric, piezoelectric accurately monitor the user's biological signals, including the electroencephalogram (EEG), electromyogram (EMG), and various physiological signals (pulse pressure, temperature, etc.) as well as physical movements and motions. (bottom) Ubiquitous healthcare systems through wireless network and feedback system to healthcare providers.

**Figure 1.2.** Electronic skin mimicking the structure and functionality of human skin.

**Figure 1.3.** Piezoresistive e-skins with pressure sensitive rubber (PSR). (a,b) E-skins combined with PSR and field-effect transistors. (K.Takei et al. *Nat. Mater.* **2010**, 9, 821, C. Wang et al. *Nat. Mater.* **2013**, 12, 899) (c-f) E-skins combined with PSR and various shapes of interconnects; (c) serpentine (D. –H. Kim et al. *Nat. Mater.* 2011, 10, 316), (d) wavy (N. Lu et al. *Adv. Funct. Mater.*, **2012**, 22, 4044), (e) hexagonal (T. Takahashi et al. *Nano Lett.* **2011**, 11, 5408), and (f) open mesh (Sekitani et al. *Nat. Mater.* **2009**, 8, 494).

**Figure 1.4.** Representative examples for recent high performance and multifunctional electronic skin. (a) Electronic skins with various microstructures for improved sensor performances. (top) Capacitive sensor with micropylamid-patterned dielectric layer and field effect transistor (G. Schwartz et al. *Nat. Commun.* **2013**, 4, 1859). (bottom) Multidirectional piezoresistive sensor with interlocked micropillar arrays (C. Pang et al. *Nat. Mater.* **2012**, 11, 795). (b) Multifunctional electronic skins integrated various sensors by interconnects which are silicon nanoribbon (top) and polyimide wire (bottom) (J. Kim et al. *Nat. Commun.* **2014**, 5, 5747, Q. Hua et al. *Nat. Commun.* **2018**, 9, 244).

**Figure 1.5.** Working principle of electronic skins with common transduction modes. (a) Piezoresistive sensor based on the modulation of conductive network. (b) Capacitive sensor of a parallel-plate capacitor. (c) Piezoelectricity generated in single film. (d) Triboelectricity. (left) Triboelectric series from positive to negative tendency for common materials. (right) Operating mechanism of pressure sensing based electrostatic induction and triboelectric effect in a short-circuit system.

**Figure 1.6.** Bio-inspired structures (interlocking, hierarchical, crack-based, whisker, and fingerprint

**Figure 1.7.** Bio-inspired nano/microstructures for electronic skin. (a) Human-skin-inspired electronic

skins with interlocked microdome arrays. (J. Park et al. *ACS Nano*, **2014**, 8, 4689, J. Park et al. *ACS Nano*, **2014**, 8, 12020). (b) Bio-inspired self-powered e-skins based on the interlocking geometry of ZnO nanowires on microstructured PDMS. (M. Ha et al. *Adv. Funct. Mater.*, **2015**, 25, 2841) (c) Crack-based ultrasensitive strain sensors inspired by the spider's sensory system. (D. Kang et al. *Nature*, **2014**, 516, 222). (d) Whiskers of a mammal and multifunctional artificial electronic whisker arrays (W. Honda et al. *Adv. Funct. Mater.* **2014**, 24, 3299).

**Figure 1.8.** 2D and 3D micro/nanostructures for electronic skins (Porous structure). (a) Piezoresistive e-skin based on CNT/PDMS composites with micropores (S. Jung et al. *Adv. Mater.*, **2014**, 26, 4825). (b) Highly sensitive pressure sensor based on hollow-sphere microstructured PPy (L. Pan et al. *Nat. Commun.*, **2014**, 5, 3002). (c) Mesoporous PVDF-film-based piezoelectric nanogenerators (Y. Mao et al. *Adv. Energy. Mater.*, **2014**, 4, 1301624).

**Figure 1.9.** 2D and 3D micro/nanostructures for electronic skins (Surface microstructure and wrinkle structure). (a) Highly sensitive pressure sensors based on conductive electrodes on micropyr amid PDMS arrays (C. L. Choong et al. *Adv. Mater.* **2014**, 26, 3451). (b) Micropatterned P(VDF-TrFE) film-based piezoelectric nanogenerators for pressure sensors (J. H. Lee et al. *Adv. Funct. Mater.* **2015**, 25, 3203). (c) Strain sensors based on Ag nanowires on buckled elastomers (K. K. Kim et al. *Nano Lett.*, **2015**, 15, 5240).

**Figure 1.10.** Applications of flexible electronics and sensors. (a) Nanopatterned-textile-based wearable triboelectric nanogenerators integrated with commercial LCD, LEDs, and remote control (W. Seung et al. *ACS Nano*, **2015**, 9, 3501). (b) Transparent-nanopaper-based smart mapping anti-fake system (X. Wang et al. *Adv. Mater.*, **2015**, 27, 2324). (c) Acoustic sound sensor based on piezoelectric e-skins with inorganic PZT thin film. (H. S. Lee et al. *Adv. Funct. Mater.* **2014**, 24, 6914). (d) Triboelectric sensors for trajectory, velocity, and acceleration tracking of moving objects. (F. Yi et al. *Adv. Funct. Mater.* **2014**, 24, 7488). (e) Triboelectric nanogenerators for harvesting water energy and applications as ethanol sensors (Q. Shao et al., *Small*, **2014**, 10, 1466).

**Figure. 1.11.** Application of e-skins for prosthetics and robotics. (a) Multifunctional prosthetic skins that can detect the strain, pressure, temperature, and humidity and associated with heater and Pt-nanowire-based multi-electrode (J. Kim et al. *Nat. Commun.*, **2014**, 5, 5747). (b) Strain sensors attached at the moving joints of robots (X Li et al., *Adv. Mater.* **2015**, 27, 4447). (c) Texture perception by scanning fingertip-skin-inspired e-skin with interlocked geometry and a fingerprint pattern over a patterned surface (Y. Cao et al. *Small*, **2018**, 14, 1703902).

**Figure 1.12.** Applications of e-skins in biomedical devices. (a) Artery pulse pressure monitoring devices (X. Wang et al., *Adv. Mater.* 2014, 26, 1336). (b) Strain sensors integrated with a supercapacitor and triboelectric nanogenerator for respiration monitoring device (B,-U, Hwang et al., *ACS Nano*, **2015**,

9, 8801). (c) Multifunctional inflatable balloon catheters in inflated states and an electrogram from the right ventricle of a rabbit heart detected by a multifunctional balloon catheter (D.-H. Kim et al, *Nat. Mater.* **2011**, 10, 316).

**Figure 2.1.** Stress–strain curves of MWNT–PDMS composites and their elastic moduli.

**Figure 2.2.** Conductive composite elastomers with interlocked microdome arrays. (a) Schematic of the fabrication procedure used to produce the CNT-composite elastomers with microdome arrays. (b) Tilted SEM image of the composite elastomers (bottom diameter:  $\sim 5\ \mu\text{m}$ ; height:  $\sim 3.5\ \mu\text{m}$ ; pitch:  $6\ \mu\text{m}$ ). The inset photo highlights the flexibility of the arrays (scale bar:  $10\ \mu\text{m}$ ). (c) Schematic (top) and cross-sectional-SEM image (bottom) of the composite films (scale bar:  $5\ \mu\text{m}$ ). (d) Schematic showing the working principle of the electronic skin. The external pressure concentrates stress at the contact spots, deforming the microdomes, which in turn causes an increase in the contact area and the tunneling currents.

**Figure 2.3.** Pressure-sensing capabilities of sensors with interlocked microdome arrays. (a) The comparison of pressure sensitivities of different sensor structures for 8 wt% CNTs: planar (black), microdome (red) and interlocked microdome (blue). (b) Log–log plot of the pressure-response curve for the interlocked microdome arrays (8 wt% CNTs), which shows the minimum detection limit ( $\sim 0.2\ \text{Pa}$ ) and the dynamic pressure range. (c) Comparison of response/relaxation times for different sensor structures for 8 wt% CNTs and 65 Pa pressure loading: planar (upper) and interlocked microdome structures (bottom). (d) The effect of temperature variation on different sensor structures for 8 wt% CNTs and 19.6 kPa pressure loading: planar (upper) and interlocked microdome structures (bottom): planar (upper) and interlocked microdome structures (bottom). (e) Finite-element calculations that show the deformation and the local stress distribution of interlocked microdome arrays with applied pressure (1.3–60.5 kPa). (f) The electrical contact area ( $A_{\text{CNT}}$ ) as a function of pressure for different CNT wt% (5–8 wt%). The solid lines represent power-law fits to  $A_{\text{CNT}}$  with an exponent of 0.7. (g) Experimental tunneling resistances (dotted plots) of the interlocked microdome arrays for different CNT concentrations (5–8 wt%) fitted to calculated tunneling resistances (solid lines).

**Figure 2.4.** Piezoresistive pressure sensitivity of composite films for three different configurations: a single planar array, a single microdome array and an interlocked microdome array.

**Figure 2.5.** Real time variation in the relative resistance of a composite film with interlocked microdome arrays (8 wt% CNTs) in response to a pressure loading/unloading of  $\sim 0.23\ \text{Pa}$ .

**Figure 2.6.** Dynamic time-resolved variation detected by our electronic skin when exposed to a string of falling water droplets of  $\sim 8.7\ \text{mg}$  weight (corresponding to an applied pressure of  $\sim 0.6\ \text{Pa}$ ).

**Figure 2.7.** (a) Relative change in resistance for the loading and unloading cycles under pressures of 6.5 kPa and 65 kPa. (b) Relative change in resistance for the multiple-cycle tests with a repeated application of a normal pressure of 58.8 kPa

**Figure 2.8.** Finite-element-method simulations of interlocked microdome arrays. (a) A model system used in FEM simulations. The geometries of the microdome arrays are given by a radius of 2.5  $\mu\text{m}$ , a height of  $2\sqrt{3}$   $\mu\text{m}$ , and an array pitch of 6  $\mu\text{m}$ . (b) Change in contact area for the interlocked microdome arrays as a function of pressure at different concentration of CNTs (5–8 wt%). (c) The maximum strain at the contact spots as a function of pressure for different CNT concentrations (5–8 wt%).

**Figure 2.9.** Total resistances for composite films. (a) Film containing interlocked microdome arrays; (b) film containing planar structures. The tunneling resistance is obtained using the relation  $R_t = R - R_f - R_{cr}$ , where  $R$  is the total resistance of composite film with interlocked microdome arrays,  $R_f$  is the bulk-film resistance and  $R_{cr}$  is the constriction resistance.

**Figure 2.10.** Electrical properties and fracture morphologies of planar composite films. (a) The sheet resistance of composite films as a function of CNT concentration. The inset shows the power-law fits of the sheet resistance as a function of the reduced mass fraction ( $m - m_c$ ), where  $m_c$  is the required critical weight fraction for the onset of the conductive network. (b) Relative variation in resistance for planar composite films as a function of pressure. (c)–(f) Representative cross-sectional SEM images of composite films with different CNT concentrations (5–8 wt%).

**Figure 2.11.** Sensing of spatial pressure distribution and real-time monitoring of tactile signals. (a) Schematic of the  $10 \times 10$  sensor arrays, which consist of interlocked microdome arrays sandwiched between platinum electrodes and PDMS cover layers. (b) Spatial pressure-mapping capability of the  $10 \times 10$  sensor arrays. The spatial pressure distribution is applied using PDMS weights that are shaped as the letters “F”, “N” and “L”. (c) Real-time monitoring of the change in resistance for snail movements (climb, crawl, descend and head shake) on the surface of the electronic skins. (d) The change in resistance for different bending degrees of a finger (left) and repetitive bending cycles (right).

**Figure 2.12.** Monitoring of gas flow and human breathing. (a) Schematic of gas-flow sensing for planar-type electronic skins (left) and changes in resistance ( $R_{\text{off}} - R_{\text{on}}$ ) as a function of flow rate for planar electronic skins (right). (b) Left: A photograph of the planar-type flow sensors attached to the front of a volunteer’s nostrils. Right: relative changes in resistance in response to human breathing. (c) Photographs of a tubular-type flow sensor composed of rolled-up electronic skin inside a plastic tube (upper left) and a schematic of a tubular-type gas flow sensor (bottom left). Right: relative changes in resistance as a function of flow rate. (d) Monitoring of human oral breathing. Left: photograph and schematic of tubular-type flow sensors integrated into the medical breathing mask for the monitoring

of oral breathing. Right: relative changes in resistance for different oral breathing modes (deep and normal breathing) during periodic breathing.

**Figure 2.13.** Vibration detection for wearable voice-monitoring systems. (a) Left: schematic of the vibration measurement. A coin-type vibration motor is used to generate vibration signals and a vibrometer is used to measure the vibration intensity. Right: relative changes in resistance ( $\Delta R/R_0$ ) as a function of vibration intensity. (b) Photograph of the electronic skin attached to a human neck for voice monitoring (right). Relative changes in resistance in response to different voices speaking ‘UNIST’ (blue) and ‘Hi’ (red).

**Figure 3.1.** Electronic skin based on carbon nanotube–poly(dimethylsiloxane) (CNT–PDMS) composite films with interlocked microdome arrays. (a) Schematic of human skin structure showing interlocked epidermal–dermal layers and mechanoreceptors (MD: Merkel disk; MC: Meissner corpuscle; PC: Pacinian corpuscle; RE: Ruffini ending). (b) Schematic of an interlocked microdome array. (c) Tilted SEM image of a composite film with microdome arrays (diameter:  $\sim 3 \mu\text{m}$ ; height:  $\sim 3.5 \mu\text{m}$ ; pitch:  $6 \mu\text{m}$ ). Scale bar:  $5 \mu\text{m}$ . (d) Cross-sectional SEM image of an interlocked composite film. Scale bar:  $5 \mu\text{m}$ . (e) Schematic of a stress-direction-sensitive electronic skin for the detection and differentiation of various mechanical stimuli including normal, shear, stretch, bending, and twisting forces.

**Figure 3.2.** Lateral-stretch-sensing capability of electronic skins. (a) Schematic of the stretch-sensing mechanism of interlocked microdome arrays. (b) SEM images of microdome arrays showing the deformation of the array pattern from hexagons to elongated hexagons under different stretch ratios (0, 30, 60, and 120%). Scale bar:  $5 \mu\text{m}$ . (c) Finite-element analysis showing the contact pressure and the contact points between interlocked microdome arrays with the increase of uniaxial stretch. (d) FEA calculated results of the change of contact area (CA) between interlocked microdome arrays as a function of stretch. (e) Comparison of stretch-sensing capabilities of interlocked microdome arrays (black) and planar films (red). (f) Comparison of response and relaxation times of interlocked microdome arrays (black) and planar films (red) exposed to a stretching ratio of 50% and stretching speed of  $3 \text{ mm s}^{-1}$ . The CNT concentration in the composite was 7 wt% and curing temperature was  $60 \text{ }^\circ\text{C}$ . CNT concentration is 7 wt% for all the results.

**Figure 3.3.** Change in piezoresistance of interlocked microdome arrays with lateral stretch for the loading and unloading cycles at 130% lateral strain. The interlocked microdome arrays were prepared with a CNT concentration of 7 wt% and curing temperature of  $60 \text{ }^\circ\text{C}$ .

**Figure 3.4.** Variation in resistance of the interlocked microdome arrays as a function of lateral stretch for (a) different CNT concentrations (6–8 wt%) and (b) different curing temperatures (60, 70, and  $80 \text{ }^\circ\text{C}$ ).



**Figure 3.5.** Normal- and shear-force-sensing capabilities of electronic skins. (a) Schematic of the deformation of interlocked microdomes during successive applications of normal and shear forces. (b) Relative electrical resistance of electronic skin sample as a function of normal force. (c) Comparison of shear-force sensitivities of interlocked microdomes (black) and planar (red) films under a normal pressure of 58.8 kPa. (d) Comparison of shear-force sensitivities of interlocked microdome arrays under different normal pressures. (e) Finite-element analysis (FEA) showing the deformation and local stress distribution of interlocked microdome arrays with increasing shear force at a normal pressure of 45 kPa. (f) Calculated FEA results of the inverse contact area as a function of shear force under different normal pressures. The CNT concentration was 7 wt% in all electronic skins used for the measurements.

**Figure 3.6.** (a) Variation in normalized resistance for the pulling and retracting cycles under different shear forces (0.196, 0.392, 0.588 N). (b) Reliability of interlocked microdome composite films through cycles of repeated pulling and retraction under a shear force of 1.96 N.

**Figure 3.7.** Change in relative resistance of interlocked microdome arrays as a function of shear force for electron skins with different CNT concentrations.

**Figure 3.8.** Stress-direction-sensitive electronic skins for the detection and differentiation of multiple mechanical stimuli. (a) Real-time monitoring of changes in the relative resistance of interlocked microdome arrays subjected to different normal and shear forces. (b–d) Change in relative electrical resistance of an electronic skin attached on the front of a human wrist under different types of wrist movements: (b) forward bending; (c) backward bending; (d) torsion. The electronic skin showed different signal patterns in response to different wrist movements. (e–j) Change in relative electrical resistance of electronic skins in response to different mechanical stimuli: (e) normal force; (f) shear force; (g) lateral stretch; (h) forward bending; (i) backward bending; (j) torsion.

**Figure 3.9.** (a) Photographic images of bending tests of electronic skins with interlocked microdome arrays. (b) Variation in relative resistance of interlocked microdome arrays as a function of radius of curvature for electronic skins with different CNT concentrations (6–8 wt%) and cured at 80 °C. (c) Variation in relative resistance of interlocked microdome arrays as a function of radius of curvature for electronic skins prepared with 7 wt% CNTs at different curing temperature (60, 70, 80 °C).

**Figure 3.10.** Stress-direction-sensitive electronic skins for directional sensing of mechanical stimuli applied in three axial directions. (a) Schematic of sensor arrays, where interlocked microdome arrays are sandwiched between the electrodes and PDMS protection layers. (b) Spatial pressure mapping capability of electronic skin for the detection of finger touch on two different pixels (R1-C3, R3-C1). (c) Detection of different finger-pushing directions: left (L), right (R), up (U), down (D). (d) Detection of different directions of fluid flow (left, right, diagonal). (e) Detection of the location of applied vibration and the gradual damping of vibration.

**Figure 4.1.** Piezoresistive e-skins with interlocked microstructures having different surface morphologies. (a) Schematic illustration of the main structure of the e-skins with interlocked microstructures. (b) Schematic showing the bulk film resistance ( $R_F$ ) and the contact resistance ( $R_C$ ) between the two neighboring microstructured films. (c) Pressure-sensing mechanism of piezoresistive e-skins having interlocked microstructures. (d) Schematic illustration of conductive composites with different microstructured arrays. (e) Top and tilted (inset) SEM images of the microstructured composites with different surface morphologies (microdome, micropyramid, and micropillar).

**Figure 4.2.** Sheet resistance of PDMS/MWNT composite with different surface microstructures.

**Figure 4.3.** Pressure-sensing capability of single microstructured e-skins. (a) Schematic illustration of the pressure-sensing principle of single microstructured e-skins with different surface morphologies. (b) Relative current changes in response to normal pressure. (c) Finite-element analysis (FEA) of localized stress distributions in response to pressure for different surface microstructure arrays (top layer: ITO, bottom layer: MWNT/PDMS composite). (d) Calculated relative contact-area changes in response to normal pressure.

**Figure 4.4.** Pressure sensitivity of e-skins with single microstructure arrays at (a) low pressure range ( $< 1$  kPa) and (b) medium pressure range (1 kPa  $\sim$  10 kPa).

**Figure 4.5.** (a) Simulated results for variation in contact area of e-skins with single microstructure arrays as a function of mechanical pressure. (b-c) Magnified graphs of contact area change for e-skins with (b) microdome and micropyramid structures and (c) micropillar structure.

**Figure 4.6.** Electrical current changes of single microstructured e-skins with different microstructure arrays in response to normal pressure.

**Figure 4.7.** (a) Simulated result showing the stress distribution and the thickness change of microstructure under pressure. (b) Simulated result for relative variation in thickness of microstructures under loading pressure.

**Figure 4.8.** Pressure-sensing capability of interlocked microstructured e-skins. (a) Relative current changes of interlocked e-skins having different microstructures as a function of applied pressure. The magnified graph to the right shows the relative current changes of micropillar and planar structures. (b) Pressure sensitivity of e-skins for low ( $< 1$  kPa), medium (1–10 kPa), and high ( $> 10$  kPa) pressure ranges. (c) Calculated contact area variations of e-skins with interlocked microstructure arrays in response to applied pressure. (d) FEA showing the localized stress distribution of interlocked microstructure arrays for the applied pressure of 10 kPa. (e) Experimental tunneling current of e-skins with interlocked microstructures fitted to theoretically calculated tunneling resistance.

**Figure 4.9.** (a) Piezoresistive current changes of e-skins with interlocked microstructures in response to normal pressure. (b) Magnified graph of current changes at the low pressure range ( $< 1$  kPa).

**Figure 4.10.** Minimum pressure detection of e-skin with interlocked microdome. (a) Relative current change of e-skin with interlocked microdome in response to nitrogen (N<sub>2</sub>) gas with different gas flow rate from 1 to 20 m/s. Inset photograph shows the weight of air flow with a flow rate of 1 m/s which is correspond to about 0.09 Pa for sensor size of 1.5 × 1.5 cm<sup>2</sup>. (b) Relative current changes of e-skin with interlocked microdome under N<sub>2</sub> gas with a flow rate of 1 m/s.

**Figure 4.11.** Pressure sensing performance of e-skin with interlocked microdome by integrating with a commercial chip. (a) Photograph of a pressure sensing measurement system with an e-skin integrated with a commercial chip. (b) Pressure-responsive voltage changes for different loading concentration of CNTs.

**Figure 4.12.** Simulated result of contact area variations of the interlocked microstructured e-skins in response to normal pressure.

**Figure 4.13.** Pressure sensitivities of e-skins with (a) planar structure and (b-d) interlocked microstructures under different normal pressure ranges of (b) < 1 kPa, (c) 1 kPa ~ 10 kPa, and (d) 10 kPa ~ 26 kPa.

**Figure 4.14.** Relative changes in thickness of microstructure with different shapes (left) and localized stress of e-skins with interlocked microdomes in response to normal pressure (right).

**Figure 4.15.** Response time and durability properties of e-skins with interlocked microstructure arrays. (a) Response and relaxation times of e-skins under a loading/unloading pressure of 10 kPa. (b) Mechanical durability of e-skins under repeating a loading/unloading pressure of 10 kPa up to 100 cycles (left) and 1,000 cycles (right).

**Figure 4.16.** SEM images of surface morphologies of electronic skins with interlocked microstructures after 1000 cycles of pressure application

**Figure 4.17.** Relative current changes and contact area variations of interlocked microstructured e-skins in response to different mechanical forces (shear, stretching, and bending). (a–f) Changes in relative resistance and contact area of e-skins having interlocked microstructures in response to applied multidirectional mechanical stresses: (a and b) shear stress, (c and d) tensile stress, and (e and f) bending stress.

**Figure 4.18.** Finite-element simulation of the interlocked e-skins showing the microstructure deformation and contact area change between interlocked microstructure arrays in response to normal preload of 30 kPa and shear forces.

**Figure 4.19.** Finite-element simulation of the interlocked e-skins showing the microstructure deformation and contact area change between interlocked microstructure arrays in response to normal preload of 30 kPa and tensile strains.

**Figure 4.20.** Comparison of strain-sensing capabilities of e-skins with different interlocked microstructures.

**Figure 4.21.** Finite-element simulation of the interlocked e-skins showing the microstructure deformation and contact area change between interlocked microstructure arrays in response to normal preload of 30 kPa and bending curvature.

**Figure 4.22.** Multidirectional force sensing capabilities of interlocked microstructured e-skins in response to different mechanical forces (normal, shear, stretching, and bending). Each e-skin exhibits unique output current patterns with different signal intensity and response times depending on the type of mechanical forces.

**Figure 4.23.** Multidirectional force sensing capabilities of e-skins with different height of micropillar structures for (a) normal pressure, (b) shear force, (c) tensile strain, and (d) bending stresses.

**Figure 4.24.** Healthcare monitoring applications of interlocked microstructured e-skins. (a) Photograph of the acoustic wave detection test using e-skins at a fixed distance of 1 cm from the speaker. (b) Relative current change of e-skins having interlocked microdome, micropyramid, and micropillar structures in response to different intensities of acoustic waves at a constant frequency of 100 Hz. (c) Acoustic sound detection capability of the e-skins with interlocked microstructures in response to sound source of “electronic skin”. (d) Photograph of the human breath detection test using e-skins placed below the nose. (e) Relative current change of e-skins in response to human breath. (f, g) Photographs of the blood pressure monitoring test of (f) artery and (g) carotid pulse pressure using e-skins attached onto human wrist and neck. (h) Relative current changes of the e-skins with interlocked microstructures while monitoring artery pulse pressure (top) and carotid pulse pressure (bottom).

**Figure 4.25.** Detection of acoustic waves at low sound intensity and different frequency. (a-b) Comparison of acoustic wave detection of e-skins with different interlocked microstructures depending on (a) sound intensity at a constant frequency of 50 Hz, (b) frequency (50, 100, and 150 Hz) at a constant sound intensity of 80 dB. (c) Acoustic wave with frequency of 100 Hz in a normal atmosphere (base frequency: 60 Hz) before (black line) and after (red line) the base frequency filtering by a high pass frequency filter (> 65 Hz). (d) Comparison of acoustic wave between experimental and theoretical acoustic waves with frequency of 100 Hz.

**Figure 4.26.** Relative current changes of interlocked microstructured e-skins in response to human breathing motion for different operation voltages.

**Figure 5.1.** Human skin-inspired multifunctional electronic skin. (a) Structural and functional characteristics of human fingertips. The fingertip skin consists of slow-adapting mechanoreceptors (Merkel [MD] and Ruffini corpuscles [RE]) for static touch, fast-adapting mechanoreceptors (Meissner

[MC] and Pacinian corpuscles [PC]) for dynamic touch, free nerve endings [FNE] for temperature, fingerprint patterns for texture, and epidermal/dermal interlocked microstructures for tactile signal amplification. (b) Flexible and multimodal ferroelectric e-skin. The functionalities of human skin are mimicked by elastomeric patterns (texture), piezoresistive (static pressure), ferroelectric (dynamic pressure and temperature), and interlocked microdome arrays (tactile signal amplification).

**Figure 5.2.** FT-IR spectra for verifying residue solvent. (a) PVDF at different preparation conditions, (b) rGO/PVDF nanocomposites with rGO contents of 0, 1, and 40 wt. % compared with pure solvent. The solvent peak at  $659\text{ cm}^{-1}$  is attributed to the O=C=N torsional bond.

**Figure 5.3.** Schematic illustrations of the double casting and micromoulding processes for the rGO/PVDF composite film with a microdome-patterned surface.

**Figure 5.4.** Experimental set-up for the detection of dynamic pressure. (a) Schematic illustration of the measurement system for the detection of dynamic touch. (b) Schematic illustration of the measurement system for the detection of acoustic waves.

**Figure 5.5.** Temperature sensing properties of flexible rGO/PVDF nanocomposite film. (a) Cross-sectional SEM image of the rGO/PVDF composite film with stacked GO sheets. Scale bar,  $1\ \mu\text{m}$ . The inset shows a photograph of a flexible and large scale ( $20 \times 15\ \text{cm}^2$ ) rGO/PVDF composite film. (b) Current-voltage curves of 1 wt. % rGO/PVDF composite films at various temperatures. (c) Relative resistance change of rGO/PVDF composite film as a function of temperature for various concentrations of rGO. (d) Detection of temperature distribution on the human palm. (top) Schematic diagram of a sensor array, where the rGO/PVDF composite film is sandwiched between gold electrode arrays ( $18 \times 12$  pixels). (middle) Photograph of a human hand on top of the sensor array. (bottom) Contour mapping of electrical resistance variations for the local temperature distribution on the human palm. (e) A representative photograph and infrared camera images of water droplets with different droplet temperatures ( $64$  to  $-2\ ^\circ\text{C}$ ) on the e-skins. (f) and (h) Relative resistance ( $R/R_0$ ) and temperature ( $T$ ) variations of the e-skins after contact with the water droplets (f) above room temperature ( $25 - 64\ ^\circ\text{C}$ ), (h) below room temperature ( $-2 - 21\ ^\circ\text{C}$ ). Temperature ( $T$ ) change is measured by IR camera. (g) and (i) Initial stages of time-domain signals in (f) and (g) showing the variation of relative resistance immediately after contact between the e-skins and the water droplets. The solid lines are model fitting to Equation (1).

**Figure 5.6.** Phase transition of the GO/PVDF composite films with various thermal treatments. (a) XRD patterns of the GO/PVDF composite films with GO loading concentrations of 0, 1, and 5 wt. % casted at  $50\ ^\circ\text{C}$  for 12 h, annealed at  $160\ ^\circ\text{C}$  for 3 h, re-melted at  $160\ ^\circ\text{C}$ , and quenched in liquid nitrogen. Background pictures are those of the GO/PVDF composite films fabricated with each process. (b) Calculated Miller indices of the  $\beta$ ,  $\alpha$ , and  $\gamma$  phases. (c) Schematic illustrations of the structural

configuration of atoms for each phase of PVDF.

**Figure 5.7.** FT-IR spectra of the GO/PVDF composite films with GO loading concentration of 0, 1, and 5 wt. %. (a) casted at 50 °C for 12 h, (b) annealed at 160 °C for 3 h, and (c) re-melted at 160 °C and quenched in liquid nitrogen. The IR peak at 765  $\text{cm}^{-1}$  is attributed by vibration mode of the in-plane bending or rocking of  $\text{CH}_2$  of  $\alpha$ -phase. And peak at 840  $\text{cm}^{-1}$  is presented by mixed mode of  $\text{CH}_2$  rocking and  $\text{CF}_2$  asymmetric stretching vibrations of  $\beta$ -phase. [Information of peaks; I: TG – 614, 765, 858, 1385  $\text{cm}^{-1}$ , II : 512, 840, 1234, 1270, 1330  $\text{cm}^{-1}$ , III : 811, 1115  $\text{cm}^{-1}$ ]

**Figure 5.8.** Crystalline structures of PVDF (a)  $\alpha$ -phase, (b)  $\gamma$ -phase, and (c)  $\gamma'$ -phase.

**Figure 5.9.** (a) Cross-sectional SEM images of the rGO/PVDF composite films with various rGO loading concentrations. Scale bar, 1  $\mu\text{m}$ . (b) Relationship between temperature coefficient resistance (TCR) and crystallinity. (c) Crystallinity of the rGO/PVDF composite films with different rGO loading concentrations. (d) Young's modulus and elongation at break of the rGO/PVDF composite films with different rGO loading concentrations.

**Figure 5.10.** The time-dependent changes in relative resistance under dropping cold water (19.6 °C) onto planar-structured rGO/PVDF composite film.

**Figure 5.11.** Piezoresistive e-skin with interlocked microdome arrays for simultaneous detection of static pressure and temperature. (a) Schematic illustration of the e-skin with interlocked microdome array. A tilted SEM image shows the microdome arrays that are 10  $\mu\text{m}$  in diameter, 4  $\mu\text{m}$  in height, and 12  $\mu\text{m}$  in pitch size. Scale bar, 10  $\mu\text{m}$ . (b) Relative resistances of e-skins with interlocked microdome (circle) and single planar (triangle) geometries as a function of applied pressure for different rGO loading concentrations. (c) Relative resistances of e-skins with interlocked microdome (red) and single planar (black) geometries as a function of temperature for 1 wt. % rGO. (d) Schematic illustration of the loading of a water droplet onto the e-skin. (e) and (f) Time-dependent variation of relative resistances and temperature immediately after the loading of the water droplets on the e-skins at (e) different temperatures (droplet pressure: 2 Pa) and (f) different pressures (droplet temperature: 40 °C). (g) Time-dependent variation of relative resistances after the loading/unloading cycles of objects with various pressure and temperature values on top of an interlocked e-skin. (h) and (i) Magnified variation of relative resistances at the moment of loading/unloading cycles in (g) showing the detection and discrimination of simultaneous temperature and pressure variations.

**Figure 5.12.** Relative resistance of e-skin as a function of wide dynamic range of applied pressure from 10 kPa to 49.5 kPa.

**Figure 5.13.** Minimum pressure detection of ferroelectric e-skins. (a) Electrical resistance changes in response to tiny normal forces generating from static (pushing) or dynamic (drawing) movements of the human hair. The pressure detection level was determined by measuring the hair pushing weight on

the e-skin (sample size of 4 cm<sup>2</sup>). (b) Electrical resistance changes in response to weak gas flows with different flow rate from 1.59 to 5.84 m/s. The inset shows a schematic illustration of a setup for the gas flow detection. The photograph shows the weight of gas flow with a flow rate of 1.59 m/s, which corresponds to the pressure of ~0.6 Pa.

**Figure 5.14.** Stability of the piezoresistive pressure sensor under repetitive application and release of 25.5 kPa of pressure over 5000 cycles.

**Figure 5.15.** Changes in the TCR and initial resistance values at different pre-loading weights.

**Figure 5.16.** Piezoresistive e-skin with interlocked microdome array for simultaneous monitoring of artery pulse pressure and temperature. (a) Photograph of a wearable e-skin for the monitoring artery pulse pressure and temperature. The enlarged schematic illustrations indicate the effect of temperature on the constriction (cold) and dilation (warm) of arterial vessels. (b) Relative resistance variations in response to artery pulse pressure. The pulse pressure waveform consists of three peaks corresponding to pulse pressure ( $P_1$ ) and reflected wave pressures from the hand ( $P_2$ ) and lower body ( $P_3$ ).  $P_1$  is the difference between the systolic ( $P_{Sys}$ ) and diastolic ( $P_{Dia}$ ) pressures. (c) Variation of the pulse pressure waveforms before (black) and after (red) physical exercise. (d) Relative resistance change of the artery pulse pressure waveforms as a function of skin temperature (20 - 42 °C). (e) Comparison of the variation of artery pulse pressure waveform at different skin temperatures. The data in (d) is used with the data-offset modification for the comparison. (f) The blood pressure and temperature information acquired from the measurements in (e); variations of relative resistance ( $R/R_0$ ) (black), radial artery augmentation index ( $AI_r = P_2/P_1$ ) (blue), radial diastolic augmentation index ( $DAI = P_3/P_1$ ) (green), and round-trip time for the reflected wave from the hand periphery ( $T_R$ ) (purple) as a function of skin temperature.

**Figure 5.17.** Piezoelectric e-skin with interlocked microdome array for dynamic touch and acoustic sound detection. (a) Piezoelectric output currents of e-skins with (upper) interlocked microdome array and (bottom) single planar geometries. (b) Piezoelectric pressure sensitivities of the e-skins fabricated with different materials and device structures. (Frequency of loading pressure: 0.5 Hz) (c) Piezoelectric output voltage and current under repetitive impact pressure loadings at different frequencies (0.1-1.5 Hz) for the static normal loading force of 8.56 kPa at a fixed pushing distance of pushing tester. The measurements (d) Schematic illustration of the sound detection tests using the piezoelectric e-skins at the sound intensity of 96.5 dB. The sensor distance from the speaker is 2 cm. (e) Variation of the piezoelectric voltage in response to acoustic waves of different frequencies. (f) The waveforms of acoustic sound for different alphabets ('s', 'k', 'i', and 'n') (black). The read-out voltage signals from the interlocked microdome (red), and planar e-skins (blue). (g) The waveform and short-time Fourier transform (STFT) signals of the original sound ('There's plenty of room at the bottom', black) extracted by the sound wave analyser, read-out signals from the interlocked e-skin (red), and microphone (blue).

**Figure 5.18.** Effect of conductivity on piezoelectric outputs. (a) Film conductivity as a function of reduction time. (b) Piezoelectric output currents of e-skins with single planar geometry as a function of applied pressure for different film reduction times.

**Figure 5.19.** Comparison of the piezoelectric and piezoresistive signal variations of e-skins in response to applied pressure with different frequencies (0.3 – 5.0 Hz). Applied pressure: 8.56 kPa.

**Figure 5.20.** Piezoelectric e-skin with fingerprint-like patterns for texture perception. (a) Schematic illustration of the texture perception measurements, for which the e-skin is attached to a microstage and scanned over a surface. (top) SEM image of the fingerprint-inspired PDMS pattern. (bottom) SEM image of the PDMS substrate with periodic line-patterns (P: 470  $\mu\text{m}$ , W: 163  $\mu\text{m}$ ). Scale bar, 200  $\mu\text{m}$ . (b) Time-dependent variation of piezoelectric currents when the e-skin is scanned over the patterned surface at different scanning speeds (0.25-2.5 mm/s). (c) FFT spectra of time-dependent piezoelectric current signals in (b). (d) STFT spectrograms of the piezoelectric current signals in (b) for the low frequency range (0-30 Hz). (e) Perception of texture with different roughness. (top) SEM images of the sandpaper, paper, and glass surfaces. (bottom) STFT spectra of the corresponding output currents when the e-skin is scanned at 2.5 mm/s. Scale bar, 200  $\mu\text{m}$ . (f) Perception of fine textures (< 100  $\mu\text{m}$ ). (top) SEM images, (middle) output current signals, and (bottom) STFT spectra of different silicon substrates with (i) planar, (ii) and (iii) line pattern (P: 80  $\mu\text{m}$ , D: 10  $\mu\text{m}$ ), (iv) square pattern (P: 80  $\mu\text{m}$ , D: 20  $\mu\text{m}$ ), and (v) pentagon pattern (P: 90  $\mu\text{m}$ , D: 20  $\mu\text{m}$ ). The arrow indicates the scanning direction. Scale bar, 100  $\mu\text{m}$ .

**Figure 5.21.** STFT spectrograms of the piezoelectric current signals for the high frequency range (>80 Hz) obtained by scanning on polydimethylsiloxane (PDMS) films with periodic line patterns as a function of scanning speed.

**Figure 5.22.** Effect of e-skin structure and fingerprint patterns for texture perception. (a) Output electrical current, (b) High frequency components of the STFT spectra, and (c) Low frequency components of the STFT spectra obtained from the surface scanning results for various structure and fingerprint patterns.

**Figure 5.23.** Perception of hardness/softness of surface. (a) High frequency components of the STFT spectra, and (b) Low frequency components for the STFT spectra resulting from scanning over parallel line patterned-PDMS surfaces with different elastic modulus.

**Figure 5.24.** Wearable e-skins for texture perception. (a) The texture perception capability of different surfaces on our hand. (i) Photographs of flexible and wearable e-skins wrapped onto the human finger and the palm and back of the human hand with indications of the different scanning directions. (ii) Magnified photographs of the fingerprints on the different sites of human hand skin; (1) centre of palm, (2) side of palm, and (3) back of hand. Scale bar, 500  $\mu\text{m}$ . (iii) Output electrical currents, and (iv) Low



frequency components of the STFT spectra obtained by scanning of textural surfaces in different scanning directions. The red arrows in the output electrical currents and STFT spectra indicate the texture signals from major lines on the palm. On the side of palm and back of hand, the strong texture signals are not observed. Instead, random lines with weaker intensities are observed in the STFT spectra due to the skin ridges on the palm and lines on the back hand. (b) Texture perception capability of different surfaces on the hair, facial skin, beard, and whisker regions of the human head. The high intensity red lines in the low frequency STFT spectra are observed when the scanning areas are on top of rough textures.

**Figure 5.25.** Perception of fine textures for the low frequency range ( $< 30$  Hz) obtained by scanning on polydimethylsiloxane (PDMS) films with periodic line patterns as a function of scanning speed. (a) SEM images of fine textures, Scale bar,  $100\ \mu\text{m}$ . (b) scanning speed of  $2.5\ \text{mm/s}$ . (c) scanning speed of  $5.0\ \text{mm/s}$ .

**Figure 6.1.** Applications and schematics of multilayer interlocked microdome e-skins. (a) Schematic showing the different pressure sensing trends between single-layered e-skins and multilayer e-skins. (b) Various applications to show the highly sensitive and large range pressure sensing by multilayer e-skins. (c) Schematic of multilayer e-skins. (d) Cross-sectional scanning electron microscopy (SEM) image of a microdome-patterned rGO/PVDF composite film with multilayer stacked structures. (e) Cross-sectional SEM image of the interlocked microdome geometry of an rGO/PVDF composite film. (f) Tilted SEM image of a microdome array of the rGO/PVDF composite film.

**Figure 6.2.** X-ray diffraction (XRD) spectroscopy of (a) a pure PVDF film, 2 wt% GO/PVDF, and 2 wt% rGO/PVDF composite films; and (b) pure PVDF and 0.3, 0.5, and 1 wt% rGO/PVDF composite films.

**Figure 6.3.** Sheet resistance of rGO/PVDF composite films as a function of the loading concentration of rGO.

**Figure 6.4.** Piezoresistive static pressure-sensing performances of multilayer interlocked microdome e-skins. (a) Relative current of e-skins with multilayer geometry with different numbers of stacked layers and planar geometry in response to the applied pressure. (b) Pressure sensitivity of e-skins converted from Figure 6.4a. (c) Comparison of the sensitivity and linear sensing performances based on this work and previous reports. (d) Finite element calculation of the contact area change as a function of pressure for different numbers of stacked layers. (e) Finite element calculations of the local stress distribution for different numbers of interlocked layers showing the concentrated and amplified stress at the small spot between interlocked microdomes under a pressure of  $355\ \text{kPa}$ . (f) Real-time pressure monitoring of e-skins at an applied pressure of  $54, 108, 163, 217, 272,$  and  $326\ \text{kPa}$ . (g) Response and relaxation times for multilayer e-skins under different pressures of  $10$  and  $200\ \text{kPa}$ . (h) Cyclic stability test of multilayer e-skins under repetitive high-pressure loading of  $272\ \text{kPa}$  at a frequency of  $0.5\ \text{Hz}$ .

**Figure 6.5** Circuit diagram of triple multilayer e-skins.

**Figure 6.6.** Static pressure-sensing performances of multilayer e-skins over three layers.

**Figure 6.7.** Finite-element calculation showing the stress distribution in multilayer e-skins with single, double, and triple layers. (a) Model systems with different number of interlocked layers. (b) Stress distribution of multilayer e-skins with single, double, and triple layers under different applied pressure.

**Figure 6.8.** (a) Static pressure-sensing performances of single-interlocked e-skins with different rGO loading concentrations. (b) Static pressure-sensing performances of triple-interlocked e-skins with different rGO loading concentrations. (c) Initial resistance of single- and triple-interlocked e-skins using 1 and 2 wt% rGO/PVDF composite films.

**Figure 6.9.** Pressure-sensing performances of multilayer e-skins based on different size of microdomes. Cross-sectional SEM images of microdome arrays with (a) 10, 15, and 4  $\mu\text{m}$ , (b) 25, 30, and 10  $\mu\text{m}$ , (c) 50, 60, 20  $\mu\text{m}$  in diameter, pitch, and height, respectively. Relative current of multilayer e-skins based on microdomes with (d) different pitch size and (e) different diameter.

**Figure 6.10.** Application of weak pressure on multilayer e-skins. (a) Schematic illustration showing the detection of weak air flow by multilayer e-skins. (b) Relative current change of multilayer e-skins as a function of gas flow rate. (c) Real-time monitoring of gas flow by multilayer e-skins. (d) Piezoelectric dynamic pressure-sensing performances of e-skins with different multilayer structure geometries with different stacked layers and planar structures. (e) Schematic of sound wave detection by multilayer e-skins. (f) Detection of the sound wave with single frequency for planar, single-interlocked, and multilayer interlocked microdome e-skins. (g) Sound waveforms and corresponding spectrograms converted by STFT from the original sound source (black), signals recorded from multilayer e-skins (red), and planar e-skins (blue). (h) Expanded frequency spectrograms in Figure 6.10g

**Figure 6.11.** Applied pressure due to weak gas flow with a flow rate of 3 L/min. Considering the size of the multilayer e-skins, the applied pressure due to gas flow with a flow rate of 3 L/min is  $\approx 1.3$  Pa.

**Figure 6.12.** (a) Dynamic pressure-sensing performances of single-interlocked e-skins with 1 and 2 wt% rGO/PVDF composite films. (b) Dynamic pressure-sensing performances of triple-interlocked e-skins with 1 and 2 wt% rGO/PVDF composite films.

**Figure 6.13.** Piezoelectric single sound frequency detection performances of (a) multilayer e-skins and (b) planar e-skins.

**Figure 6.14.** (a) Sound waveforms and corresponding spectrograms converted by STFT of the original sound from a piano, guitar, and electric guitar (black). (b) Recorded piezoelectric waveforms and corresponding spectrograms from multilayer e-skins, converted by STFT of sound from a piano, guitar, and electric guitar (red).

**Figure 6.15.** Application of medium pressure on multilayer e-skins. (a) Photograph showing the

detection of human breath by attaching multilayer e-skins to the nostril of a volunteer. (b) Monitored real-time signals of weak and deep breathing detected by multilayer e-skins. (c) Photograph showing the pulse pressure detection after attaching multilayer e-skins to wrist skin. (d) Real-time monitoring of the pulse signals and expanded pulse wave containing three peaks, i.e.,  $P_1$  (incident wave),  $P_2$  (tidal wave), and  $P_3$  (diastolic wave), recorded by multilayer e-skins. (e) Schematic of the  $3 \times 3$  sensor array for the multilayer e-skins with an ability to perceive the magnitude and spatial distribution of the applied pressure. (f–h) Schematics of the detection of applied pressure from different shapes and weights of loads and their corresponding pressure maps.

**Figure 6.16.** Application of high pressure to multilayer e-skins. (a) Schematic of the smart insole consisting of  $4 \times 8$  pixel arrays of multilayer e-skins, patterned electrodes, and supporting PET layers. (b) Photograph of  $4 \times 8$  pixel arrays of multilayer e-skins with pressure applied by an upside-down petri dish. (c) Corresponding pressure map. (d) Schematics of five walking motions on the smart insole to monitor the foot pressure distribution and their corresponding pressure maps.

**Figure 7.1.** Hierarchical NP-MP architecture in porous mechanochromic composites. (a) Schematic of the working mechanism of porous mechanochromic composites with hierarchical NP-MP architecture. (b) Photograph and SEM images of porous (pore-5) mechanochromic composites comprising PDMS, SP and 300-nm SNPs (SNP-300). The SEM images show uniform spherical pores and SNPs decorated on the inner pore surfaces. (c) Stress–strain behaviours of the stretchable mechanochromic polymers with planar, porous and SNP-decorated porous structures.

**Figure 7.2.** Schematic of the fabrication procedure for porous mechanochromic composites with PDMS/SP/SNPs. SP, PDMS and SNPs are mixed in hydrophilic co-solvents (water and ethanol) and solvents are evaporated during the hydrosilylation curing process.

**Figure 7.3.** (a) Scanning electron microscope (SEM) image of a porous mechanochromic composite with an average pore size of  $5 \mu\text{m}$  before freeze-drying. SEM images of a fabricated porous mechanochromic composite after three days before (b) and after (c) freeze-drying. Due to the capillary force-induced pore closure during solvent evaporation, freeze-drying is required to completely evaporate the solvent and obtain uniform pores.

**Figure 7.4.** (a) Schematic of the mechanism of pore formation in composites based on the addition of hydrophilic solvents. (b) Cross-sectional SEM images of porous PDMS/SP composites with different mixed solvent ratios (PDMS : water : ethanol = 3:2:0, 3:1.5:0.5 and 3:1:1). The lower row shows magnified SEM images. (c) Pore size distributions of porous PDMS/SP composites with different mixed solvent ratios.

**Figure 7.5.** (a) Simulated surface areas of porous mechanochromic composites with different pore sizes based on face-centered cubic (FCC) unit cell arrays. The porous structures are modelled according to

average pore sizes of 25, 10 and 5  $\mu\text{m}$  with the same porosity (26%) based on FCC unit cell arrays. Volume is determined as the total material volume, excluding the pore volume. Area is the total surface area of the porous structure. (b) Material densities of the fabricated porous mechanochromic composites with different pore sizes. (c) Porosity and surface area of porous mechanochromic composites as functions of pore size.

**Figure 7.6.** (a) Schematic of SNP decoration on the inner pore surfaces of a mechanochromic composite during heat-induced solvent evaporation. (b) Cross-sectional SEM images of porous PDMS/SP composites (pore size = 5  $\mu\text{m}$ ) with different SNP sizes (20, 100 and 300 nm). (c) Magnified SEM images showing that the SNPs are uniformly decorated on the inner pore surfaces.

**Figure 7.7.** Properties of porous mechanochromic composites under tensile strain. (a) Photographs of mechanochromic polymers with different structures exhibiting colour changes in response to tensile strain. (b) Colour change of the pore-5/SNP-300 mechanochromic composite at the first and 100th stretching and releasing cycles. (c) Changes in the average colour coordinates of the mechanochromic polymers with different structures under applied tensile strain. (d) Normalised luminance as a function of wavelength for the pore-5/SNP-300 mechanochromic composite under tensile strains up to 400%.

**Figure 7.8.** (a) Strain–stress curves of porous PDMS/SP composites with different pore sizes. (b) S–S curves of porous PDMS/SP composites (pore size = 5  $\mu\text{m}$ ) with different SNP sizes.

**Figure 7.9.** Schematic of a measurement system using a spectroradiometer for investigating the colour transition properties of porous mechanochromic composites in response to tensile strain.

**Figure 7.10.** Photographs showing the colourimetric strain sensing properties of porous mechanochromic composites with different pore sizes.

**Figure 7.11.** Photographs showing the colourimetric strain sensing of porous PDMS/SP composites (pore size = 5  $\mu\text{m}$ ) decorated with SNPs with different sizes: (a) 20 nm, (b) 100 nm and (c) 300 nm.

**Figure 7.12.** Strain–stress curves of a porous mechanochromic composite (pore size = 5  $\mu\text{m}$ ; SNP size = 300 nm) under repeated loading/unloading strain of up to 250%.

**Figure 7.13.** (a) Average colour coordinates of planar mechanochromic composites under loading tensile strain. (b) Average colour coordinates of porous mechanochromic composites with different pore sizes under loading tensile strain. (c) Average colour coordinates of mechanochromic composites with different SNP sizes under loading tensile strain.

**Figure 7.14.** Recovery time of a porous mechanochromic composite (pore size = 5  $\mu\text{m}$ , SNP size = 300 nm) under different tensile strains. (a) Time-dependent tensile strains of 125%, 150% and 175% (top) and the corresponding change in relative intensity ( $I_{\text{Rel}}$ ) of green colour in response to loading strain

(bottom). (b) Relaxation under a loading/unloading strain of 175% depending on exposure to white light.

**Figure 7.15.** Structure-dependent strain sensitivity of porous mechanochromic composites. (a) Normalised colour intensity ratio as a function of strain for mechanochromic polymers with different pore sizes (left) and with different SNP sizes at a pore size of 5  $\mu\text{m}$  (right). The colour intensity in response to strain is measured by spectroradiometer. (b) Enlarged plot from (a) in the strain range 20%–100%. (c) Strain sensitivity [ $S = (\Delta C/C_0)/(\Delta \epsilon)$ , where  $C$  is the colour intensity ratio and  $\epsilon$  is the applied strain] of mechanochromic polymers with different structures. Sensitivity is estimated from the plot in (a) for the linear regimes of mechanochromic response. (d) Finite-element analysis (FEA)-determined stress distributions of mechanochromic polymers with different pore sizes (left) and with 300-nm SNPs and a 5- $\mu\text{m}$  pore size (right) under a tensile strain of 50%. (e, f) FEA-determined maximum localised stress near the pore surface in porous mechanochromic polymers with (e) different pore sizes and (f) different SNP sizes and a pore size of 5  $\mu\text{m}$  as a function of strain (see Figures 7.17 and 7.18 for additional details).

**Figure 7.16.** Variation in colour component intensities (R, G and B) of porous mechanochromic composites under loading strain at different wavelengths: (a, b) 488 nm, (c, d) 544 nm and (e, f) 612 nm. The intensity of each colour component initially increases because of the decrease in light absorption caused by the concurrent decrease in film thickness. The intensity subsequently decreases because of the colouration of SP.

**Figure 7.17.** Stress distributions of porous PDMS/SP composites with different pore sizes (25, 10 and 5  $\mu\text{m}$ ) placed under 50% tensile strain calculated numerically using ABAQUS software. For simplicity, the elastic modulus is set to 1 MPa with the same porosity (26%) for all porous composites (see Figure 7.5 for the initial system configuration).

**Figure 7.18.** Stress distribution of porous PDMS/SP composites (pore size = 5  $\mu\text{m}$ ) decorated with SNPs with different sizes (300, 100 and 20 nm) placed under 50% tensile strain calculated numerically using ABAQUS software. For simplicity, to understand the role of the SNPs at the pore walls, the elastic modulus of the porous matrix is set to 0.24 MPa (consistent with the experimental data shown in Figure 7.8). The elastic modulus of the SNPs is set to a general value of 180 GPa for all sizes.

**Figure 7.19.** Normal force detection capabilities of porous mechanochromic composites. (a) Relative intensities of the colour components (red, green and blue) of mechanochromic polymers with different structures as functions of normal force. The colour intensity in response to normal force is measured by I-phone camera and colour picker program. (b) Relative green intensity as a function of normal force for mechanochromic polymers with different pore sizes and different SNP sizes with 5- $\mu\text{m}$  pores. (c) Optical images showing the local colour distributions of the porous mechanochromic composites after

contact with various objects (microtips and needle).

**Figure 7.20.** (a) Measurement system used to evaluate the colour transition properties of porous mechanochromic composites in response to normal stress. (b) Photographs of the mechanochromic composites with different porous structures under a loading normal stress of 6 N.

**Figure 7.21.** (a) Relative colour changes of porous PDMS/SP composites with different pore sizes in response to applied normal pressure. (b) Finite-element analysis-determined stress distributions in porous PDMS/SP composites with different pore sizes under applied normal pressure. The simulation conditions are identical to those in Figure 7.17.

**Figure 7.22.** (A) Relative colour intensities of porous PDMS/SP composites (pore size = 5  $\mu\text{m}$ ) decorated with SNPs of different sizes (20, 100, 300 nm) as functions of pressure. (B) Finite-element analysis-determined stress distributions at the surfaces of pores in porous PDMS/SP composites with SNPs under applied pressure. The simulation conditions are identical to those in Figure 7.18.

**Figure 7.23.** Applications of porous mechanochromic composites in wearable e-skins and dual-mode static/dynamic touch and audio sensors. (a) Images of wearable mechanochromic e-skins for the detection of various hand gestures (folding/unfolding, rock, scissor and grasp). (b) Schematic of a dual-mode mechanochromic and triboelectric force sensor that enables the spatiotemporal detection of both writing force and speed. (c) Waveforms of the sound sources of the words ‘electronic’ and ‘skin’: waveforms of the detected read-out signals (left) and short-time Fourier transform of the sound source along with the read-out signals from the dynamic force sensor (right). These applications are based on the pore-5/SNP-300 porous mechanochromic composite.

**Figure 7.24.** Schematic of the working mechanism of the single-electrode triboelectric sensor, which comprises a porous mechanochromic composite and silver nanowire-based electrode. Object is the plastic pen in this work.

**Figure 7.25.** (a) Output triboelectric current of a mechanochromic composite in response to normal pressure. The sensitivity is  $0.18 \mu\text{A kPa}^{-1}$  below 0.4 kPa and  $0.002 \mu\text{A kPa}^{-1}$  in the range 1–108 kPa. (b) Triboelectric output voltage and (c) power density of porous PDMS/SP composites with 5- $\mu\text{m}$  pores and 300-nm SNPs as functions of applied pressure. (d) Output current of the porous mechanochromic composite in response to dynamic normal pressure with different loading frequencies (0.1–4 Hz).

**Figure 7.26.** Schematic showing the setup used to detect dynamic acoustic waves.

## List of Tables

**Table 4.1.** Summary of the key parameters of recently reported e-skins.

**Table 4.2.** Summary of the acoustic sensing capabilities of recently reported acoustic sensors.

**Table 6.1.** Summary of pressure sensors with linear pressure responses and their performances.

**Table 7.1.** Summary of recently reported mechanophore systems.

## Nomenclature

---

<b>E-skin</b>	Electronic skin
<b>PSR</b>	Pressure sensitive rubbers
<b>CNT</b>	Carbon nanotube
<b>MWNT</b>	Multi-walled carbon nanotube
<b>AgNW</b>	Silver nanowire
<b>ITO</b>	Indium tin oxide
<b>PET</b>	Polyethylene terephthalate
<b>FFT</b>	Fast fourier transform
<b>STFT</b>	Short-time fourier transform
<b>SP</b>	Spiropyran
<b>MC</b>	Merocyanine
<b>FEA</b>	Finite element analysis
<b>PDMS</b>	Polydimethylsiloxane
<b>PVDF</b>	Poly(vinylidene fluoride)
<b>rGO</b>	reduced graphene oxide
<b>DMF</b>	Dimethyl formamide
<b>PVA</b>	Polyvinyl alcohol
<b>NTC</b>	Negative temperature coefficient
<b>PTC</b>	Positive temperature coefficient
<b>TCR</b>	Temperature coefficient of resistance
<b>RIE</b>	Reactive ion etching
<b>DRIE</b>	Deep reactive ion etching
<b>SAM</b>	Self-assembled monolayer
<b>SEM</b>	Scanning electron microscopy
<b>TEM</b>	Transmission electron microscope
<b>UV-vis</b>	Ultraviolet-visible
<b>XRD</b>	X-ray diffraction
<b>PAI</b>	Pressure augmentation index
<b>IoT</b>	Internet of Thing

---



## Chapter 1. Introduction.

Wearable electronic devices are an important driving force behind the recent development of the “Internet of Things (IoT)”, which connects the user with surrounding machines and electronic devices through Internet infrastructure for personalized healthcare and wellness. The rapid growth of electronic technologies dramatically increased the population using smart electronics including smartphones, smartwatches, and smartbands for communication, monitoring environmental changes, and checking personal health conditions everywhere in real-time.<sup>1, 2</sup> However, current wearable electronics are still in an early stage of development and require further innovations in terms of electronics and materials for user-friendly and unobtrusive communication and monitoring. Key enabling technologies of wearable devices include sensors; wireless communication; and energy devices in lightweight, miniaturized, and flexible forms.<sup>2, 3</sup>

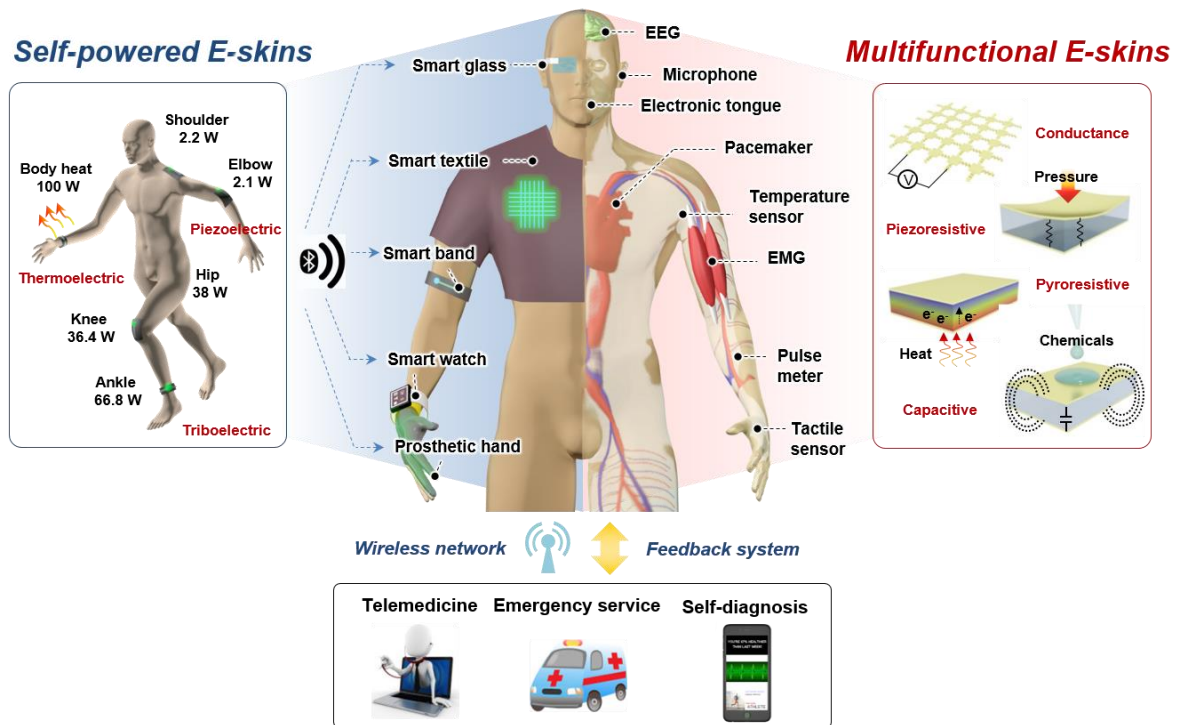


**Figure 1.1.** Wearable devices and sensors with self-powered systems and multifunctional abilities. (left) Self-powered wearable electronic skins based on piezoelectric, triboelectric, and thermoelectric harvest mechanical and thermal energy from the human body. Through the physical movements of various body parts and the heat dissipation from the body, high power of several to tens of watts are generated. (right) Multifunctional electronic skins based on resistive, capacitive, triboelectric, piezoelectric accurately monitor the user’s biological signals, including the EEG, EMG, and various physiological signals as well as physical movements and motions. (bottom) Ubiquitous healthcare systems through wireless network and feedback system to healthcare providers.

With these great demands for wearable electronics, the importance to develop new type of sensors that can accurately monitor the user's physiological activities and motions have been considerably increased. Accordingly, considerable advances in wearable sensors have been recently represented with two categories of self-powered and multifunctional sensors. Firstly, self-powered sensors with both energy-harvesting and sensing capabilities in a single device are currently drawing much attention for application in wearable devices (Figure.1.1, left). In principle, the mechanical and thermal energy can be harvested via various energy-harvesting technologies including piezoelectric, triboelectric, pyroelectric, and thermoelectric devices. In addition, the voltage and current-output signals from these energy harvesting devices can be directly employed for the detection of mechanical and thermal stimuli. Without the need for integrating power-supply devices with wearable sensors, self-powered wearable sensors allow much more freedom to choose the form factors, enabling flexible and skin-like sensors or electronic skins (e-skins). Numerous self-powered e-skins have been reported for applications in robotics, prosthetics, healthcare devices, flexible electronics, and environmental monitoring devices. However, low stretchability/conformability and limited sensing capabilities remain significant challenges for the advancement of wearable electronics.

In accordance with the requirement of wearable sensors to accurately monitor the user's biological signals in healthcare/wellness applications, including the electroencephalogram (EEG), electrocardiogram (ECG), electromyogram (EMG)), and various physiological signals (pulse pressure, temperature, etc.) as well as physical movements and motions (Figure 1.1, center), multifunctional and highly-sensitive sensory systems are required to perceive a variety of stimuli such as mechanical stimuli (dynamic/static touches and normal, shear, tensile, and bending stresses), texture/roughness of surfaces, and environmental changes (humidity, light, temperature, etc.). The challenging issue for the realization of these multifunctional e-skins is to detect various external stimuli exactly without crosstalk between multiple signals. To address the above-mentioned issues, it is necessary to employ various signal-transduction modes (Figure 1.1, right) properly according to the sensing targets. While piezoelectric and triboelectric sensors are fast-responsive, and thus suitable for the detection of dynamic stimuli,<sup>4, 5</sup> piezoresistive and capacitive sensors can detect static pressure and other forces applied in different directions.<sup>6</sup> In addition, the resistive and capacitive modes of sensors provide high-accuracy response to temperature,<sup>7</sup> humidity,<sup>8</sup> and chemicals.<sup>9, 10</sup>

Self-powered and multifunctional e-skins lead to wearable and all-in-one electronics with user-interactive and unobtrusive properties, combining with energy storage and wireless-communication devices. However, there are still several issues including low multidirectional force sensitivities, difficulty of sensing multiple stimuli, narrow and nonlinear response, and need of external power source for sustainable operation.

To address those issues, this thesis introduces novel type of electronic skins based on functional composite materials with uniquely designed micro/nanostructures. By introducing micro/nanostructures inspired by various bio-systems in nature, it is possible to achieve high-performance electronic skins with both high sensitivity and multifunctionality. In addition, these structural modifications of composites enable e-skins with wide and linear force sensing capabilities, and enhanced mechanochromic sensing capability for stimuli visualization. We believe that our electronic skins will be a powerful platform to open a new route to future soft and wearable electronic devices.

### 1.1 Electronic skin (E-skin)

Electronic skin refers to the electronic device mimicking the functionalities of human skin, which can detect and discriminate various mechanical/chemical stimuli and environmental conditions by converting into various electrical and optical signals. Skin-like sensing capabilities of e-skins for multiple mechanical, thermal, and chemical stimuli provide a great opportunity for diverse application fields such as human-assistive robots, prosthetics, and augmenting surgical devices. As shown in Figure 1.2, the real skin at human fingertips can detect and discriminate various static/dynamic touches, strain, shear forces, vibration, and temperature by various mechanoreceptors (Meissner corpuscle, Merkel disks, Ruffini endings, Pacinian corpuscle) and free nerve ending in the interlocked microstructure between the epidermal and dermal layers. In addition, the fingerprint pattern enables the perception of fine texture by amplifying the vibrotactile signals. The multifunctional ability of human skin to detect and discriminate multiple stimuli individually plays critical roles in grasping and handling objects, perceiving slip moment, surface texture detection, etc. Furthermore, continuous temperature and humidity monitoring, and self-healing properties are critical in maintaining human activities and healing of cutaneous wounds.

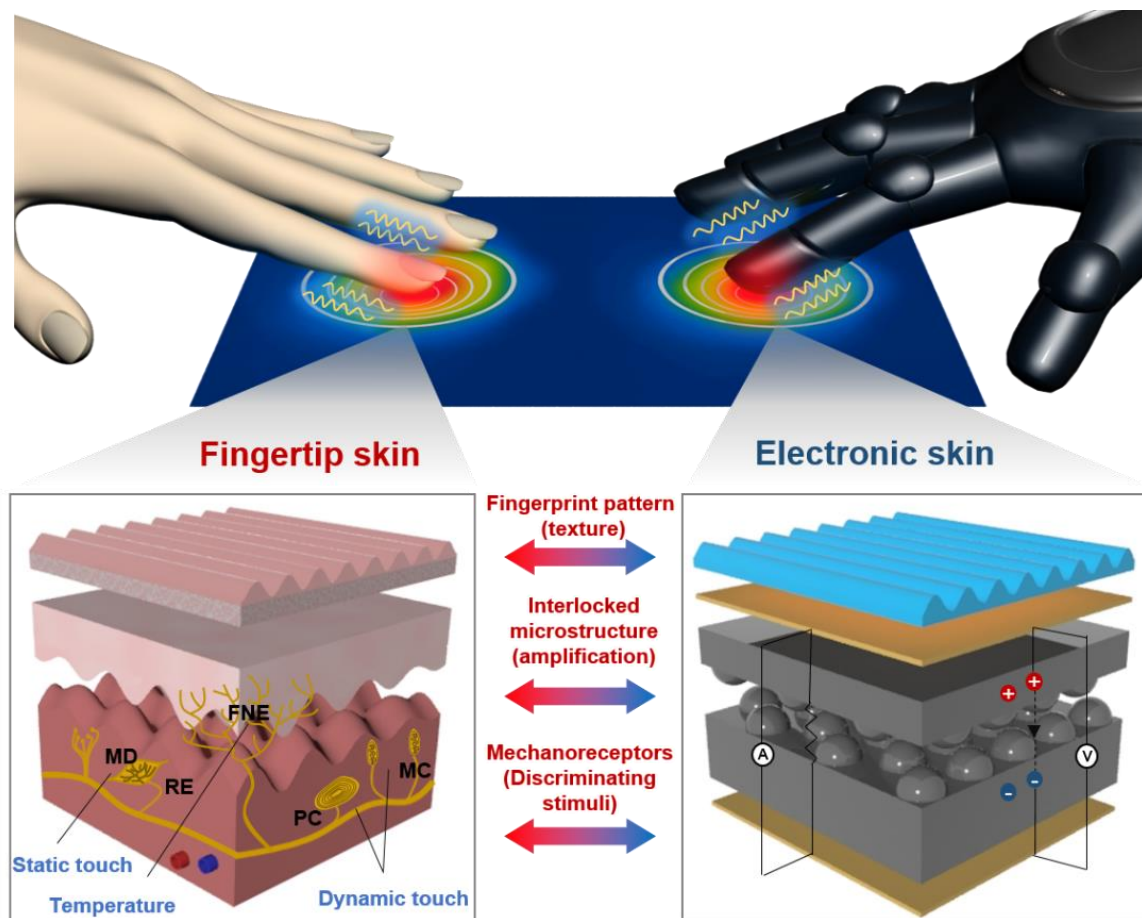


**Figure 1.2.** Electronic skin mimicking the structure and functionality of human skin.

## 1.2 Limitation of conventional electronic skins

For the development of e-skin that possess those abilities of human skin, initially pressure sensitive rubbers (PSRs) composed of conductive filler and elastomeric polymer are demonstrated. Owing to their simple structure and operating mechanism, conventional PSRs consisting of conductive filler/elastomer composites have been frequently used as a pressure-sensing component integrated with field-effect transistors, which is advantageous for signal amplification by FET and available for pressure mapping with high resolution.<sup>11-13</sup> The PSRs have also been combined with various shapes of interconnects such as wavy/serpentine,<sup>14, 15</sup> hexagonal<sup>16</sup> and open mesh<sup>17</sup> to demonstrate high-performance pressure/strain sensors. These electronic skins exhibited high stretchability and can be easily combined with other sensing devices (temperature, light, flow, ECG sensors, light-emitting diode etc.).<sup>15</sup> However, the low sensitivity, large hysteresis in response to pressure and single sensing capability are a challenge to be addressed.

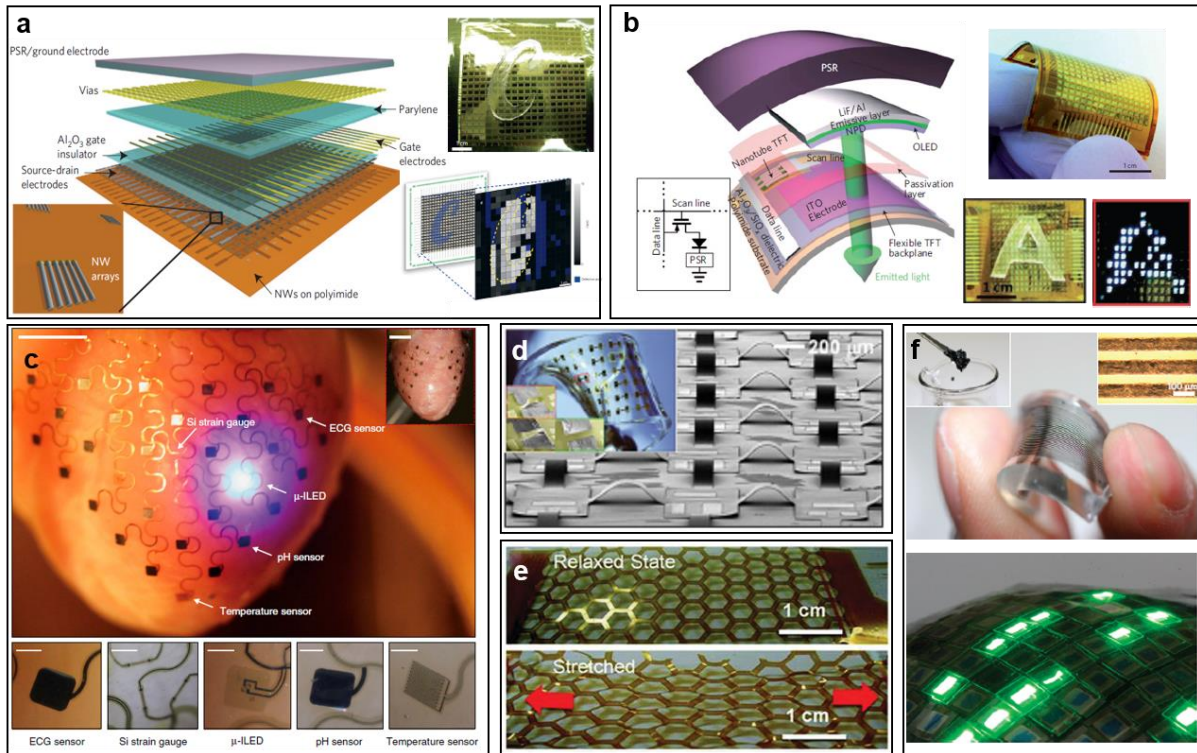


**Figure 1.3.** Piezoresistive e-skins with pressure sensitive rubber (PSR). (a,b) E-skins combined with PSR and field-effect transistors. (K.Takei et al. *Nat. Mater.* **2010**, 9, 821, C. Wang et al. *Nat. Mater.* **2013**, 12, 899) (c-f) E-skins combined with PSR and various shapes of interconnects; (c) serpentine (D. –H. Kim et al. *Nat. Mater.* 2011, 10, 316), (d) wavy (N. Lu et al. *Adv. Funct. Mater.*, **2012**, 22, 4044), (e) hexagonal (T. Takahashi et al. *Nano Lett.* **2011**, 11, 5408), and (f) open mesh (Sekitani et al. *Nat. Mater.* **2009**, 8, 494).

In order to overcome these challenges, new approaches based on the introduction of microstructures into mechanical sensors have recently suggested for enhanced performances of e-skins (Figure 1.4. left).<sup>18, 19</sup> Various micro/nanostructures inspired by bio-systems or 2D/3D microstructures allow a significantly enhanced mechanical sensitivity and a multidirectional force sensing property due to the unique structural advantages such as high contact area, and high compressibility. However, most of microstructured e-skins have a difficulty of multiple stimuli detection in single devices and narrow range of linear response, which prevent the use of e-skins in practical applications. Another approach for multifunctional e-skins is the integration of the multiple sensors onto a single substrate in combination with flexible interconnects (Figure 1.4. right).<sup>20, 21</sup> Although there have been several reports on the development of multifunctional e-skins that can detect and differentiate various mechanical and thermal stimuli, these approaches typically require the complex fabrication and high cost. In addition, sophisticated layouts of interconnected lines such as open mesh and serpentine layouts are needed to minimize mechanical strain effects. In this respect, it is important to find the complementary e-skin devices that possess the high sensitivity in multi-directional force and sensing capability to multiple stimuli, as well as linear and wide sensing range for various practical applications.

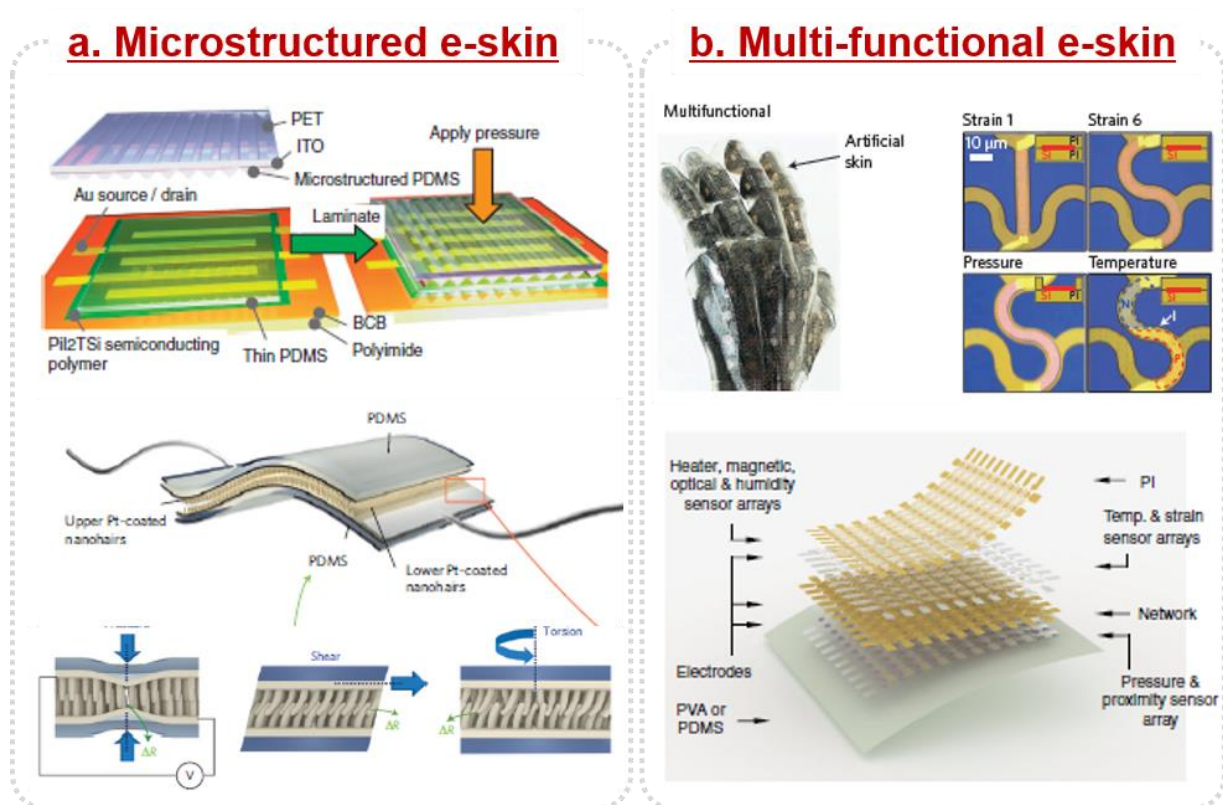


**Figure 1.4.** Representative examples for recent high performance and multifunctional electronic skin. (a) Electronic skins with various microstructures for improved sensor performances. (top) Capacitive sensor with micropyramid-patterned dielectric layer and field effect transistor (G. Schwartz et al. *Nat.*

*Commun.* **2013**, 4, 1859). (bottom) Multidirectional piezoresistive sensor with interlocked micropillar arrays (C. Pang et al. *Nat. Mater.* **2012**, 11, 795). (b) Multifunctional electronic skins integrated various sensors by interconnects which are silicon nanoribbon (top) and polyimide wire (bottom) (J. Kim et al. *Nat. Commun.* **2014**, 5, 5747, Q. Hua et al. *Nat. Commun.* **2018**, 9, 244).

### 1.3 Working principles of various electronic skins

Various types of electronic skins can be classified depending on their signal transduction modes; piezoresistivity, capacitance, piezoelectric, and triboelectricity (Figure 1.5). According to their intrinsic working principles, electronic skins show different properties such as responsivity, reactivity to specific stimuli, and self-power generation, which can determine the target applications. Specifically, piezoelectric and triboelectric sensors show spontaneous responsivity and energy harvesting properties, which are suitable for applications requiring the detection of dynamic stimuli without external power source. On the other hand, the piezoresistive and capacitive sensors are suitable for the detection of static forces applied in different directions and environmental conditions such as temperature, humidity, and chemicals. The detailed working principles of each electronic skins are described as below.

*Piezoresistivity:* The piezoresistive sensors, one of the most widely used transduction modes, recognize various tactile stimuli through the change of electrical resistance. In this system, the resistance change can be attributed to several factors including the band-structure changes in semiconductors,<sup>22, 23</sup> variations in contact resistance between conducting materials,<sup>24</sup> and alternation of conductive networks under mechanical deformations.<sup>25</sup> As representative examples, various carbon materials such as carbon particles, carbon nanotubes, and graphenes are used as conductive fillers in the elastomeric matrix for the fabrication of piezoresistive films (Figure 1.5a). When the mechanical stress is applied to piezoresistive films, the morphology of conductive fillers within the matrix is changed, thus resulting in the modulation of conductive networks and the electrical conductivity. In this materials configuration, the amounts of conductive fillers are controlled close to the percolation threshold of fillers, resulting in highly sensitive piezoresistive films. In addition to internal conductive network changes in composites, the resistivity change of single conductive films by the reversible fracture formation can be another operation principle in piezoresistive sensors.

*Capacitance:* Capacitive sensors have recently attracted much attention owing to their high sensitivity to external stimuli, fast response time, low power consumption and simple device structures. The capacitance ( $C$ ) of a parallel-plate capacitor is expressed as  $C = (\epsilon \cdot A)/d$ , where  $\epsilon$  is the dielectric constant,  $A$  is electrode area, and  $d$  is the distance between two electrodes, respectively. As is evident from the equation, all the variables can be sensitively changed under mechanical stimuli, resulting in the realization of capacitive e-skins (Figure 1.5b). In particular, the control of micro/nanostructures in dielectric layers has been widely investigated to increase the pressure-sensitive variation of effective dielectric constants, which results in the improvement of sensitivity and response/relaxation time in capacitive sensors.

*Piezoelectricity:* Piezoelectricity is the ability of certain materials to generate electrical charges in response to mechanical stress. The mechanical stress on piezoelectric materials induces the deformation of oriented non-centrosymmetric crystal structures, leading to the separation of electric dipole moments



and the generation of piezoelectric voltage (Figure 1.5c).<sup>26, 27</sup> This stress-responsive property of piezoelectric materials has been utilized in the development of energy-harvesting devices that convert mechanical stimuli into useable electrical energy.<sup>28, 29</sup> In addition to energy-harvesting devices, the ability of piezoelectric materials to generate different levels of electricity in response to various mechanical stimuli enabled the realization of self-powered piezoelectric skins with tactile sensing capabilities. Because of their high sensitivity to dynamic pressure and fast response time, self-powered piezoelectric e-skins have been widely used in the detection of dynamic pressures, such as vibration, sound, and slip.

Piezoelectricity can be observed in various inorganic and organic materials. Inorganic piezoelectric materials such as ZnO,<sup>30</sup> lead zirconium titanate (PZT),<sup>31</sup> and BaTiO<sub>3</sub><sup>32</sup> exhibit high piezoelectric coefficients ( $d_{33}$ ), but their intrinsic rigidity restricts their applications in flexible e-skins. On the other hand, organic materials (PVDF and PVDF-based copolymers)<sup>33-35</sup> with high flexibility are applicable to flexible e-skins, but their low  $d_{33}$  should be improved for high-performance e-skins. To address these issues, hybridized inorganic piezoelectric materials with flexible substrates and composites of inorganic fillers and PVDF matrix have been introduced. In addition, the formation of micro/nanostructures in piezoelectric materials is regarded as another method to improve the piezoelectric performances.

*Triboelectricity:* Triboelectricity induces electrical charges on the surface of materials, when two different materials are rubbed with each other via contact motions such as vertical touch, shear friction from sliding motion, and torsional stress. The amount of charges generated via the triboelectric charging process depend on the difference in triboelectric polarities between the two contacting materials.<sup>36, 37</sup> The larger the difference in triboelectric polarities, the larger the amount of opposite charges on each of the surfaces. When the triboelectric charging effect is combined with the phenomenon of electrostatic induction, the accumulated charges can be driven to flow through an external circuit, resulting in the flow of electrical current and thus the conversion of mechanical energy into electrical energy.

The principle of triboelectric generators that convert mechanical energy into electrical energy is shown in Figure 1.5d. When the two materials with different triboelectric polarities come into contact with each other, the triboelectric effect induces the formation of opposite charges on each side of surfaces. Subsequently, when the two materials are separated by releasing external stress, compensating charges are generated at each side of the top and bottom electrodes to maintain electrostatic equilibrium. This electrostatic induction process drives the electron flow from the top to bottom electrodes along the external circuit. Similarly, when the two materials are forced into contact with each other, the electrical charges flow in the opposite direction to maintain electrostatic equilibrium. This process enables the triboelectric device to generate electrical signals in response to various mechanical stimuli, leading to the realization of self-powered sensors.<sup>38, 39</sup>

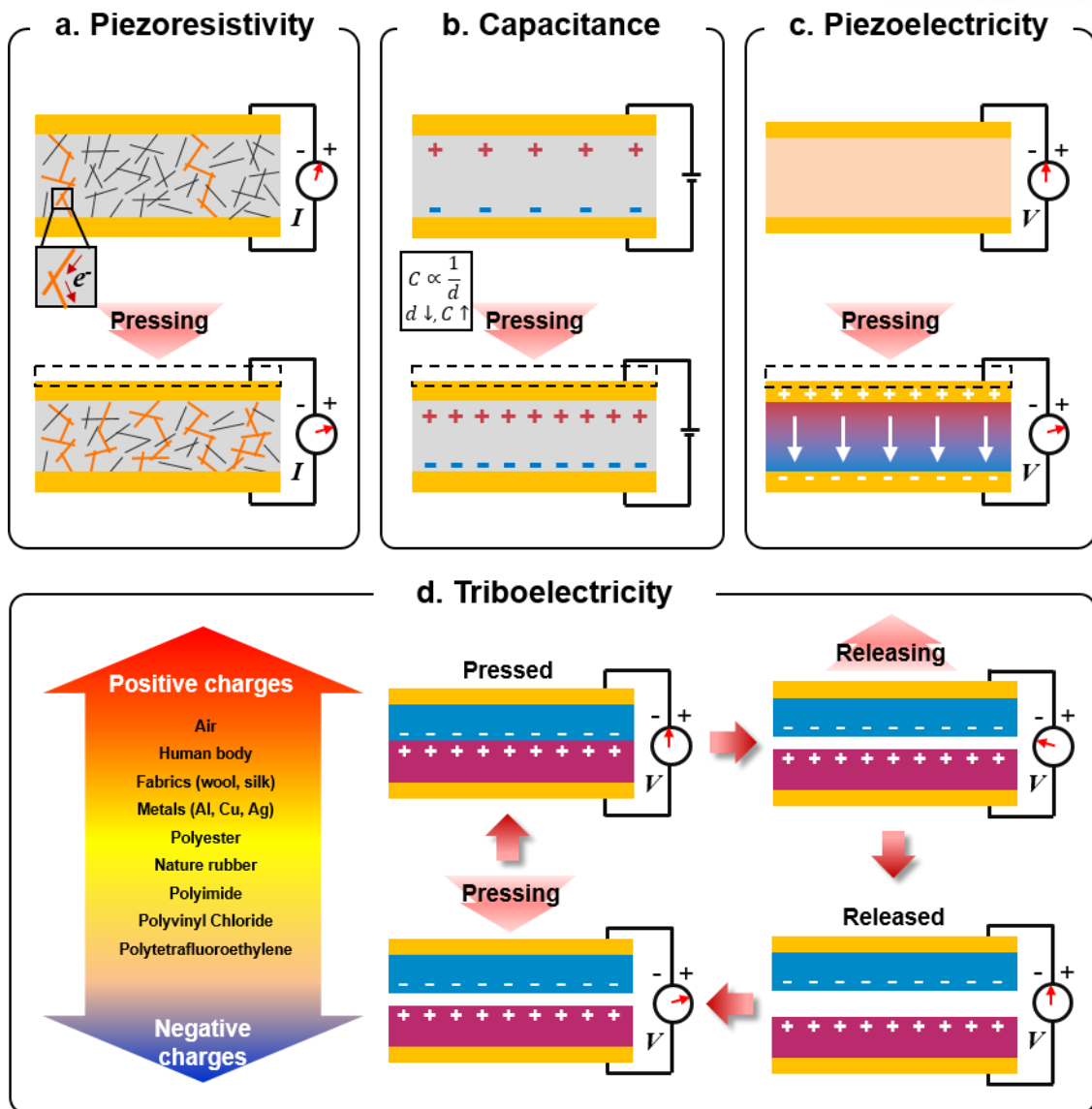


**Figure 1.5.** Working principle of electronic skins with common transduction modes. (a) Piezoresistive sensor based on the modulation of conductive network. (b) Capacitive sensor of a parallel-plate capacitor. (c) Piezoelectricity generated in single film. (d) Triboelectricity. (left) Triboelectric series from positive to negative tendency for common materials. (right) Operating mechanism of pressure sensing based electrostatic induction and triboelectric effect in a short-circuit system.

#### 1.4 Microstructured electronic skin

Owing to the growing demands for the improved performance of self-powered and multifunctional e-skins, many efforts have been made to introduce novel materials and structural designs. In particular, various design strategies based on bio-inspired micro/nanostructures and 2D/3D structures have been reported to increase the e-skin's sensitivity, selectivity, response time, mechanical compliance, and device pixel resolution (Figure 1.6). In bio-inspired micro/nanostructures, interlocking,<sup>19</sup> hierarchical,<sup>6</sup> crack,<sup>40</sup> and whisker<sup>41, 42</sup> structural designs have mimicked the biological structures to acquire high surface area, easy deformation, and the stress-direction-sensitive variation of structural deformations, leading to the highly sensitive response to normal, tensile, shear, and vibration forces as well as multidirectional stress sensing. The unique fingerprint patterns and epidermal-dermal microstructures of the skin at human fingertips amplify the pressure and vibration signals for texture perception and slip detection, which help in exactly recognizing various surfaces of arbitrary objects.<sup>43</sup> Similarly, 2D and 3D microstructures such as pyramid-<sup>44</sup> or dome-shaped<sup>45, 46</sup> surfaces and porous structures<sup>47, 48</sup> have been also utilized to improve the sensor performances. In addition, wavy, wrinkle, and serpentine structures have been utilized to enhance the stretchability of interconnect electrodes and sensor devices.<sup>49-51</sup> Controlling unique microstructures in sensor systems is an effective way to develop high-performance electronic skins for various applications.

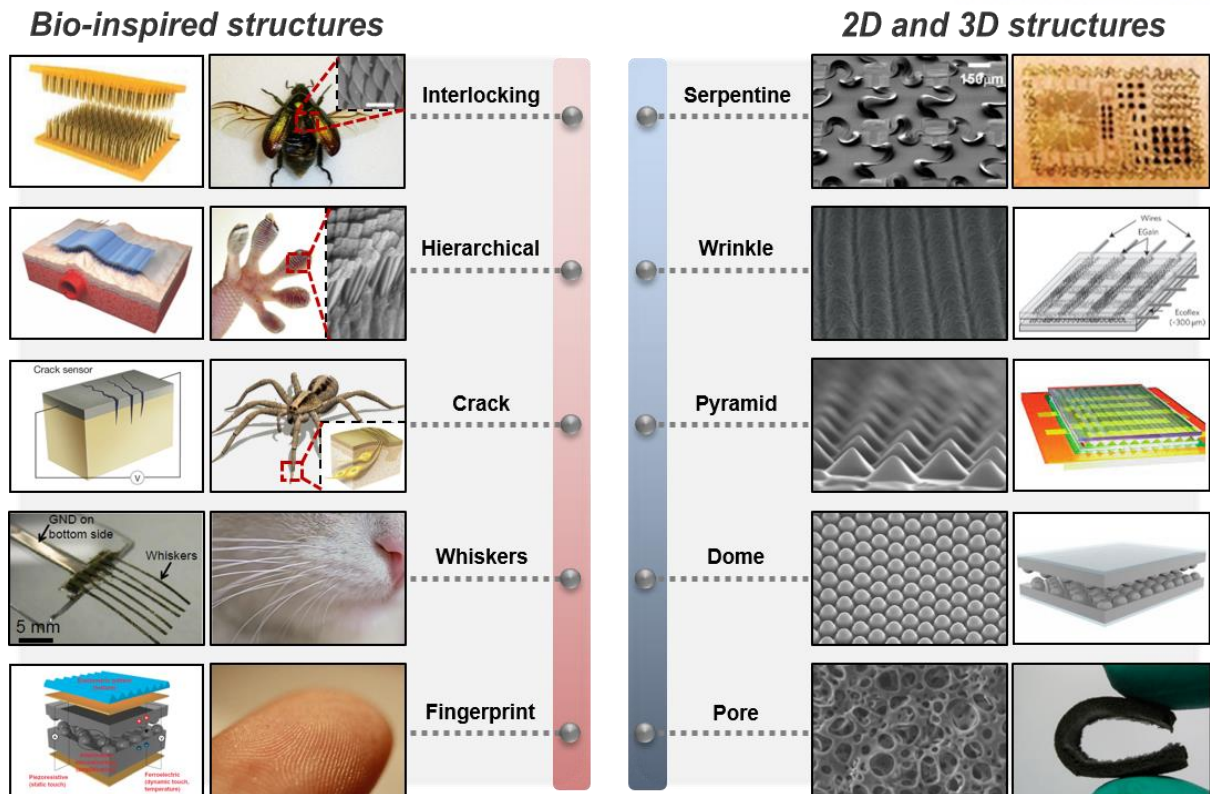


**Figure 1.6.** Bio-inspired structures (interlocking, hierarchical, crack-based, whisker, and fingerprint structures) and 2D and 3D structures (serpentine, wrinkle, pyramid, dome, and pore structures). “Interlocking:” C. Pang et al. *Adv. Mater.* **2012**, 24, 475. “Hierarchical:” C. Pang et al. *Adv. Mater.* **2015**, 27, 634. “Crack:” D. Kang et al. *Nature*, **2014**, 516, 222. “Whiskers:” K. Takei et al. *Proc. Natl. Acad. Sci.* **2014**, 111, 1703. “Fingerprint:” J. Park et al. *Sci. Adv.* **2015**, 1, e1500661. “Serpentine:” D.-H. Kim et al. *Science*, **2011**, 333, 838. “Wrinkle:” D. J. Lipomi et al. *Nat. Nanotechnol.*, **2011**, 6, 788. “Pyramid:” G. Schwartz et al. *Nat. Commun.*, **2013**, 4, 1859. “Dome:” J. Park et al. *ACS Nano*, **2014**, 8, 4689. “Pore:” Y. Qin et al. *ACS Nano*, **2015**, 9, 8933.

### 1.3.1 Bio-inspired microstructures for electronic skin

The bio-inspired micro/nanostructures provide an efficient strategy to improve the sensitivity and to obtain multiple sensing capabilities. As mentioned previous chapter, in human fingertip skin, the interlocked geometry of intermediate ridges at the epidermal–dermal junction plays a critical role in the efficient magnification and transduction of tactile stimuli to nearby mechanoreceptors. This capability of interlocked intermediate ridges has been attributed to the stress concentration on the intermediate ridge tips.<sup>52, 53</sup> Motivated by the interlocked epidermal–dermal layers, our group demonstrated tactile-direction-sensitive e-skins with an interlocked microstructure geometry (Figure 1.7a).<sup>45, 46</sup> In this sensor system, the localized stress at the contact points between neighbouring microdome arrays can provide a large variation of contact area and thus the large variation of tunnelling piezoresistance, leading to high pressure sensitivity. Furthermore, the unique geometry of interlocked microdome arrays also provides different levels of deformation in response to various mechanical stimuli (normal, shear, stretching, bending, and twisting forces), which resulted in the demonstration of tactile-direction-sensitive e-skins. In addition to human skin, the bio-inspired interlocked and hierarchical structure, which can be founded beetle wings and dragonflies, induce effective stress propagation and a large contact-area change between neighboring microstructures in response to mechanical stress, resulting in high piezoelectric sensitivity (Figure 1.7b).<sup>6, 54, 55</sup>

As another bio-inspired structure, the formation of micro/nanoscale cracks on the sensor materials has been suggested for improving mechanical sensitivity. The nanoscale cracks can easily be deformed in response to small external forces, which leads to the sensitive variation of electrical resistance in response to mechanical stimuli including vibrations and static mechanical forces (pressure, strain, etc.) (Figure 1.7c).<sup>40</sup> In addition, bio-inspired sensing structures found in whisker structures in insects and mammals, which have functions to monitor and recognize air-flow and surrounding obstacles through the deformation of hair-like structures (Figure 1.7d).<sup>42, 56, 57</sup> Additionally, the bending direction of whiskers helps to distinguish the direction of applied forces.

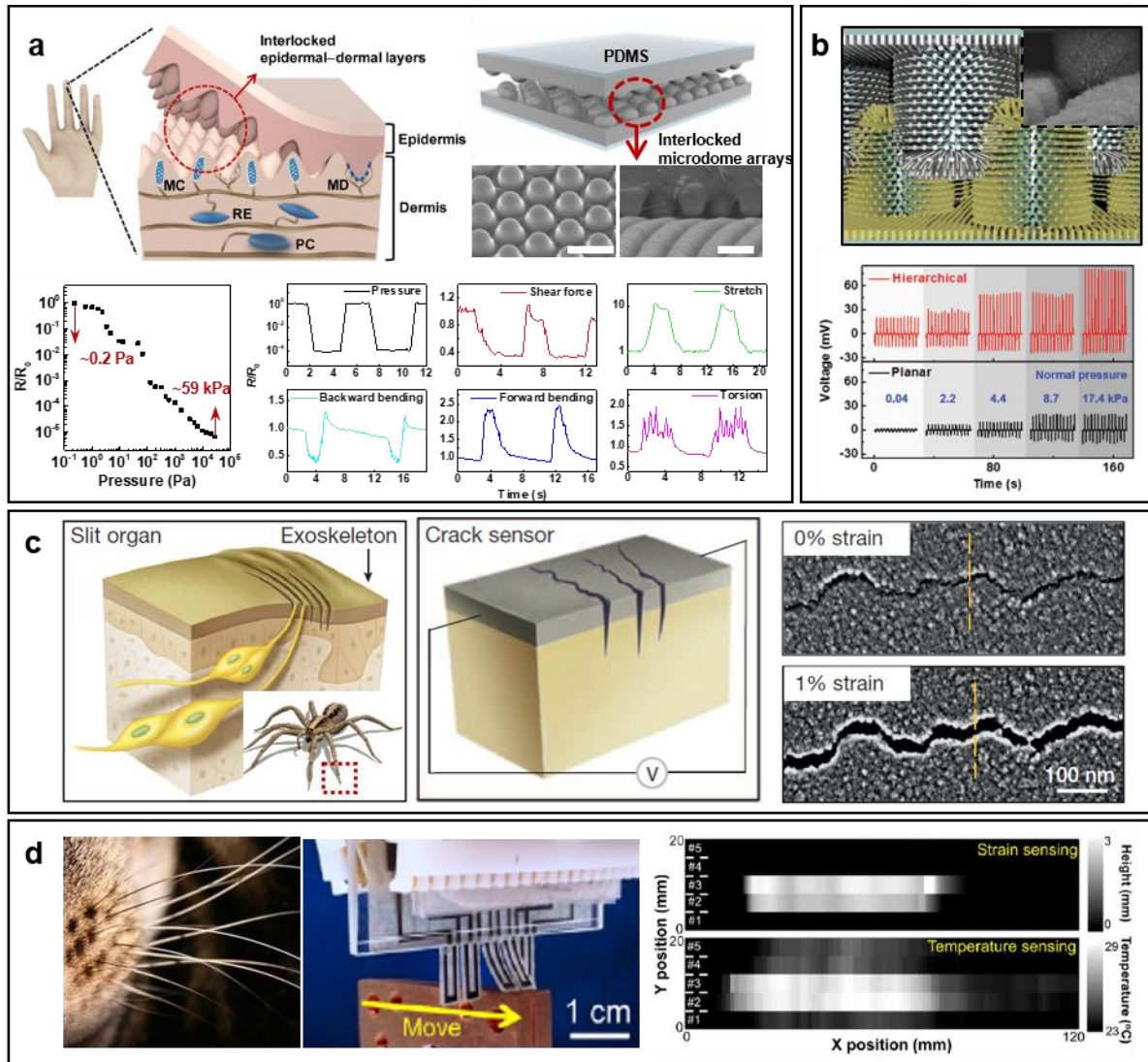


**Figure 1.7. Bio-inspired nano/microstructures for electronic skin.** (a) Human-skin-inspired electronic skins with interlocked microdome arrays. (J. Park et al. *ACS Nano*, **2014**, 8, 4689, J. Park et al. *ACS Nano*, **2014**, 8, 12020). (b) Bio-inspired self-powered e-skins based on the interlocking geometry of ZnO nanowires on microstructured PDMS. (M. Ha et al. *Adv. Funct. Mater.*, **2015**, 25, 2841) (c) Crack-based ultrasensitive strain sensors inspired by the spider's sensory system. (D. Kang et al. *Nature*, **2014**, 516, 222). (d) Whiskers of a mammal and multifunctional artificial electronic whisker arrays (W. Honda et al. *Adv. Funct. Mater.* **2014**, 24, 3299).

### 1.3.2 2D and 3D microstructures for electronic skin

In addition to bio-inspired electronic skins, the introduction of various 2D/3D micro/nanostructures to electronic skins has been suggested to improve the performance of sensors. While conventional sensing elements based on non-structured composite materials have issues such as narrow sensing range, low sensitivity, slow response/relaxation, and large hysteresis, the formation of micro/nanoporous structures in the sensing elements provides high deformability, fast response/relaxation speed, and increased contact area under the applied mechanical forces. Porous structures provide uniform and large contact area changes and high compressibility, which can enhance significantly the performance of e-skins including force sensitivity, response/relaxation time, and resilience (Figure 1.8).<sup>47</sup> For example, the hollow-sphere structure possesses high flexibility and a structure-derived low effective elastic modulus, leading to easy deformation and fast recovery under external pressure.<sup>24</sup> Furthermore, the porous structures in PVDF film induce a large film displacement between the pores, leading to large electric power generation under mechanical stimuli.<sup>58</sup>

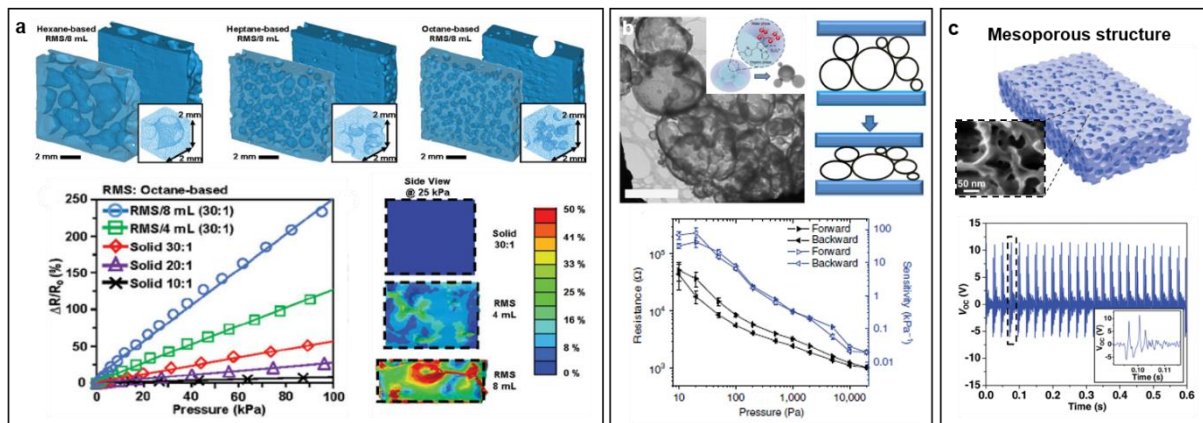


**Figure 1.8. 2D and 3D micro/nanostructures for electronic skins (Porous structure).** (a) Piezoresistive e-skin based on CNT/PDMS composites with micropores (S. Jung et al. *Adv. Mater.*, **2014**, 26, 4825). (b) Highly sensitive pressure sensor based on hollow-sphere microstructured PPY (L. Pan et al. *Nat. Commun.*, **2014**, 5, 3002). (c) Mesoporous PVDF-film-based piezoelectric nanogenerators (Y. Mao et al. *Adv. Energy Mater.*, **2014**, 4, 1301624).

Surface structuring into microscale pyramid, pillar, and dome shapes is an efficient way to increase piezoresistive properties. The microstructured surfaces provide a large contact-area variation and high compressibility under mechanical stimuli, leading to piezoresistive e-skins with high sensitivities and wide dynamic ranges (Figure 1.9a). In addition, microstructured piezoelectric e-skin with trigonal line-shaped and pyramid-shaped micropatterned P(VDF-TrFE) produce nearly several times larger voltage output, compared to flat-film-based piezoelectric e-skin (Figure 1.9b). Through the modulation of conductive networks and morphologies of films, wrinkles and buckled structures are also used to achieve strain-sensing property (Figure 1.9c).

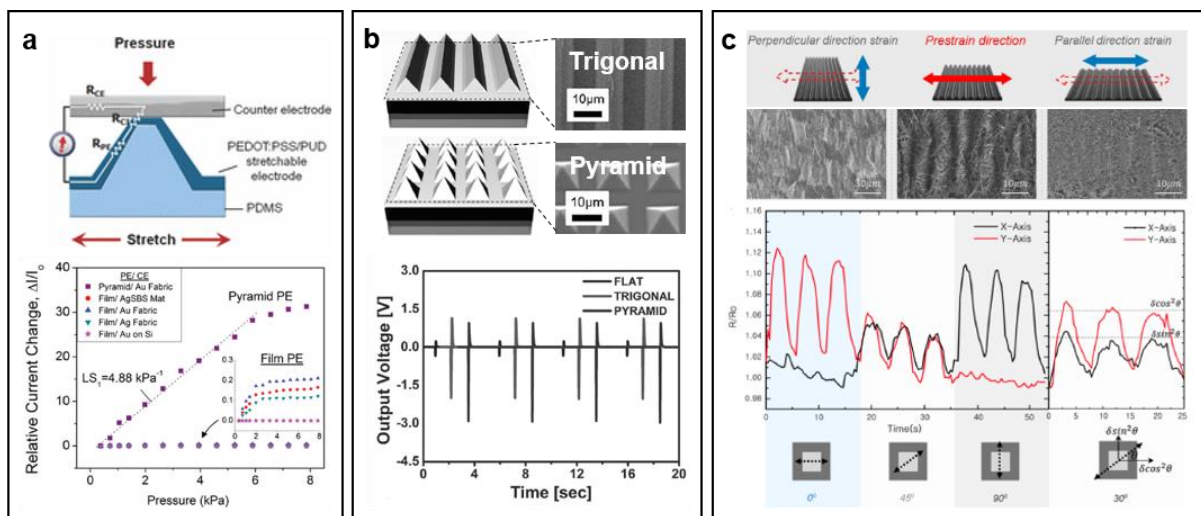


**Figure 1.9. 2D and 3D micro/nanostructures for electronic skins (Surface microstructure and wrinkle structure).** (a) Highly sensitive pressure sensors based on conductive electrodes on micropyramid PDMS arrays (C. L. Choong et al. *Adv. Mater.* **2014**, 26, 3451). (b) Micropatterned P(VDF-TrFE) film-based piezoelectric nanogenerators for pressure sensors (J. H. Lee et al. *Adv. Funct. Mater.* **2015**, 25, 3203). (c) Strain sensors based on Ag nanowires on buckled elastomers (K. K. Kim et al. *Nano Lett.*, **2015**, 15, 5240).



## 1.4 Applications

### 1.4.1 Flexible electronics & sensors

Flexible and self-powered e-skins can find wide applications in wearable, skin-attachable, and implantable electronics for future human–machine interfacing and healthcare monitoring systems.<sup>59-63</sup> For the user-friendly wearable devices, highly flexible and foldable textiles decorated with nanowires have been used in triboelectric systems to demonstrate a self-powered suit that powers the displays and remote controllers for human–machine interface systems (Figure 1.10a).<sup>64</sup> This textile-type triboelectric system has a potential advantage of enabling an intimate contact with the human body, and can thus provide facile energy harvesting from daily human motions. Invisibility in self-powered electronics is advantageous in applications in anti-theft and anti-fake systems (Figure 1.10b). Transparent and flexible triboelectric systems have been demonstrated based on the electrostatic induction effect on CNT and nanocellulose papers, which can detect finger pressure and generate energy to light LCD monitors for future security surveillance.<sup>65</sup> Similarly, self-powered systems can harvest energy from wind flow and raindrops and subsequently use the harvested energy to activate electrochromic materials for smart window applications.<sup>66</sup>

Piezoelectric self-powered e-skins with excellent sensitivity and fast response time to dynamic mechanical stimuli can be used to detect acoustic sounds with high-frequency vibrations (Figure 1.10c).<sup>67</sup> This device structure enables the instantaneous deformation and relaxation of flexible inorganic PZT thin film and thus the subsequent variations in piezoelectric voltage, resulting in the detection of high-frequency sounds. The precise monitoring of sound waveforms by piezoelectric e-skins can be used for next generation wearable microphone which can selectively detect the specific frequency. Triboelectric self-powered sensors with extremely fast response can detect and trace instantaneous human-body motion and mobile objects. Single-electrode-based triboelectric sensors modified with polymeric nanowires accurately detect moving objects and human-body motion (Figure 1.10d).<sup>68</sup> Furthermore, charge-susceptible triboelectric sensors enable the detection of different charged solvents and molecules for chemical sensors. TiO<sub>2</sub>-nanostructure-based triboelectric sensors can detect water molecules with positive tribo-charges as well as the mechanical force exerted by a falling water droplet (Figure 1.10e).<sup>69</sup> In addition, the chemically modified nanostructure arrays can even recognize catechin<sup>70</sup> or dopamine molecules<sup>63</sup> from the variation of the triboelectric effect. These results demonstrate that triboelectric sensors can be a promising candidate for chemical sensors.

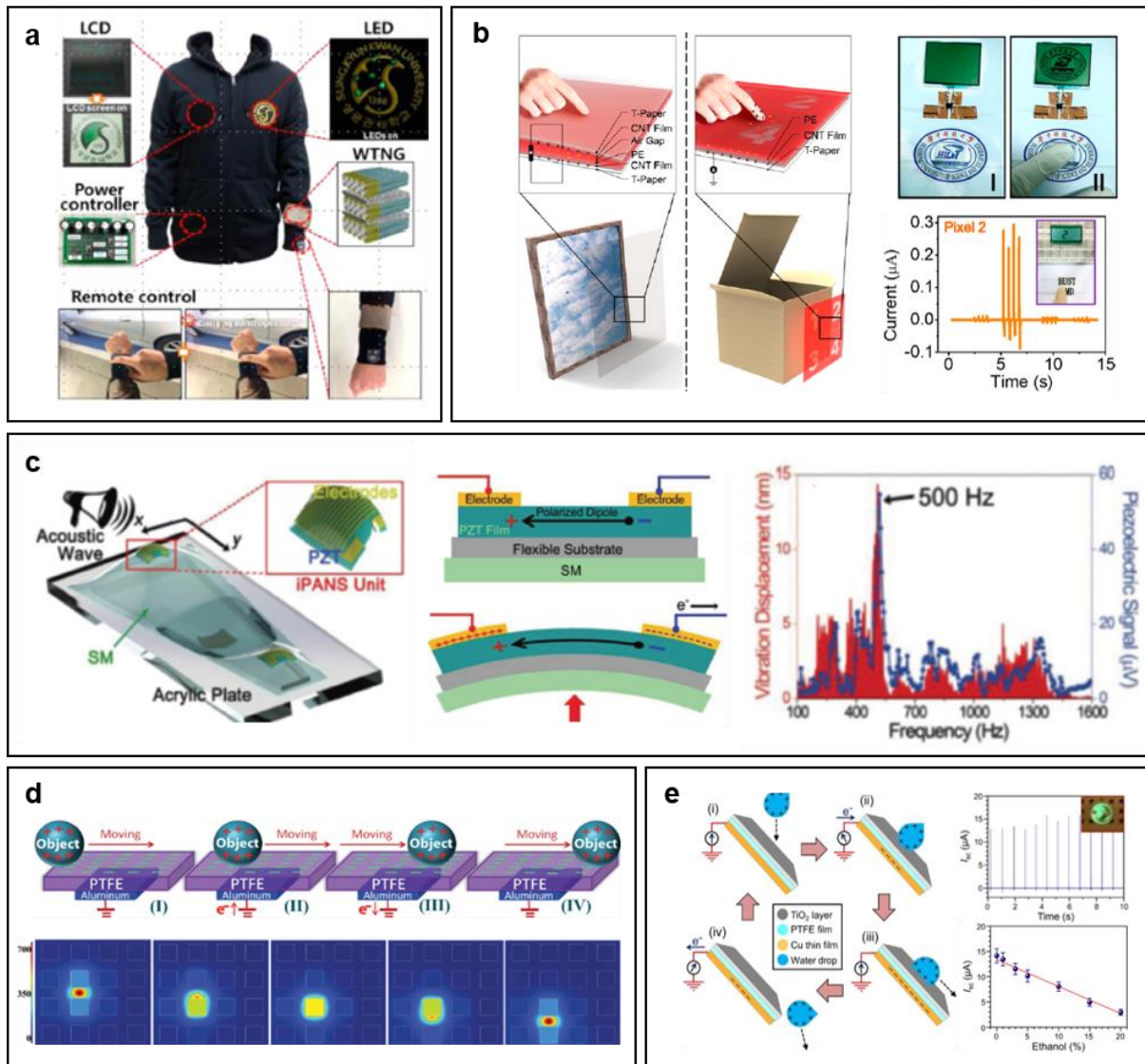


**Figure 1.10. Applications of flexible electronics and sensors.** (a) Nanopatterned-textile-based wearable triboelectric nanogenerators integrated with commercial LCD, LEDs, and remote control (W. Seung et al. *ACS Nano*, **2015**, 9, 3501). (b) Transparent-nanopaper-based smart mapping anti-fake system (X. Wang et al. *Adv. Mater.*, **2015**, 27, 2324). (c) Acoustic sound sensor based on piezoelectric e-skins with inorganic PZT thin film. (H. S. Lee et al. *Adv. Funct. Mater.* **2014**, 24, 6914). (d) Triboelectric sensors for trajectory, velocity, and acceleration tracking of moving objects. (F. Yi et al. *Adv. Funct. Mater.* **2014**, 24, 7488). (e) Triboelectric nanogenerators for harvesting water energy and applications as ethanol sensors (Q. Shao et al., *Small*, **2014**, 10, 1466).

#### 1.4.2. Prosthetics and robotics

E-skins with mechanical reliability and high sensitivity to complex mechanical stimuli can be used in prosthetics and robotics.<sup>71, 72</sup> Kim and co-workers demonstrated flexible prosthetic skins based on stretchable silicon nanoribbon electronics that can simultaneously detect multiple external stimuli of strain, pressure, temperature, and humidity (Figure 1.11a).<sup>20</sup> For robotics applications, the highly sensitive strain sensor can perceive multiple deformations such as strain, bending, and torsion stimuli and thus monitor complicated robotic movements in real time (Figure 1.11b).<sup>73</sup> In addition to sensing simple mechanical stimuli including normal pressure, strain, and bending, texture perception is an important functionality of human fingertip skin (Figure 1.11c).<sup>74-76</sup> The fingerprint pattern on the sensing element amplifies vibrotactile signals when the e-skin is scanned over the surface of objects. Subsequently, the piezoresistive composite of PDMS and CNT with interlocked geometry under the fingerprint pattern perceives the amplified vibrotactile signals from various surface textures (e.g. different fabrics) and discriminates various surface morphologies and information including the pattern shapes and surface hardness/softness. The e-skins with texture-perception capability will accelerate the development of multifunctional prosthetics and intelligent robotics that exceed the capabilities of existing e-skins.<sup>77</sup>

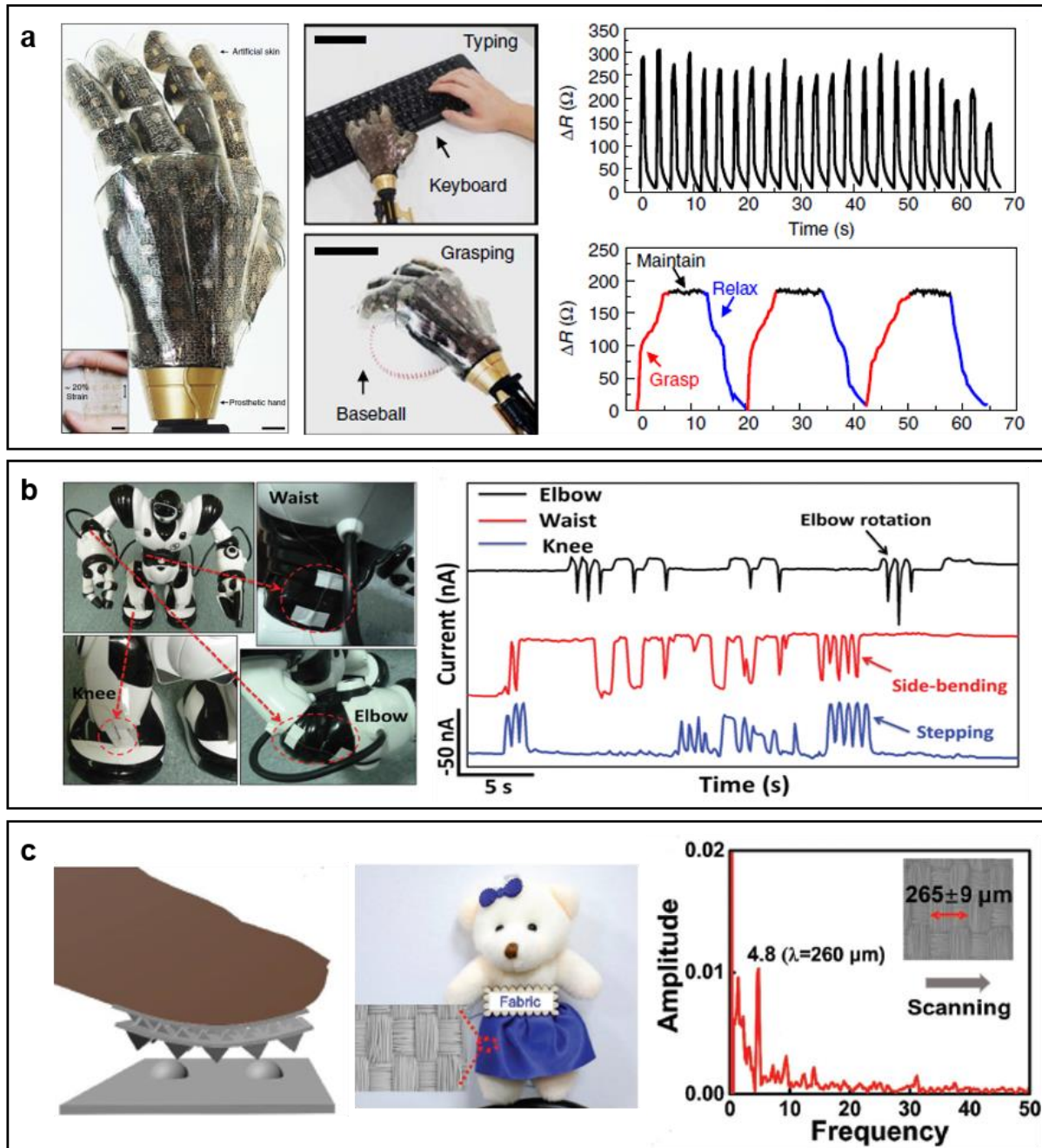


**Figure. 1.11. Application of e-skins for prosthetics and robotics.** (a) Multifunctional prosthetic skins that can detect the strain, pressure, temperature, and humidity and associated with heater and Pt-nanowire-based multi-electrode (J. Kim et al. *Nat. Commun.*, **2014**, 5, 5747). (b) Strain sensors attached at the moving joints of robots (X Li et al., *Adv. Mater.* **2015**, 27, 4447). (c) Texture perception by scanning fingertip-skin-inspired e-skin with interlocked geometry and a fingerprint pattern over a patterned surface (Y. Cao et al. *Small*, **2018**, 14, 1703902).

### 1.4.3. Biomedical devices

Flexible e-skins with high sensitivity to mechanical stimuli can be used to monitor the vital signals of the human body precisely, thereby providing efficient and non-invasive medical diagnosis (Figure 1.12). For example, the real-time monitoring of arterial pulse provides useful information such as arterial blood pressure and heart rate, which are associated with cardiovascular diseases such as arteriosclerosis, diabetes, and hypertension.<sup>78, 79</sup> In addition to arterial pulse, the detection of respiration is another important application of e-skins because respiration rate and breathing pattern are important vital signs that can indicate a person's lung function and quality of sleep.<sup>80-82</sup> Rogers and coworkers demonstrated flexible and stretchable e-skins integrated on the brain, heart, and skin to monitor disease states and improve surgical procedures.<sup>51, 83</sup> This multifunctional inflatable balloon catheter, which is an invasive medical device, integrated with tactile, optical, temperature, electrocardiogram (ECG), and flow sensors as well as radiofrequency electrodes for the ablation of tissue.<sup>15</sup>

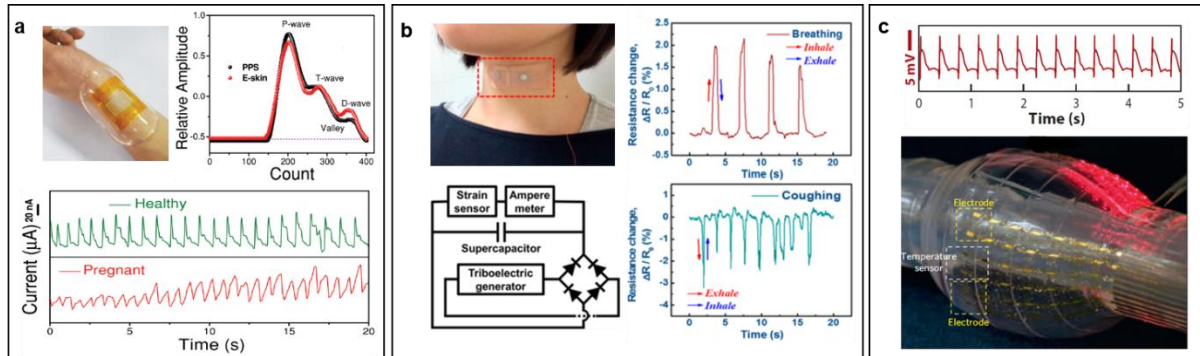


**Figure 1.12. Applications of e-skins in biomedical devices.** (a) Artery pulse pressure monitoring devices (X. Wang et al., *Adv. Mater.* **2014**, 26, 1336). (b) Strain sensors integrated with a supercapacitor and triboelectric nanogenerator for respiration monitoring device (B.-U. Hwang et al., *ACS Nano*, **2015**, 9, 8801). (c) Multifunctional inflatable balloon catheters in inflated states and an electrogram from the right ventricle of a rabbit heart detected by a multifunctional balloon catheter (D.-H. Kim et al, *Nat. Mater.* **2011**, 10, 316). Reproduced with permission.<sup>130</sup> Copyright 2011, Nature Publishing Group.

## Chapter 2. Piezoresistive composite elastomers with interlocked microdome arrays for ultrasensitive and multimodal electronic skins

### 2.1 Introduction

Human skin possesses a high degree of flexibility and stretchability and can sense pressure, shear, strain, temperature, humidity, fluid flow and pain. As such, it is an ideal system to model multifunctional and flexible electronic skins,<sup>84,85</sup> which are used in wearable electronics, prosthetic limbs, robotic skins, and remote surgery, as well as in a wide range of other electronic and biomedical applications.<sup>11, 12, 15, 18, 19, 34, 72, 86-91</sup> Proposed and implemented approaches for realizing flexible and sensitive electronic skins include systems based on resistive<sup>11, 12, 19, 72, 87, 89, 91</sup>, capacitive<sup>18, 88, 90</sup>, piezoelectric<sup>34, 92</sup> and triboelectric<sup>93</sup> modes of operation. Although such systems have yielded performances that satisfy or exceed the sensing capabilities of human skin, the development of flexible electronic skins that possess multimodal sensing capabilities for the detection of subtle environment changes remains challenging.

Piezoresistive composite elastomers hold substantial promise for the realization of electronic skins, owing to their inherent flexibility, stretchability and chemical stability and simple, scalable and low-cost fabrication processes. Traditionally, conductive fillers such as carbon blacks, graphites, metal particles and carbon nanotubes (CNTs) are incorporated into elastomers to generate piezoresistive behavior. The piezoresistivities are primarily attributed to the variation in tunneling resistance when the inter-filler distance changes under external stress.<sup>94-96</sup> To maximize these piezoresistive effects, the concentration of conductive fillers is kept near the percolation threshold; under external stress, the resistance then changes sharply. However, sensors that are based on composite elastomers suffer from poor sensitivities and are not suitable for detection in low-pressure regimes (< ~10 kPa). Moreover, they exhibit negative effects under temperature variation, due to polymer swelling and changes in inter-filler distances.<sup>97, 98</sup> Finally, the intrinsic viscoelastic properties of composite elastomers result in significant hysteresis and slow response/relaxation times<sup>99</sup>, which present a significant challenge for their applications in high-performance electronic skins. In this study, we demonstrate a novel design for conventional piezoresistive composite films that overcomes many of the shortcomings listed above.

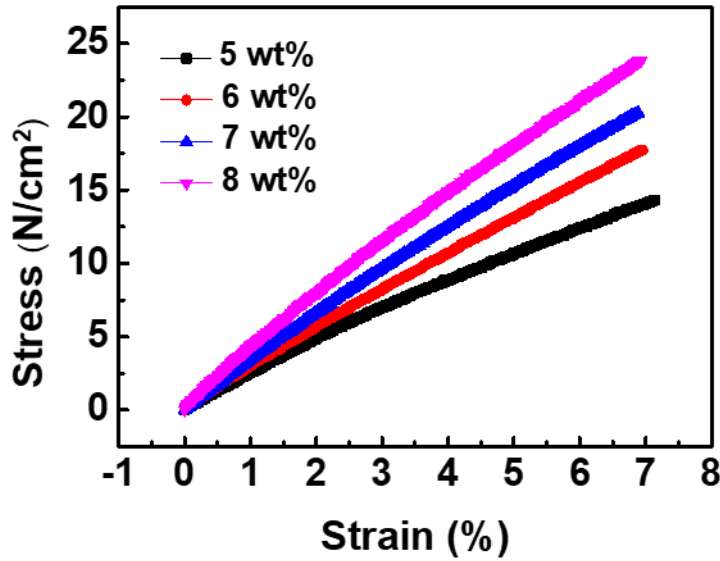
## 2.2 Experimental Details

**Elastomeric composite films with microdome arrays:** For the fabrication of the pre-cured CNT–PDMS composite mixtures, multi-walled nanotubes (MWNTs, Sigma Aldrich) with diameter ranging from 110 to 190 nm and length ranging from 5 to 9  $\mu\text{m}$  were dispersed in chloroform by sonication for 6 hours. The dispersed MWNT solution was completely mixed with a PDMS base (Sylgard 184, Dow Corning) using a vortex mixer. Chloroform was subsequently removed by evaporation for 6 hours at 90°C on a hot plate. Immediately prior to the micromolding process, hexane and the PDMS curing agent (1:10 ratio for curing agent to base) were added to the dried MWNT–PDMS composite mixtures (at a ratio of 1 ml hexane for each 500 mg of PDMS) and mixed with a vortex mixer for 5 minutes. For the fabrication of composite microdome arrays, the composite mixture was cast onto a silicon micromold with periodic hole arrays (dimensions: 3.5  $\mu\text{m}$  diameter, 6  $\mu\text{m}$  pitch, and 1 cm  $\times$  1.5 cm surface area) and thermally cured at 90°C for 3 hours. The thicknesses of the composite films were controlled to be  $\sim$ 500  $\mu\text{m}$ . For the fabrication of the sensor arrays, platinum electrode lines with widths of  $\sim$ 5  $\mu\text{m}$  were deposited on thin PDMS films ( $\sim$ 500  $\mu\text{m}$ ) by sputter coating (EMITECH, K575X). The interlocked composite films were sandwiched between two PDMS films with platinum electrode lines. The tubular-type flow sensors were fabricated by inserting the interlocked films into micropipette tips (with a diameter of 1.2 cm and length of 5 cm).

**Characterization:** The microstructures of the composites were characterized using a field-emission scanning-electron microscope (SEM) (S-4800, Hitachi). The sheet resistance of the planar composite films was measured using a four-point-probe method (4200-SCS, Keithley). The change in electrical resistance of the microdome-patterned composites under various force conditions was measured using a two-probe method in which copper tapes were attached to each side of the microdome-patterned composite with silver paste and annealed at 100°C for 1 hour. A home-built microstage system (Micro Motion Technology, Korea) was used to apply normal forces to the composite films and a weight balance underneath was used to measure the forces. To evaluate the flow-detection capability, the skin sensors were exposed to argon flow (ranging from 1 to 5.3 m/s). The skin’s vibration-detection capability was measured using a coin-type vibration motor (DVM1034, Motorbank Co., Korea) that controlled the intensity of the vibrations (0–2  $\text{m/s}^2$ ) and a vibrometer (ACO 3116, Guangzhou Orimay Electronic Co., Japan) that picked up the vibration intensities. The young’s moduli of composites were measured by tensile testing (universal testing machine, WL2100, WITHLAB Co., Korea) at a speed of 5mm/min.

**Finite-element method:** In the contact-area calculations, we performed structural analyses using finite-element simulations. We modeled composites that were reinforced by different weight percentages of CNTs as linear elastic materials using experimentally measured elastic constants (Figure

2.1). Periodic boundary conditions were applied to the in-plane directions and the bottom surface was fixed. All loading conditions were assigned through displacement control and converted to the corresponding pressure from reacting forces. We used more than 2.8 million four-node linear tetrahedral elements with an adaptive mesh-refinement scheme around the contact area. To model the mechanical contact between two deformable surfaces, a surface-to-surface contact scheme was employed.



CNT concentrations (wt%)	Elastic modulus (MPa)
5	2.3
6	2.6
7	3.3
8	3.9

**Figure 2.1.** Stress–strain curves of MWNT–PDMS composites and their elastic moduli.



### 2.3 Results and Discussion

The defining feature of our design is that we shape the composite elastomer films into interlocked microdome arrays. These films were fabricated by micromolding a liquid mixture composed of CNTs, polydimethylsiloxane (PDMS) prepolymer and a curing agent with a microhole-patterned silicon mold (Figure 2.2a). The micromolding process produces a flexible composite film with regular microdome arrays, characterized by a height of  $\sim 3 \mu\text{m}$ , a diameter of  $\sim 4 \mu\text{m}$  and a pitch of  $6 \mu\text{m}$  (Figure 2.2b). For the fabrication of electronic skins, two composite films with microdome arrays are combined with the patterned sides facing each other. This construction produces an interlocked geometry of microdome arrays (Figure 2.2c). The basic working principles of our electronic skins are illustrated in Figure 2.2d. The external pressure induces stress concentrations at the small contact spots and local deformations in the microdomes. In turn, the contact area between the interlocked microdome arrays increases significantly and affects the tunneling resistance at the contact spots. The result is a giant tunneling piezoresistance in the flexible films.

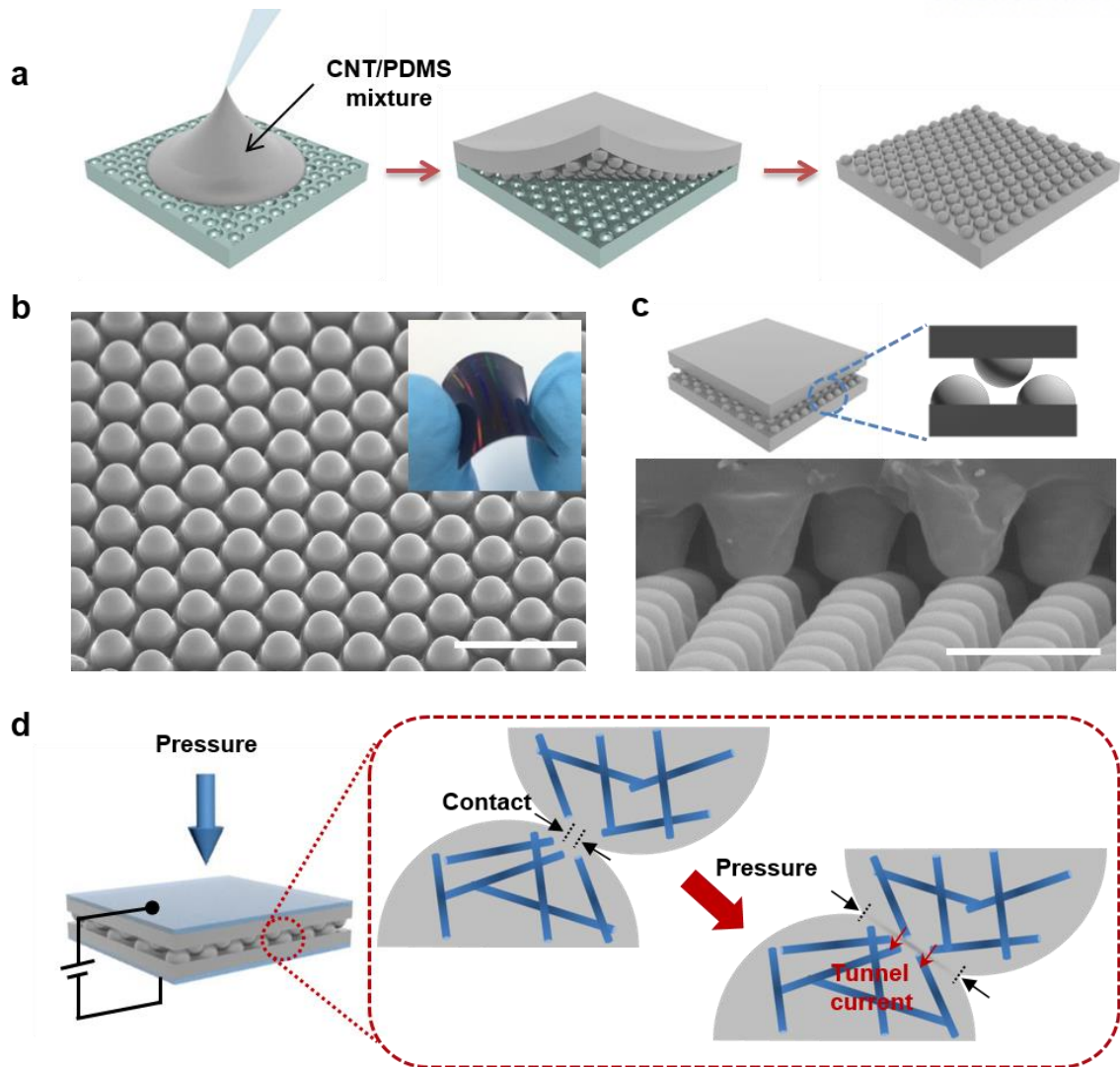


**Figure 2.2.** Conductive composite elastomers with interlocked microdome arrays. (a) Schematic of the fabrication procedure used to produce the CNT-composite elastomers with microdome arrays. (b) Tilted SEM image of the composite elastomers (bottom diameter:  $\sim 5 \mu\text{m}$ ; height:  $\sim 3.5 \mu\text{m}$ ; pitch:  $6 \mu\text{m}$ ). The inset photo highlights the flexibility of the arrays (scale bar:  $10 \mu\text{m}$ ). (c) Schematic (top) and cross-sectional-SEM image (bottom) of the composite films (scale bar:  $5 \mu\text{m}$ ). (d) Schematic showing the working principle of the electronic skin. The external pressure concentrates stress at the contact spots, deforming the microdomes, which in turn causes an increase in the contact area and the tunneling currents.

To demonstrate and quantify the effects of the interlocked geometry on piezoresistance, we compared the relative electrical resistances ( $R/R_0$ ) of composite films for three different configurations: a single planar array, a single microdome array and an interlocked microdome array (Figure 2.3a). Composite films with interlocked microdome arrays exhibit an abrupt switching behavior with  $R_{OFF}/R_{ON}$  ratios on the order of  $10^5$  when the applied pressure is increased from 0 to  $\sim 10$  kPa. For composite films with single microdome arrays and composite films with planar structures, the ratio  $R_{OFF}/R_{ON}$  is  $\sim 100$  and  $\sim 2$ , respectively. All these systems display a decrease in resistance as the pressure is increased. A switching ratio of  $10^5$  in a low-pressure range ( $< \sim 10$  kPa) compares favorably with the pressure-induced switching ratios in a high-pressure range achieved with piezoresistive composites<sup>100</sup> ( $\sim 10^6$  at  $\sim 1$  MPa) and rare-earth chalcogenide films<sup>101</sup> ( $\sim 10^3$  at  $\sim 2$  GPa). We attribute the significant decrease in resistance of the interlocked microdome arrays relative to the planar film primarily to the deformation of the microdome structures and the resulting variation in contact area, which affects the contact resistance ( $R_c$ ) between the microdome arrays. Conversely, the piezoresistance of planar films is mainly affected by the change in film resistance ( $R_f$ ) due to the decrease in inter-tube distances in the CNT conductive network within the composite film. We also note that the strong piezoresistive-switching behavior causes a nonlinear dependence of the resistance on pressure, which is in general observed for piezoresistive composites that exhibit tunneling effects.<sup>95</sup>

For quantitative analyses, the piezoresistive pressure sensitivity,  $S$ , is defined as  $S = (\Delta R/R_0)/(\Delta P)$  in the linear regime, where  $R$  and  $P$  are the resistances of the sensors and the applied pressure, respectively. In the low-pressure range ( $< 0.5$  kPa) of the linear regime, the sensitivities of interlocked microdome films ( $-15.1$  kPa<sup>-1</sup>) are  $\sim 3$  and  $\sim 24$  times higher than the sensitivities of single microdome films ( $-5.4$  kPa<sup>-1</sup>) and planar films ( $-0.6$  kPa<sup>-1</sup>), respectively, (Figure 2.4). They are also significantly higher than the sensitivities recently reported for a resistive graphene-polyurethane sponge<sup>102</sup> ( $0.26$  kPa<sup>-1</sup>) and capacitive microstructured films<sup>18</sup> ( $0.84$  kPa<sup>-1</sup>). The log-log plot (Figure 2.3b) of relative resistance as a function of pressure shows a linear decrease in relative resistance with an increase in pressure over a wide dynamic range ( $\sim 0.2$ – $59,000$  Pa), which indicates an exponential dependence of resistance on the applied pressure. In particular, we observed that the sensors can detect a minimum applied pressure of  $\sim 0.2$  Pa (Figure 2.5), which is below the gentle touch ( $\sim 1$  KPa) of human fingertips,<sup>103</sup> the minimum detection limits ( $> \sim 1$  kPa) of traditional piezoresistive composites,<sup>11</sup> and comparable with values recently reported for resistive ( $5$  Pa),<sup>19</sup> capacitive ( $3$  Pa),<sup>88</sup> piezoelectric ( $0.1$  Pa)<sup>34</sup> and triboelectric ( $0.4$  Pa)<sup>93</sup> sensors. The high sensitivities of our sensors are also verified by monitoring the dynamic time-resolved change in relative resistance as water droplets with a weight of  $\sim 8.7$  mg (corresponding to a pressure of  $\sim 0.6$  Pa) continuously fall onto the electronic skins (Figure 2.6).

The interlocked-microdome-array design offers the advantage of rapid response and relaxation times as compared with the planar composite films. This is due to the immediate pressure-induced surface

deformation of the microdomes, which overcomes the limitation of the slow viscoelastic behavior of bulk composites. The films with interlocked microdome arrays exhibit response/relaxation times of  $\sim 0.04$  s, which is an order of magnitude faster than the response/relaxation times of planar films ( $\sim 0.38\text{--}0.44$  s) (Figure 2.3c) and compares favorably with recent studies of other sensors (0.01–0.3 s).<sup>18, 19, 104</sup> A further advantage of the interlocked geometry is the reduced temperature dependence of the piezoresistance, which remains a challenging issue for conventional elastomeric composites, where the inter-filler distances change during the thermal expansion of the composites.<sup>98</sup> As the tunneling resistance of our sensors depends primarily on the variation in contact area, our sensors show minimal changes in relative resistances with temperature changes in the range from 30 to 90 °C (Figure 2.3d). In contrast, the planar composite films show temperature-dependent variations in the relative resistances. Moreover, our electronic skins also display minimal hysteresis effects (Figure 2.7a) and maintain their initial resistance after 1000 loadings of  $\sim 59$  kPa (Figure 2.7b).

To elucidate the working principles underlying the pressure sensitivity of our electronic skins, we calculated the tunneling resistance between the interlocked microdome arrays and compared these numbers with the experimental results. The tunneling resistance ( $R_t$ ) at the contact spots between the interlocked microdome arrays is given by  $R_t = (V/J)(1/A_{\text{CNT}})$ , where  $V$  is the applied voltage,  $J$  is the current density through the insulating layer between the interlocked microdome arrays and  $A_{\text{CNT}}$  is the electrical-contact area through which the current passes between electrically conductive CNT portions at the surface of the interlocked microdome arrays. The current density is estimated within the so-called Simmons model (Section S2.1).<sup>105</sup> In this model, when the applied voltage is smaller than the barrier height, the current  $J$  tunneling through a thin layer of insulating material between metal electrodes is expressed as:

$$J = \frac{e}{2\pi h \Delta s^2} \left[ \bar{\varphi} \exp\left(-\frac{4\pi \Delta s \sqrt{2m}}{h} \sqrt{\bar{\varphi}}\right) - (\bar{\varphi} + eV) \exp\left(-\frac{4\pi \Delta s \sqrt{2m}}{h} \sqrt{\bar{\varphi} + eV}\right) \right]$$

where  $e$  is the elementary charge,  $h$  is Planck's constant,  $\Delta s$  and  $\bar{\varphi}$  are the effective barrier thickness and average barrier height of the insulating layer, respectively,  $m$  is the electron mass and  $V$  is the applied voltage.

In order to obtain the electrical-contact area ( $A_{\text{CNT}}$ ) as a function of pressure, we performed finite-element simulations of a model system with interlocked microdome arrays (Section S2.1). As shown in Figure 2.3e, when pressure is applied to the electronic skin, the unique geometry of a spherical microdome induces a local-stress concentration at the small contact spots between the interlocked microdome arrays, in which the local stress field widens and the stress intensity increases with normal pressure. In particular, the local stress induces a deformation of the microdomes, which in turn causes an increase in the contact area between the interlocked microdomes (Figure 2.8b). The degree of increase in contact area with applied pressure depends on the elastic modulus of the microdome; the

large deformation of microdomes with low elastic moduli of the composites produces a large increase in contact area. The contact area between the interlocked microdome arrays comprises the geometrical contact area ( $A_{\text{dome}}$ ), which contains distributed portions of the electrical-contact area ( $A_{\text{CNT}}$ ). We can estimate the area  $A_{\text{CNT}}$  by considering the CNT areal fraction in the cross-sectional area of the composites (Section S2.1). Figure 2.3f shows how  $A_{\text{CNT}}$  increases with pressure, according to a power-law function  $y = ax^b$  with exponent  $b = 0.7$  for all samples with different CNT concentrations. This particular power-law dependence of  $A_{\text{CNT}}$  on pressure is similar to that within an analytical Hertzian contact model,<sup>106</sup> where  $b = 2/3$ . This suggests that the contact between two spheres is nonadhesive and elastic for pressures below 80 kPa. As higher CNT concentrations result in a larger CNT areal fraction, the electrical contact area increases with CNT concentration.

Experimental tunneling resistance can be expressed as  $R_t = R - R_f - R_{\text{cr}}$ , where  $R$  is the total resistance of the composite film (Figure 2.9a),  $R_f$  is the bulk-film resistance and  $R_{\text{cr}}$  is the constriction resistance. The resistance  $R_f$  is obtained from planar composite films (Figure 2.9b). The constriction resistance  $R_{\text{cr}}$ , which is attributed to impeded electron flow when current passes through a small contact area, can be neglected in our system, because the diameters of the CNTs and the inter-tube contact areas are comparable; constriction resistance can be disregarded when the ratio  $D/d < \sim 10$  (where  $D$  denotes the diameter of filler material and  $d$  the diameter of the contact spot).<sup>94</sup> Figure 2.3g represents the experimental tunneling resistances, which are obtained using the equation for  $R_t$  as given above and the theoretical tunneling resistance fitted to the experimental data using an adjustable initial thickness of the insulating layer ( $s_0$ ). Figure 2.3g shows fair agreement between the experimental data and the calculated data with an initial barrier thickness of  $s_0 = 15.8, 14.8, 13.5$  and  $11.5 \text{ \AA}$  for 5, 6, 7 and 8 wt% CNTs, respectively. We also observe that the variation in relative resistance with pressure increases with CNT concentration, due to the larger electrical contact area for higher CNT concentrations. This behavior differs distinctly from that of a planar composite film, in which the resistance between the CNT junctions is a dominant contributor to the variation in CNT-network resistance and the composite resistance. Therefore the CNT concentration near the percolation threshold for a planar composite film ( $\sim 6 \text{ wt\%}$ ; Section S2 and Figure 2.10a) exhibits the strongest piezoresistive behavior, whereas the smallest change in resistance is observed for a concentration of 8 wt%, which exceeds the percolation threshold (Figure 2.10b).

### S2.1 Calculation of tunneling resistances

The tunneling resistance ( $R_t$ ) at the contact spots between the interlocked microdome arrays was obtained using the relation  $R_t = (V/J)(1/A_{\text{CNT}})$ , where  $V$  is the applied voltage,  $J$  is the current density through the insulating layer between the interlocked microdome arrays, and  $A_{\text{CNT}}$  is the electrical-

contact area through which the current passes between electrically-conductive CNT portions at the surface of the interlocked microdome arrays. The current density can be obtained by applying the Simmons model,<sup>105</sup> in which the tunneling current  $J$  through a thin layer of insulator between metal electrodes is expressed as

$$J = \frac{e}{2\pi h \Delta s^2} \left[ \bar{\varphi} \exp\left(-\frac{4\pi \Delta s \sqrt{2m}}{h} \sqrt{\bar{\varphi}}\right) - (\bar{\varphi} + eV) \exp\left(-\frac{4\pi \Delta s \sqrt{2m}}{h} \sqrt{\bar{\varphi} + eV}\right) \right]$$

where  $e$  is the elementary charge;  $h$  is the Planck's constant;  $\Delta s$  and  $\bar{\varphi}$  are the effective barrier thickness and the average barrier height of the insulating layer, respectively;  $m$  is the electron mass; and  $V$  is the applied voltage. The effective barrier thickness is given by  $\Delta s = s_2 - s_1$ , where  $s_1$  and  $s_2$  are the distances between the two contacts and the barrier at the Fermi level. When  $V < \varphi_0/e$ ,  $s_1$  and  $s_2$  are obtained by

$$s_1 = 1.2\lambda s / \varphi_0$$

$$s_2 = s \left[ 1 - \frac{9.2\lambda}{3\varphi_0 + 4\lambda - 2eV} \right] + s_1$$

where  $s$  is the thickness of the barrier and  $\lambda$  is given by

$$\lambda = \frac{e^2 \ln 2}{8\pi \varepsilon_0 \varepsilon s}$$

where  $\varepsilon_0$  is the vacuum permittivity and  $\varepsilon$  is the relative dielectric constant of the barrier layer. The average barrier height with the image-charge effects is given by

$$\bar{\varphi} = \varphi_0 - \frac{eV(s_1 + s_2)}{2s} - \left[ \frac{1.15\lambda s}{(s_2 - s_1)} \right] \ln \left[ \frac{s_2(s - s_1)}{s_1(s - s_2)} \right]$$

Here, the image-charge effect is included to round off the corners of the rectangular barrier and to reduce the thickness of the barrier, which causes an increase in the tunneling currents. To fit the tunneling resistance in Figure 2.3g, the rectangular-barrier height  $\varphi_0$  is approximated by the work function of multi-walled carbon nanotubes (4.95 eV).<sup>107</sup> The relative dielectric constant of the barrier  $\varepsilon$  is 2.65 for the PDMS insulating layer.

We performed simulations using the finite element method (FEM), considering a model system with interlocked microdome arrays (Figure 2.8a). The geometries of the microdome arrays used in the FEM simulation are defined by a radius of 2.5  $\mu\text{m}$ , a height of  $2\sqrt{3}$   $\mu\text{m}$ , and an array pitch of 6  $\mu\text{m}$ . From the FEM simulations based on the elastic-modulus values of composites with different CNT concentrations (Figure 2.1), we obtained the contact area between the interlocked microdome arrays (Figure 2.8b). This area consists of the geometrical contact area ( $A_{\text{dome}}$ ), which in turn contains the

distributed portions of the electrical contact area ( $A_{\text{CNT}}$ ). The electrical-contact area ( $A_{\text{CNT}}$ ) was obtained by considering the CNT areal fraction in the cross-sectional area of the composites, which can be approximated as  $V_f/2\pi$  for CNTs with 3D random orientations, where  $V_f$  is the volume fraction of the CNTs in the composite.<sup>108</sup> Considering the probability of two distributed CNT portions that are in contact with the interlocked microdome arrays,  $A_{\text{CNT}}$  can be estimated as  $A_{\text{CNT}} = A_{\text{dome}}(V_f/2\pi)^2$ . The barrier thickness  $s$  changes with applied pressure and can be expressed as  $s = s_0(1-\varepsilon)$ , where  $\varepsilon$  is the compressive strain at the contact spot, as derived from FEM simulations (Figure. 2.8c). The calculated tunneling resistance is fitted to the experimental values with the adjustable initial thickness of the insulating layer ( $s_0$ ).

## S2.2 Percolation threshold of CNT composites

We investigated the percolation behavior of CNT–PDMS composite films by measuring the sheet resistance as a function of CNT concentration (Figure 2.10a) and observed a sharp decrease in the sheet resistance near 6 wt% CNT. This sharp decrease indicates the formation of a conductive network near the percolation threshold and is attributed to the uniform distribution of individual CNT fillers inside the PDMS matrix without aggregation (Figure 2.10c-f). According to percolation theory, the sheet resistance ( $R_{\text{sh}}$ ) of CNT–PDMS composites is given by

$$R_{\text{sh}} \propto (m - m_c)^{-\alpha} \text{ for } m > m_c \quad (1)$$

where  $m_c$  is the critical weight fraction required for the onset of a conductive network and  $\alpha$  is a critical exponent with an approximate value of 1.3 for two-dimensional percolation networks and 2.0 for three-dimensional percolation networks.<sup>109, 110</sup> The inset in Figure 2.10a shows the best fit to the sheet resistance as a function of  $(m-m_c)$ , at a CNT percolation concentration of 5.9 wt%. This fit suggests a critical exponent of 1.79, which is similar to the typical critical exponent in 3D systems. The pressure-sensitive properties of planar composite films were investigated by measuring the electrical resistance  $R$  as a function of the normal pressure on the films. As expected, the 6-wt%-CNT sample shows the highest pressure sensitivity (Figure 2.10b) as the concentration is close to the percolation threshold. The 8-wt%-CNT sample shows the lowest pressure sensitivity because the concentration is substantially higher than the percolation threshold.

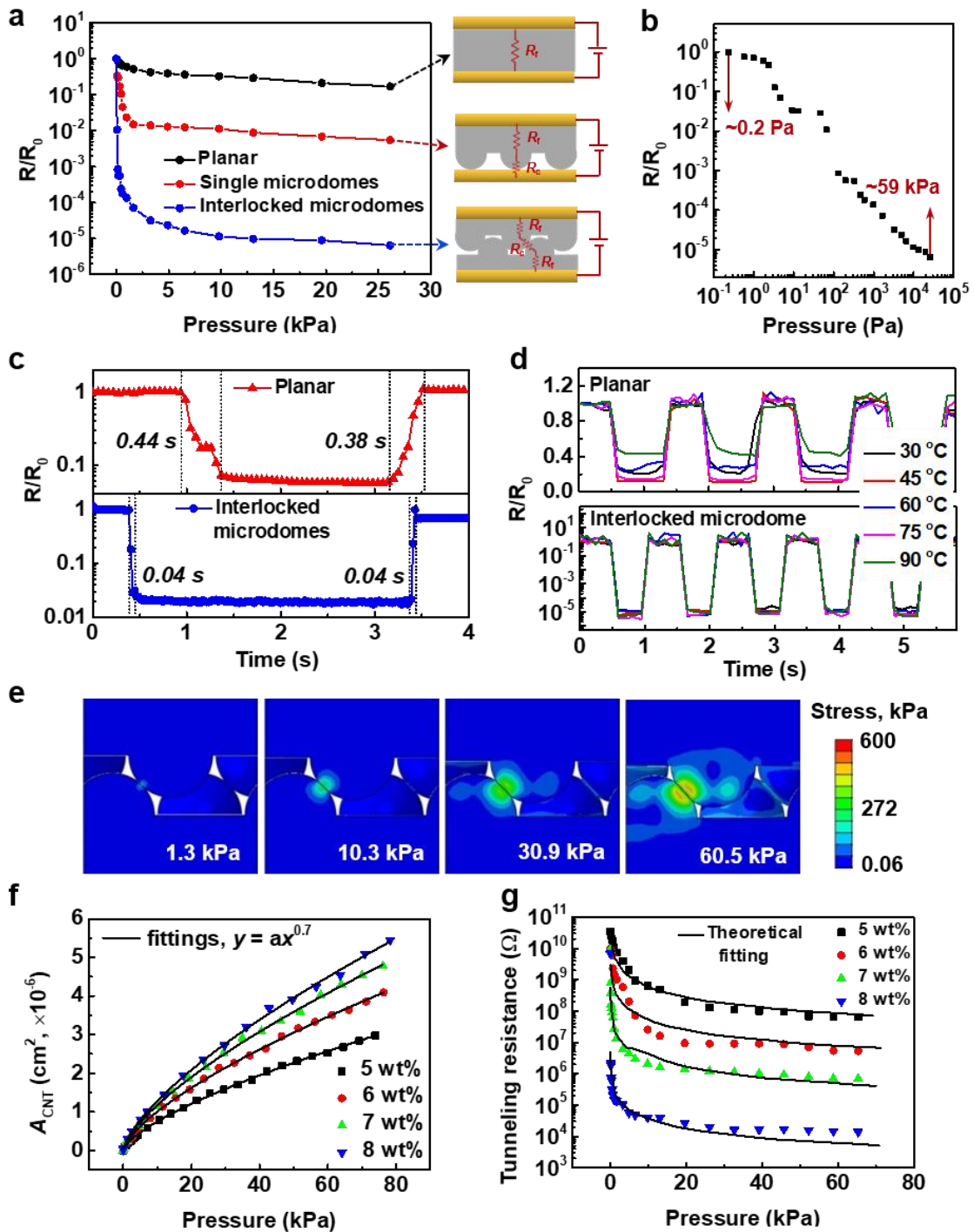


**Figure 2.3.** Pressure-sensing capabilities of sensors with interlocked microdome arrays. (a) The comparison of pressure sensitivities of different sensor structures for 8 wt% CNTs: planar (black), microdome (red) and interlocked microdome (blue). (b) Log–log plot of the pressure-response curve for the interlocked microdome arrays (8 wt% CNTs), which shows the minimum detection limit ( $\sim 0.2$  Pa) and the dynamic pressure range. (c) Comparison of response/relaxation times for different sensor structures for 8 wt% CNTs and 65 Pa pressure loading: planar (upper) and interlocked microdome



structures (bottom). (d) The effect of temperature variation on different sensor structures for 8 wt% CNTs and 19.6 kPa pressure loading: planar (upper) and interlocked microdome structures (bottom): planar (upper) and interlocked microdome structures (bottom). (e) Finite-element calculations that show the deformation and the local stress distribution of interlocked microdome arrays with applied pressure (1.3–60.5 kPa). (f) The electrical contact area ( $A_{\text{CNT}}$ ) as a function of pressure for different CNT wt% (5–8 wt%). The solid lines represent power-law fits to  $A_{\text{CNT}}$  with an exponent of 0.7. (g) Experimental tunneling resistances (dotted plots) of the interlocked microdome arrays for different CNT concentrations (5–8 wt%) fitted to calculated tunneling resistances (solid lines).

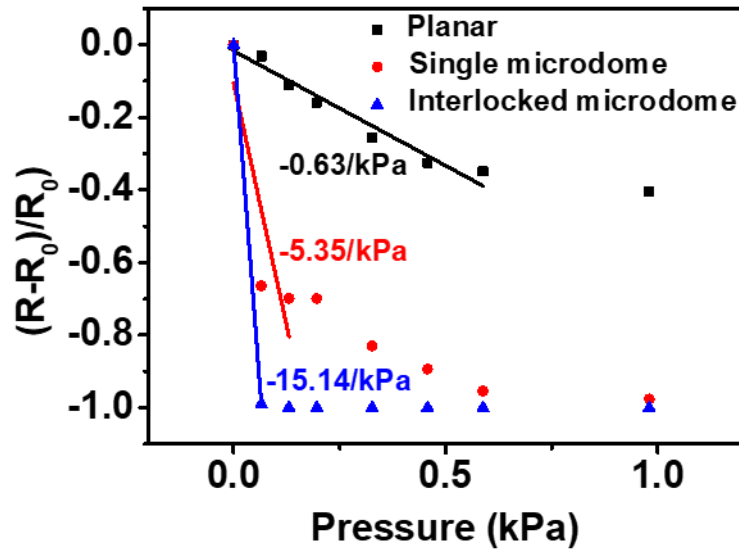


**Figure 2.4.** Piezoresistive pressure sensitivity of composite films for three different configurations: a single planar array, a single microdome array and an interlocked microdome array.

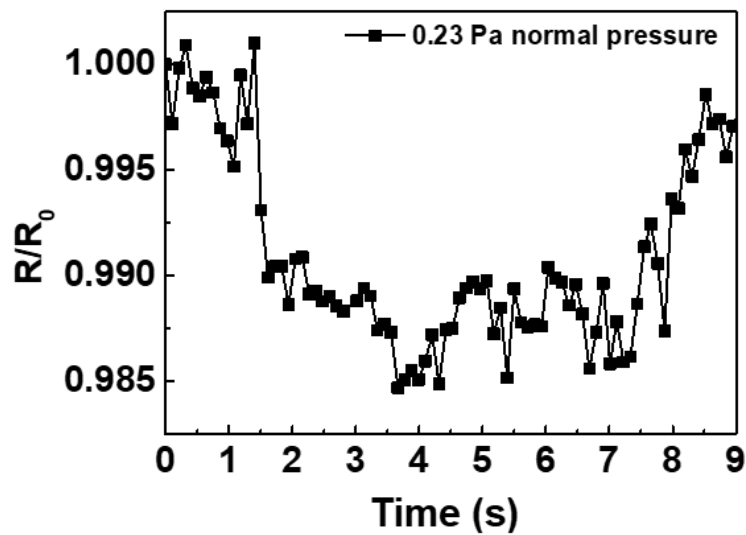


**Figure 2.5.** Real time variation in the relative resistance of a composite film with interlocked microdome arrays (8 wt% CNTs) in response to a pressure loading/unloading of ~0.23 Pa.

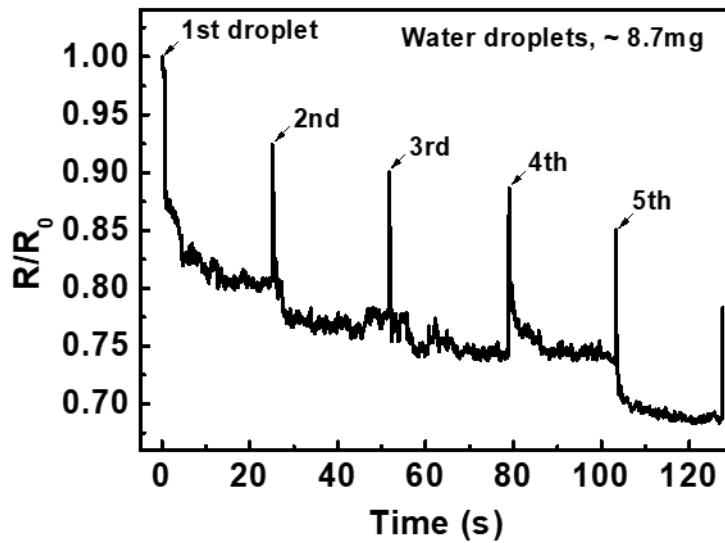


**Figure 2.6.** Dynamic time-resolved variation detected by our electronic skin when exposed to a string of falling water droplets of  $\sim 8.7$  mg weight (corresponding to an applied pressure of  $\sim 0.6$  Pa).

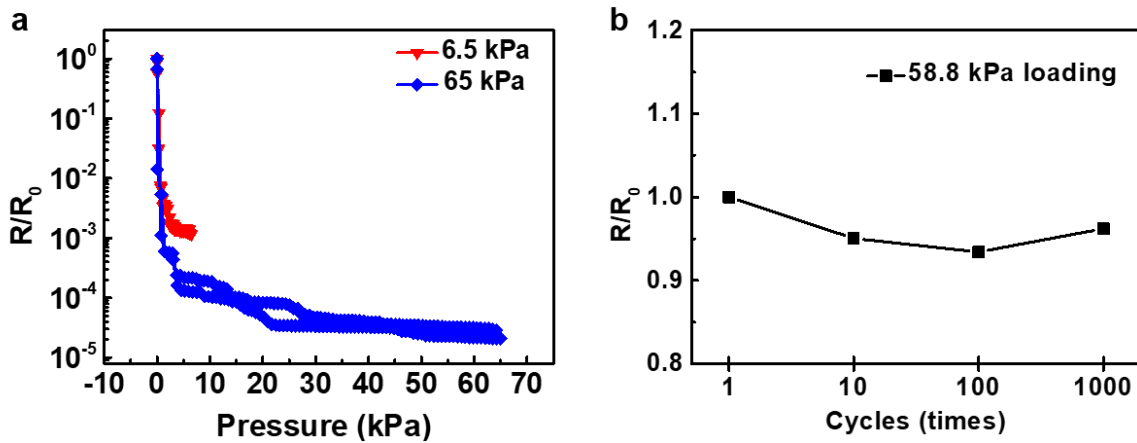


**Figure 2.7.** (a) Relative change in resistance for the loading and unloading cycles under pressures of 6.5 kPa and 65 kPa. (b) Relative change in resistance for the multiple-cycle tests with a repeated application of a normal pressure of 58.8 kPa

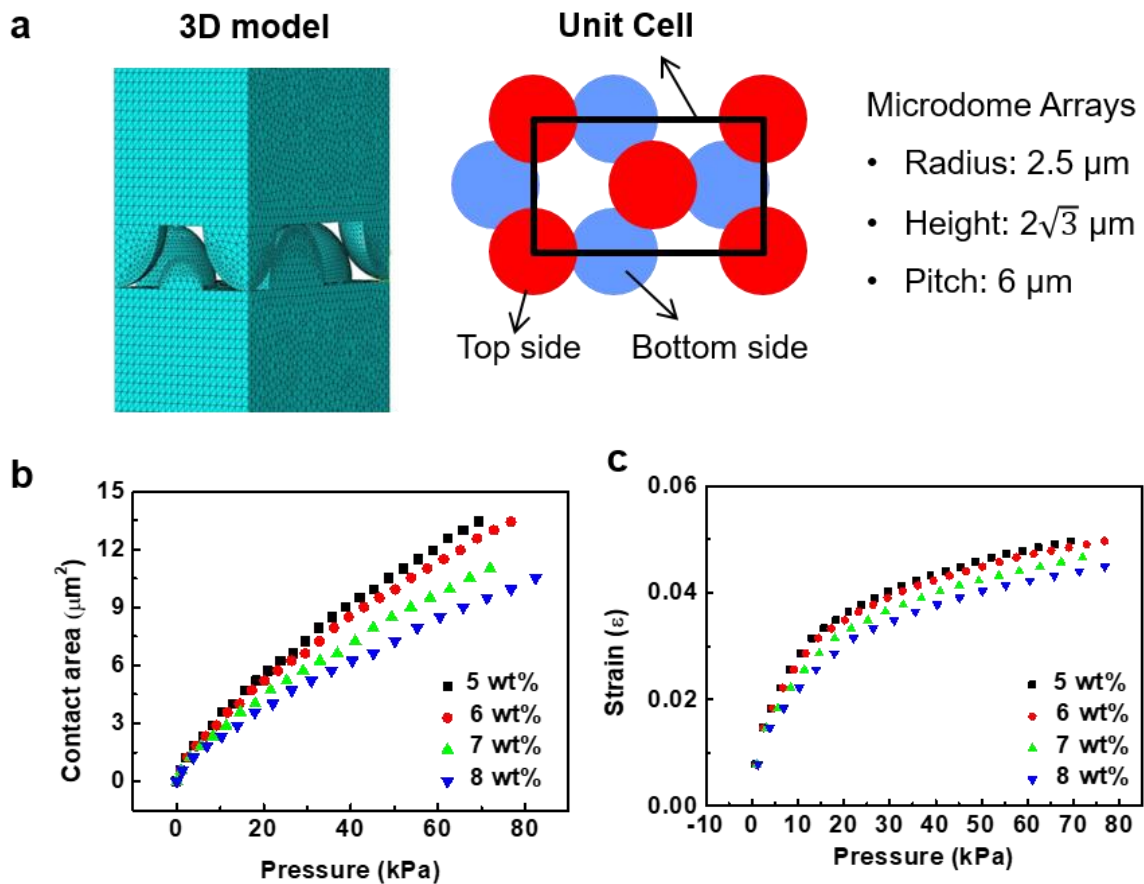


**Figure 2.8.** Finite-element-method simulations of interlocked microdome arrays. (a) A model system used in FEM simulations. The geometries of the microdome arrays are given by a radius of  $2.5 \mu\text{m}$ , a height of  $2\sqrt{3} \mu\text{m}$ , and an array pitch of  $6 \mu\text{m}$ . (b) Change in contact area for the interlocked microdome arrays as a function of pressure at different concentration of CNTs (5–8 wt%). (c) The maximum strain at the contact spots as a function of pressure for different CNT concentrations (5–8 wt%).

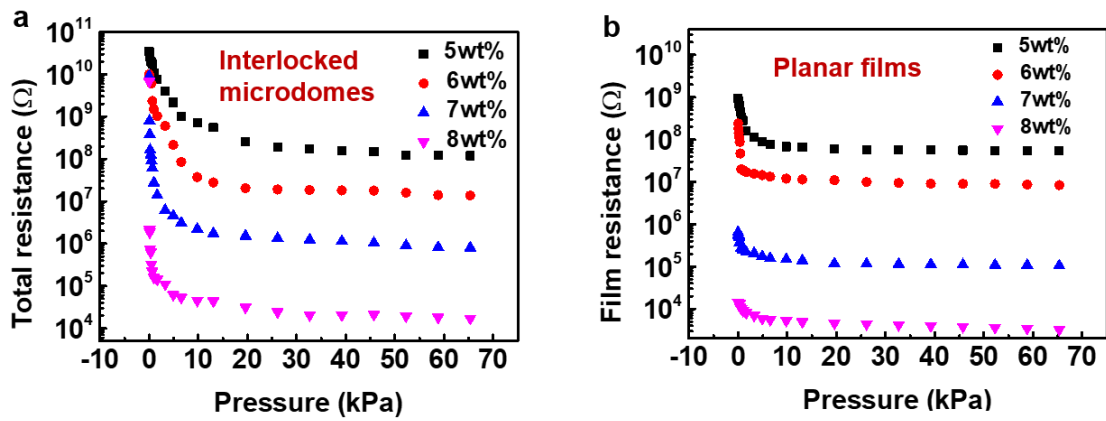


**Figure 2.9.** Total resistances for composite films. (a) Film containing interlocked microdome arrays; (b) film containing planar structures. The tunneling resistance is obtained using the relation  $R_t = R - R_f - R_{cr}$ , where  $R$  is the total resistance of composite film with interlocked microdome arrays,  $R_f$  is the bulk-film resistance and  $R_{cr}$  is the constriction resistance.

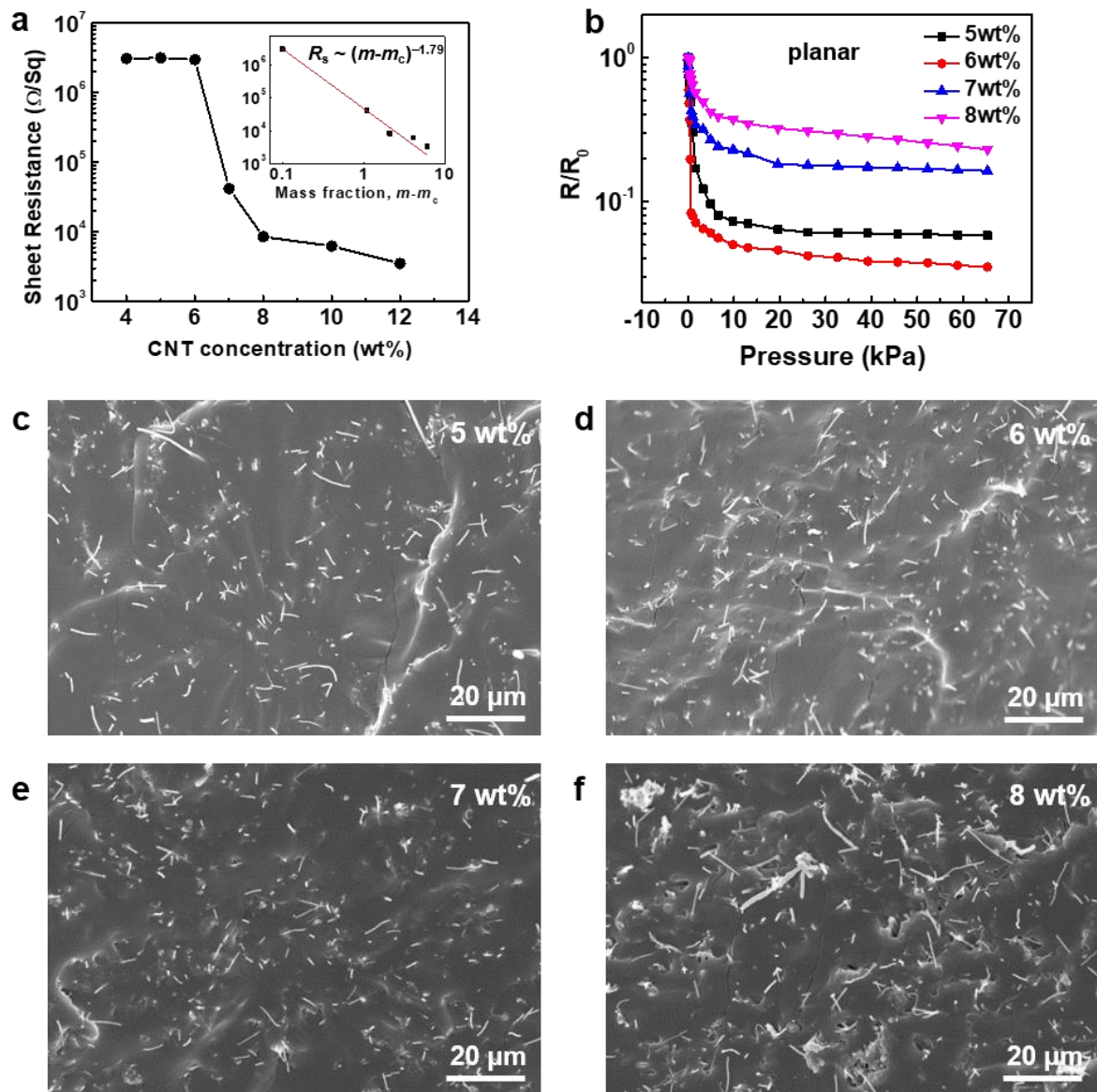


**Figure 2.10.** Electrical properties and fracture morphologies of planar composite films. (a) The sheet resistance of composite films as a function of CNT concentration. The inset shows the power-law fits of the sheet resistance as a function of the reduced mass fraction ( $m-m_c$ ), where  $m_c$  is the required critical weight fraction for the onset of the conductive network. (b) Relative variation in resistance for planar composite films as a function of pressure. (c)–(f) Representative cross-sectional SEM images of composite films with different CNT concentrations (5–8 wt%).

In order to explore the ability of our sensors to resolve the spatial distribution and magnitude of applied pressure, we fabricated  $10 \times 10$ -pixel arrays of electronic skin sandwiched between a cross-array of platinum electrodes (Figure 2.11a). Pressures of 1–2 kPa were applied to the sensors via three different pieces of PDMS (shaped to form the letters “F”, “N”, and “L”) placed on top of the sensor array (Figure 2.11b). The contact regions under the PDMS letters were compressed due to the local pressure, resulting in decreased resistance in those regions, differentiating these regions from the uncompressed regions. In addition to detecting the static-pressure distributions, our sensors were also used to detect dynamic pressure variations, which is important for real-time monitoring of environmental changes. Figure 2.11c shows the real-time variation in relative resistance under continuous locomotions (climb, crawl, descend, and head shake) of a live snail weighing ~540 mg. The resistance directly responded to the movement of the snail on top of the electronic skin. This real-time monitoring capability can also be used to monitor human motion, for example finger-bending motion (Figure 2.11d). The relative resistance decreases in response to changes in finger bending, and consistently changes for repeated bending cycles.

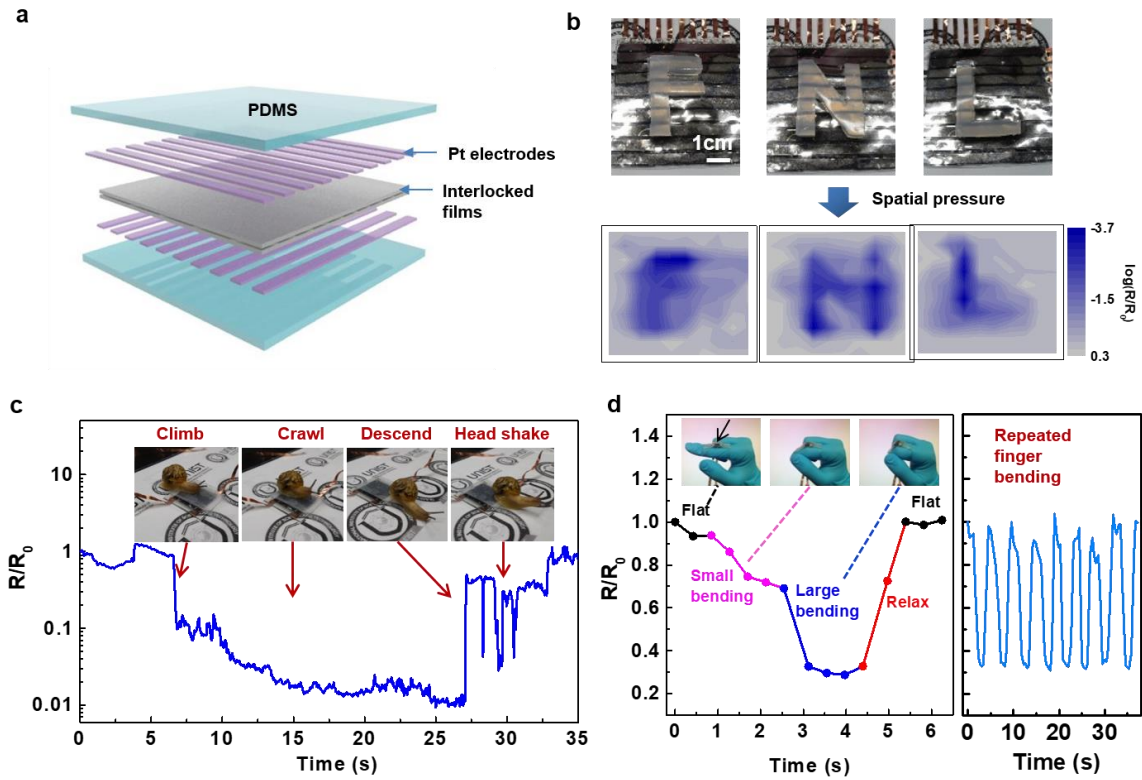


**Figure 2.11.** Sensing of spatial pressure distribution and real-time monitoring of tactile signals. (a) Schematic of the 10×10 sensor arrays, which consist of interlocked microdome arrays sandwiched between platinum electrodes and PDMS cover layers. (b) Spatial pressure-mapping capability of the 10×10 sensor arrays. The spatial pressure distribution is applied using PDMS weights that are shaped as the letters “F”, “N” and “L”. (c) Real-time monitoring of the change in resistance for snail movements (climb, crawl, descend and head shake) on the surface of the electronic skins. (d) The change in resistance for different bending degrees of a finger (left) and repetitive bending cycles (right).



The analysis of human-breathing patterns provides a non-invasive and repeatable monitoring technology that can be used in a variety of healthcare applications.<sup>111</sup> Traditionally, thermal flow sensors have been used to study human breath for the purpose of screening for cardiovascular diseases<sup>112</sup> or to monitor sleep apnea-hyponea syndrome.<sup>113</sup> However, these sensors consume a large amount of power ( $> 0.1\text{--}1\text{ W}$ ) and are therefore not suitable for integration into flexible electronic skins. The ability to sensitively detect applied pressure makes our sensors well suited to monitoring breathing rates. As schematically shown in Figure 2.12a, gas flow on the electronic skin's surface can impart normal pressures that deform the interlocked microdome arrays and cause a decrease in resistance. This change in electrical resistance ( $R_{\text{off}} - R_{\text{on}}$ ) of the interlocked microdome arrays increases linearly with an increase in gas-flow rate ( $1\text{--}6\text{ m/s}$ ); the slope indicates flow sensitivity ( $\Delta R/\text{m/s}$ ) of  $1280\ \Omega/\text{m/s}$  (Figure 2.12a). Conversely, the planar composite films exhibit a flow sensitivity of only  $13\ \Omega/\text{m/s}$ . We explored the potential for using our electronic skin to monitor human breathing in an experiment in which the electronic skin was attached to the front of the nostrils of a volunteer and the amount of air exhaled was measured (Figure 2.12b). The periodic breathing generates reliable and stable changes in resistance. Each exhalation event results in an 80% change in resistance.

For the analysis of oral breathing, we wrapped our electronic skins into a tube shape and monitored gas or breath flow (Figure 2.12c). The resistance of the tubular electronic skins increased linearly with the amount of air flowing through it, with a sensitivity of  $2135\ \Omega/\text{m/s}$ . This sensitivity is significantly higher than that of flow sensors previously reported for conductive composite microcantilevers ( $66\ \Omega/\text{m/s}$ ),<sup>114</sup> silicon microcantilevers ( $150\text{--}350\ \Omega/\text{m/s}$ )<sup>115</sup> and silicon nanowires ( $198\ \Omega/\text{m/s}$ ).<sup>116</sup> For demonstration purposes, the tubular flow sensor was also integrated into a medical breathing mask to monitor oral breathing (Figure 2.12d). The sensor can monitor different breathing modes (deep and normal breathing) with consistent changes in resistance under repeated breathing. Because our sensors are based on cost-effective and simple designs, they could be well suited as breathing sensors in cardiorespiratory monitoring, medical diagnosis and rehabilitation.

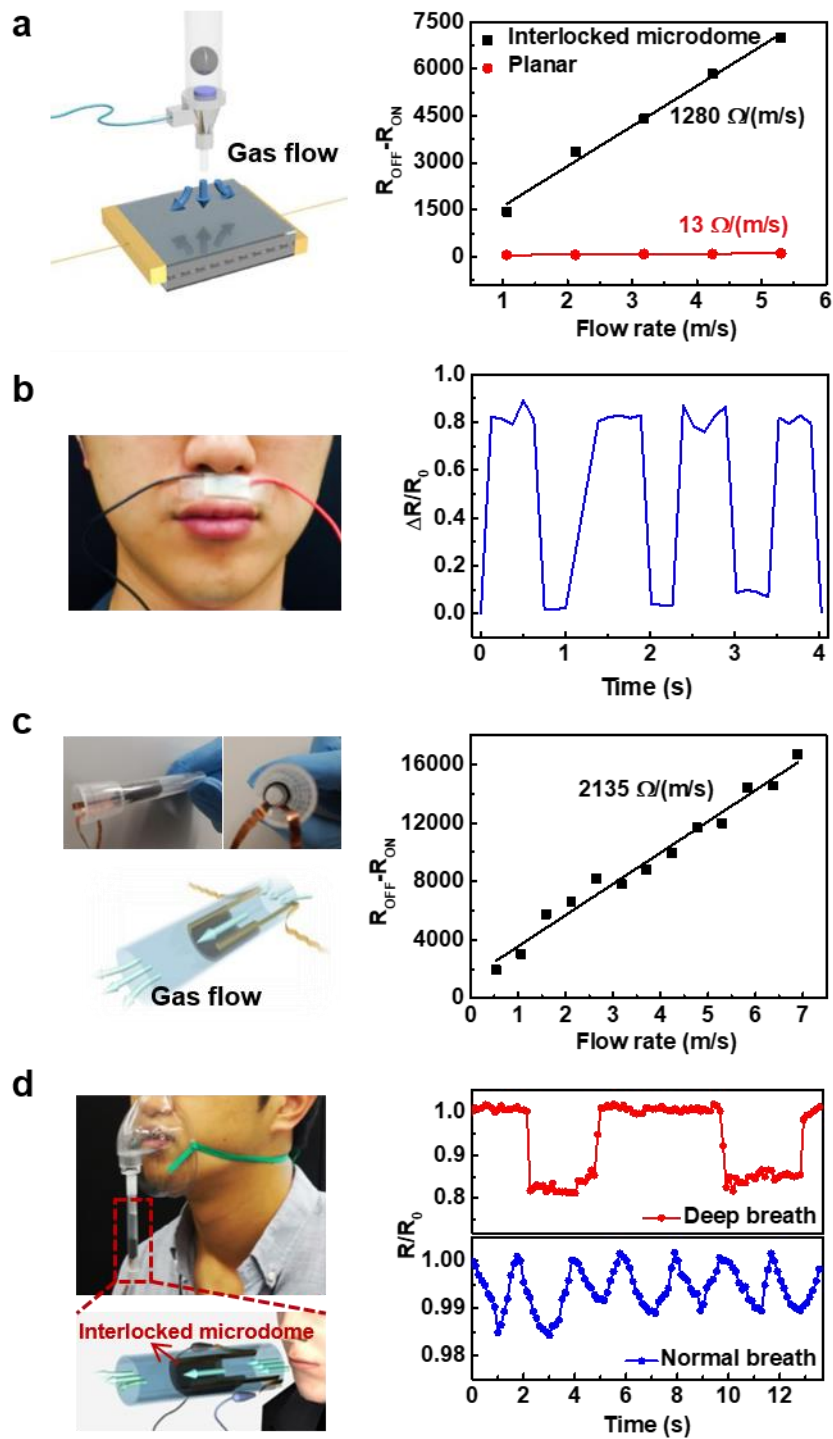


**Figure 2.12.** Monitoring of gas flow and human breathing. (a) Schematic of gas-flow sensing for planar-type electronic skins (left) and changes in resistance ( $R_{\text{off}} - R_{\text{on}}$ ) as a function of flow rate for planar electronic skins (right). (b) Left: A photograph of the planar-type flow sensors attached to the front of a volunteer's nostrils. Right: relative changes in resistance in response to human breathing. (c) Photographs of a tubular-type flow sensor composed of rolled-up electronic skin inside a plastic tube

(upper left) and a schematic of a tubular-type gas flow sensor (bottom left). Right: relative changes in resistance as a function of flow rate. (d) Monitoring of human oral breathing. Left: photograph and schematic of tubular-type flow sensors integrated into the medical breathing mask for the monitoring of oral breathing. Right: relative changes in resistance for different oral breathing modes (deep and normal breathing) during periodic breathing.

As a final demonstration, we explored the potential use of our piezoresistive sensors for picking up vibrations, specifically those associated with speaking. Voice monitoring systems are critical for the clinical assessment of voice hyperfunction and disorders, as well as in electro-larynx devices.<sup>117</sup> Voice monitoring is typically performed using accelerometer-based devices.<sup>117, 118</sup> To test the ability of our electronic skins to pick up voice vibrations, we attached a coin-type vibration motor to the interlocked films and placed a vibrometer in contact with the film to measure the vibration intensity (Figure 2.13a). The relative resistance of our sensor shows a linear increase with vibration intensity and a sensitivity of  $\sim 0.37/(\text{m/s}^2)$ , which is significantly higher than the sensitivity of  $0.06/(\text{m/s}^2)$  associated with planar composite films. For use in wearable voice-monitoring systems, the sensors can be attached to the skin of the neck to monitor the voice directly (Figure 2.12b). The sensors distinctly discriminate the different vibration patterns produced when the words “UNIST” and “Hi” are spoken. Further optimization of the sensor design in combination with radio frequency devices may enable wireless communication systems avoiding noise disturbance.

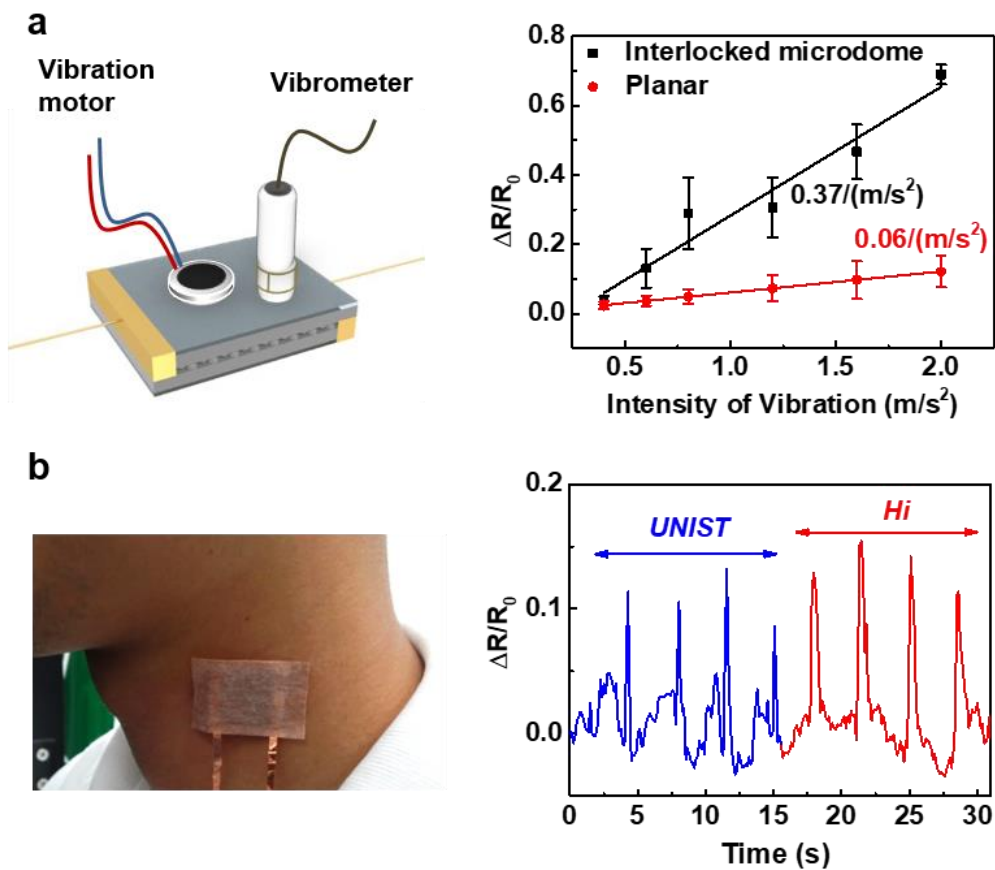


**Figure 2.13.** Vibration detection for wearable voice-monitoring systems. (a) Left: schematic of the vibration measurement. A coin-type vibration motor is used to generate vibration signals and a vibrometer is used to measure the vibration intensity. Right: relative changes in resistance ( $\Delta R/R_0$ ) as a function of vibration intensity. (b) Photograph of the electronic skin attached to a human neck for voice monitoring (right). Relative changes in resistance in response to different voices speaking ‘UNIST’ (blue) and ‘Hi’ (red).

## 2.4 Conclusions

In conclusion, we have developed an electronic skin that consists of a CNT-composite-based elastomer film featuring interlocked microdome arrays, which lead to the giant tunneling piezoresistance and thus the high pressure sensitivity. The materials design and operational principles introduced here present a robust technology platform to further advance the sensitivity and response time of conventional composite elastomers for various sensor applications. We anticipate that other types of fillers and the geometry of microstructures could expand the current sensing capabilities to enable electronic skins with new functionalities. In addition, when integrated with other type of sensors and active electronic devices, the current platform could be a key component for the development of multifunctional electronic skin for applications in medical diagnostic tools and wearable human-health monitoring systems. Finally, the extreme resistance-switching behavior demonstrated here could enable highly efficient piezotronic transistors.<sup>119, 120</sup>

## Chapter 3. Piezoresistive composite elastomers with interlocked microdome arrays with multidirectional force capability

### 3.1 Introduction

Artificial electronic skins which mimic the sensing capabilities of biological skins have recently attracted much attention for a broad range of applications in wearable electronics, prosthetic limbs, robotics, remote surgery, and biomedical devices.<sup>4, 86</sup> As an ideal model system for artificial electronic skins, human skin with various sensory receptors (mechanoreceptor, thermoreceptor, nociceptor, etc.) enables the perception of external stimuli like pressure, shear, strain, vibration, temperature, and pain. In particular, various mechanoreceptors such as the Merkel disk (MD), Meissner corpuscle (MC), Pacinian corpuscle (PC), and Ruffini ending (RE) distributed in the epidermis and dermis layers (see schematic illustration in Figure 3.1a) provide spatiotemporal recognition of the magnitude, location, and direction of contact forces, which is critically essential when a human manipulates an object.<sup>121</sup> For example, the distribution of normal and shear tangential stresses while making contact with an object provides information on its shape and surface texture, friction between the skin and object, and the accidental slip.<sup>86</sup> The strain pattern on the skin during finger movements is critical to the brain's perception of the position of finger joints relative to the body.<sup>122</sup> In addition to the magnitude of stress, the directional sensitivity to force is critical to maintaining the balance between normal and tangential fingertip forces, which enables the handling of irregular-shaped objects.<sup>123-126</sup>

To fabricate electronic skins which mimic the tactile-sensing capability of human skin, diverse approaches based on various transduction modes, such as those employing resistive,<sup>11, 12, 72, 87, 89</sup> capacitive,<sup>18, 88, 90, 127</sup> piezoelectric,<sup>34, 92</sup> and triboelectric sensors,<sup>93, 128</sup> have been suggested. In particular, for the detection of various mechanical and environmental stimuli, multi-modal electronic skins have been demonstrated based on the integration of mechanical and physical sensors on flexible substrates,<sup>15, 129-131</sup> nanostructured conductive composites,<sup>132, 133</sup> and organic transistor arrays.<sup>134</sup> However, most of the previous studies either focused on the detection of only one type of mechanical stimuli or developed electronic skins that were not capable of discriminating multiple mechanical stimuli and their directions. There have been several reports on the detection and differentiation of normal and in-plane forces applied to electronic skins.<sup>19, 135-137</sup> Pang *et al.* demonstrated the piezoresistive detection and differentiation of normal, tangential, and torsional forces using Pt-coated micropillar arrays.<sup>19</sup> Gong *et al.* employed tissue papers impregnated with gold nanowires to enable the perception of pressure, bending, torsional forces, and acoustic vibrations.<sup>137</sup> Stretchable electronic skins with multi-directional sensing capabilities have not yet been demonstrated, however. In addition, the low sensitivities of sensors in previous studies provided only small differences in transduced signals under different

external forces, which reduced the sensors' capabilities to clearly resolve the intensity and direction of the forces.

In human tactile systems, it has been reported that the intermediate ridges present at the epidermal–dermal junction enhance the tactile perception of mechanoreceptors.<sup>52</sup> Intermediate ridges with the geometry of interlocked microstructures (Figure. 3.1a) are known to provide strong adhesion between the epidermis and dermis. They also magnify and transduce the tactile stimuli from the skin surface to the mechanoreceptors by concentrating stress near the ridge tips, where mechanoreceptors like MDs and MCs are located.<sup>52, 86, 138</sup> Although there are several recent reports on bio-inspired adhesion systems<sup>54, 139, 140</sup> and electronic skins<sup>19, 45</sup> which mimic the interlocked microstructures of beetles and dragonflies, multi-directional, stretchable electronic skins mimicking the interlocked microstructures in human skin have yet to be reported. We have previously reported piezoresistive electronic skins with interlocked microdome arrays for the ultrasensitive detection of normal pressure.<sup>45</sup> In this study, inspired by the interlocked epidermal–dermal ridges in human skin, we further explored the interlocked microdome arrays for stress-direction-sensitive and stretchable electronic skins which can detect directional mechanical stimuli applied along three different axes. We fabricated piezoresistive, interlocked microdome arrays, in which the interlocked geometry of dome-shaped conductive elastomers enabled stress concentration at the contact points, resulting in the exclusive deformation of microdomes and thus enhanced sensitivity of the piezoresistive response to various tactile stimuli. We also demonstrated that a fully functional wearable electronic skin with 3×3 sensor arrays can selectively monitor different intensities and directions of air flow and vibration stimuli.



### 3.2 Experimental Details

**Fabrication of elastic composite film with microdome arrays:** For the fabrication of composite elastomers, MWNTs (Sigma Aldrich) with diameters of 110–190 nm and lengths of 5–9  $\mu\text{m}$  were first dispersed in chloroform by sonication for 6 h. Using a vortex mixer, the dispersed solution was mixed with a PDMS base (Sylgard 184, Dow Corning) at different ratios (5–8 wt%) of MWNTs to PDMS, followed by heating at 90  $^{\circ}\text{C}$  on a hot plate to remove the chloroform. For the micromoulding process, hexane and a PDMS curing agent (1:10 ratio for the curing agent and PDMS base) were added to each MWNT–PDMS composite mixture (concentration of 500  $\text{mg ml}^{-1}$ ) and then mixed with a vortex mixer for 5 min. These composite mixtures were cast onto silicon micromoulds with hexagonal hole arrays (diameter: 3.5  $\mu\text{m}$ , pitch size: 6  $\mu\text{m}$ ) and stored in a vacuum desiccator for 1 h to remove the residual hexane. Finally, different microdome-patterned MWNT–PDMS composite films (thickness of 500  $\mu\text{m}$ ) were prepared by thermal curing at 60–80  $^{\circ}\text{C}$  (strain and curvature sensors: 60  $^{\circ}\text{C}$ , pressure and shear force sensors: 70 $^{\circ}\text{C}$ ) for 3 h. For the electronic-skin applications, the interlocked microdome-patterned films were coated with platinum on both sides by a sputter coating system (K575X, Quorum Emitech) to form electrode arrays.

**Characterization:** The surface morphologies of the microdome composite films were characterized by a field-emission SEM (FE-SEM; S-4800, Hitachi) and an optical microscope (PSM-1000, Olympus). The piezoresistive properties of the electronic skins were measured using a two-probe method (4200-SCS, Keithley) at 10 V. To apply mechanical forces on the electronic skins, a pushing tester (JIPT-100, Junil Tech) was used to provide normal forces and a tensile/bending machine (JIBT-200, Junil Tech) was used to provide lateral and bending strain. For the tangential-shear tactile-sensing measurements, a polyethylene terephthalate (PET) film was attached on one side of a composite film and one end of the PET film was connected to a force gauge in the tangential direction. A constant normal force was then applied on the electronic skin using a lab-built microstage system (Micro Motion Technology, Korea), after which a shear force was applied to the electronic skin. For the evaluation of the directional tactile-sensing properties, a flow meter (Ar gas, flow rate of 5.3  $\text{m s}^{-1}$ ) and a vibrator (2.0  $\text{m s}^{-2}$ ) were used to provide mechanical stimuli in different directions.

**Finite-Element Method:** For the contact area calculations under stretching and shearing, we conducted structural analyses using finite-element method. Composite films with interlocked microdome arrays were modeled as linear elastic materials described by experimentally measured elastic constants.<sup>45</sup> We employed more than 2.8 million four-node linear tetragonal elements with adaptive mesh-refinement scheme around the contact area. All calculations were static under proper loading conditions and the mechanical contact between two deformable surfaces was calculated by a surface-to-surface contact scheme.

### 3.3 Results and Discussion

**Bio-inspired interlocked microdome arrays.** The biomimetic design of the interlocked microdome arrays was based on carbon-nanotube (CNT) composite elastomer films with surface microstructures of hexagonal microdome arrays. The interlocked geometry was accomplished by engaging two microdome-patterned CNT composite films with the patterned sides contacting each other. Each elastomeric film with a microdome pattern was fabricated by casting a viscous solution containing multi-walled carbon nanotubes (MWNTs) and poly(dimethylsiloxane) (PDMS) onto a silicon micromould. Figure 3.1c shows a representative scanning-electron microscope (SEM) image of a microdome-patterned conductive film with microdomes measuring 3  $\mu\text{m}$  in height and 4  $\mu\text{m}$  in diameter, and an array pitch of 6  $\mu\text{m}$ . The electronic skin was configured by interlocking two microdome composite films, with the microdomed surfaces facing each other (cross-sectional SEM image in Figure 3.1d). When the interlocked microdome arrays were attached on human skin in the arm and wrist areas, it was possible to monitor the magnitude and direction of various mechanical stimuli (pressure, shear, strain, and curvature) applied on the electronic skins (Figure. 3.1e).

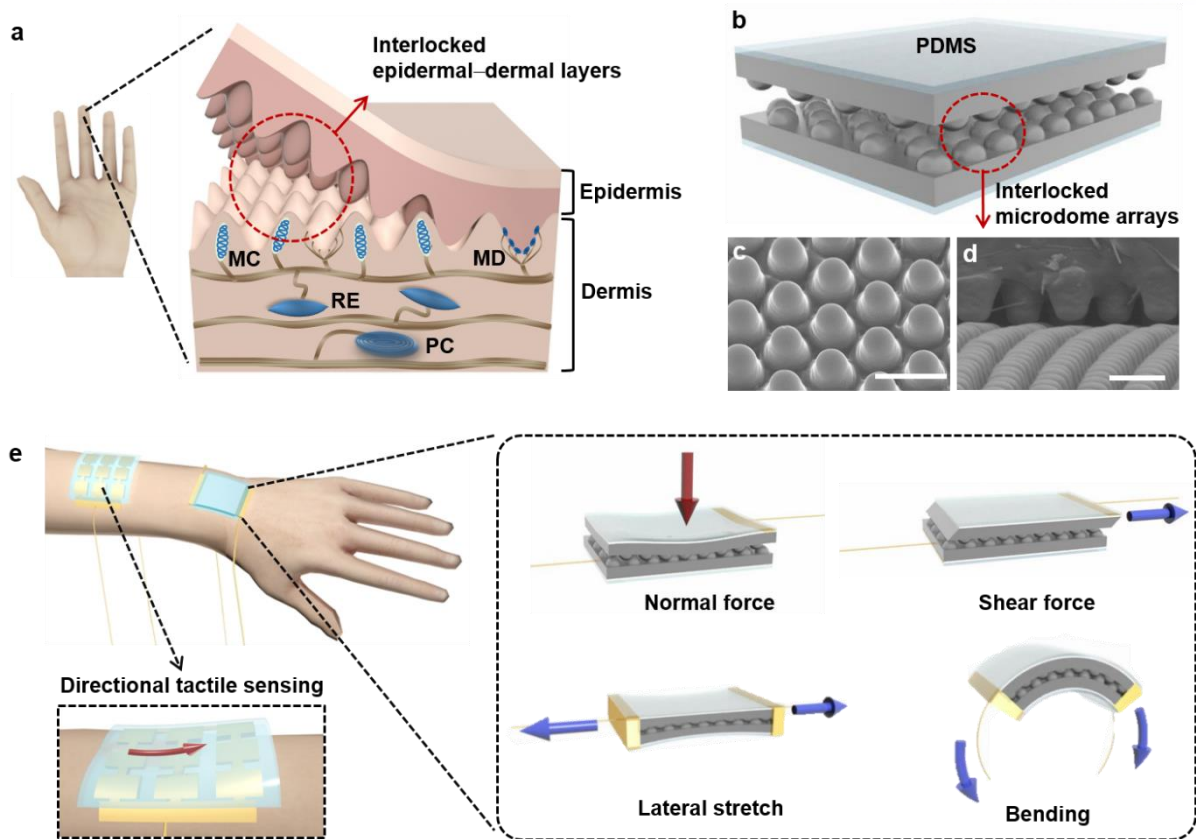


**Figure 3.1.** Electronic skin based on carbon nanotube–poly(dimethylsiloxane) (CNT–PDMS) composite films with interlocked microdome arrays. (a) Schematic of human skin structure showing interlocked epidermal–dermal layers and mechanoreceptors (MD: Merkel disk; MC: Meissner corpuscle; PC: Pacinian corpuscle; RE: Ruffini ending). (b) Schematic of an interlocked microdome array. (c) Tilted SEM image of a composite film with microdome arrays (diameter:  $\sim 3 \mu\text{m}$ ; height:  $\sim 3.5 \mu\text{m}$ ; pitch:  $6 \mu\text{m}$ ). Scale bar:  $5 \mu\text{m}$ . (d) Cross-sectional SEM image of an interlocked composite film. Scale bar:  $5 \mu\text{m}$ . (e) Schematic of a stress-direction-sensitive electronic skin for the detection and differentiation of various mechanical stimuli including normal, shear, stretch, bending, and twisting forces.

**Stretchable electronic skins.** The perception of stretch in human skin is critical to the sense of position and movement of fingers, elbows, and knees.<sup>122, 141</sup> The stretch-sensing mechanism of the interlocked microdome arrays was based on variations in the contact area between microdomes with changes in the stretch ratio. Figure 3.2a illustrates the variations in the contact ( $R_c$ ) and film ( $R_f$ ) resistances when the interlocked microdome arrays were stretched. The contact resistance ( $R_c$ ) significantly increased with the decrease in contact area between the microdomes when the gaps between them increased under lateral strain. Compared to the large change in  $R_c$ , however, the stretching-induced change in  $R_f$  had a minimal effect on the change in overall resistance because the change of intertube distance within the composite film is small and thus results in the small change of  $R_f$  compared to the change of  $R_c$ . The small change of  $R_f$  is evident from the low gauge factor of planar films in Figure 3.2e. To elucidate the working principle of the interlocked microdome arrays behind their stretch-sensing capability, we investigated the deformation of the microdome array pattern as a function of lateral strain. As can be seen in the SEM images in Figure. 3.2b, the microdome arrays changed their geometry from hexagons to elongated hexagons in the stretching direction with increasing lateral strain, resulting in the decrease of contact pressure and increases in gap distances between the microdomes. These increased gap distances decreased the contact area between the interlocked microdomes, thus increasing the contact resistance of the interlocked microdome arrays. In order to verify the variations in contact area with the application of lateral strain, we performed finite-element simulations of the change in contact area in the interlocked microdome arrays. Figure 3.2c shows the changes in contact pressure at various contact points between interlocked microdome arrays with the increase of lateral strain. As the lateral strain increases, both the contact pressure and the number of contact points decrease. Consequently, the decreased contact pressure and the number of contact points results in the decrease of the contact area. The simulation result in Figure 3.2d shows that the inverse contact area increases exponentially with the increase of lateral strain. Since the inverse contact area is directly proportional to tunneling resistance between contact points,<sup>45</sup> the electrical resistance interlocked microdome arrays increases exponentially as a function of lateral strain, as can be seen in Figure 3.2e.

Based on a comparison of sensitivity as functions of CNT concentration and curing temperature (Figure 3.4), we chose a CNT concentration of 7 wt% and a curing temperature of 60 °C as the optimal conditions for the fabrication of stretchable electronic skins. In our previous report, the increase of CNT concentration above the electrical percolation threshold (6 wt%) resulted in the increase of tunnelling piezoresistance of interlocked microdome arrays, but also caused the increase of an elastic modulus of composite films.<sup>45</sup> Therefore, 7 wt% e-skins with higher tunnelling piezoresistance than 6 wt% and larger stretchability than 8 wt% ones, results in the highest sensitivity to lateral stretch. E-skins cured at 60 °C showed the highest sensitivity because the decrease of curing temperature leads to the decrease

of elastic modulus and thus the increased deformability in response to mechanical stress. Figure 3.2e shows the change in relative (or normalized) electrical resistance ( $\Delta R/R_0$ ) as a function of applied lateral strain ( $\Delta L/L_0$ ) for the interlocked microdome arrays prepared under these conditions. Here,  $R_0$  and  $L_0$  denote the resistance and length of an electronic skin with and without stretch, respectively. The relative resistance of the interlocked microdome arrays increased significantly with increasing lateral strain, while the planar composite films without interlocked structures showed minimal change in relative electrical resistance. For a quantitative analysis of the strain sensitivity of the electronic skins, the strain gauge factor ( $GF$ ) is defined as  $GF = (\Delta R/R_0)/\varepsilon$ , where  $\varepsilon$  is the lateral strain and is defined as  $\varepsilon = \Delta L/L_0$ . The interlocked microdome arrays showed different  $GF$  values depending on the lateral strain: 27.8 at a strain of 0–40%, 1084 at a strain of 40–90%, and 9617 at a strain of 90–120%. These  $GF$  values are significantly (10–395 times) higher than the values for the planar films (2.7 at a strain of 0–110%), sandwiched Ag-nanowire composites (2–14 at 0–70%),<sup>142</sup> three-dimensional macroporous graphene paper (7.1 at 0–100%),<sup>143</sup> and ZnO–polystyrene nanofibre hybrid films (116 at 0–50%).<sup>144</sup> Although  $GF$  values comparable to those of the interlocked microdome arrays have been reported for single-nanotube or single-nanowire sensors (600–1250 at a strain of 0–1.5%)<sup>145, 146</sup> and woven graphene films ( $\sim 10^3$  at a strain of 0–6%),<sup>147</sup> their sensing ranges are narrow.

In addition to the high  $GF$  values, the interlocked microdome arrays exhibited a narrow hysteresis curve for repeated stretch–release cycles (Figure 3.3). One of the additional advantages of our electronic skins with interlocked geometry is the fast response time. Generally, the bulk polymer composite films exhibit slow response owing to the viscoelastic behaviour of bulk polymers.<sup>148</sup> On the other hand, the interlocked-microdome strain sensor operated mainly through the change in contact area between interlocking microdome arrays, overcoming the viscoelastic delay of bulk polymers. Figure 3.2f shows the short response ( $\sim 18$  ms) and relaxation ( $\sim 10$  ms) times of the interlocked microdome arrays under repeated strain cycles at 50% lateral strain and a stretching speed of  $3 \text{ mm s}^{-1}$ , which are 3–4 times faster than those of planar composite films (response and relaxation times of  $\sim 58$  ms and  $\sim 46$  ms, respectively). The arrays' response and relaxation times are comparable to those of ZnO-nanowire piezotronic strain sensors ( $\sim 10$  ms)<sup>145</sup> and much shorter than values obtained for Sb-doped ZnO nanobelt sensors (0.6–3 s)<sup>149</sup> and CNT–silver nanoparticle composite sensors ( $\sim 100$  ms).<sup>42</sup>

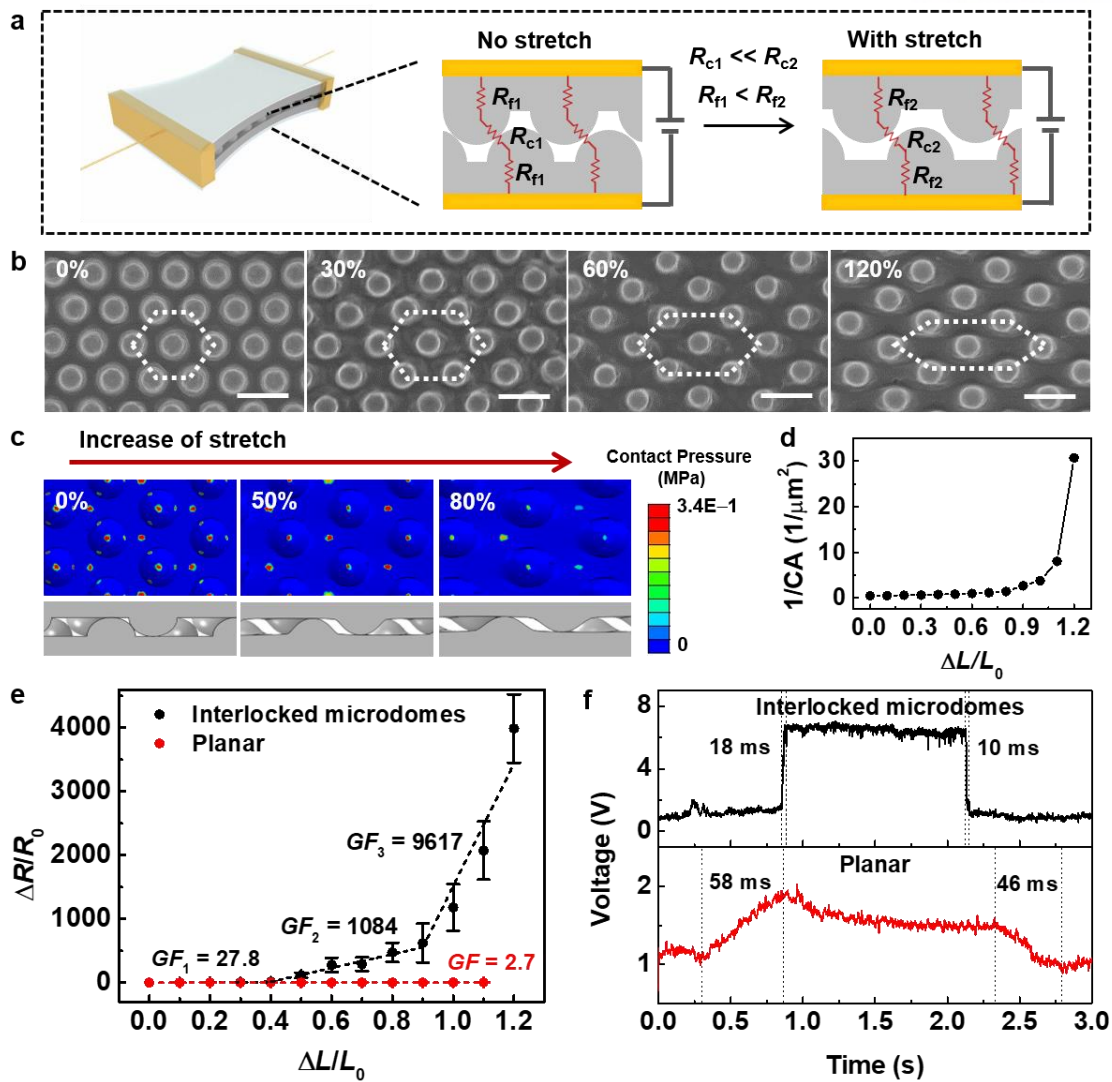


**Figure 3.2.** Lateral-stretch-sensing capability of electronic skins. (a) Schematic of the stretch-sensing mechanism of interlocked microdome arrays. (b) SEM images of microdome arrays showing the deformation of the array pattern from hexagons to elongated hexagons under different stretch ratios (0, 30, 60, and 120%). Scale bar: 5  $\mu\text{m}$ . (c) Finite-element analysis showing the contact pressure and the contact points between interlocked microdome arrays with the increase of uniaxial stretch. (d) FEA calculated results of the change of contact area (CA) between interlocked microdome arrays as a function of stretch. (e) Comparison of stretch-sensing capabilities of interlocked microdome arrays (black) and planar films (red). (f) Comparison of response and relaxation times of interlocked microdome arrays (black) and planar films (red) exposed to a stretching ratio of 50% and stretching speed of 3  $\text{mm s}^{-1}$ . The CNT concentration in the composite was 7 wt% and curing temperature was 60  $^{\circ}\text{C}$ . CNT concentration is 7 wt% for all the results.

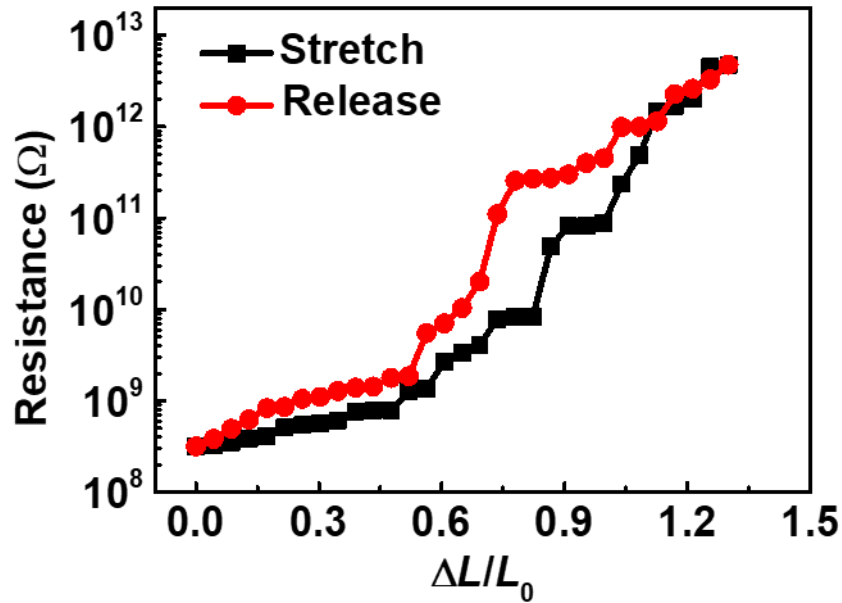


**Figure 3.3.** Change in piezoresistance of interlocked microdome arrays with lateral stretch for the loading and unloading cycles at 130% lateral strain. The interlocked microdome arrays were prepared with a CNT concentration of 7 wt% and curing temperature of 60 °C.

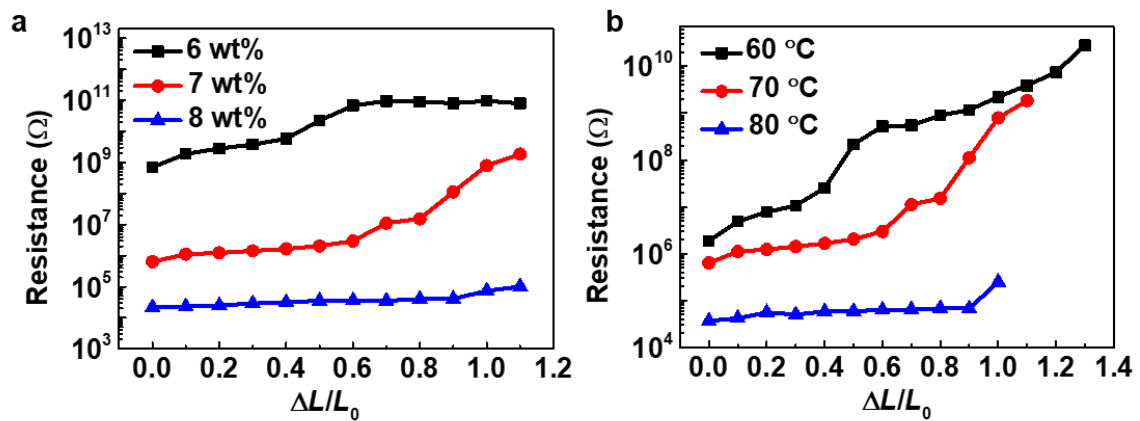


**Figure 3.4.** Variation in resistance of the interlocked microdome arrays as a function of lateral stretch for (a) different CNT concentrations (6–8 wt%) and (b) different curing temperatures (60, 70, and 80 °C).

**Shear-force sensitivity.** In addition to their stretch-sensing capability with high  $GF$  values, the capability of electronic skins to detect and differentiate normal and shear forces is critical in the perception of slip motion, force direction, and strength, as well as the dexterous manipulation of objects for applications in bionic hands, grippers, and tactile displays.<sup>150-153</sup> Our sensor is ideal for the detection of shear stress because the interlocked geometry of microdome arrays provides a strong joint without slip and thus enables the concentration of shear stress at the contact spots. In addition, in our system, the changes in contact resistance were different in response to the normal and shear forces, leading to the differentiation between normal and shear stresses. To test the normal- and shear-force sensitivity, the samples were preloaded with a normal pressure to engage the upper and lower microdome arrays and subsequently subjected to a known value of shear force (Figure 3.5a). The applied normal force immediately induced the surface deformation of microdomes in the interlocked geometry, resulting in an increase in contact area and thus a decrease in contact resistance between the interlocked microdomes. Figure 3.5b shows that the interlocked microdome arrays exhibited a systematic and consistent decrease and increase in relative resistance when the applied normal pressure was reversibly varied from 100 Pa to 25 kPa. As demonstrated in our previous study,<sup>45</sup> the high sensitivity to the normal force can be attributed to the significant change in tunnelling piezoresistance at the contact spots between the interlocked microdome arrays.

The subsequent application of a shear force resulted in the microdome deformation in the lateral direction, which led to a further increase in contact area between the microdomes and decrease in contact resistance. Figure 3.5c shows the change in relative resistance of interlocked microdome arrays as a function of shear force under a normal force ( $F_N$ ) of 58.8 kPa. For the quantitative analysis, we define a shear-force sensitivity ( $S$ ) in the linear range for different normal pressure loadings as  $S = (\Delta R/R_0) / (\Delta F_s)$ , where  $R$  and  $F_s$  are the resistance and applied shear force, respectively. The interlocked microdome arrays exhibited a shear-force sensitivity of  $-0.15 \text{ N}^{-1}$ , which is approximately four times the sensitivity of a planar film. Because the normal pressure affected the initial contact area between the interlocked microdome arrays, the shear-force sensitivity could be manipulated by controlling the normal pressure to engage the microdome arrays. Figure 3.5d shows the change in relative resistance as a function of shear force for different loadings of normal pressure for electronic skins with 7 wt% CNTs. We observed that the shear-force sensitivity increased with a decrease in normal pressure. The largest sensitivity was  $-2.21 \text{ N}^{-1}$  for a normal pressure of 65 Pa, which is  $\sim 13$  times the sensitivity ( $-0.15 \text{ N}^{-1}$ ) at a normal pressure of 58.8 kPa. This behaviour can be explained by the decreased initial contact area between microdome arrays at a lower normal pressure, providing the possibility to further increase the contact area by applying a shear force. Figure 3.6 shows the decrease and increase in the relative resistance of interlocked microdome arrays during pulling and retracting cycles under different shear forces, which also demonstrate their reliability.



In order to verify the variations in contact area with the application of normal and shear forces, we performed finite-element simulations of the change in contact area in the interlocked microdome arrays. The simulation results in Figure 3.5e indicate that the unique structure of interlocked microdome arrays leads to stress concentration and thus deformation of microdomes at the contact spots between spherical microdomes under normal pressure. The subsequent application of shear strain induces further deformation of microdomes at the contact spots, resulting in an increase in contact area. The contact area gradually increases with further increase in shear force, but more importantly, this increase in contact area depends on the normal pressure loadings. As can be seen in Figure. 3.5f, the change in the inverse contact area as a function of shear force is greatest for a normal pressure of 0.2 kPa. At higher values of normal pressure, the variation in inverse contact area decreases with increasing shear force. In addition to the normal force, our experiments showed that the shear-force sensitivity could be further manipulated by controlling the CNT concentration. As shown in Figure 3.7, the shear-force sensitivity increased with decreasing CNT concentration, with a sensitivity of  $-0.44 \text{ N}^{-1}$  for 5 wt% CNTs, which is  $\sim 3$  times the sensitivity of the sensor with 7 wt% CNTs ( $-0.15 \text{ N}^{-1}$ ) at a normal pressure of 58.8 kPa.

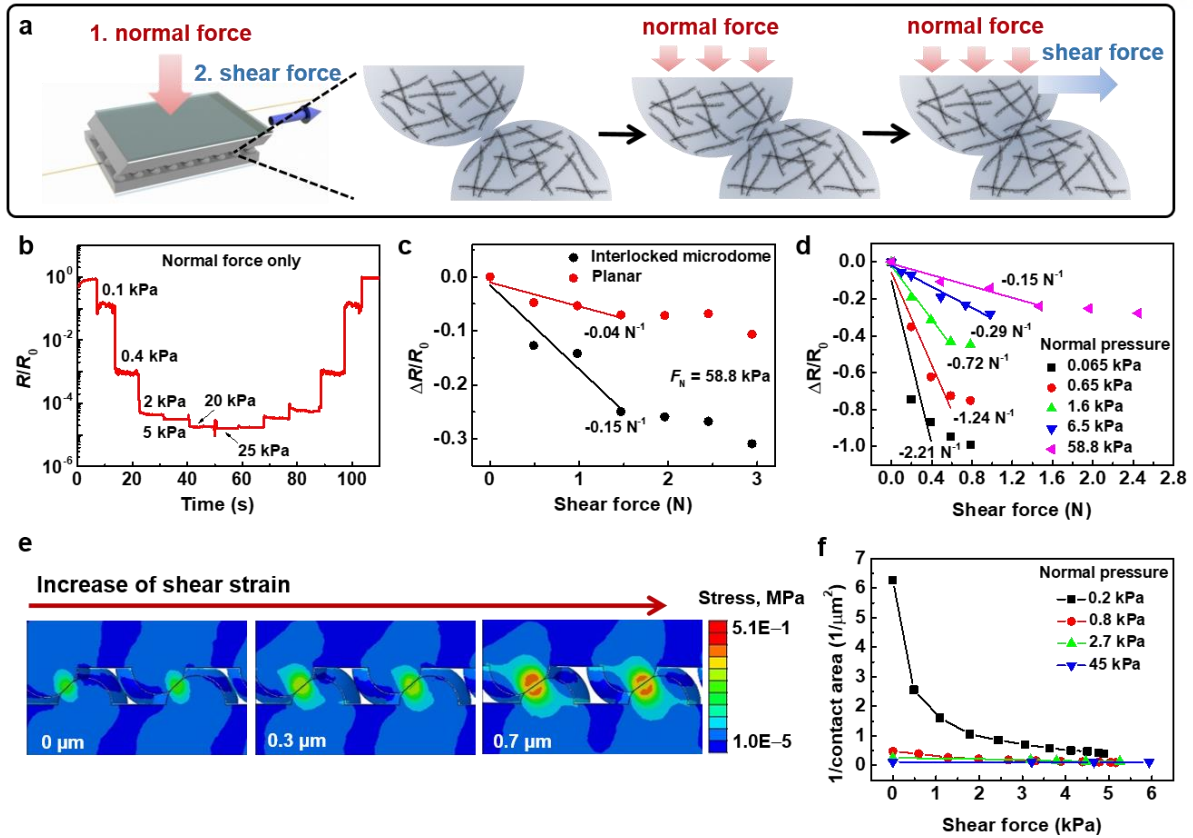


**Figure 3.5.** Normal- and shear-force-sensing capabilities of electronic skins. (a) Schematic of the deformation of interlocked microdomes during successive applications of normal and shear forces. (b) Relative electrical resistance of electronic skin sample as a function of normal force. (c) Comparison of shear-force sensitivities of interlocked microdomes (black) and planar (red) films under a normal pressure of 58.8 kPa. (d) Comparison of shear-force sensitivities of interlocked microdome arrays under different normal pressures. (e) Finite-element analysis (FEA) showing the deformation and local stress distribution of interlocked microdome arrays with increasing shear force at a normal pressure of 45 kPa. (f) Calculated FEA results of the inverse contact area as a function of shear force under different normal pressures. The CNT concentration was 7 wt% in all electronic skins used for the measurements.

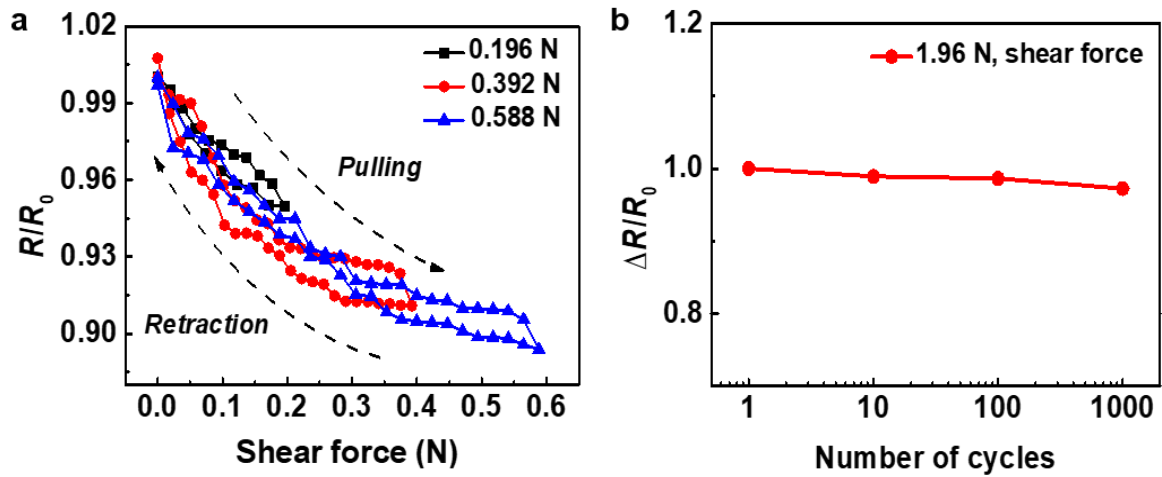


**Figure 3.6.** (a) Variation in normalized resistance for the pulling and retracting cycles under different shear forces (0.196, 0.392, 0.588 N). (b) Reliability of interlocked microdome composite films through cycles of repeated pulling and retraction under a shear force of 1.96 N.

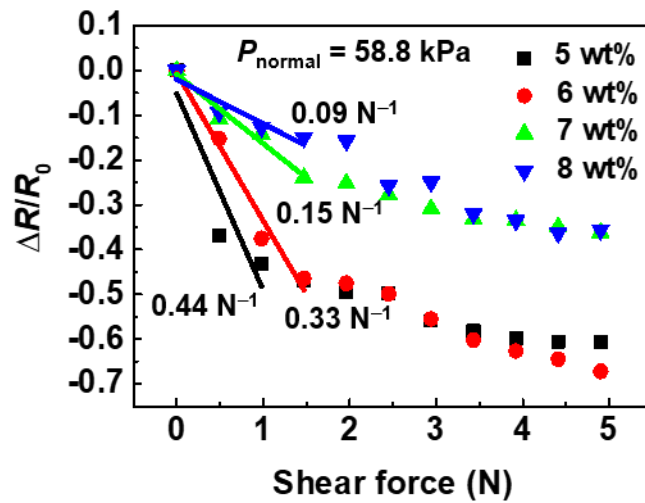


**Figure 3.7.** Change in relative resistance of interlocked microdome arrays as a function of shear force for electron skins with different CNT concentrations.

**Differentiation of multiple mechanical stimuli.** Since the interlocked geometry of the microdome arrays provided different deformation patterns specific to the type of mechanical stress, the interlocked microdome arrays were able to detect and differentiate multiple mechanical stimuli. To test their skin-like sensing capabilities, we monitored the normal and shear forces through simple finger contact on the electronic skins attached on human skin. Figure 3.8a shows the change in relative electrical resistance with repeated application of normal forces of 1 kPa and then shear forces. The electronic skin showed different signal intensities and patterns for different types of mechanical stimulus. While a finger touching the electronic skin in the normal direction ( $F_N$ ) resulted in an immediate decrease in relative resistance, a finger touching the electronic skin in the shear direction, which contained both normal and shear forces ( $F_N + F_S$ ), resulted in additional decreases in the relative electrical resistance. It is worth noting that the patterns of decrease in relative resistance resulting from  $F_N$  and  $F_S$  were different, therefore allowing the differentiation between normal and shear forces.

Figure 3.8b–d show that the electronic skin attached on the front of a human wrist could detect and differentiate different types of wrist movements such as forward bending ( $F_{FB}$ ), backward bending ( $F_{BB}$ ), and torsion ( $F_T$ ). In this experiment, we utilized a curing temperature of 60 °C since we observed that a lower curing temperature resulted in higher bending sensitivity (Figure 3.9). When the electronic skin was bent forward ( $F_{FB}$ ), the relative electrical resistance increased (Figure 3.8b); a gradual increase in forward bending resulted in the gradual increase in relative resistance. On the other hand, the relative electrical resistance decreased under backward bending (Figure. 3.8c), while the twisting of the wrist ( $F_T$ ) resulted in an increase in electrical resistance. In particular, twisting also generated oscillating signals resulting from the repeated contact-on/contact-off behaviour during the twisting. These different signal patterns in response to different mechanical stimuli are attributed to the unique interlocked geometry of microdome arrays, which, depending on the direction of mechanical stress, could result in distinct variations in contact area. During forward bending, the gap between the neighbouring microdome arrays increased because the upper microdome layer tends to detach from lower microdome layer due to the strain mismatch between the upper (under tension) and lower (under compression) microdome arrays, leading to an increase in relative resistance. Backward bending decreased the electrical resistance because the lower microdome layer is sandwiched between the human skin and the upper microdome layer, resulting in the decreased gaps between adjacent microdome arrays.

Figures 3.8e–j show that the different deformation patterns of interlocked microdome arrays depending on the type of mechanical stress result in the differentiation of multiple mechanical stimuli. Here, each of the electrical signal under different mechanical stimuli provide a unique output pattern specific to the type of mechanical input, leading to the differentiation of multiple mechanical stimuli. This capability is facilitated by the tactile-direction-sensitive deformation of interlocked microdome arrays, which results in the different magnitudes of deformations and response/relaxation times. As can

be seen in Figures 3.8e-j, the relative resistances decrease for pressure, shear, and backward bending forces and increase for stretch, forward bending, and torsional forces. In particular, the pattern of resistance variation can be differentiated by the different magnitude, shape, and response/relaxation times. In addition, the torsional force generates unique oscillation patterns in the resistance variation, which can be attributed to the repeated contact area variation during the continuous twisting of regular microdome arrays. Although the basic principle of differentiating various tactile stimuli in our e-skin is different from that of human skin with various mechanoreceptors, the results in this study also suggest that the interlocked microstructures of human skin may have profound effects on the differentiation of various tactile signals. In the future, mimicking the mechanoreceptors in epidermis and dermis layers of human skin in addition to the interlocked microstructures may enable e-skins with realistic human-skin-like tactile sensing capabilities.

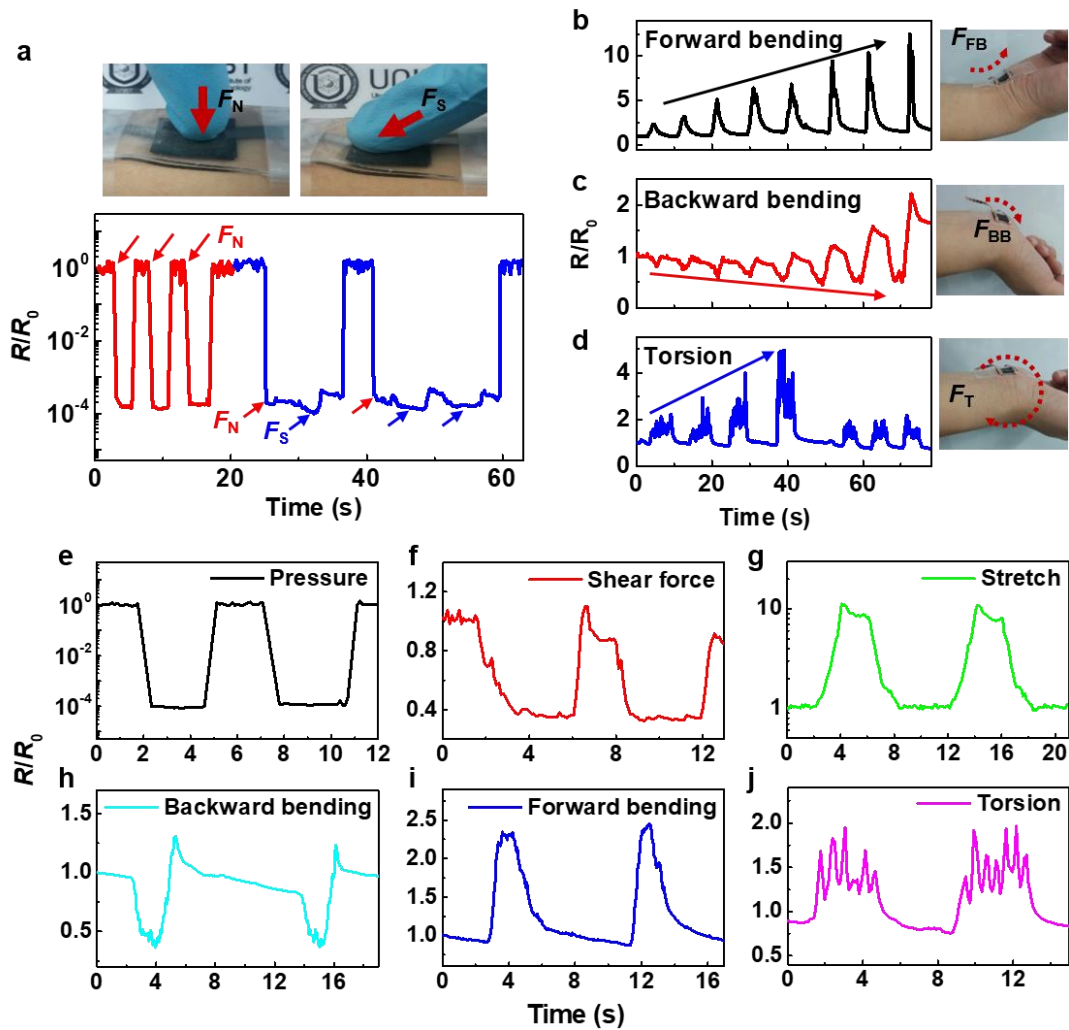


**Figure 3.8.** Stress-direction-sensitive electronic skins for the detection and differentiation of multiple mechanical stimuli. (a) Real-time monitoring of changes in the relative resistance of interlocked microdome arrays subjected to different normal and shear forces. (b–d) Change in relative electrical resistance of an electronic skin attached on the front of a human wrist under different types of wrist movements: (b) forward bending; (c) backward bending; (d) torsion. The electronic skin showed different signal patterns in response to different wrist movements. (e–j) Change in relative electrical resistance of electronic skins in response to different mechanical stimuli: (e) normal force; (f) shear force; (g) lateral stretch; (h) forward bending; (i) backward bending; (j) torsion.

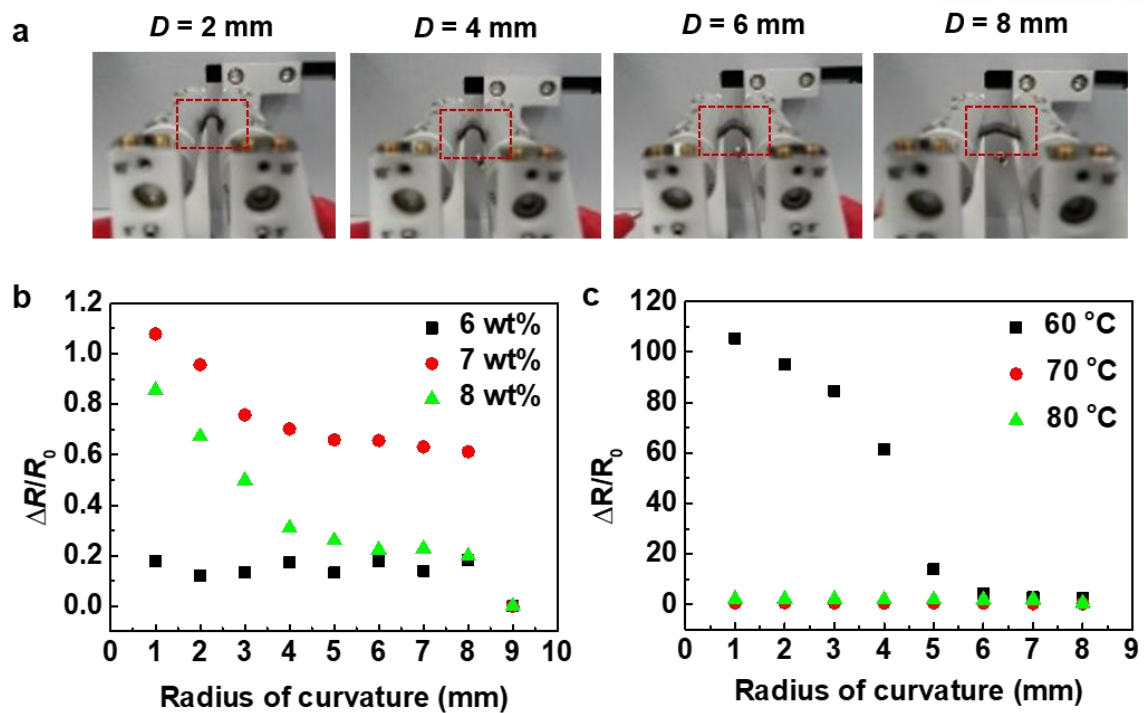


**Figure 3.9.** (a) Photographic images of bending tests of electronic skins with interlocked microdome arrays. (b) Variation in relative resistance of interlocked microdome arrays as a function of radius of curvature for electronic skins with different CNT concentrations (6–8 wt%) and cured at 80 °C. (c) Variation in relative resistance of interlocked microdome arrays as a function of radius of curvature for electronic skins prepared with 7 wt% CNTs at different curing temperature (60, 70, 80 °C).

**Wearable electronic skins with stress-direction sensitivity.** For the proof-of-concept wearable electronic skins to resolve the spatial distribution and the directions of applied external stimuli such as touch, flow, and vibration, we fabricated  $3 \times 3$  pixel arrays of electronic skin sandwiched between cross arrays of platinum electrodes (Figure 3.10a). When we touched two different pixels (R1-C3 and R3-C1 in Figure 3.10b) on the electronic skin, it could provide spatially resolved mapping of the touch positions. The high sensitivity of each pixel on the electronic skin could also provide the ability to resolve gradual changes in mechanical stimuli, therefore enabling the detection of the direction of mechanical stress. Figure 3.10c shows that depending on the finger-pushing directions (left, right, up, and down), the electronic skin exhibited different spatially resolvable patterns, indicating the perception of the intensity and direction of tactile stimuli. Figure 3.10d also demonstrates the directional sensing capability of the electronic skin, where fluid flows in different directions (left, right, and diagonal) could be clearly resolved by the signal patterns. The sensitivity to gradual changes and directions of external stimuli was also verified by applying a vibrational stimulus on the electronic skin. Figure 3.10e shows the application of radial vibration on one pixel located at the corner (R1-C1) of the electronic skin and the resulting spatial mapping of the vibrational stimulus. Owing to vibrational damping, the change in relative resistance gradually decreased as the pixel location was farther away from the original pixel at which vibration was applied, which led to gradually decreasing changes in the relative resistance.



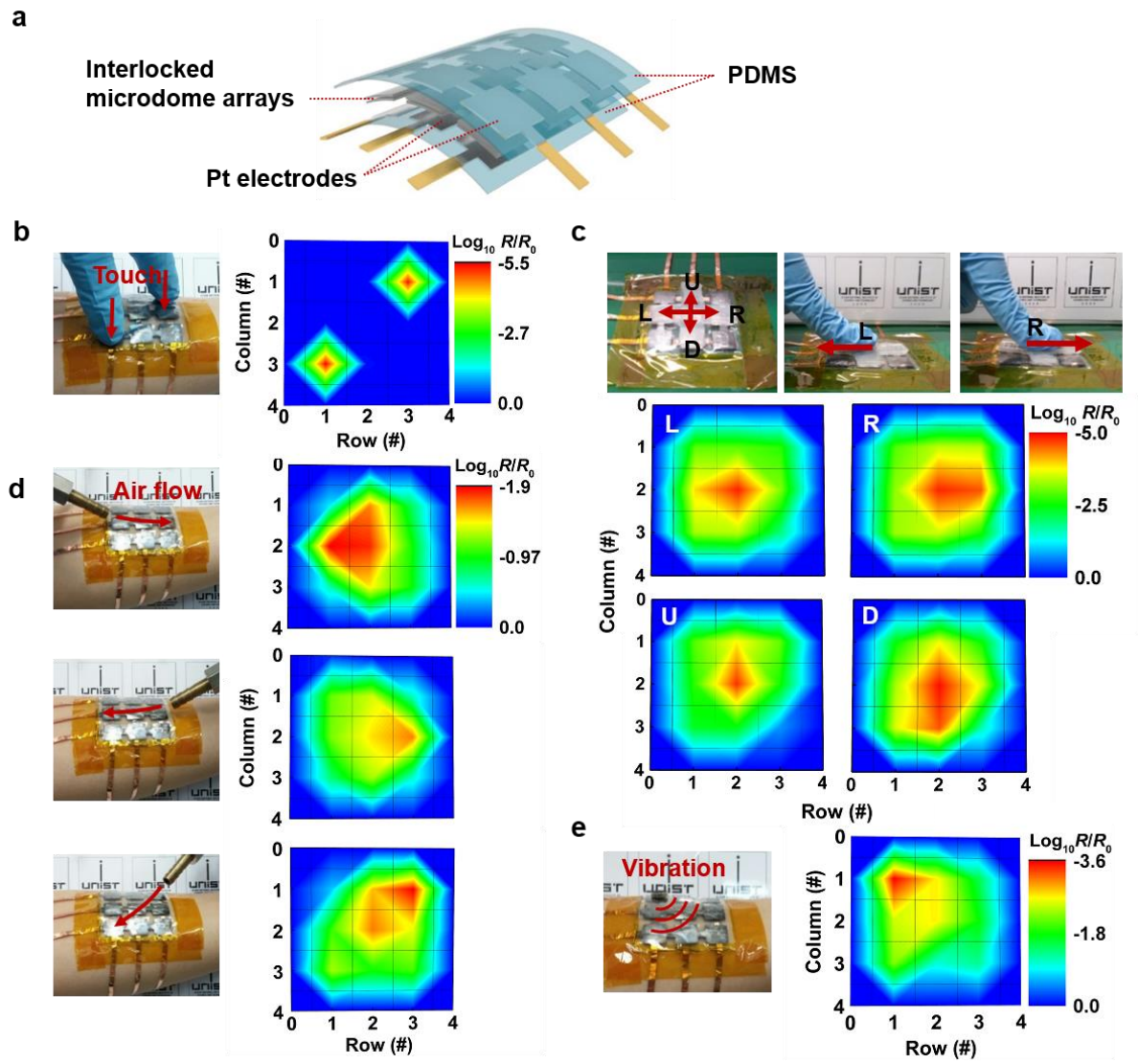


**Figure 3.10.** Stress-direction-sensitive electronic skins for directional sensing of mechanical stimuli applied in three axial directions. (a) Schematic of sensor arrays, where interlocked microdome arrays are sandwiched between the electrodes and PDMS protection layers. (b) Spatial pressure mapping capability of electronic skin for the detection of finger touch on two different pixels (R1-C3, R3-C1). (c) Detection of different finger-pushing directions: left (L), right (R), up (U), down (D). (d) Detection of different directions of fluid flow (left, right, diagonal). (e) Detection of the location of applied vibration and the gradual damping of vibration.

### 3.4 Conclusions

In summary, we have demonstrated stress-direction-sensitive and stretchable electronic skins with three-axial stress-sensing capabilities. We employed piezoresistive, interlocked microdome arrays which were inspired by the interlocked epidermal–dermal layers in human skin. Similar to the stress concentrating function of interlocked epidermal-dermal ridges which magnify the tactile stimuli, the arrays could induce exclusive stress concentration at the contact spot and thus deformation of the microdomes, resulting in enhanced sensitivity of the piezoresistive response to stress. In particular, the unique geometry of the interlocked microdome arrays led to different deformation patterns which depend on the type and direction of mechanical stress, enabling detection and differentiation of various mechanical stimuli including normal, shear, stretch, bending, and twisting forces. Owing to the direction-sensitive tactile-sensing properties, various electronic skins attached on human skin were successfully employed to monitor different intensities and directions of finger touches, air flows, and vibrations. Because our design is the simplified version of complicated human skin, where papillary ridges, location of mechanoreceptors, the elastic moduli of layers, and the shape and size of intermediate ridges are all closely related to each other to efficiently transduce and magnify tactile stimuli, we expect that the interlocked geometry can be further explored to develop bio-inspired electronic skins with human-skin-like tactile-sensing capabilities. Finally, we anticipate that our stretchable electronic skins with multi-directional stress-sensing capabilities can find applications in robotic skins, prosthetic limbs, and rehabilitation devices to monitor motion and stress distribution.

## Chapter 4. Microstructure engineering of multidirectional electronic skins for tailoring force sensitivity and selectivity

### 4.1 Introduction

Recently, a large number of electronic skins with capabilities of detecting physical/chemical stimuli have been reported for applications in robotics, wearable electronics, and healthcare monitoring devices.<sup>130, 154-160</sup> Owing to their wearable or body-attachable features, many types of e-skins have been actively utilized as innovative tools for monitoring radial and carotid blood pressure,<sup>154, 155</sup> and electrophysiological signals<sup>156, 157</sup> and for oximetry<sup>158</sup> as well as drug delivery.<sup>130</sup> For accurate and reliable monitoring of those signals, e-skins with enhanced sensitivity, selectivity, response time, and mechanical durability are required. In accordance with these demands, e-skins with various bio-inspired micro/nanostructures (e.g., interlocking, hierarchical, crack, whisker, and fingerprint) and 2D or 3D shapes (e.g., serpentine, wrinkle, pyramid, dome, and porous) have been reported aiming to obtain high-performance and multifunctional e-skins.<sup>161</sup> In particular, owing to their effective geometrical advantages, regular arrays having various microstructures (e.g., hemisphere, pyramid, and pillar) have been used to improve the performance of e-skins based on different operation modes (e.g., resistive, capacitive, piezoelectric, and triboelectric). Specifically, dome- or hemisphere-shaped microstructures have been reported to induce a large change in contact area and localized stress concentration, which are advantageous for fabricating high-performance piezoresistive sensors<sup>162</sup> and triggering a large amount of triboelectric charge<sup>163</sup> and a high piezopotential in the piezoelectric devices.<sup>35</sup> On the other hand, a large variation in local strain and compressibility of pyramid-shaped microstructures enhance force sensitivity and expand the dynamic sensing range of e-skins.<sup>44, 88, 164</sup> Inspired by the hierarchical structures in nature, such as insect legs, gecko feet, and beetle wings, pillar-shaped microstructures have been reported to provide selective and directional force-sensing properties as well as stress-confinement effects.<sup>19, 165-167</sup> In addition, the strong adhesion properties of pillar structures provide a new possibility for skin-attachable and wearable healthcare devices.<sup>154</sup>

Considering these geometrical effects of microstructure arrays on the performance of e-skins, previously, geometrical parameters such as shape, size, and space of microstructure arrays have been controlled to enhance the mechanical sensitivity and operation range of piezoresistive<sup>168</sup> and capacitive e-skins<sup>164</sup> and the power generation of self-powered e-skins.<sup>19, 93, 165, 166, 169, 170</sup> Since the geometrical shape of microstructure significantly affects the contact area and localized stress of microstructure under pressure, several attempts to find the relationship between the shape of microstructure and the sensitivity of various e-skins have been performed. For example, Wang et al. controlled the surface of triboelectric sensors with different shapes of microstructure.<sup>93</sup> Kim et al. Investigated the structural

shape effect on the formation of piezoelectric potential to optimize sensor performances.<sup>170</sup> Yang et al. studied the dependence of interfacial shape of microstructures (cuboid, cylinder, and pyramid) on the sensitivity of capacitive sensors.<sup>171</sup> Although previous e-skins having different microstructures have successfully shown improved tactile sensing performances, specific to some of desired applications, there have been no systematic studies of the effects of microstructure geometry on force-induced microstructure-deformation and the resulting force sensitivity and selectivity in response to multidirectional mechanical stimuli. In particular, the sensing performance of piezoresistive e-skins with microstructure arrays critically depends on the localized stress distribution of microstructures and the resulting contact area change when external mechanical forces are applied in different directions. Although the interlocked microdome structures have been reported to exhibit high pressure sensitivity,<sup>45, 46</sup> in-depth investigation of the effects of microstructures on the multidirectional sensing performances has not been done. A systematic and in-depth analysis of geometrical effects on sensing performance is important to enable the design of tunable e-skins having high force sensitivity and selectivity, which can be customized for diverse applications.

In this study, multidirectional force sensitive e-skins are shown to possess customizable force sensitivity and selectivity by controlling the specific microstructure geometry. To investigate the underlying relationship between microstructure geometry and force sensing capability, three kinds of piezoresistive sensors were fabricated based on carbon nanotube/elastomer composites having different surface microstructures (e.g., dome, pyramid, and pillar). To facilitate comparison of the geometrical shape effect on the stress sensing properties, an interlocked geometry of the different microstructure arrays was employed. This has been reported to enhance the variation in contact area and localized stress in the microstructures, thereby improving the stress sensitivity and multidirectional force sensing capabilities of e-skins.<sup>43, 45, 46, 172</sup> For the fundamental understanding of the sensing mechanisms, experimental piezoresistive properties were compared to the finite-element simulation of contact-area change and the localized stress distribution of microstructured e-skins. It was found that piezoresistive e-skins having different microstructures exhibit distinct force sensitivity and selectivity mainly due to the specific variation in contact area, which depended on the geometrical shape of the microstructures, in response to multidirectional forces (e.g., normal, shear, tensile, and bending). As a result, microdome structures presented the best force sensitivities for normal, tensile, and bending stresses. On the other hand, for shear stress, micropillar structures exhibited the highest sensitivity. As proof-of-concept demonstrations for potential applications in wearable healthcare devices, highly sensitive pressure sensors were used for detecting various bio-signals, including sound, human breath, and artery/carotid pulse pressures.

## 4.2 Experimental Details

**Fabrication of Conductive Composites with Interlocked Microstructures:** The synthesis of conductive composites was initiated by dispersion (5 mg/ml) of multi-walled carbon nanotubes (Sigma-Aldrich, 110–190 nm diameter and 5–9  $\mu\text{m}$  length) in chloroform (Samchun, Korea). After 6 h of sonication, well-dispersed MWNTs solution was mixed with PDMS base (Sylgard 184, Dow Corning) with an 8 wt% ratio of MWNTs to PDMS. Subsequently, the MWNT/PDMS solution was mixed with a vortex and dried at 90  $^{\circ}\text{C}$  for 12 h, in order to completely evaporate the chloroform. Prior to the micromolding process, the MWNT/PDMS precursor was combined with a curing agent (PDMS base: curing agent 10:1) and hexane (1 ml per 0.5 g of PDMS) was added for reducing the viscosity of the dried precursor. The prepared MWNT/PDMS composite solution was poured into silicon molds with different micropatterns (i.e., dome, pyramid, and micropillar), followed by air bubble removal and thermal treatment at 90  $^{\circ}\text{C}$  for 4 h, resulting in the preparation of micropatterned MWNT/PDMS composite films.

Silicon molds with micropattern arrays were fabricated via photolithography and etching processes. For manufacturing microdome- and micropillar-patterned PDMS molds, hexagonally patterned photomasks (diameter and pitch: 3  $\mu\text{m}$  and 15  $\mu\text{m}$  for the microdome structure and 10  $\mu\text{m}$  and 15  $\mu\text{m}$  for the micropillar structure, respectively) and a positive photoresist (PR, AZ 5214E) were used for photolithography (mask aligner, MA/BA-6-8, Succ Microtec) on bare silicon wafers. To conduct the dry-etching process, a reverse patterning process was performed by deposition of a 50 nm-thick chrome layer using the thermal evaporation technique and lift-off process of PR using acetone. The chrome layer acted as a hard mask during the dry-etching process. Each chrome-patterned silicon wafer was isotropically or anisotropically etched via reactive ion etching (RIE) or deep reactive ion etching (DRIE) processes, respectively. Finally, each silicon mold for fabricating microdome- and micropillar-patterned PDMS was prepared by removing the chrome layer through wet-etching and coating a self-assembled monolayer (SAM) on each silicon wafer to ease the PDMS-unmolding process. For the micropyramid-patterned PDMS mold, negative PR (AZ nLOF 2035) was patterned on a  $\text{SiO}_2/\text{Si}$  wafer ( $\text{SiO}_2$  layer thickness of 50 nm) via photolithography employing a hexagonally-patterned photomask with a 10  $\mu\text{m}$  diameter and 15  $\mu\text{m}$  pitch. The exposed  $\text{SiO}_2$  was then etched via a RIE process and PR was removed with acetone. The remaining  $\text{SiO}_2$  acted as a hard mask in the crystallographic wet-etching process of silicon, which was conducted by immersing it in 30 wt% potassium hydroxide for 10 min at 70  $^{\circ}\text{C}$ . Next, the  $\text{SiO}_2$  mask was completely removed by wet-etching using 4 % hydrofluoric acid. After SAM-coating this silicon wafer, the fabrication process was completed.

**Characterizations:** The geometrical information at the surface of micro-patterned composite films was obtained using field-emission SEM (FE-SEM; S-4800, Hitachi). Surface conductivity of the micro-

patterned composites having different fabricating conditions was measured using the four-probe method with a semiconductor analyzer (4200-SCS, Keithley). In addition, the mechanical modulus of the composite films was obtained using a tensile strain tester (Universal Testing Machine, WL2100, WITHLAB Co., Korea) with a strain rate of 500 mm/min.

**Measurements of the Multifunctional Sensing Performances of the E-skins:** To measure the electrical properties of the e-skins under mechanical forces, a copper electrode is attached uniformly onto the fabricated composite film with silver paste and then thermally annealed at 90 °C for 30 min to minimize the electrical loss at the composite–electrode interface. Next, both composite films were placed facing each other and connected to the electrical measurement systems. To measure the electrical property of e-skins in response to tensile and bending stress, copper electrodes are attached at the side of composite films and polyimide tapes were used to fasten the electrode on the e-skins. The electrical properties of e-skins that depend on mechanical forces were measured using the two-probe method of the semiconductor analyzer (4200-SCS, Keithley) with an applied voltage of 1–5 V. To precisely apply the mechanical forces, a pushing tester (JIPT-100, Junil Tech) was used for normal pressure, and a tensile/bending test machine (JIPT-200, Junil Tech) was used to apply stretching/bending forces. Shear force was applied with a microstage system (Micro Motion Technology, Korea). In order to evaluate the capability of sound detection, e-skins were exposed to acoustic waves with a 100 Hz frequency from a speaker (SMS-A490, Samsung) at a constant distance of 1 cm and then electrical resistance signals were collected. For the healthcare signal detection, 1 cm<sup>2</sup> e-skins were covered with polyimide film and bandaged onto the wrist, neck, and below nose, and the change in electrical signals was recorded to monitor artery and carotid pulse pressures and human breath. To show the possibility of integration with commercially available chip, e-skin was connected to the commercial chip (STM32F030C6T6, STMicroelectronics) and signals are detected by oscilloscope (DPO2022B, Tektronix).

**Finite-Element Method:** In order to calculate the contact area and localized stress of microstructured e-skins, structural analysis was conducted using finite–element simulations. Linear elastic materials with experimentally measured mechanical properties followed composite models with different microstructures. For the basic model for numerical analysis of contact area, more than 0.5 million linear tetrahedral and wedge elements (element size: 0.2 (Min.) and 2 (Max.)) with an adaptive mesh-refinement scheme were employed. Each element in case of interlocked microdome, micropyramid, and micropillar has element/volume ratio of 31.8, 55.4, 73.0 and average aspect ratio of 1.54, 1.57, 1.56, respectively. Multidirectional loading conditions were modulated by displacement controls and converted to the corresponding normal, shear, tensile, and bending forces forms. Based on the surface-to-surface contact scheme between two deformable bodies, mechanical contact, localized stress, and thickness of the composite can be obtained under proper loading conditions.

### 4.3 Results and Discussion

**Electronic Skins having Interlocked Microstructures and Different Geometries.** Figure 4.1a shows a schematic representation of a piezoresistive e-skin constituting multi-walled carbon nanotubes/polydimethylsiloxane (MWNT/PDMS) composite films having interlocked microstructure arrays. In this case, the piezoresistive properties of the e-skin depend mainly on the bulk film resistance ( $R_F$ ) and the contact resistance ( $R_C$ ) between the two neighboring microstructures of conductive composite films (Figure 4.1b). While the piezoresistance of conventional e-skins constituting a planar composite film is affected predominantly by the  $R_F$  change, the piezoresistance of the interlocked microstructures is dominated by variations in  $R_C$ . For conductive composites, the piezoresistance is affected mainly by the tunneling resistance.<sup>94, 95</sup> Similarly, in the interlocked MWNT/PDMS composite films of the present work, contact resistance is dominated by the tunneling resistance ( $R_T$ ) between microstructured composite films, which is inversely proportional to the variation in contact area according to the equation  $R_T = (V/J) \times (1/A_{CNT})$ , where  $V$  is the applied voltage,  $J$  is the current density, and  $A_{CNT}$  is the electrical contact area between MWNTs, which is in turn proportional to the physical contact area ( $A_C$ ) between interlocked microstructures.<sup>45</sup> Therefore, the contact-area change critically affects contact resistance. In addition, the tunneling current ( $J$ ) through a thin PDMS insulating layer at the interface of interlocked microstructures exponentially increases with decreasing insulating layer thickness ( $T_{PDMS}$ ).<sup>173</sup> As schematically shown in Figure 4.1c, the pressure sensing mechanism can be explained as follows. When an external pressure is applied on interlocked microdomes, stress accumulates at the tips of dome structures, and this concentrated stress can easily deform the microdomes and thus increase  $A_C$  between interlocked microstructures and decrease  $T_{PDMS}$  of the PDMS insulating layer between CNTs. These changes in contact area and barrier thickness significantly affect the tunneling currents through the thin PDMS insulating layer, causing a drastic increase in relative-current change as a response to pressure loading.

To investigate the effects of microstructure shape on piezoresistance, e-skins having three different surface morphologies (i.e., dome, pyramid, and pillar) were fabricated using the micromolding process (Figures 4.1d and e). For this process, silicon replica molds with different micropattern arrays were produced via photolithography and etching processes (the detailed methodology is in the Experimental details). The fabricated microstructures had equal feature sizes; 10  $\mu\text{m}$  diameter, 15  $\mu\text{m}$  pitch, and 6  $\mu\text{m}$  height (Scanning electron microscope (SEM) images in Figure 4.1e). For interlocked composite microstructures, high surface conductivity is preferred for enhancing pressure sensitivity due to the drastic  $R_C$  change with changing contact area under proper loading pressure.<sup>45</sup> In this study, interlocked composite microstructures having 8 wt% CNTs were utilized. For the different microstructure composites, sheet resistance exhibited similar values, around  $1 \times 10^4$  ohm/sq (Figure 4.2).

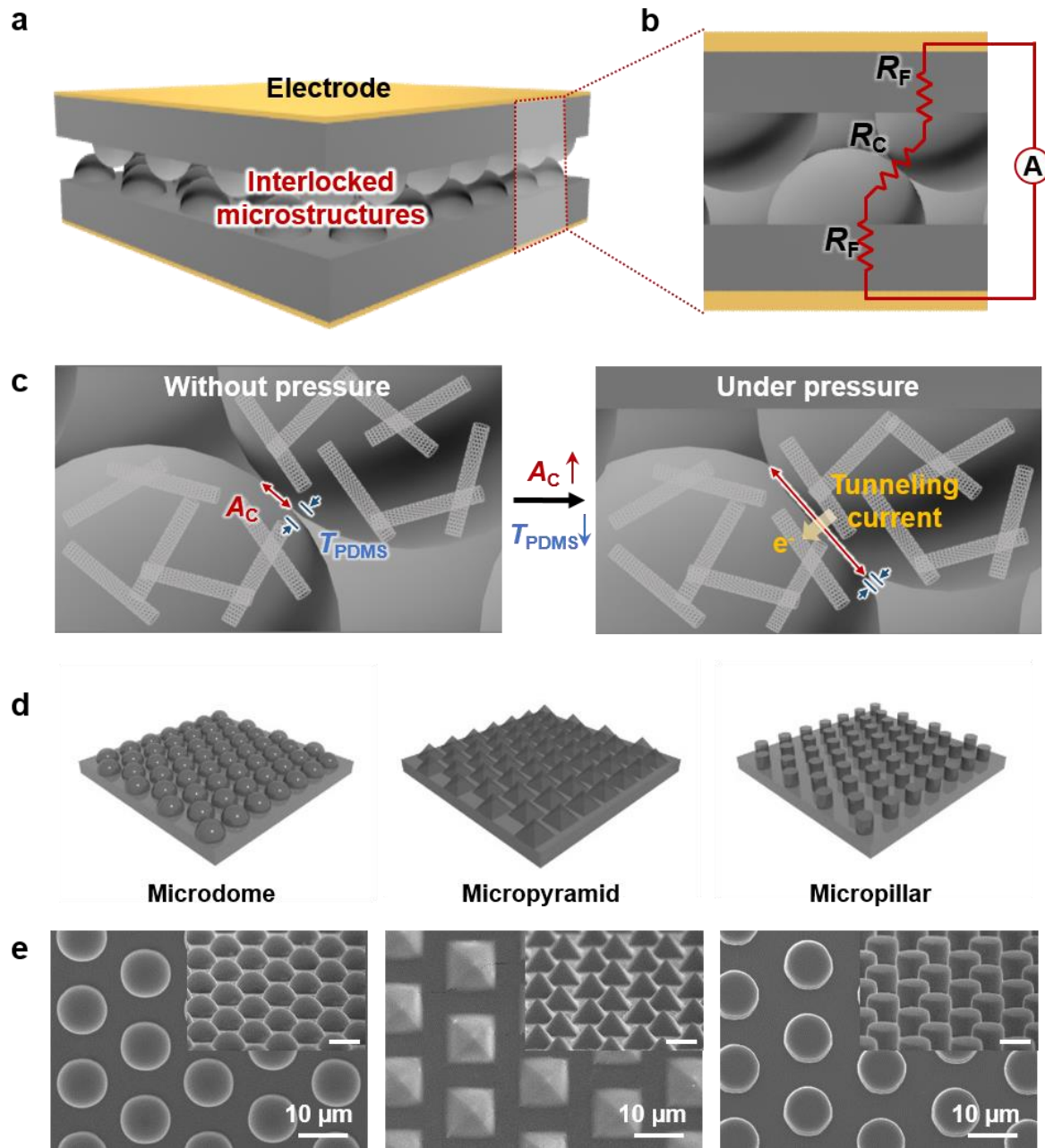


**Figure 4.1.** Piezoresistive e-skins with interlocked microstructures having different surface morphologies. (a) Schematic illustration of the main structure of the e-skins with interlocked microstructures. (b) Schematic showing the bulk film resistance ( $R_F$ ) and the contact resistance ( $R_C$ ) between the two neighboring microstructured films. (c) Pressure-sensing mechanism of piezoresistive e-skins having interlocked microstructures. (d) Schematic illustration of conductive composites with different microstructured arrays. (e) Top and tilted (inset) SEM images of the microstructured composites with different surface morphologies (microdome, micropyramid, and micropillar).



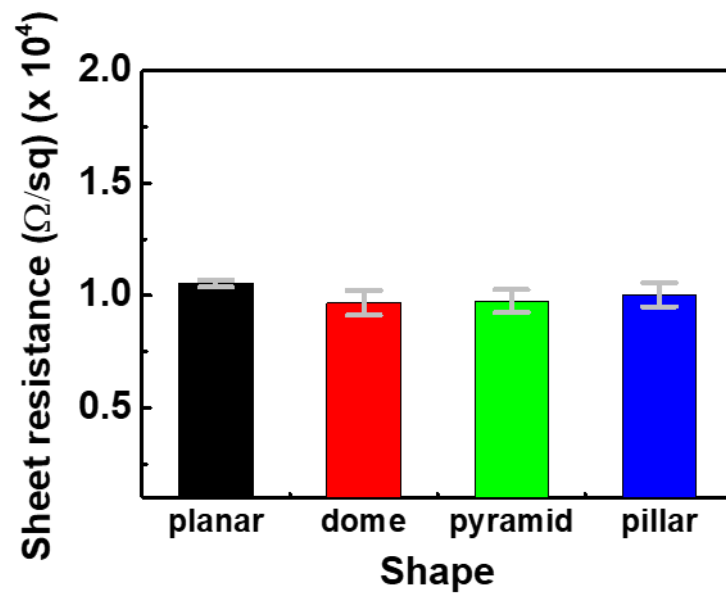


**Figure 4.2.** Sheet resistance of PDMS/MWNT composite with different surface microstructures.

**Pressure-Sensing Capability of Single Microstructured E-skins.** Before discussing the structural effect of piezoresistance on interlocked CNT/PDMS composite microstructures, the pressure-sensing properties of single-sided composite films having different surface microstructures was investigated. Single-sided microstructured films have been widely employed to enhance the performance of flexible pressure sensors<sup>44, 162, 165, 174</sup> and triboelectric generators.<sup>93, 163</sup> For pressure-sensitive piezoresistance, a flat indium tin oxide (ITO) film was used as the top electrode on the surface of micropatterned composite films (Figure 4.3a). In this case, the output current depends on the  $R_F$  of the bulk film and the  $R_C$  between the microstructure and electrode. The relative electrical current change ( $\Delta I/I_0$ ) as a function of normal pressure applied on top of the ITO electrode increased with increasing applied pressure (Figure 4.3b). The  $\Delta I/I_0$  values of single microstructured films increased as a function of pressure more rapidly in comparison to that of single planar structure. For quantitative analysis, the pressure sensitivity ( $S$ ) can be calculated using the equation  $S = (\Delta I/I_0)/\Delta P$ , where  $I_0$  is the initial current,  $\Delta I$  is the change in current after pressure loading, and  $\Delta P$  is the change in normal pressure. The linear pressure sensitivity exhibited different values depending on the microstructure shape (18.3, 12.6, and 5.3  $\text{kPa}^{-1}$  for microdome, micropyramid, and micropillar structures, respectively), all of which were much higher than that of a planar structure ( $0.5 \text{ kPa}^{-1}$ ) in the low-pressure range ( $<1 \text{ kPa}$ ) (Figures 4.3b and 4.4a). As will be discussed later, the enhanced sensitivity of microstructured films, compared to the planar one, can be attributed to stress concentration at the small contact spot between the microstructure and ITO electrode, which resulted in an increase in contact area and decrease in PDMS barrier thickness, thereby increasing the tunneling current between the microstructure and electrode. For the planar structure, the external pressure mainly induced a change in inter-tube distance within the bulk composite film without affecting the contact area much, resulting in the lower pressure sensitivity than those of microstructures. Compared to the low pressure range, in the medium pressure range (1–10  $\text{kPa}$ ), the pressure sensitivity decreased: 10.3, 3.3, 0.4, and  $0.2 \text{ kPa}^{-1}$  for microdome, micropyramid, micropillar, and planar structures, respectively (Figures 4.3b and 4.4b), but the effect of microstructure on the sensitivity did not change; sensitivity showed the same tendency as that in the low-pressure range (microdome  $>$  micropyramid  $>$  micropillar  $>$  planar).

To further understand the piezoresistance of single-sided composite microstructures, finite-element simulations of contact-area variation of the microstructures under normal pressure were performed. When a pressure of 10  $\text{kPa}$  was applied on the composite films, microdome and micropyramid structures exhibited a local stress-concentration at the small contact spots, which was not observed for micropillar structures that do not have those small contact spots (Figure 4.3c). In addition to the local stress-accumulation, the applied pressure induced a contact-area change, where dome and pyramid structures exhibited a significantly larger change than planar structures (Figure 4.3d). As compared to pillar structures, the significantly smaller initial contact area of dome and pyramid structures under zero

pressure led to a greater change in contact area under mechanical pressure (Figure 4.5), which resulted in a drastic increase in output current (Figure 4.6). In addition to the contact area, the concentrated stress can decrease the thickness of the PDMS dielectric barrier between the CNT and electrode, which is known to induce an exponential increase in tunneling current.<sup>173</sup> The change of microstructure thickness in response to pressure (Figure 4.7) implies that the barrier thickness decreases with increasing pressure. These changes in contact area and barrier thickness significantly increased the tunneling currents through the interface between the electrode and CNT composite as a response to pressure loading.

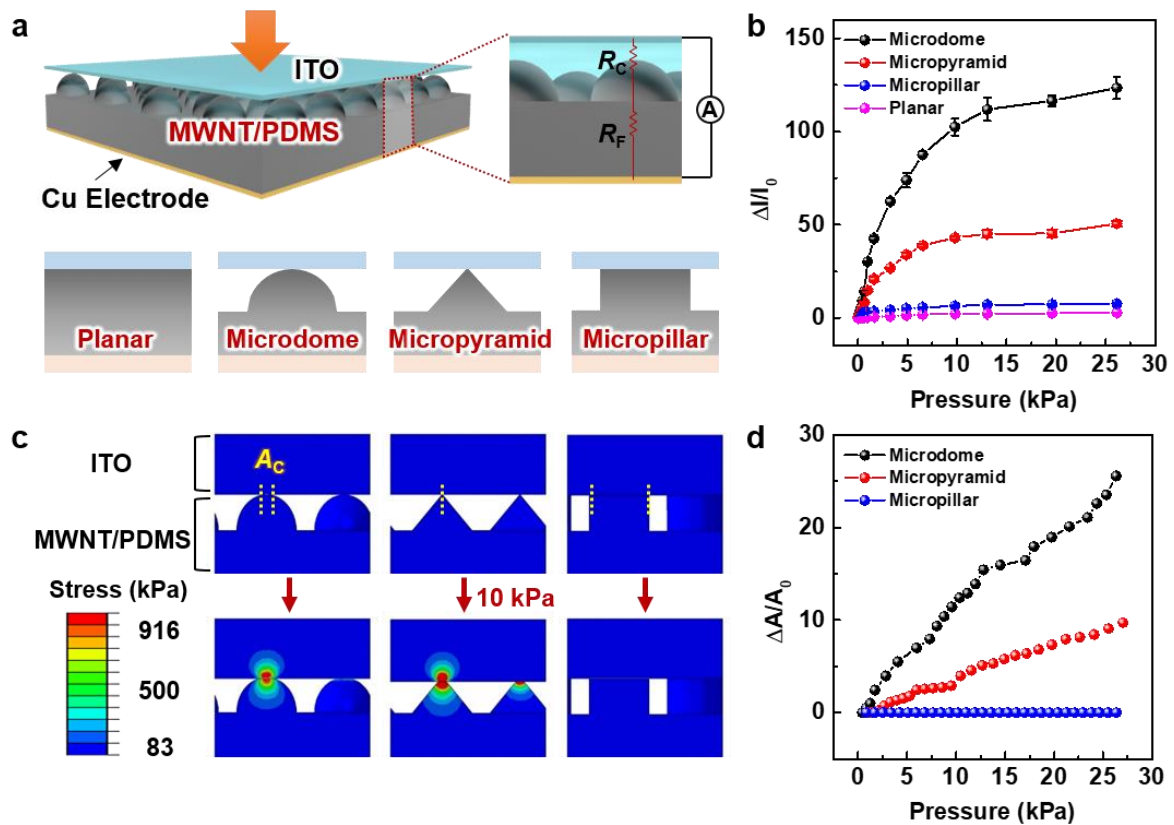


**Figure 4.3.** Pressure-sensing capability of single microstructured e-skins. (a) Schematic illustration of the pressure-sensing principle of single microstructured e-skins with different surface morphologies. (b) Relative current changes in response to normal pressure. (c) Finite-element analysis (FEA) of localized stress distributions in response to pressure for different surface microstructure arrays (top layer: ITO, bottom layer: MWNT/PDMS composite). (d) Calculated relative contact-area changes in response to normal pressure.

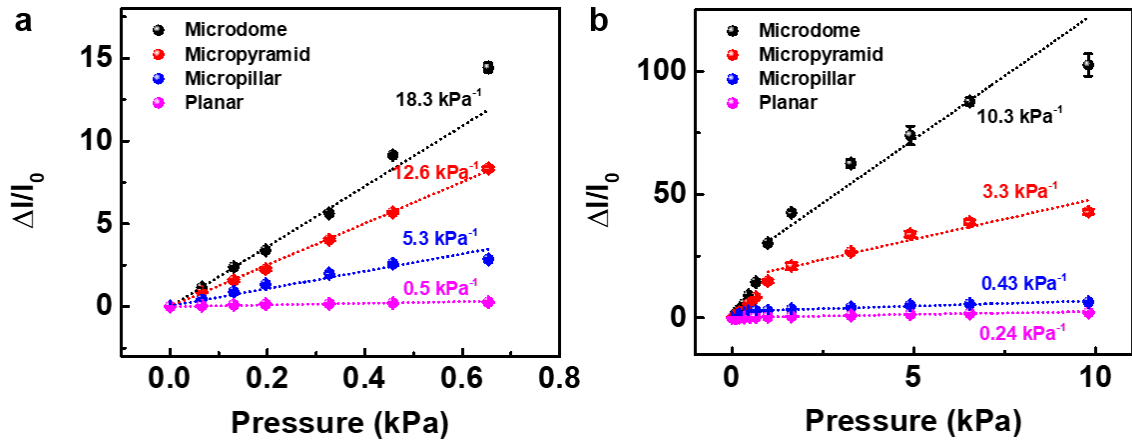


**Figure 4.4.** Pressure sensitivity of e-skins with single microstructure arrays at (a) low pressure range (< 1 kPa) and (b) medium pressure range (1 kPa ~ 10 kPa).

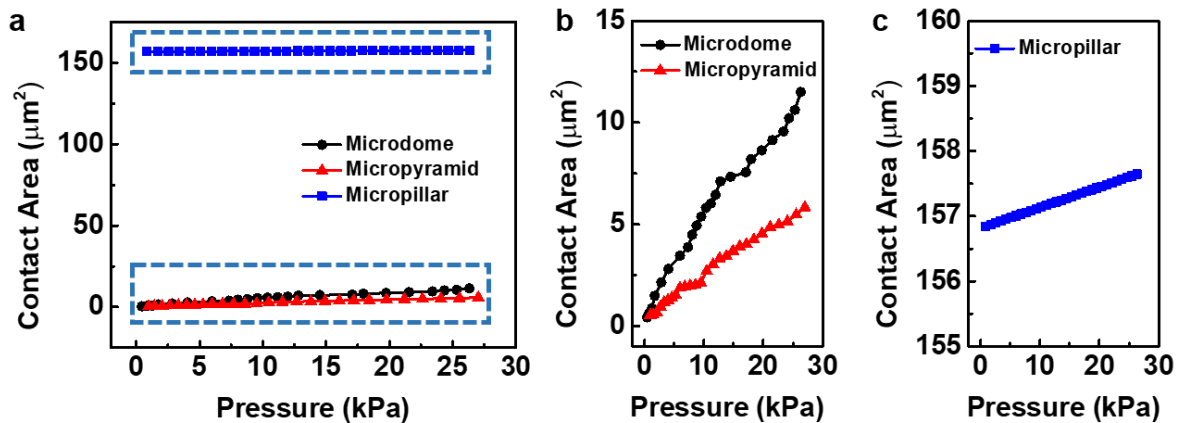


**Figure 4.5.** (a) Simulated results for variation in contact area of e-skins with single microstructure arrays as a function of mechanical pressure. (b-c) Magnified graphs of contact area change for e-skins with (b) microdome and micropyramid structures and (c) micropillar structure.

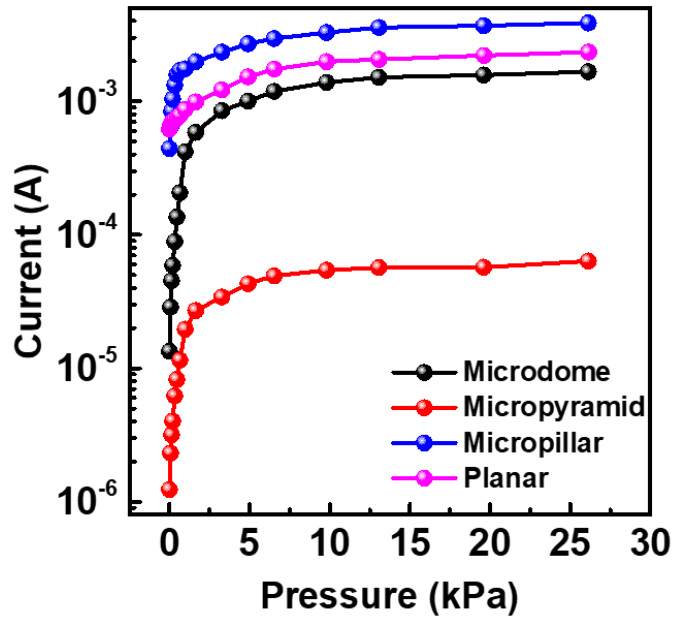


**Figure 4.6.** Electrical current changes of single microstructured e-skins with different microstructure arrays in response to normal pressure.

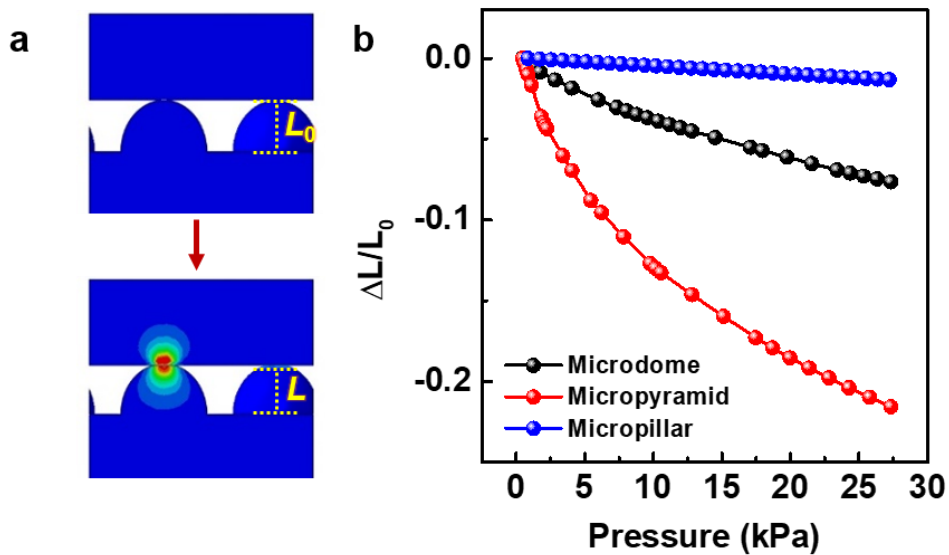


**Figure 4.7.** (a) Simulated result showing the stress distribution and the thickness change of microstructure under pressure. (b) Simulated result for relative variation in thickness of microstructures under loading pressure.

**Pressure-Sensing Capability of Interlocked Microstructured E-skins.** Considering the pressure-sensing capabilities of single-sided microstructured composites, interlocked composites having double microstructured surfaces are expected to further enhance pressure sensitivity owing to larger pressure-induced deformation of interlocked microstructures. Figure 4.8a shows the change in output current of CNT/PDMS composites having planar and interlocked microstructures under normal pressure. The interlocked composites with microdome, micropyramid, and micropillar arrays exhibited abrupt increases in current on application of a pressure up to 26 kPa, corresponding to  $\Delta I/I_0$  values of approximately  $1.38 \times 10^6$ ,  $4.05 \times 10^5$ , and  $3.91 \times 10^3$ , respectively, which are significantly higher than those of single microstructured films ( $\Delta I/I_0 < 130$ ). This behavior can be attributed mainly to the larger initial thickness of the insulating layer for interlocked microstructures, which resulted in a significantly lower initial current at the low-pressure range (Figure 4.9) and thus higher  $\Delta I/I_0$  values compared to single microstructured films (Figure 4.6). It is worth noting that the interlocked microdome structures exhibited the largest change in current in response to pressure and the lowest minimum detection level (0.09 Pa, corresponding to air flow of 1 m/s on  $1.5 \times 1.5 \text{ cm}^2$  of sensor) compared to the other microstructures, indicating the critical role of inter-microdome contacts on the enhanced piezoresistance (Figure 4.10). To show the possibility of integration with commercially available chip, e-skin was connected to the commercial chip and was detectable signals on application of pressure (Figure 4.11). To understand the different trend on  $\Delta I/I_0$  variations depending on microstructure shapes, finite-element simulations of contact-area change under normal pressure were performed. Figure 4.8c indicates that the microdome structure exhibited the largest increase in relative contact area ( $A/A_0$ ) as compared to micropyramid and micropillar arrays (the absolute values are shown in Supplementary Figure 4.12), supporting the shape-dependent trend of  $\Delta I/I_0$  variations in Figure 4.8a. This simulation result indicates that the rate of contact-area change with respect to pressure decreased in the following order: dome > pyramid > pillar, which is the same tendency as that for single-sided microstructured films.

To elucidate the sensing performances of interlocked microstructure e-skins, pressure sensitivity was analyzed (Figure 4.8b and Figure 4.13). All of the e-skins having interlocked microdome, micropyramid, and micropillar structures exhibited great pressure sensitivity:  $47,062 \text{ kPa}^{-1}$ ,  $4,569 \text{ kPa}^{-1}$ , and  $2,733 \text{ kPa}^{-1}$  in the low-pressure range (<1 kPa);  $90,657 \text{ kPa}^{-1}$ ,  $21,308 \text{ kPa}^{-1}$ , and  $85 \text{ kPa}^{-1}$  in the medium-pressure range (1–10 kPa); and  $30,214 \text{ kPa}^{-1}$ ,  $12,219 \text{ kPa}^{-1}$ , and  $29 \text{ kPa}^{-1}$  in the high-pressure range (>10 kPa), respectively. Compared to the planar structure, these microstructures exhibited extremely high pressure sensitivity and a wide dynamic pressure range before saturation. This can be attributed to the larger change in contact area (Figure 4.8c) and insulating layer thickness (Figure 4.14) at the interface of interlocked microstructures. Since the tunneling current of interlocked microstructures primarily depends on variations of contact area and insulating layer thickness, it is worth to compare the theoretical calculation of tunneling current with the experimental one to further understand the

working mechanism of piezoresistive interlocked microstructures. The experimental tunneling resistance can be extracted by using the relation  $R_T = R - R_F - R_{CR}$ , where  $R$  is the total resistance of interlocked composite film,  $R_F$  is the bulk composite film resistance, and  $R_{CR}$  is the constriction resistance.  $R_{CR}$  can be neglected in our system due to the comparable size between the diameter of MWNTs and intertube contact area.<sup>94</sup> The theoretical tunneling resistance ( $R_T = (V/J) \times (1/A_{CNT})$ ) can be estimated by calculating the tunneling current density ( $J$ ) according to Simmons model<sup>105</sup> and the actual electrical contact area ( $A_{CNT}$ ). Figure 4.8e exhibits theoretical tunneling current of different microstructures, which are fitted to experimental tunneling current. The theoretical and experimental results match well, which support that variations of contact area and insulating layer thickness significantly affect the tunneling current and thus the pressure sensitivity.

In particular, the interlocked microdome structures exhibited remarkable sensitivities over broad pressure ranges, which are much better than those of previously reported e-skins (Table 4.1). It is also worth noting that there is a critical difference in sensitivity values depending on whether the sensitivity is expressed in terms of either current ( $S = (\Delta I/I_0)/\Delta P$ ) or resistance ( $S = (\Delta R/R_0)/\Delta P$ ). In the e-skin system with a drastic variation in electrical response reported in the present study, the sensitivity expressed in terms of current is more adequate for the precise analysis of sensitivity because the relative resistance change becomes 1 ( $\Delta R = R - R_0 \approx R_0$  and  $\Delta R/R_0 \approx 1$ ) and thus underestimates the sensitivity when the initial resistance is significantly higher than the resistance under pressure.

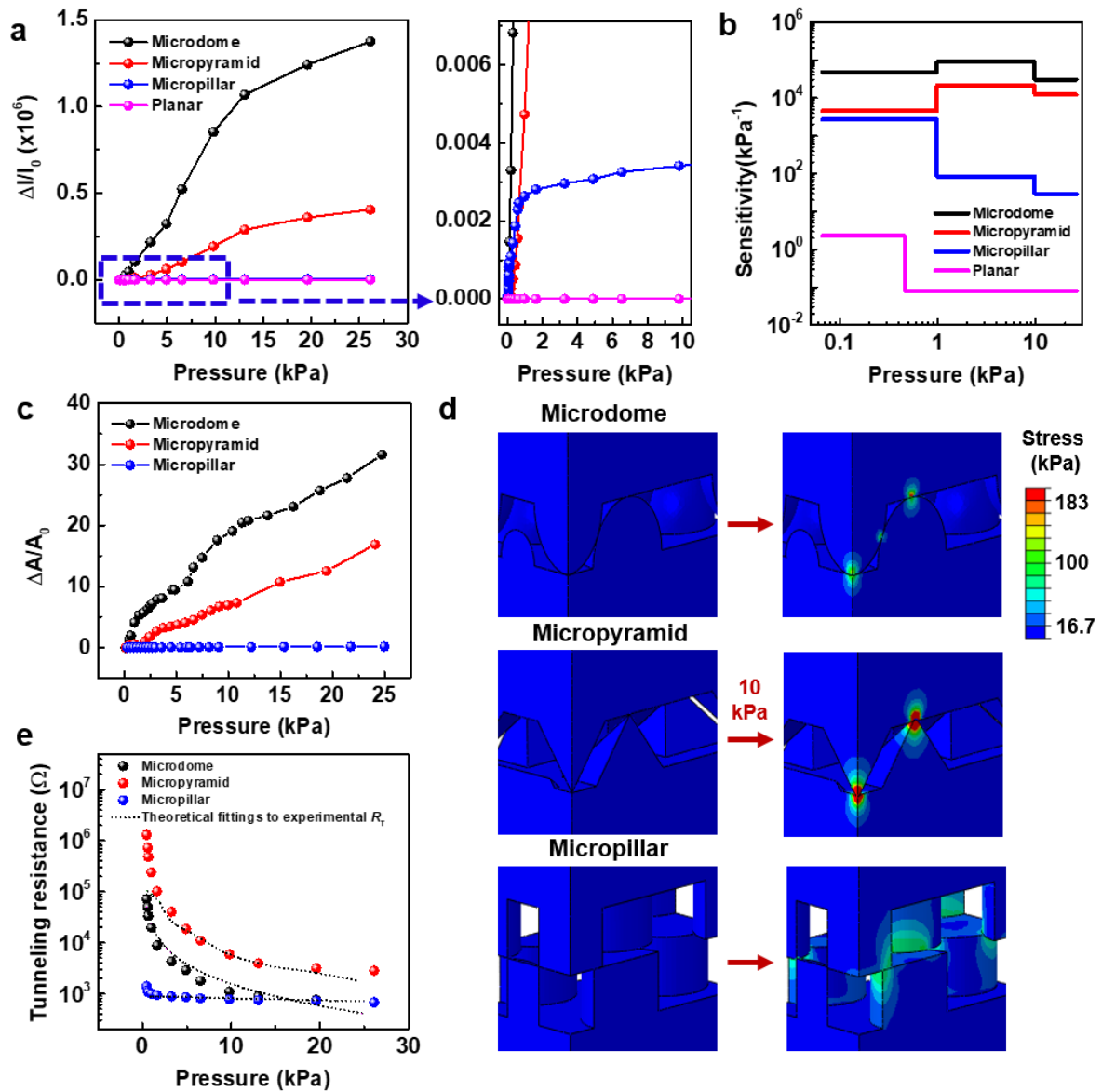


**Figure 4.8.** Pressure-sensing capability of interlocked microstructured e-skins. (a) Relative current changes of interlocked e-skins having different microstructures as a function of applied pressure. The magnified graph to the right shows the relative current changes of micropillar and planar structures. (b) Pressure sensitivity of e-skins for low ( $<1$  kPa), medium (1–10 kPa), and high ( $>10$  kPa) pressure ranges. (c) Calculated contact area variations of e-skins with interlocked microstructure arrays in response to applied pressure. (d) FEA showing the localized stress distribution of interlocked microstructure arrays for the applied pressure of 10 kPa. (e) Experimental tunneling current of e-skins with interlocked microstructures fitted to theoretically calculated tunneling resistance.



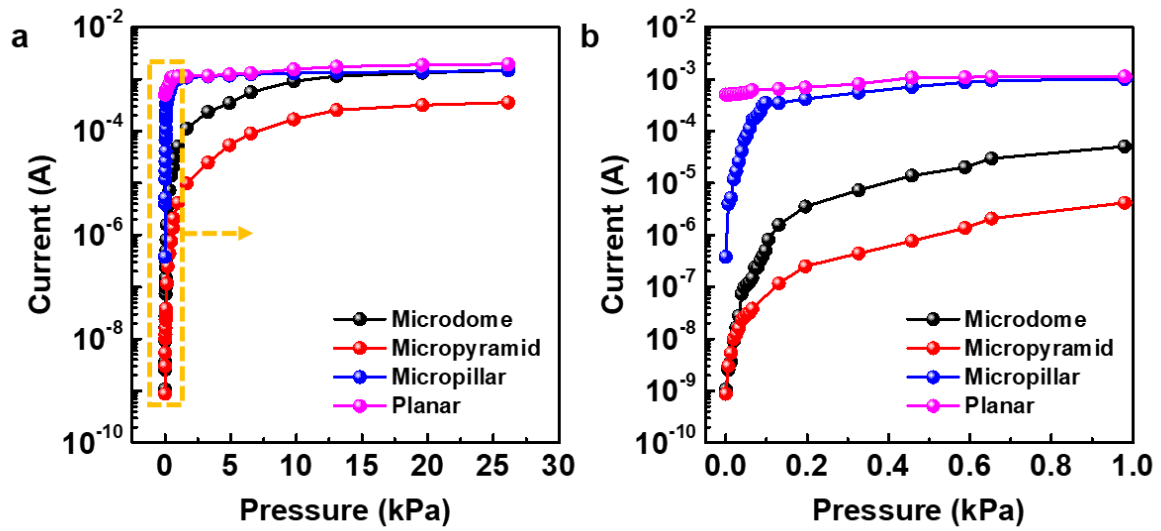


**Figure 4.9.** (a) Piezoresistive current changes of e-skins with interlocked microstructures in response to normal pressure. (b) Magnified graph of current changes at the low pressure range (< 1 kPa).

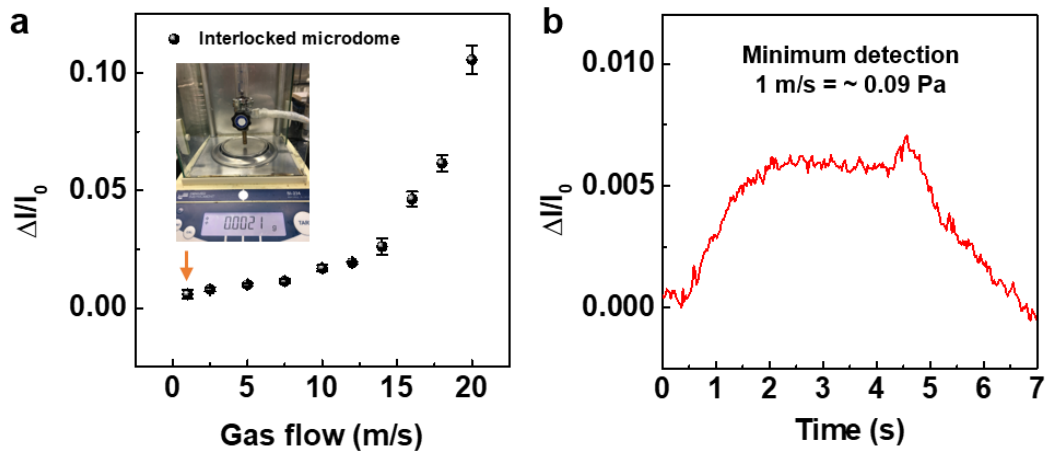


**Figure 4.10.** Minimum pressure detection of e-skin with interlocked microdome. (a) Relative current change of e-skin with interlocked microdome in response to nitrogen ( $N_2$ ) gas with different gas flow rate from 1 to 20 m/s. Inset photograph shows the weight of air flow with a flow rate of 1 m/s which is correspond to about 0.09 Pa for sensor size of  $1.5 \times 1.5 \text{ cm}^2$ . (b) Relative current changes of e-skin with interlocked microdome under  $N_2$  gas with a flow rate of 1 m/s.

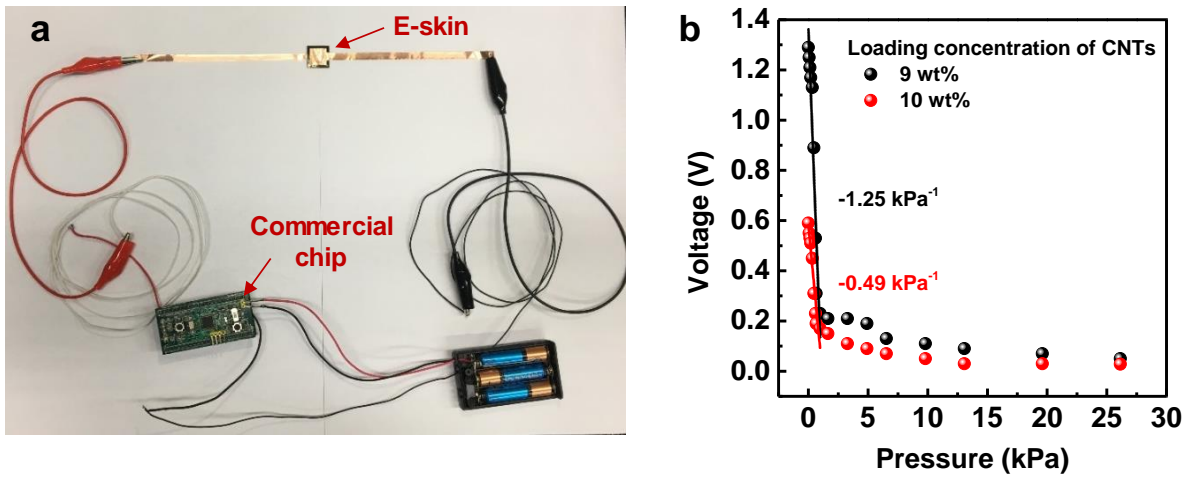


**Figure 4.11.** Pressure sensing performance of e-skin with interlocked microdome by integrating with a commercial chip. (a) Photograph of a pressure sensing measurement system with an e-skin integrated with a commercial chip. (b) Pressure-responsive voltage changes for different loading concentration of CNTs.

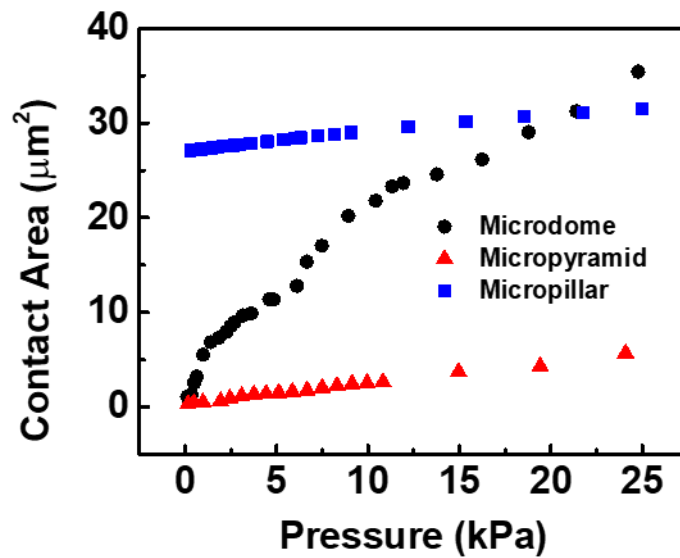


**Figure 4.12.** Simulated result of contact area variations of the interlocked microstructured e-skins in response to normal pressure.

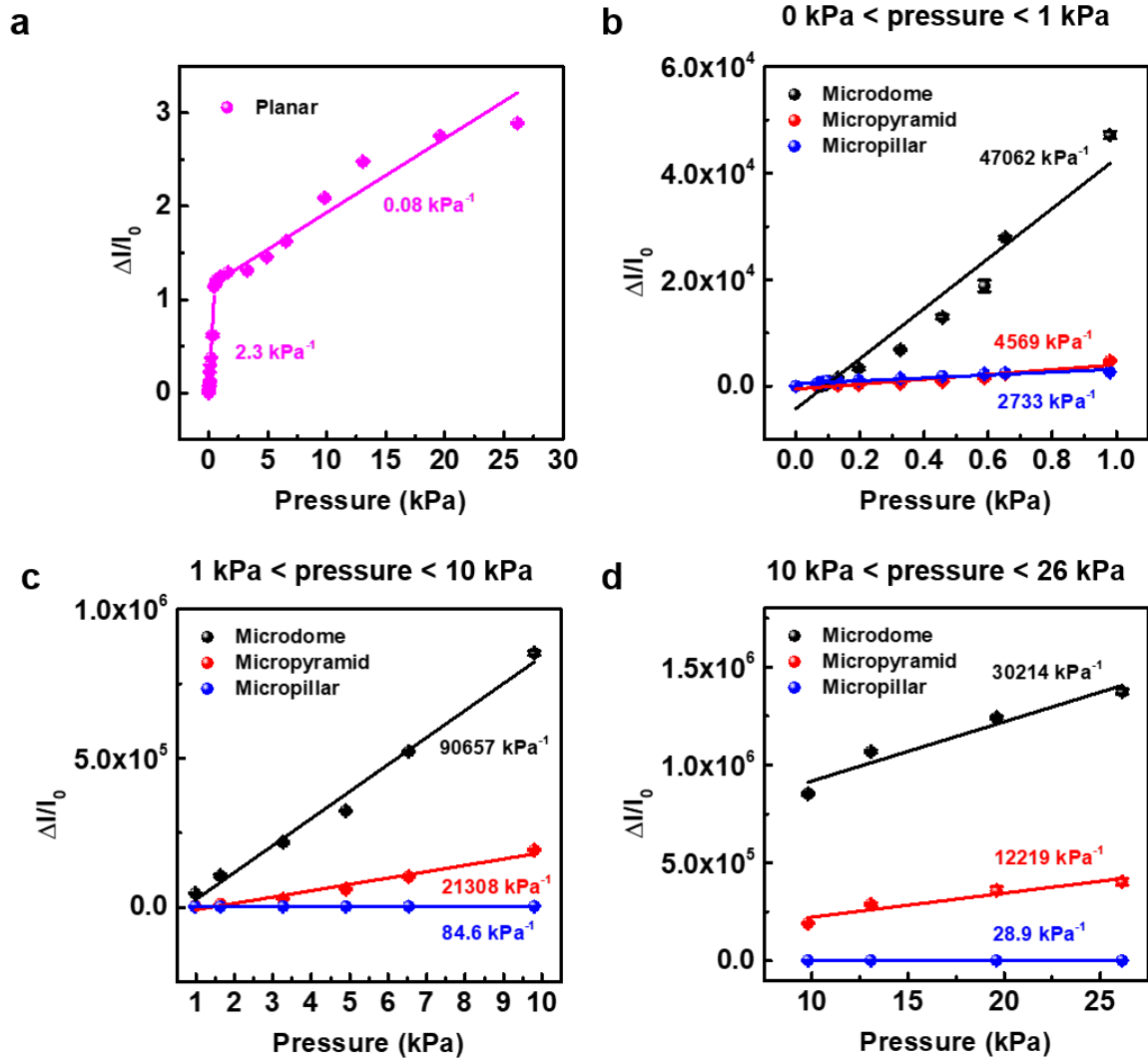


**Figure 4.13.** Pressure sensitivities of e-skins with (a) planar structure and (b-d) interlocked microstructures under different normal pressure ranges of (b)  $< 1 \text{ kPa}$ , (c)  $1 \text{ kPa} \sim 10 \text{ kPa}$ , and (d)  $10 \text{ kPa} \sim 26 \text{ kPa}$ .

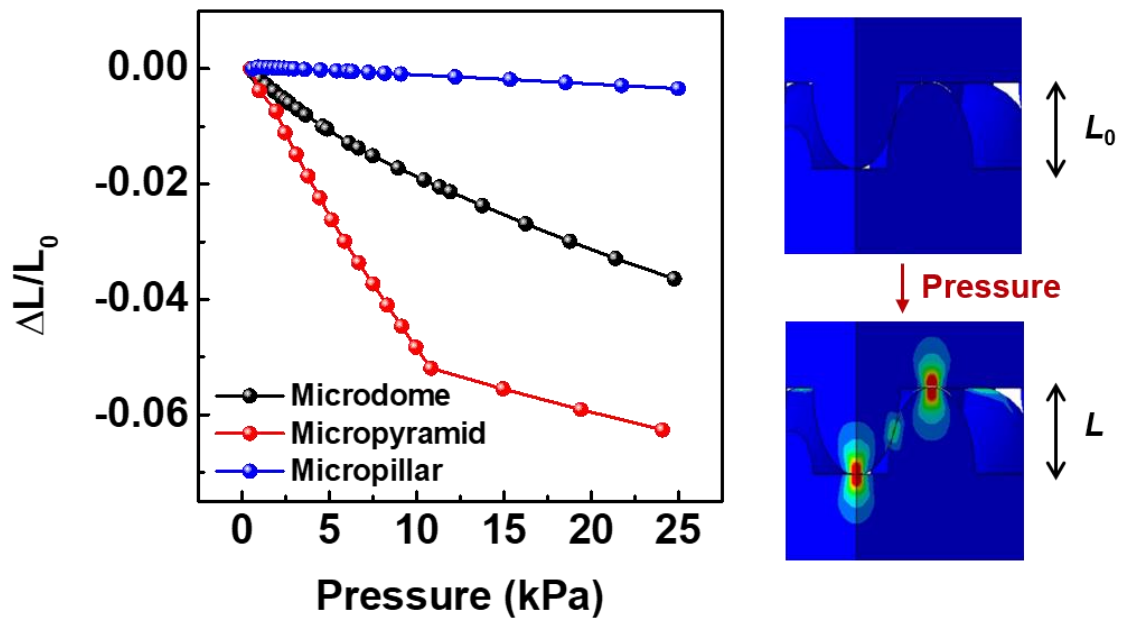


**Figure 4.14.** Relative changes in thickness of microstructure with different shapes (left) and localized stress of e-skins with interlocked microdomes in response to normal pressure (right).

**Table 4.1.** Summary of the key parameters of recently reported e-skins.

NO.	Materials	Electrical signal	Pressure sensitivity [kPa <sup>-1</sup> ]	Pressure range [kPa]	Minimum pressure detection [Pa]	Operating voltage [V]	Ref.
1	Au Nanowire paper	Current	1.14	< 5	13	1.5	[137]
2	Microstructured SWNT/PDMS	Current	1.80	< 0.3	0.6	2	[79]
3	PANI/Au/PDMS micropillars	Current	2.0	< 0.22	15	1	[165]
4	Hierarchical graphene/PDMS	Current	8.5	< 12	1	1	[162]
5	PEDOT:PSS/PU D micropyramid	Current	56.8	< 0.2	23	0.2	[44]
6	Microstructured Au film	Current	50.17	< 0.07	10.4	0.01	[175]
7	Suspended gate organic thin film transistor	Current	192	< 5	0.3	60	[176]
8	SWCNT/PDMS Micropyramid	Current	2760 8655.6 1874.5	< 0.4 0.4-0.9 0.9-1.2	7.3	30	[174]
9	PVDF/rGO interlocked microdome ZnO	Resistance	31.9	< 0.02	0.6	1	[43]
10	Nanowire/PDM S micropillar	Resistance	6.8	< 0.3	0.6	10	[6]
11	Polypyrrole hollow-sphere	Resistance	133.1	< 0.03	0.8	N/A	[24]
12	<b>CNT/PDMS Interlocked microdome</b>	<b>Current</b>	<b>47062</b> <b>90657</b> <b>30214</b>	<b>&lt; 1</b> <b>1-10</b> <b>10-26</b>	<b>0.075</b>	<b>0.1</b>	<b>This work</b>

Applications of pressure-sensitive e-skins in robotics and healthcare devices require fast response time and repeated usability. Figure 4.15a shows the response time of interlocked composites having different microstructures upon loading and unloading of a 10 kPa pressure. The response time of interlocked composites with microdome, micropyramid, and micropillar arrays were 12, 162, and 160 ms, respectively, which were significantly faster than that of planar composite films (420 ms). The slow piezoresistive response time of planar composites can be attributed to the viscoelastic properties of PDMS, which induces a time delay for bulk film deformation in response to stress. On the other hand, the piezoresistive property of interlocked microstructures is dominated by surface microstructure deformation rather than bulk film deformation, leading to minimization of time-delay behavior. Additionally, sufficient void spaces between the interlocked microstructures enabled a facile release of energy, resulting in faster recovery times than that for the planar structure.<sup>88</sup> In particular, the interlocked microdome array exhibited the fastest response time (35 times faster than that of planar structures, Figure 4.15a) due to the largest variation in contact area (Figure 4.8c), which facilitates the immediate formation of a conductive path. The interlocked microstructures also exhibited excellent mechanical stability over repeated cycles (Figure 4.15b). Piezoresistive e-skins having interlocked microstructures presented uniform piezoresistive properties upon repetitive pressure loadings (10 kPa) over 1,000 times without any surface crack (Figure 4.16). In contrast, e-skins having planar structures exhibited non-uniform and unstable piezoresistive properties over repetitive cycles, which can be attributed to incomplete recovery to their original state due to a slow response/relaxation time and a strong stiction between two planar surfaces.

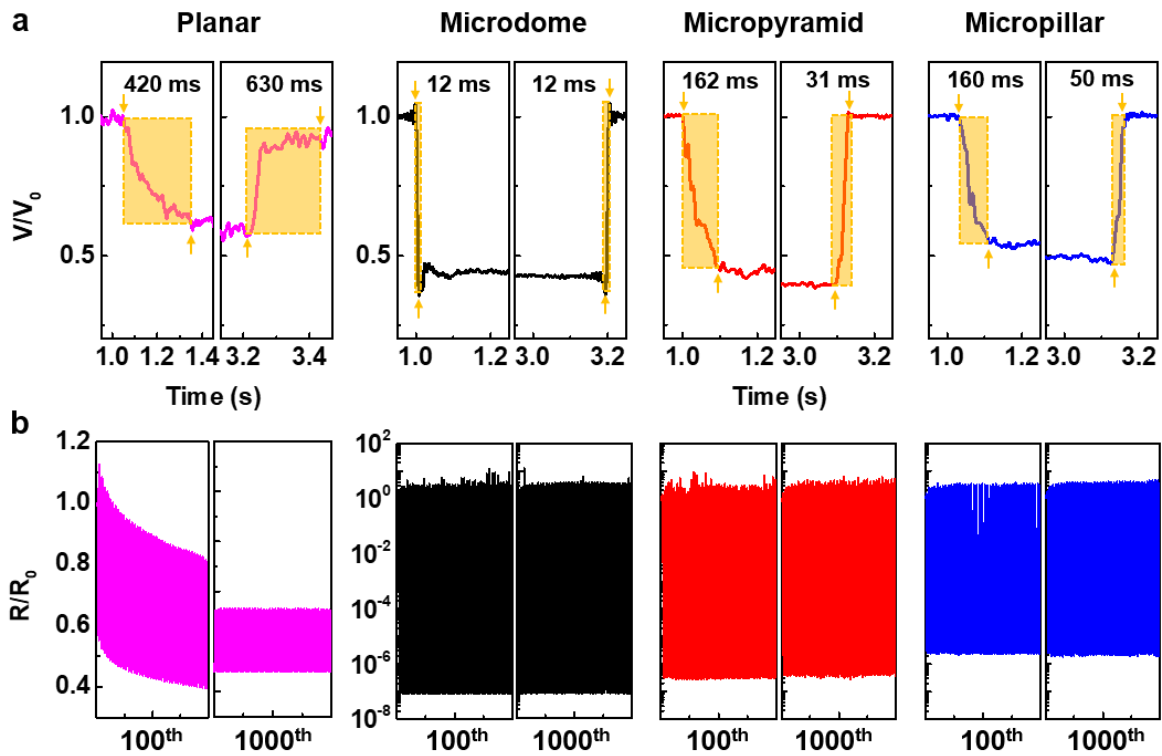


**Figure 4.15.** Response time and durability properties of e-skins with interlocked microstructure arrays. (a) Response and relaxation times of e-skins under a loading/unloading pressure of 10 kPa. (b) Mechanical durability of e-skins under repeating a loading/unloading pressure of 10 kPa up to 100 cycles (left) and 1,000 cycles (right).

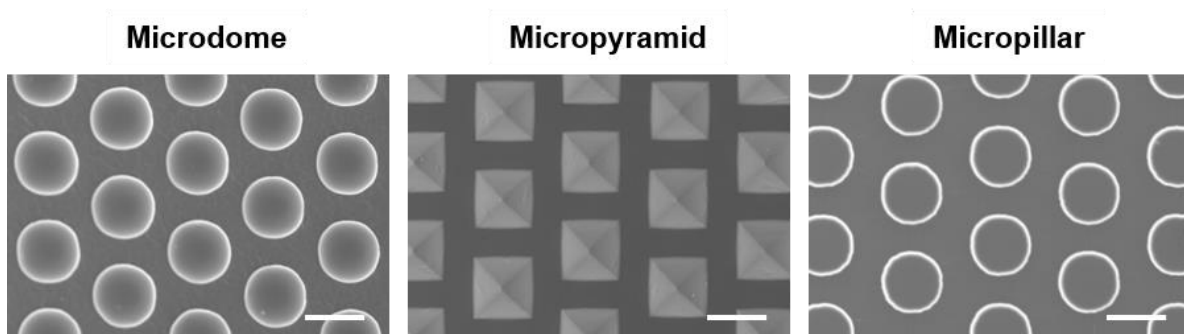


**Figure 4.16.** SEM images of surface morphologies of electronic skins with interlocked microstructures after 1000 cycles of pressure application.

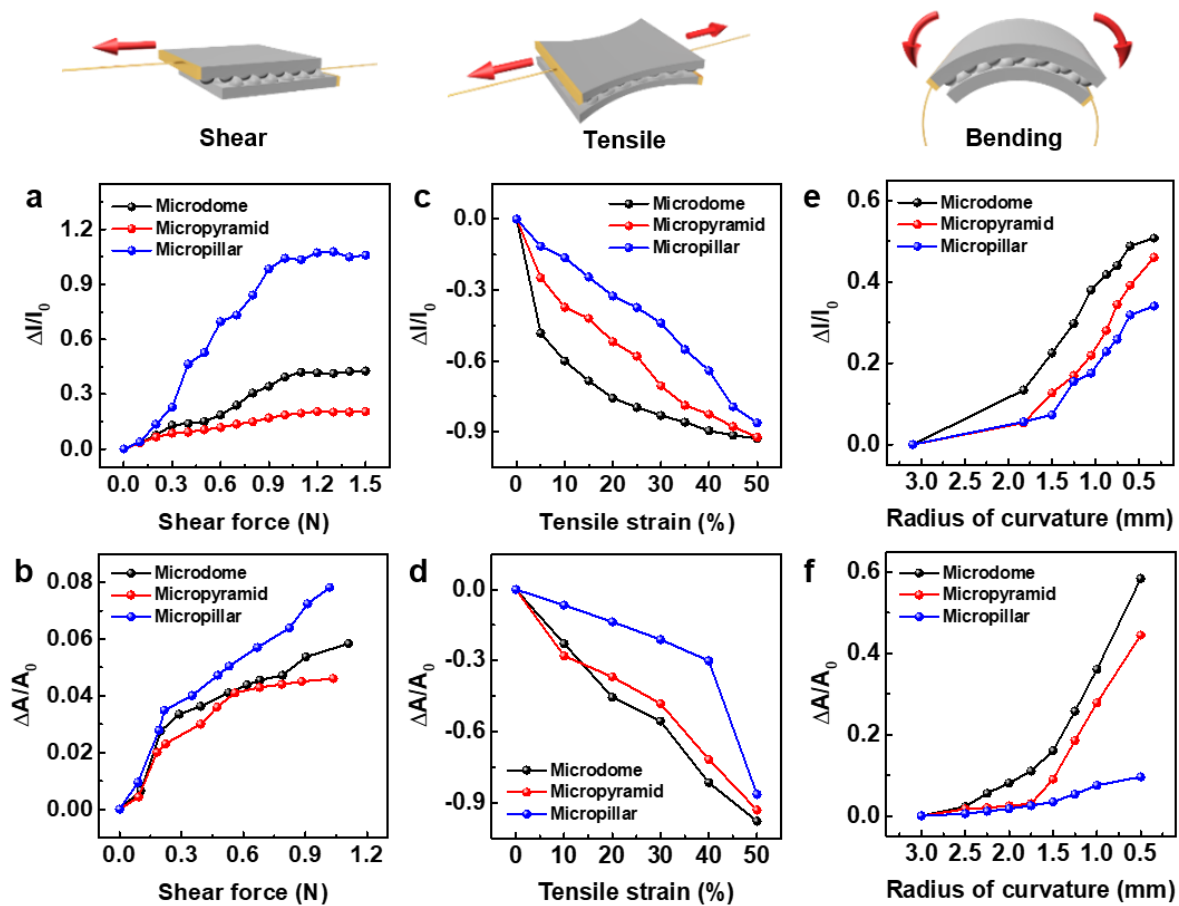
**Multidirectional Force-Sensing Capability of Interlocked Microstructured E-skins.** In human fingertip skin, various mechanoreceptors and interlocked epidermal-dermal ridges enable spatiotemporal recognition of intensity, direction, and location of forces applied in different directions, which is critical for hand-manipulation of objects with different shapes. Artificial e-skins that can detect and discriminate multidirectional forces are required in robotic skins, gesture monitoring devices, and other healthcare sensors. Interlocked microstructures can induce a unique microstructure deformation tendency specific to each microstructure geometry depending on the direction of applied forces. This would result in sensitive and selective piezoresistance in multidirectional force sensing. Figure 4.17 shows the piezoresistive sensing properties of interlocked microstructures having different geometries in response to shear, tensile, and bending stresses.

Figure 4.17a shows the shear-force detection properties of interlocked microstructures. In order to engage the upper and lower microstructure layers, a normal preload ( $\sim 45$  kPa) was applied on the upper layer prior to applying shear force. In the linear regime of Figure 4.17a, the pillar structure exhibited the highest shear sensitivity ( $0.54 \text{ N}^{-1}$ ), which is  $\sim 2$  and  $\sim 4$  times larger than that of the dome ( $0.27 \text{ N}^{-1}$ ) and pyramid ( $0.14 \text{ N}^{-1}$ ) structures. The finite-element simulation results (Figure 4.18) exhibit that the normal preload induced a microstructure deformation at the contact spots, and the subsequent application of shear force further increased the microstructure deformation in the lateral direction and the contact area between interlocked microstructures. The calculated contact-area change in response to shear force shows that the rate of contact-area variation decreases in the following order: pillar, then dome, and finally the pyramid structure (Figure 4.17b), which is the same tendency observed in the experimental results. It is worth noting that the pillar structure exhibited the smaller contact-area change for normal pressure compared to dome and pyramid structures due to the large initial contact area (Figure 4.8c). These results imply that once the initial contact is formed between the opposing microstructures under a predefined normal preload, the pillar structure deforms more easily than the other microstructures in response to lateral shear force, which results in the enhanced contact area change and thus improved shear-force sensitivity.

For detecting tensile strain, the micropillar structure exhibited the least sensitive piezoresistance compared to the microdome and micropyramid structures (Figure 4.17c). For tensile strain, the output current decreases due to the deformation of hexagonal microstructure arrays into elongated hexagonal arrays in the tensile direction, which results in a decreased contact area and thus decreased output current.<sup>46</sup> The simulation results indicate that the lateral tensile strain induced a decrease in concentrated stress at the contact spots and in the contact area between opposing microstructured films (Figure 4.19), leading to a decrease in output current. For the quantitative comparison of strain-sensing properties, a gauge factor ( $GF$ ) was analyzed. This is defined by the equation  $GF = (\Delta R/R_0)/(\Delta L/L_0)$ , where  $R$  is the electrical resistance and  $L$  is the length of film. The interlocked microdomes exhibited the largest  $GF$



(~16), which was about 2 and 7 times larger than those of the micropyramid (~7) and micropillar (~2.2) structures for tensile strains up to 30 % (Figure 4.20). The calculated contact-area change in Figure 4.17d also exhibits a similar tendency with the order microdome, then micropyramid, and finally micropillar for the rate of contact area change in response to tensile strain. As a result of bending strain, the concentrated stress and contact area of interlocked microstructures increased with bending curvature (Figure 4.21). Similar to normal-pressure and tensile-strain sensing, the interlocked microdome structure exhibited the largest bending strain sensitivity, followed by the micropyramid and micropillar structures (Figure 4.17e). The calculated contact-area change in Figure 4.17f similarly exhibits the largest contact-area change for interlocked microdome structures.



**Figure 4.17.** Relative current changes and contact area variations of interlocked microstructured e-skins in response to different mechanical forces (shear, stretching, and bending). (a–f) Changes in relative resistance and contact area of e-skins having interlocked microstructures in response to applied multidirectional mechanical stresses: (a and b) shear stress, (c and d) tensile stress, and (e and f) bending stress.

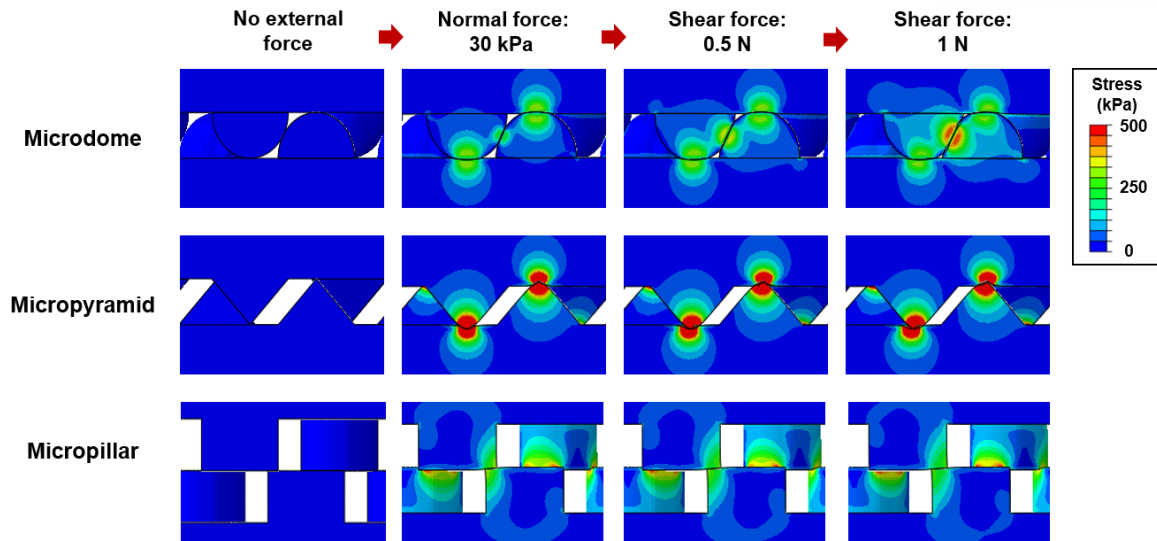


**Figure 4.18.** Finite-element simulation of the interlocked e-skins showing the microstructure deformation and contact area change between interlocked microstructure arrays in response to normal preload of 30 kPa and shear forces.

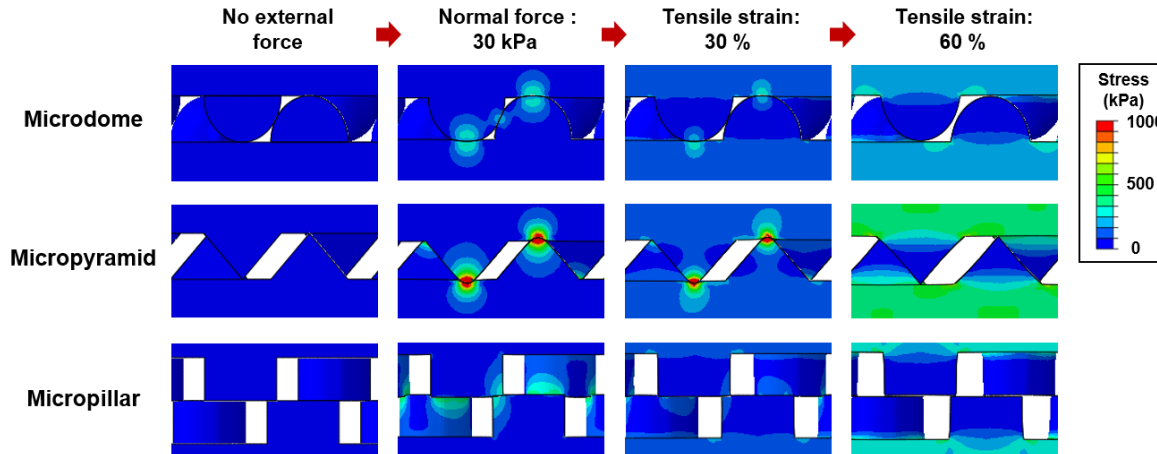


**Figure 4.19.** Finite-element simulation of the interlocked e-skins showing the microstructure deformation and contact area change between interlocked microstructure arrays in response to normal preload of 30 kPa and tensile strains.

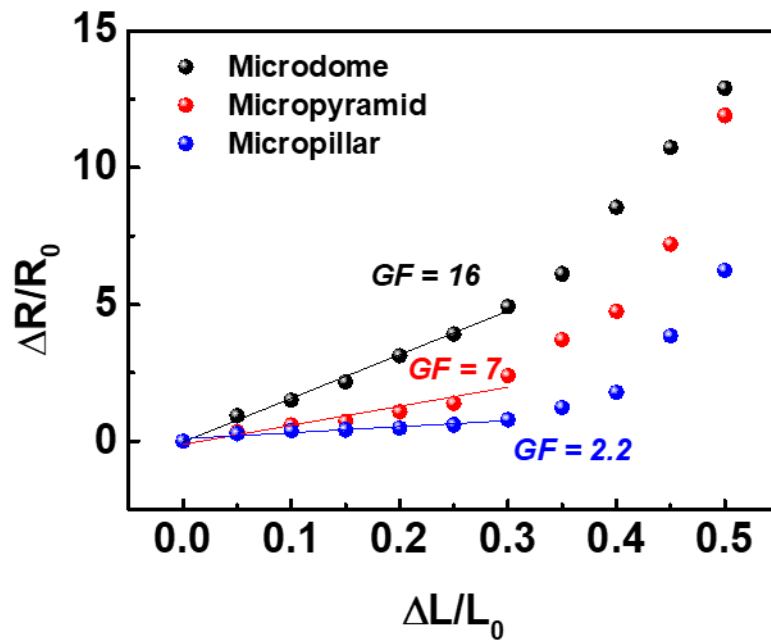


**Figure 4.20.** Comparison of strain-sensing capabilities of e-skins with different interlocked microstructures.

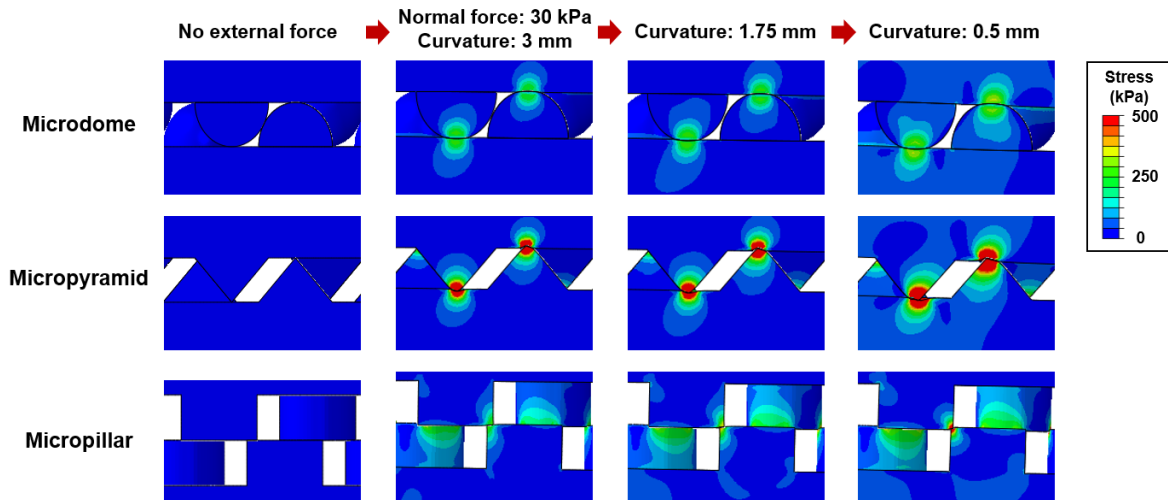


**Figure 4.21.** Finite-element simulation of the interlocked e-skins showing the microstructure deformation and contact area change between interlocked microstructure arrays in response to normal preload of 30 kPa and bending curvature.

In addition to force sensitivity, discrimination of multidirectional forces is an essential requirement for practical applications of e-skins. In an interlocked geometry of microstructures, distinct deformation patterns depending on the type of mechanical forces induce unique output current signals specific to the applied forces.<sup>46</sup> This geometry-specific force-responsive behavior exhibited by interlocked microstructures enables detection and differentiating of multidirectional mechanical stimuli. Each e-skin having different microstructures exhibited unique output current patterns with different signal intensity and response times depending on the type of mechanical forces (normal, shear, tensile, and bending; Figure 4.22). It was also observed that differently shaped microstructures exhibited different signal intensities and patterns under the same mechanical stimuli. In particular, microdome structures exhibited the most sensitive piezoresistance for normal pressure, tensile strain, and bending stimuli. In contrast, the micropillar structures showed the most sensitive piezoresistance in response to shear force. All of these different signal patterns are attributed to different magnitudes of deformations of the interlocked microstructures and to response/relaxation times depending on the direction of the applied forces and the shape of the microstructures. Although the microdome structures exhibited the most sensitive piezoresistance for normal pressure, tensile strain, and bending stimuli compared to micropyramid and micropillar structures for the equal microstructures feature sizes (10  $\mu\text{m}$  diameter, 15  $\mu\text{m}$  pitch, and 6  $\mu\text{m}$  height), it is worth to note that the force sensitivity of e-skins also depends on the feature size such as the height, diameter, and pitch of periodic microstructures in addition to the microstructure shape. For example, as shown in Figure 4.23, the increase of pillar height of micropillar structures results in the enhanced force sensing capabilities. It is expected that the variation of other feature sizes (diameter, pitch) of microstructures significantly affect the multidirectional force sensitivities, which requires further in-depth and systematic studies.

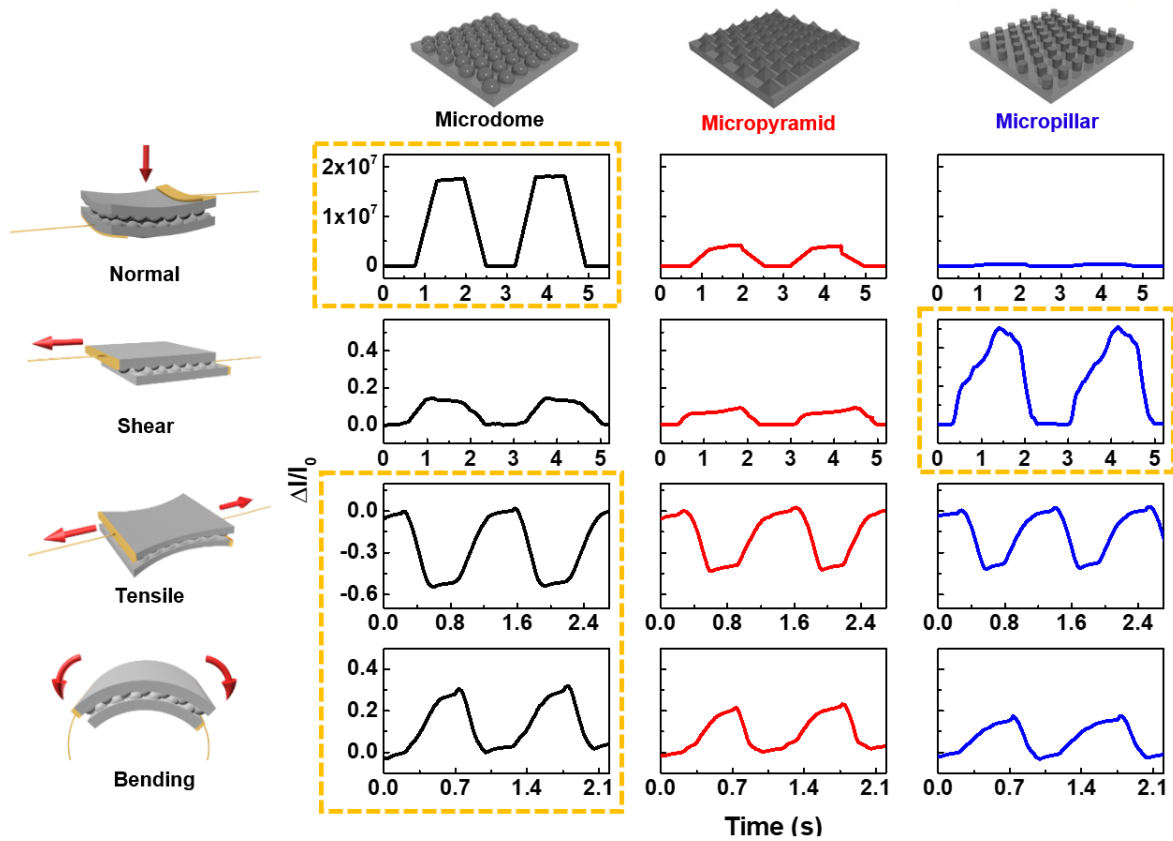


**Figure 4.22.** Multidirectional force sensing capabilities of interlocked microstructured e-skins in response to different mechanical forces (normal, shear, stretching, and bending). Each e-skin exhibits unique output current patterns with different signal intensity and response times depending on the type of mechanical forces.

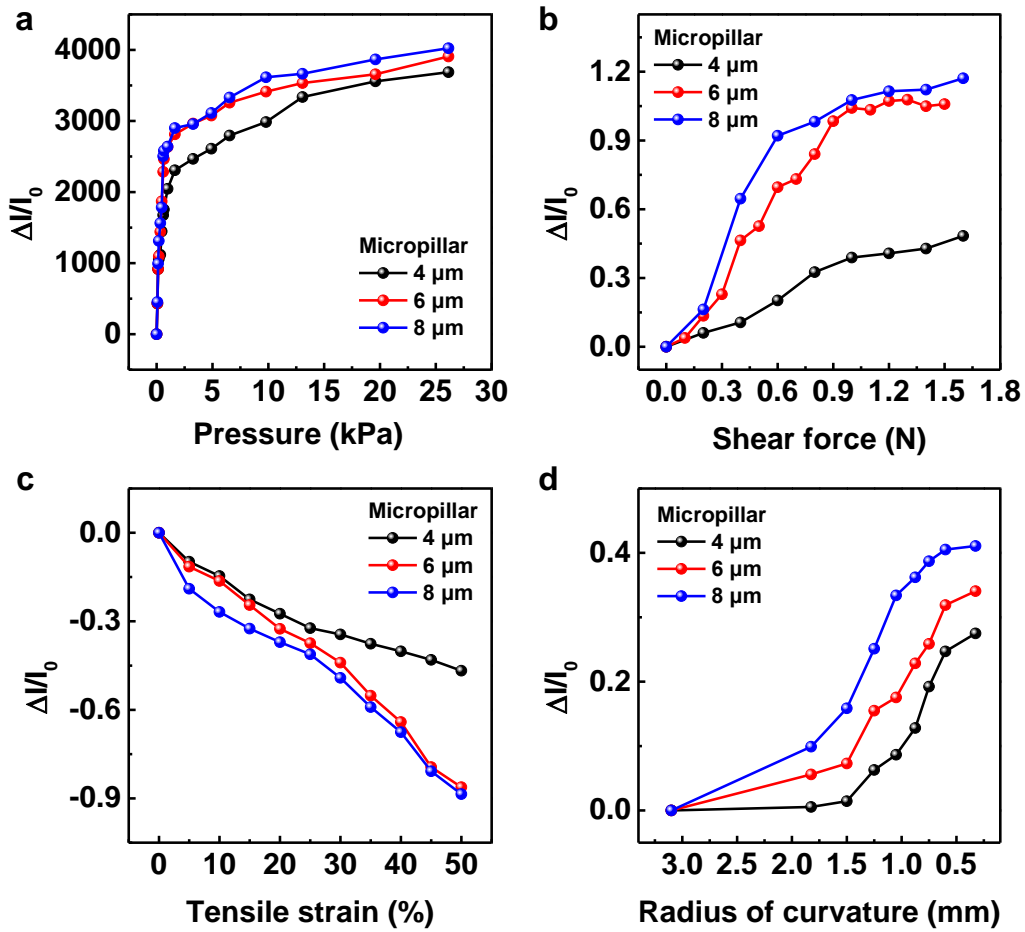


**Figure 4.23.** Multidirectional force sensing capabilities of e-skins with different height of micropillar structures for (a) normal pressure, (b) shear force, (c) tensile strain, and (d) bending stresses.

**Healthcare Device Applications of Microstructured E-Skins.** For practical applications of the piezoresistive e-skins in healthcare monitoring devices, the detection of various bio-signals was compared over a wide range of pressures, from acoustic wave (<1 Pa) and human breath (1 Pa–1 kPa) to human pulse pressure (1–10 kPa, e.g. artery pulse pressure, average 30–40 mmHg, 4–5.3 kPa) and carotid pulse pressure (average 35 mmHg, 4.67 kPa).<sup>177, 178</sup> The detection of acoustic waves allows for the application of e-skins in hearing-aid devices, highly sensitive microphones, and human–machine interfaces. In order to analyze the capability of sound detection, the e-skins were positioned 1 cm away from the speaker (Figure 4.24a) and the output currents were measured in response to acoustic waves with sound pressure levels varying from 90 to 110 dB at a constant frequency of 100 Hz (Figure 4.24b). As the sound pressure levels increased, the vibration-induced fluctuation of current gradually increased. In particular, the micropillar structure exhibited the best capability to detect acoustic waves, which can be attributed to the vibration-induced fluctuation of large initial contact area of interlocked micropillar structures. The detection of acoustic waves at low acoustic pressure and different frequency is also applicable to verify the precise detection of acoustic wave (Figure 4.25). Figure 4.25a and 4.25b show the detection capability of acoustic wave depending on the sound intensity (60–85 dB) under fixed frequency (50 Hz) and different frequency (50–150 Hz) under fixed intensity (80 dB), respectively. Furthermore, to verify the precise detection, we extracted the detected frequency by a high pass frequency filter (> 65 Hz) (Figure 4.25c) and compared the experimental and theoretical acoustic waves (Figure 4.25d). The great acoustic wave sensing capabilities of our piezoresistive e-skins are caused by the high pressure sensitivity, which can be favorably compared with the previous acoustic sensors (Table 4.2). Based on the capability to perceive acoustic waves, these e-skins can also recognize the specific words by detecting unique signal patterns with noise filtering process as shown in Figure 4.24c. When the e-skins are exposed to sound source of the word “electronic skin” with intensity of 110 dB, different signal patterns can be observed. As expected, the micropillar structure shows the most distinct signal patterns due to the large fluctuation of contact area under tiny vibration. For the detection of human breathing motion, the e-skin was attached right below the nose (Figure 4.24d). For repeated breathing motion, all the e-skins exhibited periodical electrical signals corresponding to inspiration/inhalation (Figure 4.24e). Particularly, the micropillar structure exhibited the largest change in output current, which can be attributed to the largest shear force sensitivity of micropillar structures, as shown in Figure 4.17a. The results also exhibit similar characteristics at low operating-voltages (0.1 and 1 V, Figure 4.26), where the low operating voltage of 0.1 V is comparable to that of previously reported e-skins (Table 4.1) and provides a great possibility for low power consumption of wearable devices.

For the detection of artery pulse signals, the output current signals of the e-skins (~1 cm<sup>2</sup>) were recorded after attaching them onto the wrist (Figure 4.24f). All the e-skins having different

microstructures showed periodic waveforms of 62 beats/min (Figure 4.24h), corresponding to the average heartbeat of adult males. An artery pulse waveform contains three distinguishable peaks:  $P_1$  for the main pulse pressure and  $P_2$  and  $P_3$  for the reflected wave pressures from the hand and lower body, respectively.<sup>179</sup> The most distinct pressure peaks were observed for the interlocked microdome structures (Figure 4.24h), which is in accordance with the highest pressure-sensitivity of microdome structures in the medium pressure regime (1–10 kPa; Figure 4.8a). For a quantitative comparison of artery pulse wave detection capabilities, the radial artery augmentation index ( $AI_r = P_2/P_1$ ) and radial diastolic augmentation ( $DAI = P_3/P_1$ ) were analyzed. The  $AI_r$  and  $DAI$  acquired for the microdome and micropyramid structures are 0.53 and 0.19 and 0.54 and 0.2, respectively; this closely matched the average values of healthy 28-year-old males.<sup>179</sup> However, the interlocked micropillar structure did not exhibit clearly distinguishable pulse pressure peaks. Furthermore, the carotid pulse pressure was measured by attaching e-skins onto the neck (Figure 4.24g). The resulting waveforms presented the distinguished peaks corresponding to the inflection point of the carotid distention pressure ( $P_1$ ) and common carotid distention pressure ( $P_2$ ) (Figure 4.24h), which provide cardiovascular information based on the pressure augmentation index (PAI),  $PAI = (P_2 - P_1)/(P_2 - P_0)$ . Similar to the results for artery pressure, the interlocked microdome structure exhibited the clearest detection peaks due to high sensitivity at the pulse pressure ranges. The PAI value acquired for the microdome structure was in good accordance with that of healthy 28-year-old males ( $PAI = -3.4$ ).<sup>180</sup>



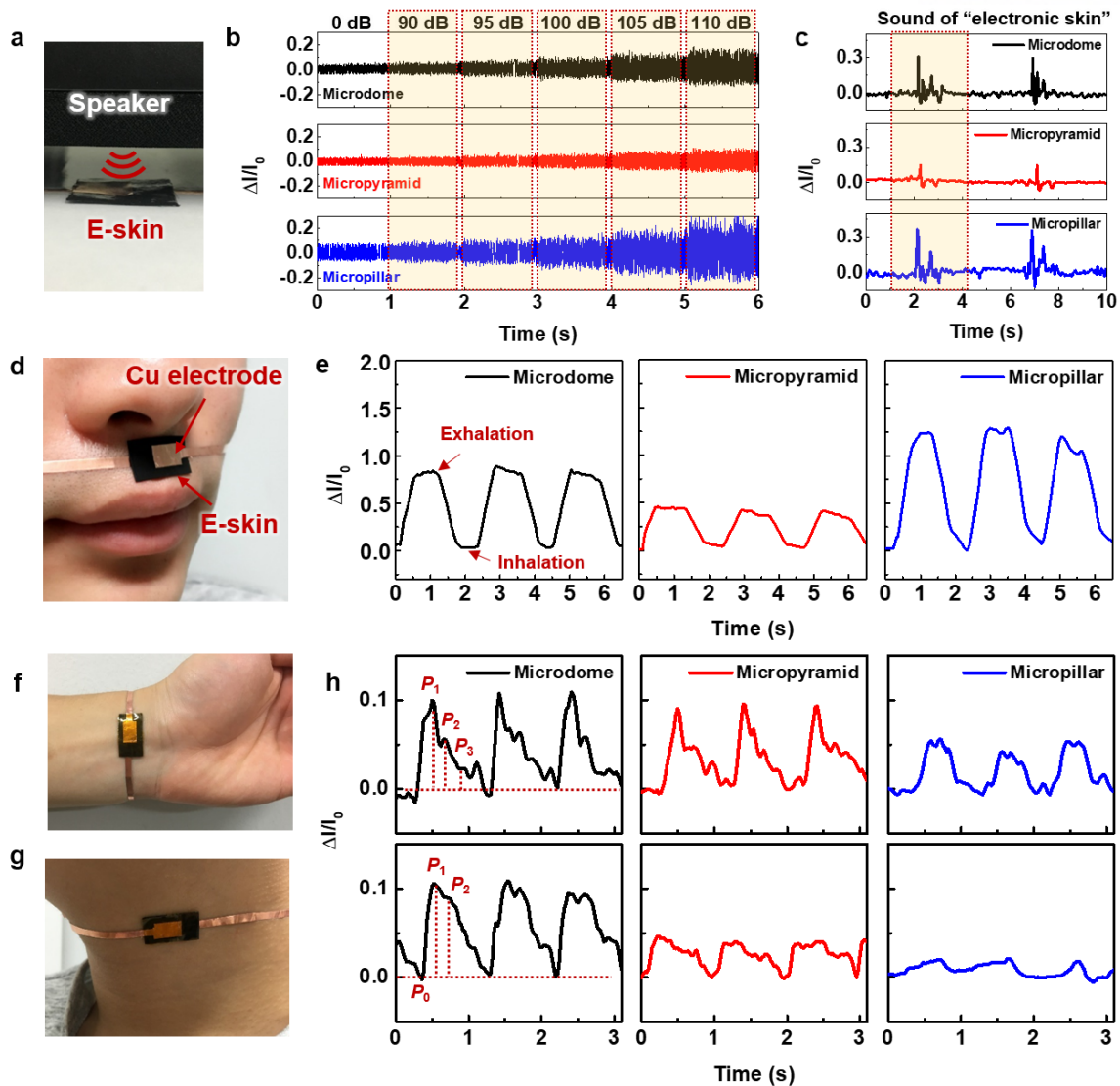


**Figure 4.24.** Healthcare monitoring applications of interlocked microstructured e-skins. (a) Photograph of the acoustic wave detection test using e-skins at a fixed distance of 1 cm from the speaker. (b) Relative current change of e-skins having interlocked microdome, micropyramid, and micropillar structures in response to different intensities of acoustic waves at a constant frequency of 100 Hz. (c) Acoustic sound detection capability of the e-skins with interlocked microstructures in response to sound source of "electronic skin". (d) Photograph of the human breath detection test using e-skins placed below the nose. (e) Relative current change of e-skins in response to human breath. (f, g) Photographs of the blood pressure monitoring test of (f) artery and (g) carotid pulse pressure using e-skins attached onto human wrist and neck. (h) Relative current changes of the e-skins with interlocked microstructures while monitoring artery pulse pressure (top) and carotid pulse pressure (bottom).

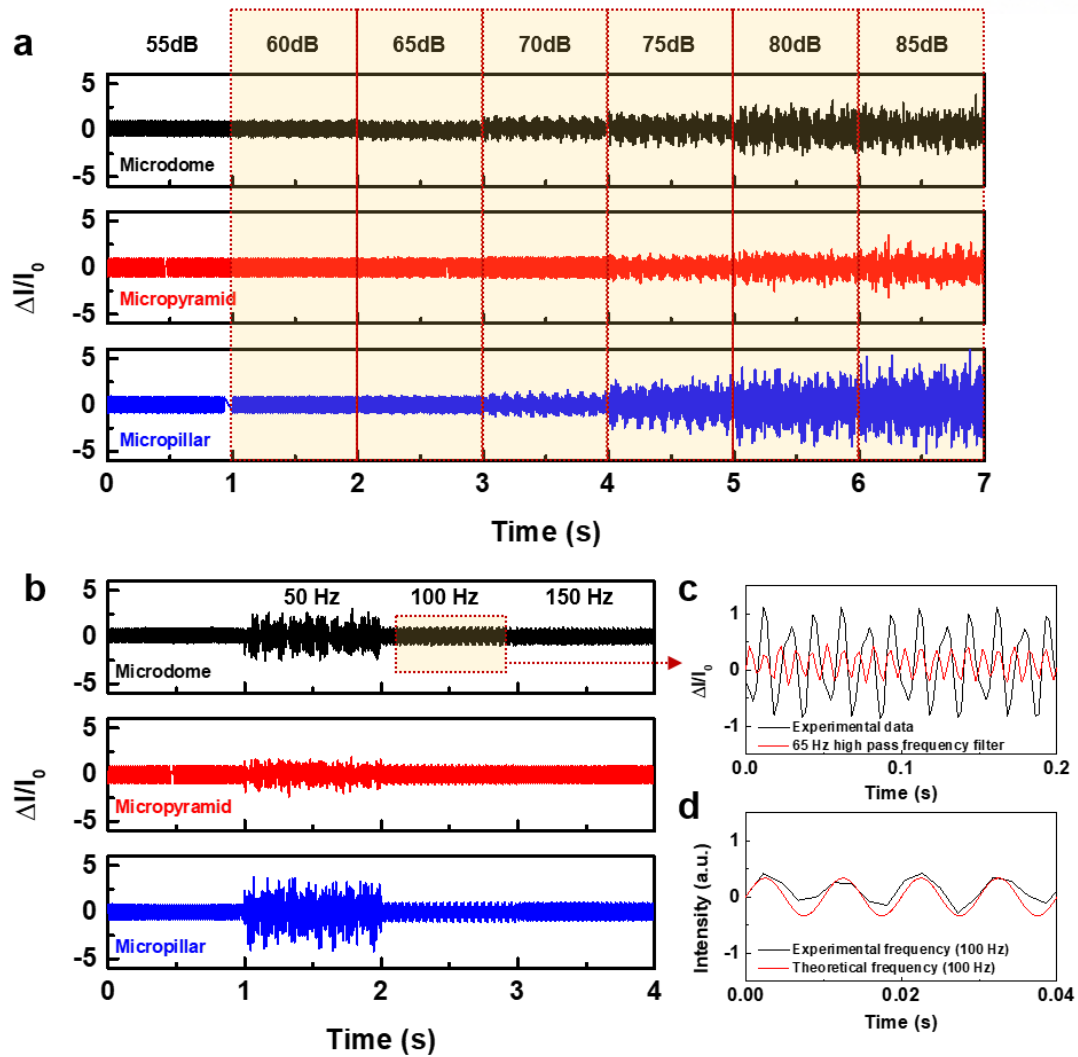


**Figure 4.25.** Detection of acoustic waves at low sound intensity and different frequency. (a-b) Comparison of acoustic wave detection of e-skins with different interlocked microstructures depending on (a) sound intensity at a constant frequency of 50 Hz, (b) frequency (50, 100, and 150 Hz) at a constant sound intensity of 80 dB. (c) Acoustic wave with frequency of 100 Hz in a normal atmosphere (base frequency: 60 Hz) before (black line) and after (red line) the base frequency filtering by a high pass frequency filter ( $> 65$  Hz). (d) Comparison of acoustic wave between experimental and theoretical acoustic waves with frequency of 100 Hz.

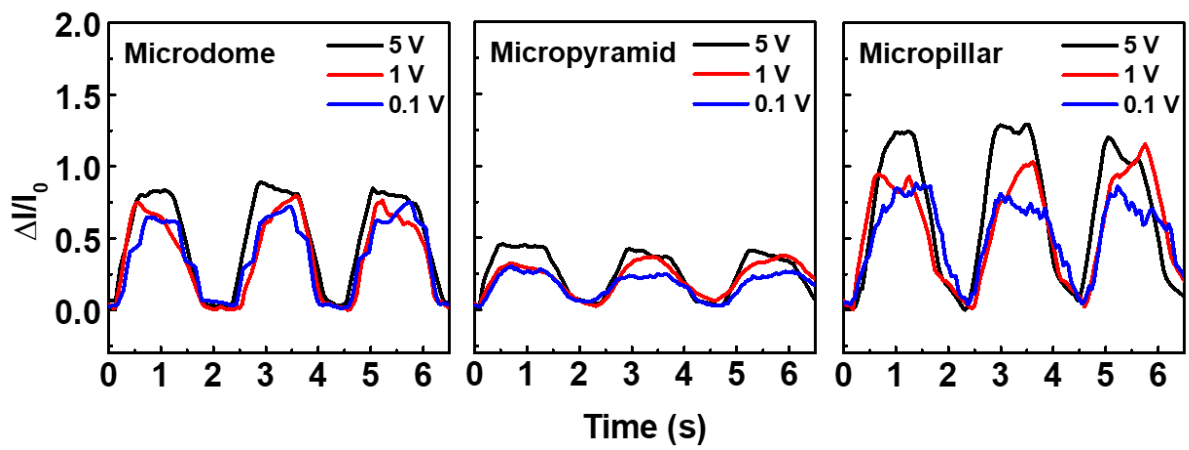


**Figure 4.26.** Relative current changes of interlocked microstructured e-skins in response to human breathing motion for different operation voltages.

**Table 4.2.** Summary of the acoustic sensing capabilities of recently reported acoustic sensors.

NO.	Materials	Transduction mode	Acoustic sensitivity	Acoustic frequency range [Hz]	Sound pressure level [dB]	Ref.
1	PVDF nanofiber web	Piezoelectric	266 mV Pa <sup>-1</sup>	2000	60-115	[181]
2	PZT thin film	Piezoelectric	-	1000	-	[67]
3	ZnO nanowire	Piezoelectric	50 mV/100dB*	100	100	[182]
4	PVDF/rGO interlocked microdome	Piezoelectric	55 mV/96.5dB*	25000	96.5	[43]
5	PTFE thin film	Triboelectric	9.54 V Pa <sup>-1</sup>	10-1700	70-110	[183]
6	Electrospun PVDF nanofiber	Triboelectric	-	50-425	74-114	[184]
7	SWNT/PDMS Interlocked micropillar	Piezoresistive	-	20-13000	-	[185]
8	ZnO nanowire Interlocked hierarchical	Piezoresistive	0.02 dB <sup>-1</sup>	-	57-90	[6]
9	<b>CNT/PDMS Interlocked microdome</b>	<b>Piezoresistive</b>	<b>0.44 Pa<sup>-1</sup> (microdome)</b> <b>0.26 Pa<sup>-1</sup> (micropillar)</b> <b>0.69 Pa<sup>-1</sup> (micropillar)</b>	<b>50-150</b>	<b>60-110</b>	<b>This work</b>

#### 4.4 Conclusions

We developed multidirectional force sensitive e-skins which possess customizable force sensitivity and selectivity by controlling the specific microstructure geometries (i.e., microdome, micropyramid, and micropillar). Different microstructure shapes of e-skins exhibited distinguishable variations in contact area and localized stress between the two opposing composite films, which critically affect force sensitivity, selectivity, and response/relaxation times of e-skins for multi-directional (i.e., normal, shear, tensile, and bending) mechanical forces. It was found that microdome structures presented the best force sensitivities for normal, tensile, and bending stresses. For shear stress, micropillar structures exhibited the highest sensitivity. All of the interlocked microstructures exhibited better sensitivities compared to single microstructures and planar films, which can be explained by the finite-element calculation of contact-area change and stress distribution. As proof-of-concept demonstrations, e-skins were successfully employed in the monitoring of various bio-signals over a wide range of pressures, from acoustic wave ( $<1$  Pa) and human breath (1 Pa–1 kPa) to human pulse pressure (1–10 kPa). The findings in this study related to direction-specific sensitivities of e-skins depending on the microstructure shape are a strong precedent for developing high-performance and customizable e-skins for applications requiring direction-specific force-sensing capabilities.

## Chapter 5. Fingertip skin-inspired microstructured ferroelectric skins with multi-stimuli detection capability

### 5.1 Introduction

Many research groups have recently demonstrated flexible electronic skins (e-skins) with high tactile sensitivities that are capable of mimicking the tactile sensing capabilities of the human skin.<sup>11, 12, 19, 24, 42, 51, 87, 88, 91-93, 137, 186, 187</sup> In particular, flexible and multifunctional e-skins can find applications in humanoid robotics,<sup>188</sup> skin prosthetics,<sup>20</sup> and wearable health monitoring devices.<sup>130</sup> In order to use the e-skins for human skin-like tactile sensor applications, one critical requirement is the ability to simultaneously perceive and differentiate between multiple spatio-temporal tactile stimuli such as static and dynamic pressure, temperature, and vibration. E-skins with these capabilities may enable, for example, humanoid robots that can precisely grasp and manipulate objects, discern the surface texture and hardness, and feel the warmth of living objects. While there have been several reports on the development of multifunctional e-skins that can detect and differentiate between mechanical and thermal stimuli,<sup>24, 51, 129, 131, 186</sup> these approaches typically require the integration of multiple sensors on heterogeneous substrates. In addition, sophisticated layouts of interconnect lines such as open mesh and serpentine layouts are needed to minimize mechanical strain effects. Recently, e-skins that can simultaneously detect pressure and thermal variations were demonstrated in a single device fabricated using ferroelectric or graphene materials.<sup>133, 134, 189</sup> However, only the perception of static pressure was demonstrated in these reports. In addition to the perception of static tactile stimuli, the spatio-temporal detection of dynamic tactile stimuli is critical in the recognition of slip between the skin and objects, enabling the perception of shape, hardness, and roughness.<sup>190</sup> E-skins that can simultaneously detect thermal and mechanical (static and dynamic) stimuli with high sensitivities are yet to be developed.

Human skin is a complex sensory system that contains unique epidermal and dermal microstructures and sensory receptors (Figure 5.1a).<sup>121, 191</sup> The fingerprint patterns enable the perception of fine surface texture by amplifying the vibrotactile signals when the finger is scanned over a surface.<sup>74, 192, 193</sup> The interlocked microstructures between the epidermal and dermal layers are known to amplify and efficiently transfer the tactile stimuli to cutaneous mechanoreceptors.<sup>52, 86</sup> Human skin can also detect and discriminate between static and dynamic mechanical stimuli. Within the human skin, while the slowly-adapting receptors (e.g., Merkel and Ruffini corpuscles) respond to sustained touch and pressure on the skin, the fast-adapting receptors (e.g., Meissner and Pacinian corpuscles) respond to dynamic touch and vibration stimuli.<sup>121</sup> In addition, the human skin is known to have both piezoelectric and pyroelectric properties originating from the presence of polar keratin, elastin, and collagen fibers with unique orientations,<sup>86, 194-196</sup> which enable the human skin to precisely perceive and differentiate

mechanical and thermal stimuli. All of these microstructures and receptors enable the human skin to simultaneously perceive and differentiate between multiple spatio-temporal tactile stimuli. However, such abilities for multifunctional tactile perceptions have not been demonstrated in artificial e-skins. Inspired by the epidermal-dermal interlocked microstructures in human skin, we have previously reported piezoresistive sensors with interlocked microdome arrays, which can detect various static mechanical stimuli including normal, shear, stretching and bending forces.<sup>45, 46</sup> However, these previous sensors are based on piezoresistive mode of operations and therefore can only detect static and low-frequency stimuli. The other sensing capabilities of human skin including texture perception by fingerprint patterns, high-frequency vibration detection by Pacinian corpuscles, piezoelectricity and pyroelectricity of skin will be also required for the detection and discrimination of various static and dynamic stimuli, temperature, and surface textures.

In this work, mimicking diverse structures and functions of sophisticated sensory system in human fingertip, we introduce human skin-inspired multimodal e-skins based on flexible and microstructured ferroelectric films (Figure 5.1b), which enhance the detection and discrimination of multiple spatio-temporal tactile stimuli such as static and dynamic pressure, temperature, and vibration. The piezoelectric and pyroelectric properties of the human skin to detect dynamic touch and temperature are realized in the e-skins by using piezoelectric and pyroelectric responses of ferroelectric polymer composites composed of poly(vinylidene fluoride) (PVDF) and reduced graphene oxide (rGO). The intrinsic inability of the ferroelectric e-skins in detecting sustained static pressures is overcome by utilizing the piezoresistive change in contact resistance between the interlocked microdome arrays in the rGO/PVDF composites.<sup>45, 46</sup> In addition, to mimic the epidermal and dermal microstructures observed in the human finger skin, fingerprint patterns and interlocked microstructures are employed in the e-skins to amplify the tactile signals by static and dynamic pressure, temperature, and vibration. We also show that the e-skin can simultaneously detect pressure and temperature variations and resolve these stimuli separately via different signal generation modes, such as sustained pressure (piezoresistive), tiny and temporal pressure (piezoelectric), and temperature (pyroelectric). As proof of concept, we demonstrate that our e-skin can perceive artery pulse pressure as well as the skin temperature simultaneously, besides perceiving high frequency dynamic sound waves, and various surface textures with different topological patterns, roughness, and hardness. All of these functions are highly desirable in robotics and wearable healthcare monitoring devices.

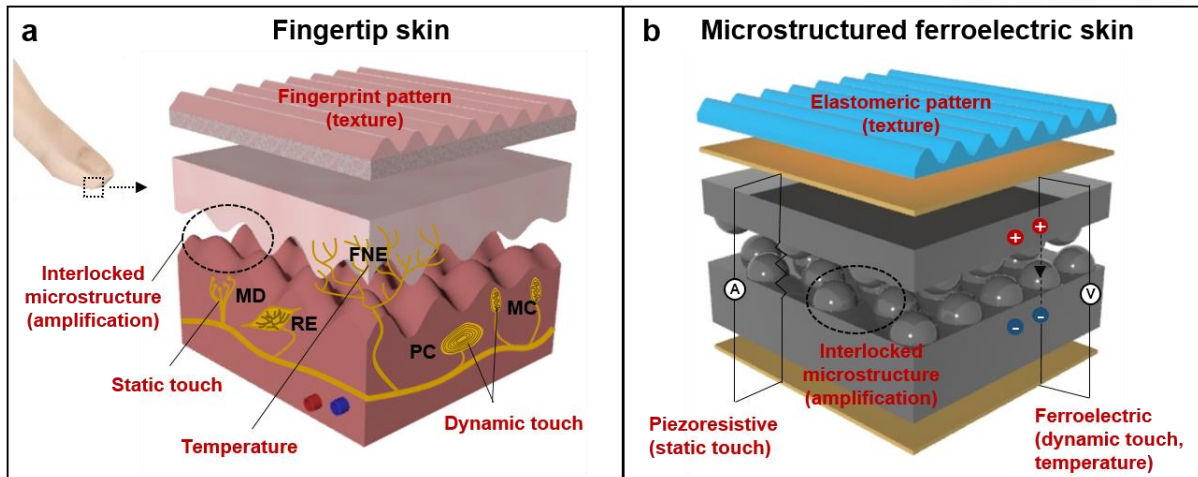


**Figure 5.1.** Human skin-inspired multifunctional electronic skin. (a) Structural and functional characteristics of human fingertips. The fingertip skin consists of slow-adapting mechanoreceptors (Merkel [MD] and Ruffini corpuscles [RE]) for static touch, fast-adapting mechanoreceptors (Meissner [MC] and Pacinian corpuscles [PC]) for dynamic touch, free nerving endings [FNE] for temperature, fingerprint patterns for texture, and epidermal/dermal interlocked microstructures for tactile signal amplification. (b) Flexible and multimodal ferroelectric e-skin. The functionalities of human skin are mimicked by elastomeric patterns (texture), piezoresistive (static pressure), ferroelectric (dynamic pressure and temperature), and interlocked microdome arrays (tactile signal amplification).



## 5.2 Experimental Details

**Material synthesis.** The synthesis of graphene oxide was initiated by adding graphite powder (2 g) into a solution containing H<sub>2</sub>SO<sub>4</sub> (20 mL), K<sub>2</sub>S<sub>2</sub>O<sub>8</sub> (1 g), and P<sub>2</sub>O<sub>5</sub> (1 g) at 353 K, followed by cooling the dark blue mixture to 293 K for 5 h. Distilled water (1 L) was added to the mixture. The mixture was then filtered and the residue on the filter was washed until the pH of the rinse water reached 7. Next, the product was dried overnight at ambient temperature in air. After preoxidation, the oxidized graphite powder (2 g) was added to H<sub>2</sub>SO<sub>4</sub> (75 mL) at 273 K in an ice bath. KMnO<sub>4</sub> (10 g) was added slowly over 10 min with stirring and cooling. During this process, the temperature of the mixture was maintained below 293 K. The mixture was then heated to 308 K and stirred for 2 h, and distilled water (160 mL) was added over 30 min. Next, the mixture was further diluted with distilled water (500 mL) and treated with 30 % H<sub>2</sub>O<sub>2</sub> (8.3 mL). After the suspension turned bright yellow, it was allowed to sit for 1 day, and the supernatant was then decanted. The residue was centrifuged and washed 3 times with 10 % HCl (800 mL) at 3000 rpm. The residue was then centrifuged and washed with distilled water repeatedly until the pH of the rinse water reached a value of 6. For the preparation of GO in DMF, the GO suspension was centrifuged at 15000 rpm for 1 h and the supernatant was then decanted. The residue was centrifuged and washed 5 times with N,N-dimethyl formamide (N,N-DMF) (Junsei, 99.5 %, density: 0.952 g/mL) (40 mL) at 15000 rpm for 1 h. PVDF (Sigma Aldrich, Mw: ~530,000, pellet) solution (10 wt. % in DMF) was mixed with the GO/DMF suspension.

**Device fabrication.** The PVDF/GO nanocomposite films were fabricated by solution-based rod casting using a glass rod on the glass plate at 50 °C and drying for 12 h. To remove the residual DMF solvent and reduce the GO into rGO, the films were dried again in a vacuum oven at 160 °C for 3 h. The residual DMF solvent was completely removed during the annealing process (Figure 5.2). A series of graphene/PVDF nanocomposite films with different graphene loadings were similarly prepared. For fabricating the interlocked microdome rGO/PVDF nanocomposite films, a polydimethylsiloxane (PDMS) replica mould was prefabricated by the double casting method. The double casting method was initiated by coating water-soluble polymer poly(vinylalcohol) (PVA) as a thin interlayer onto an as-prepared PDMS film fabricated by the micromoulding of a silicon substrate with microdome patterns (10 μm in diameter, 12 μm in pitch, and 4 μm in height). The PDMS prepolymer was then poured onto the PVA-coated microdome-patterned PDMS film, following which the fully cured replica mould was peeled off along with the microdome arrays at 90 °C for 3 h. Finally, by removing the residual PVA on the surface of the PDMS replica mould by soaking in water, the fabrication of the replica mould was completed. Using the micromoulding process, ferroelectric rGO/PVDF nanocomposite films with microdome arrays were prepared (Figure 5.3). The resulting films had the following feature sizes: diameter - 10 μm, pitch - 12 μm, and height - 4 μm. Prior to the micromoulding of the GO/PVDF composite, we treated the prepared replica PDMS mould with oxygen plasma for 1 min in order to make

the surface less adhesive to the hydrophobic GO/PVDF solution. The GO/PVDF precursor (500  $\mu\text{L}$ ) was then cast onto the oxygen plasma-treated replica mould, and subsequently stored in a vacuum oven at 160  $^{\circ}\text{C}$  for 6 h. Finally, the fingerprint-inspired micropattern for texture perception was prepared by the PDMS micromoulding process with regular dimensions of around 500  $\mu\text{m}$  in pitch and 160  $\mu\text{m}$  in ridge width. The thickness of the fingerprint-patterned PDMS film was 50  $\mu\text{m}$ .

**Characterization.** Field-emission scanning-electron microscopy (FE-SEM; S-4800, Hitachi) was used to observe the morphology of the GO/PVDF composite films. Differential scanning calorimetry (DSC) measurements (DSC Q10, TA instrument) of the GO/PVDF nanocomposites were conducted under nitrogen gas in the 193 to 473 K temperature range with cooling/heating speeds of 20 K/min. The crystalline structure of GO/PVDF nanocomposites was determined using XRD (Rigaku Ultima IV) with Cu  $K\alpha$  radiation. FT-IR (NICOLET 380, Thermo Scientific) measurements were conducted to examine the changes in the bonding structure. The electrical properties of the rGO/PVDF nanocomposites under controlled temperatures were measured by a source meter (S-2400, Keithley). For the TCR measurements, the temperature of the hot stage was controlled by the Advanced Peltier System (APS) attached to ARES-G2 TA Instruments.

**Measurements of the sensing performance of the e-skins.** To measure the electrical properties of the e-skin devices as a function of pressure and temperature variation, two Cu electrodes were attached to the top and bottom of the sandwiched microdome-patterned nanocomposite films (size : 1.5 cm  $\times$  1.5 cm) using silver paste and annealed at 90  $^{\circ}\text{C}$  for 1 h to minimise contact resistance. A thin PDMS film (thickness:  $\sim$  300  $\mu\text{m}$ ) was used as a supporting layer to fix the e-skin and reduce electrical noise. To measure the pressure-induced electrical properties, piezoresistive and piezoelectric signals were collected using a semiconductor parameter analyser (4200-SCS, Keithley) and source meter (S-2400, Keithley), respectively. A static normal pressure was applied by the pushing tester (JIPT, JUNIL TECH, Korea) with a pushing speed of 3 mm/s as controlled moving displacement. For the frequency-dependent pressure measurements via piezoelectric sensors, the frequencies of applied pressure were modulated by varying the pushing speed (0.3-4.5 mm/s) under a fixed moving distance of the pushing tester (schematic illustration in Figure 5.4a). Here, the piezoelectric output signals were measured by a source meter with infinitely large input impedance ( $>10\text{ G}\Omega$ ). The number of power line cycles (NPLC) of 1 were used to increase the measurement resolution and accuracy. To evaluate the detection of simultaneous temperature and pressure variations, loading/unloading cycles of water-filled glass vials with different temperature and pressure were performed onto the e-skin (sensor size: 1  $\text{cm}^2$ ) with the 2 s intervals. To monitor the variation in the artery pressure pulse, the wearable e-skin (sensor size: 1  $\text{cm}^2$ ) encapsulated by polyimide films on both sides, was wrapped onto the wrist. The changes in the artery pressure pulse with exercise and body temperature were monitored after running for 5 min and immersing the wrist in warm and cold water for 2 min. To evaluate the sensing of dynamic pressure, a

speaker (SMS-A90, Samsung) connected with a frequency sound generator (APKCRAFT) was used to generate acoustic sound waves, which were dictated via an electronic dictionary (oxford) program (Figure 5.4b). The sound waves (sound intensity: 96.5 dB) were then applied to the e-skin using a speaker placed at a distance of 2 cm from the e-skin. The electrical voltage generated was analysed by an oscilloscope (DPO 2022B, Tektronix). A spectrogram of the original acoustic waves was displayed by an audio editor program (Wavesurfer). To evaluate the perception of surface textures, a lab-built microstage system (Micro Motion Technology, Korea) was used for cyclic displacement within 1 cm at constant moving speeds (0.25-2.5 mm/s) and loading pressure (0.3 N). For this measurement, various target substrates such as PDMS substrates with parallel line patterns (D: 160  $\mu\text{m}$ , P: 500  $\mu\text{m}$ ), sandpaper, glass, paper, and silicon substrates with different geometric patterns were used. For the discrimination of surface hardness/softness, the parallel line patterned PDMS substrates with different modulus were prepared by adjusting the mixing ratio of PDMS base to curing agent (10:1, 15:1, 20:1).<sup>197</sup>

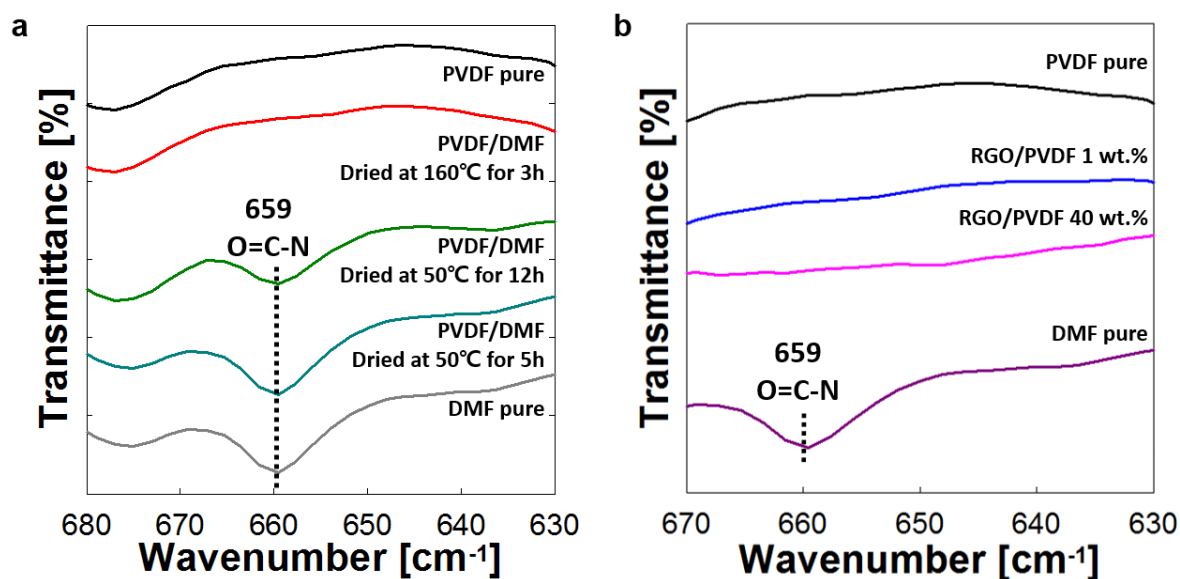


**Figure 5.2.** FT-IR spectra for verifying residue solvent. (a) PVDF at different preparation conditions, (b) rGO/PVDF nanocomposites with rGO contents of 0, 1, and 40 wt. % compared with pure solvent. The solvent peak at 659  $\text{cm}^{-1}$  is attributed to the O=C=N torsional bond.

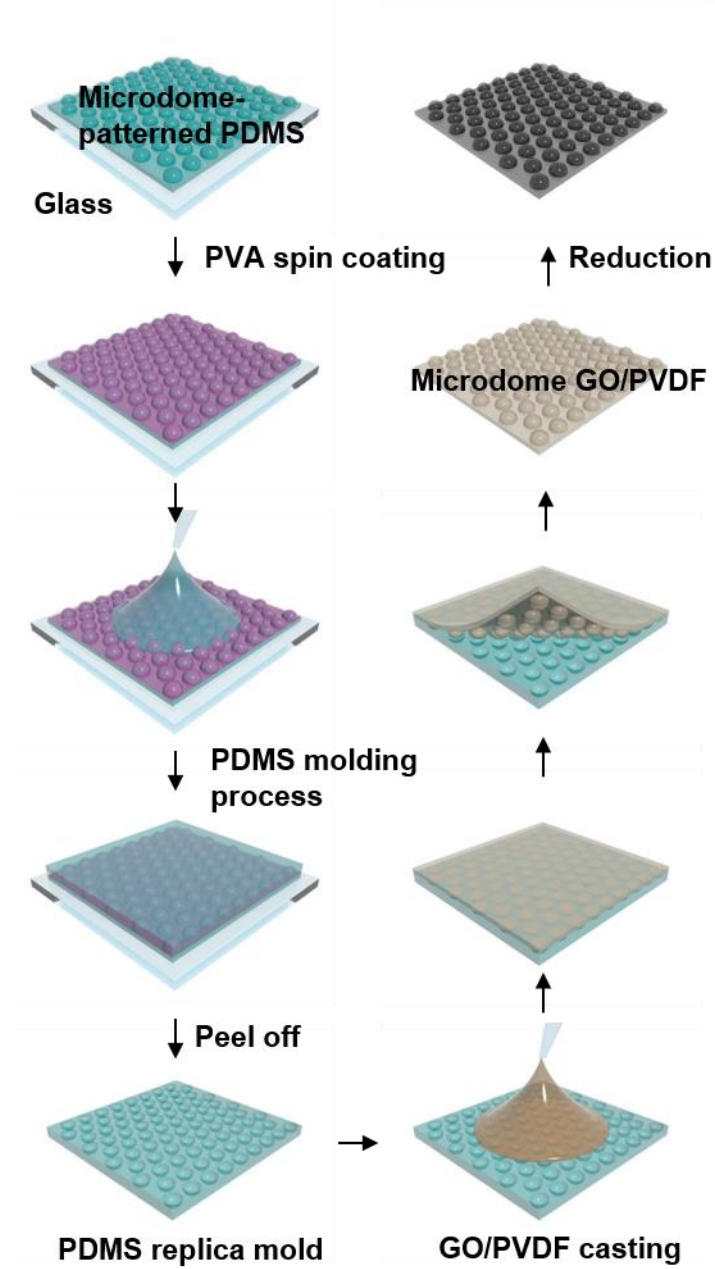


**Figure 5.3.** Schematic illustrations of the double casting and micromoulding processes for the rGO/PVDF composite film with a microdome-patterned surface.

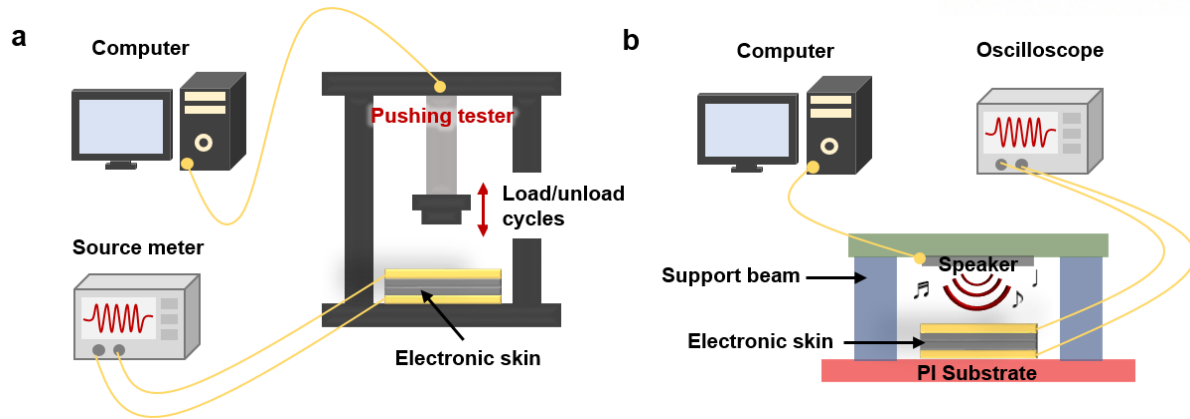


**Figure 5.4.** Experimental set-up for the detection of dynamic pressure. (a) Schematic illustration of the measurement system for the detection of dynamic touch. (b) Schematic illustration of the measurement system for the detection of acoustic waves.

### 5.3 Results and Discussion

**Ferroelectric rGO/PVDF composite films for temperature mapping.** Flexible ferroelectric films were fabricated by introducing graphene oxide (GO) sheets in the PVDF matrix and subsequently rod casting at a low temperature (50 °C for 12 h). At this low crystallization temperature, both PVDF/GO mixtures as well as pure PVDF crystallize into polar phases ( $\beta$ - phase). The formation of polar phases in PVDF was confirmed by X-ray diffraction (XRD) and Fourier transform infrared (FT-IR) spectroscopy analyses (Section S5.1 and Figures 5.6–5.8). Next, to increase the conductivity of the composite films for use as piezoresistive sensors, the GO in the composite films was further reduced by annealing at 160 °C for 3 h, during which the brownish transparent film turned black (Figure 5.6a). It is worth noting that even after annealing, the polar crystal structure of PVDF is still maintained in the composite films (Figure 5.6a), which is not the case for pure ferroelectric PVDF made by solution casting at low temperature (Figure 5.6a) or made by conventional electric poling process.<sup>198</sup> This may be ascribed to the steric effect by the existence of GO sheets adjacent to crystalline PVDF and to the interaction between PVDF molecules and GO surface atoms. The solution rod casting method used in this study for fabricating ferroelectric PVDF/rGO composite films is scalable. Flexible and large-area composite films that are 20 × 15 cm<sup>2</sup> are easily obtained (inset in Figure 5.5a). A cross-sectional SEM image of the rGO/PVDF composite film with an rGO concentration of 1 wt. % indicates that the rGO sheets are uniformly dispersed and stacked within the PVDF matrix (Figure 5.5). An increase in the rGO content in the composite further increases the tendency to form stacked rGO structures (Figure 5.9a).

The current-voltage (IV) curves of the ferroelectric composite film (1 wt. % rGO) as a function of temperature show that the current increases with increase in temperature from 0 to 100 °C (Figure 5.5b). When the relative resistance ( $\Delta R/R_0$ ) is plotted as a function of temperature for all the PVDF/rGO composites with various rGO contents, the resistance decreases with increase in the temperature (Figure 5.5c). This negative temperature coefficient (NTC) of resistance is not common for conductive composites, since most of them show a positive temperature coefficient (PTC) behaviour, owing to thermal swelling of the polymer matrix.<sup>199-201</sup> The NTC behaviour observed in our composite film can be attributed to the change in the contact resistance between the rGO sheets<sup>202</sup> by thermo-mechanical variation as well as the intrinsic NTC behavior of rGO.<sup>203</sup> Temperature-dependent resistance change can be quantified by means of the temperature coefficient of resistance (TCR) parameter, which is defined as  $TCR = (\Delta R/R)/\Delta T$ , where  $R$  is the resistance of the film and  $T$  is the temperature. TCR is reduced with increase in the rGO content (Figure 5.5c). This is attributed to the decrease in the crystallinity of PVDF with increase in the rGO content in the composites (Figure 5.9b and c). For demonstration, we fabricated flexible temperature-sensitive e-skins by placing gold electrode arrays on

the top and bottom of the film ( $18 \times 12$  pixels). When a human hand is placed on top of the e-skins, the temperature variation over the entire contact area can be mapped by the temperature sensor (Figure 5.5d). This temperature mapping capability of cost-effective flexible films is beneficial for the continuous monitoring of the temperature variation of human skin, which can provide clinical information for medical diagnosis.<sup>91</sup>

To further investigate the temporal response of e-skins to continuous temperature variations, we analysed the dynamic changes in the e-skin resistance immediately after contact with a water droplet at various temperatures. Figure 5.5e shows a representative optical image and infrared camera images of water droplets on e-skins with different droplet temperatures. The solid lines in Figure 5.5f and h show the time-dependent resistance change of the e-skins, while the dotted lines show the droplet temperatures, as monitored by an IR camera. When a water droplet at room temperature ( $25\text{ }^{\circ}\text{C}$ ) falls on the e-skin at  $25\text{ }^{\circ}\text{C}$ , the electrical resistance of the e-skin does not change (Figure 5.5f). On the other hand, the falling of warm water droplets ( $38, 50, \text{ and } 64\text{ }^{\circ}\text{C}$ ) induces an instantaneous decrease in the relative resistance to  $0.74\text{-}0.92$  (Figure 5.5g). Although the resistance rapidly decreases immediately after contact with the warm water droplets, it then gradually increases due to the cooling of the warm water droplet over time, and finally reaches the original value of 1 at thermal equilibrium. On the other hand, the falling of cold water droplets ( $-2, 9, \text{ and } 21\text{ }^{\circ}\text{C}$ ) on the e-skins at  $36\text{ }^{\circ}\text{C}$  shows the opposite behaviour (Figure 5.5h). In this case, the relative resistance instantaneously increases immediately after contact with the cold water droplets and then gradually decreases due to the warming up of the droplet to a local steady state temperature. Here, the relative resistance at a local steady state ( $R/R_0 = 1.02$ ) is slightly higher than the original value ( $R/R_0 = 1.00$ ), which can be attributed to the temperature difference between the water droplet at local steady state ( $30\text{ }^{\circ}\text{C}$ ) and the original e-skin temperature ( $36\text{ }^{\circ}\text{C}$ ). The local steady state temperature ( $30\text{ }^{\circ}\text{C}$ ) of a water droplet can be reached due to the temperature difference between the e-skin ( $36\text{ }^{\circ}\text{C}$ ) and the atmosphere ( $25\text{ }^{\circ}\text{C}$ ). When the water droplet is removed from the e-skin surface, the relative resistance recovers to the original value (Figure 5.10). This result verifies that the e-skin can also detect a wetting state by a cold water. For both the warm and cold water droplet measurements, the instantaneous and subsequent gradual variation in the relative resistances (solid lines) agree with the temperature variation behaviour of the water droplets. The instantaneous variation in the resistance leads to local equilibria in the initial time domain ( $< 0.2\text{ s}$ ) after water contact (Figure 5.5g and i). This behaviour can be modelled as follows (Equation (1)):

$$\frac{R}{R_0}(t) = \left(\frac{R}{R_0}\right)_{L.E.} + \left[1 - \left(\frac{R}{R_0}\right)_{L.E.}\right] \exp\left(-\frac{t}{\tau_T}\right) \quad (1)$$

where  $R$  is the resistance of the e-skin,  $t$  is the time, and  $\tau_T$  is the characteristic time (Section S5.2). The experimental data fits well to Equation (1) with  $\tau_T = 11$  ms for both the warm and cold water droplets (Figure 5.5g and i). The  $\tau_T$  value of 11 ms corresponds to the time scale required for the overall system composed of the e-skin and water droplet to reach local thermal equilibrium (Section S5.3). The above results demonstrate that our e-skins enable fast and precise monitoring of temporal and spatial changes in temperature.

### S5.1 Ferroelectric crystalline structures in poly(vinylidene fluoride)/graphene oxide (PVDF/GO) composites

The  $\beta$ -phase with the orthorhombic phase structure has high polarity, owing to the two all-trans (TTTT) chains whose dipoles point to the same direction. In contrast, the nonpolar monoclinic  $\alpha$ -phase composed of two chains in the TG+TG- conformation has antiparallel dipole components normal to the chain axis. Pure PVDF and PVDF/GO composite films contained only the  $\beta$ -phase when they were solution-casted in N,N-dimethyl formamide (DMF) and dried at 50 °C for 12 h (Figure 5.6). The characteristic X-ray diffraction (XRD) peaks at  $2\theta = 20.6^\circ$  and  $36.5^\circ$  can be assigned to  $\beta$  (200, 110) and  $\beta$  (020), respectively. For the pure PVDF film, the  $\beta$ -phase was transformed into the  $\alpha$ -phase when the films were annealed at 160 °C for 3 h or casted at 160 °C. The characteristic XRD peak at  $2\theta = 17.9^\circ, 18.3^\circ, 20.0^\circ, 26.7^\circ, 33.8^\circ, 37.2^\circ,$  and  $39.2^\circ$  can be assigned to  $\alpha$  (100),  $\alpha$  (020),  $\alpha$  (110),  $\alpha$  (021),  $\alpha$  (121),  $\alpha$  (040), and  $\alpha$  (002), respectively. On the contrary, for the PVDF/GO (95/5) composite film, the  $\beta$ -phase was retained in the films after the same thermal processing procedure as those employed for pure PVDF. For the PVDF/GO (99/1) composite films,  $\beta$  and  $\gamma$ -phases were observed by XRD and Fourier transform infrared spectroscopy (FT-IR) analyses as seen in Figures 5.6 and 5.7. For the  $\gamma$ -phase, the ab base is the same as that for the  $\alpha$ -phase (Figure 5.6c), characterised by peaks at  $2\theta = 17.9^\circ, 18.3^\circ,$  and  $20.0^\circ$ . In addition, an XRD peak corresponding to  $\gamma$  (021) is observed at  $2\theta = 20.4^\circ$ . Therefore, the PVDF/GO (99/1) composite contains both  $\beta$  and  $\gamma$ -phases, whereas the PVDF/GO (95/5) composite contains only the  $\beta$ -phase. In addition, the chemical structure of the pure PVDF and PVDF/GO composite film was analysed. After annealing at 160 °C for 3 h, pure PVDF exhibited a characteristic peak at approximately  $765\text{ cm}^{-1}$  arising from the vibration mode of the in-plane bending or rocking of  $\text{CH}_2$  of the  $\alpha$ -phase. Compared to pure PVDF, the characteristic peaks of the PVDF/GO (99/1) and (95/5) composites are observed at  $840\text{ cm}^{-1}$ , which can be attributed to the mixed mode of  $\text{CH}_2$  rocking and  $\text{CF}_2$  asymmetric stretching vibrations of the  $\beta$ -phase. Note that the PVDF/GO (99/1) composite retains additional TTTG chain peaks, which corresponds to the  $\gamma$ -phase.

When the molten composites after annealing at 160 °C are quenched in liquid nitrogen, only the  $\alpha$ -phase is observed in the case of pure PVDF. However, a new phase ( $\gamma'$ -phase) is observed in the



PVDF/GO composites as seen in Figure 5.6. In the quenched PVDF/GO composites, the peaks observed at  $18.3^\circ$  and  $20.0^\circ$  can be assigned to the ab base of the  $\alpha$  or  $\gamma$ -phases. However, peaks corresponding to  $\alpha$  (021) or  $\gamma$  (021) are missing for the quenched PVDF/GO composites, which are expected to appear at  $2\theta = 26.7^\circ$  or  $20.4^\circ$ . In the XRD analysis, no peak related to ordering in the c-axis direction is observed in the quenched PVDF/reduced graphene oxide (rGO) composites. FT-IR analysis shows that the composites have TG, TT, and TTTG conformations as seen in Figure 5.7. Therefore, it can be concluded that the quenched PVDF/GO composites have the same ab base as the  $\alpha$ -phase, but disordered structure in the c-axis. We refer to this new phase as the  $\gamma'$ -phase, which is depicted schematically in Figure 5.8.

### S5.2 Local temperature equilibrium model for the water droplet on e-skins

Heat balance may be given by Equation (1), assuming the thickness of the e-skin is small enough that the temperature of water can be treated as constant in the initial response state.

$$\frac{dT}{dt} = -\frac{UA}{mC_p} (T(t) - T_{\text{water}}) \quad (1)$$

In the above equation, U is the overall heat transfer coefficient;  $U = 1/(1/h_i + d/k)$ , where  $h_i$  is the heat transfer coefficient at the water-film interface, k is the thermal conductivity of the e-skin, and d is the thickness of the e-skin. The explicit solution to Equation (1) is given by Equation (2):

$$T(t) = T_{\text{water}} + (T(0) - T_{\text{water}}) \exp(-t/\tau_T) \quad (2)$$

where  $\tau_T$  is the characteristic time;  $\tau_T = mC_p/UA$

Equation (2) can be rewritten in terms of resistivity as follows (Equation (3)), since the resistivity of the film is almost linearly proportional to the reciprocal of temperature.

$$\frac{R}{R_0}(t) = \left(\frac{R}{R_0}\right)_{\text{L.E.}} + \left[1 - \left(\frac{R}{R_0}\right)_{\text{L.E.}}\right] \exp\left(-\frac{t}{\tau_T}\right) \quad (3)$$

For both the hot water and cold water droplets, local equilibria are observed at the initial stages of contact between the e-skin and the water droplets (Figures 5.5g and i). Equation (3) with the characteristic time ( $\tau_T$ ) of 11 ms fits the experimental data for both hot and cold water droplets, indicating that the e-skin senses the temperature of the water droplets by pyroelectric effect in very short amounts of time. The characteristic time can be engineered by varying the thickness of the e-skin or coating the surface of the e-skin for specific purposes. The e-skin with interlocked microdome arrays senses the weight of water droplet as well as the temperature of the droplets, simultaneously. The characteristic time for detecting the weight of water droplets by piezoresistive effect is about 100 ms under isothermal condition, which is 10 times longer than the temperature detection time. Therefore, the e-skin discerns the temperature and weight stimuli by a single ferroelectric response. Furthermore,

the e-skin is much more sensitive to the stimulus of pressure modulus.

### S5.3 Characteristic time to reach thermal equilibrium for the water droplet on e-skins

The characteristic time of 11 ms corresponds to the overall heat transfer of the system composed of the e-skin and water droplet. The phonon velocity in the PDVF/rGO film can be estimated from the velocity of sound ( $v$ );  $v = (E/\rho)^{1/2}$  where  $E$  is the Young's modulus and  $\rho$  is the density. The phonon velocity in the PVDF/rGO film is estimated to be 831 m/s from the measured Young's modulus at room temperature (Figure 5.9). Further, the thermal diffusivity ( $\alpha$ ) of the PVDF/rGO film is estimated to be  $1.51 \times 10^{-7}$  m<sup>2</sup>/s. The thermal diffusivity may be given by  $\alpha = k/(\rho c_p) \sim vl$ , where  $k$  is the thermal conductivity,  $c_p$  is the specific heat capacity, and  $l$  is the mean free path of the phonon. The time scale to reach local thermal equilibrium through the film (10  $\mu$ m) can be estimated by using the heat equation ( $\delta T/\delta t = \alpha \nabla^2 T$ ) and this time is close to the characteristic time of 11 ms. The NTC behaviour of the PVDF/r-GO film may also be attributed to the change in contact resistance between the rGO sheets by thermo-mechanical variation as well as to the ferroelectricity of polar PVDF crystallites, since the time scale for the thermo-mechanical variation may also be much smaller than the characteristic time for the overall heat transfer of the system. In fact, the resistance of the e-skin was measured using current bias of several mA. On the other hand, the current generate by the ferroelectricity of polar PVDF is of the order of several nA. Thus, the NTC behaviour is mainly attributed to the change in contact resistance between the rGO sheets.

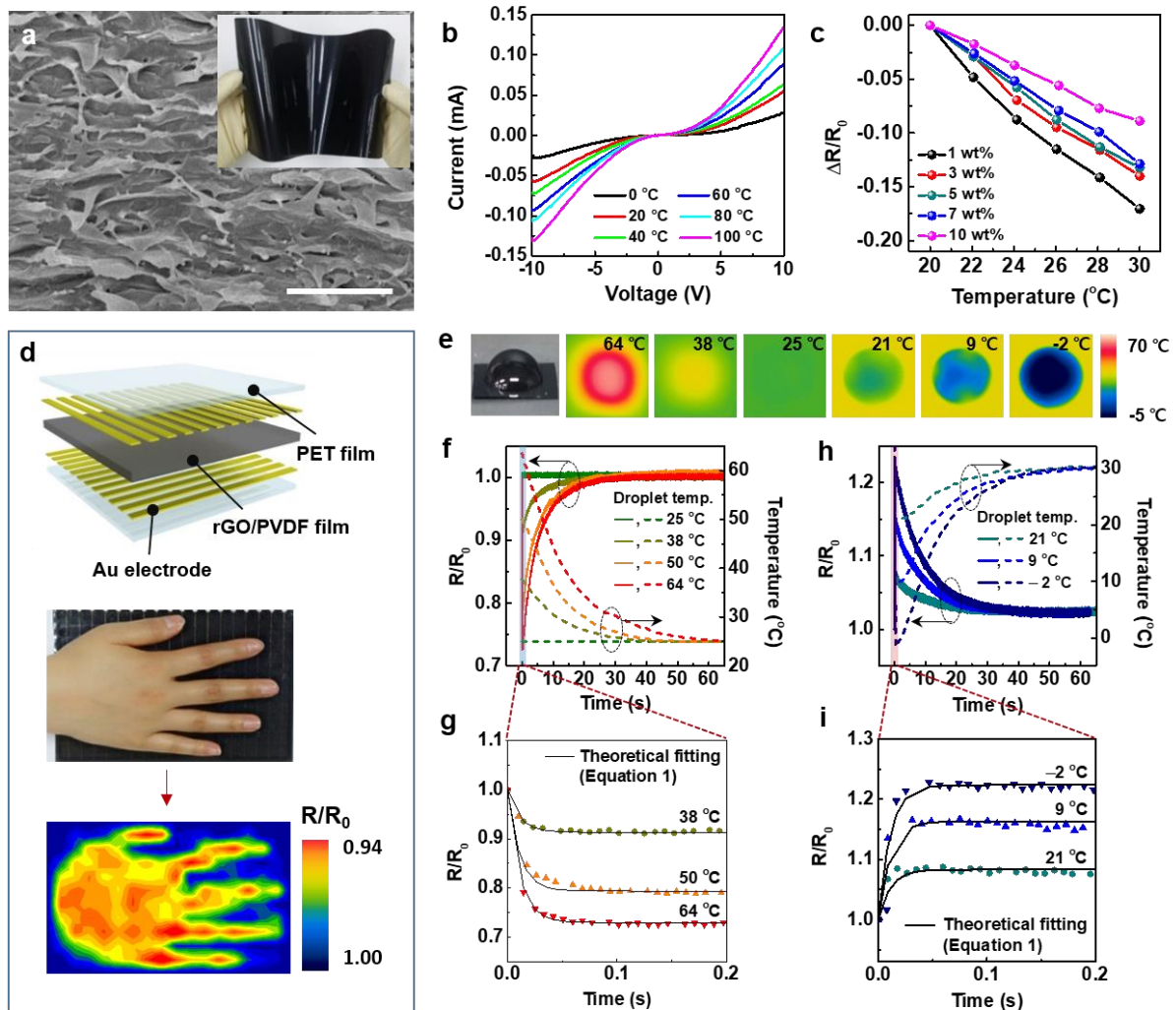


**Figure 5.5.** Temperature sensing properties of flexible rGO/PVDF nanocomposite film. (a) Cross-sectional SEM image of the rGO/PVDF composite film with stacked GO sheets. Scale bar, 1  $\mu\text{m}$ . The inset shows a photograph of a flexible and large scale (20  $\times$  15  $\text{cm}^2$ ) rGO/PVDF composite film. (b) Current-voltage curves of 1 wt. % rGO/PVDF composite films at various temperatures. (c) Relative resistance change of rGO/PVDF composite film as a function of temperature for various concentrations of rGO. (d) Detection of temperature distribution on the human palm. (top) Schematic diagram of a sensor array, where the rGO/PVDF composite film is sandwiched between gold electrode arrays (18  $\times$  12 pixels). (middle) Photograph of a human hand on top of the sensor array. (bottom) Contour mapping of electrical resistance variations for the local temperature distribution on the human palm. (e) A representative photograph and infrared camera images of water droplets with different droplet temperatures (64 to -2  $^\circ\text{C}$ ) on the e-skins. (f) and (h) Relative resistance ( $R/R_0$ ) and temperature ( $T$ ) variations of the e-skins after contact with the water droplets (f) above room temperature (25 - 64  $^\circ\text{C}$ ), (h) below room temperature (-2 - 21  $^\circ\text{C}$ ). Temperature ( $T$ ) change is measured by IR camera. (g) and

(i) Initial stages of time-domain signals in (f) and (g) showing the variation of relative resistance immediately after contact between the e-skins and the water droplets. The solid lines are model fitting to Equation (1).

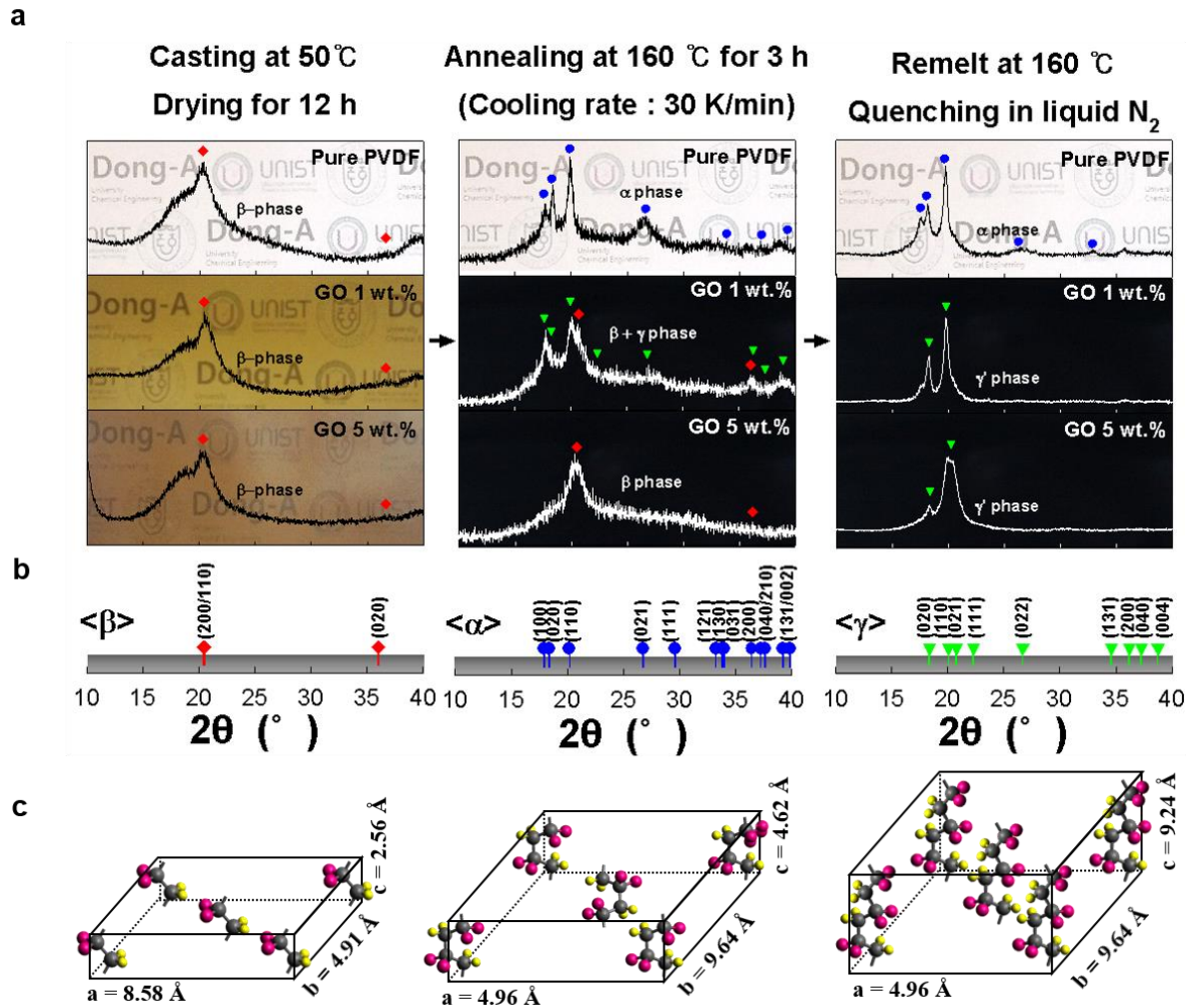


**Figure 5.6.** Phase transition of the GO/PVDF composite films with various thermal treatments. (a) XRD patterns of the GO/PVDF composite films with GO loading concentrations of 0, 1, and 5 wt. % casted at 50 °C for 12 h, annealed at 160 °C for 3 h, re-melted at 160 °C, and quenched in liquid nitrogen. Background pictures are those of the GO/PVDF composite films fabricated with each process. (b) Calculated Miller indices of the  $\beta$ ,  $\alpha$ , and  $\gamma$  phases. (c) Schematic illustrations of the structural configuration of atoms for each phase of PVDF.

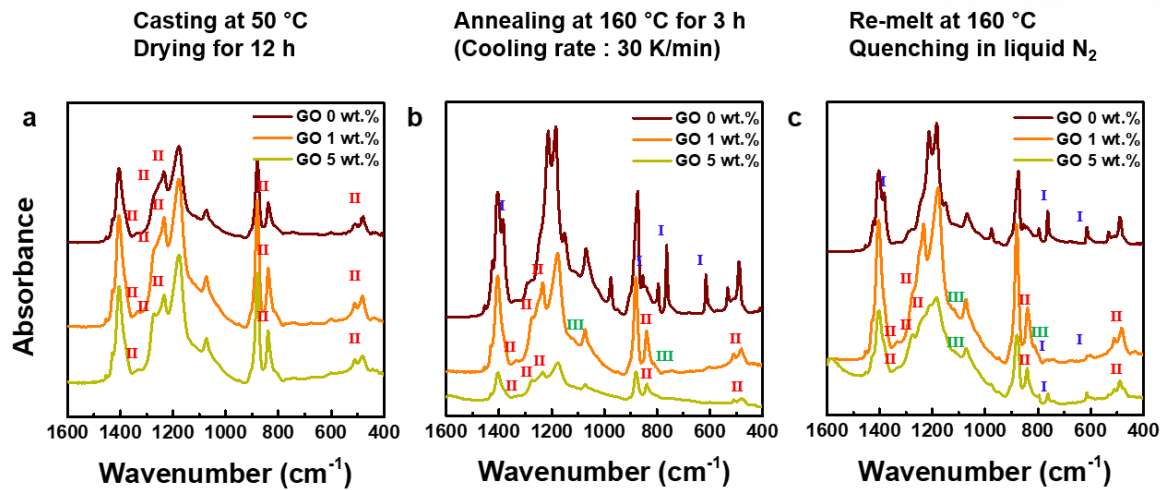


**Figure 5.7.** FT-IR spectra of the GO/PVDF composite films with GO loading concentration of 0, 1, and 5 wt%. (a) casted at 50 °C for 12 h, (b) annealed at 160 °C for 3 h, and (c) re-melted at 160 °C and quenched in liquid nitrogen. The IR peak at 765  $\text{cm}^{-1}$  is attributed by vibration mode of the in-plane bending or rocking of  $\text{CH}_2$  of  $\alpha$ -phase. And peak at 840  $\text{cm}^{-1}$  is presented by mixed mode of  $\text{CH}_2$  rocking and  $\text{CF}_2$  asymmetric stretching vibrations of  $\beta$ -phase. [Information of peaks; I: TG – 614, 765, 858, 1385  $\text{cm}^{-1}$ , II : 512, 840, 1234, 1270, 1330  $\text{cm}^{-1}$ , III : 811, 1115  $\text{cm}^{-1}$ ]

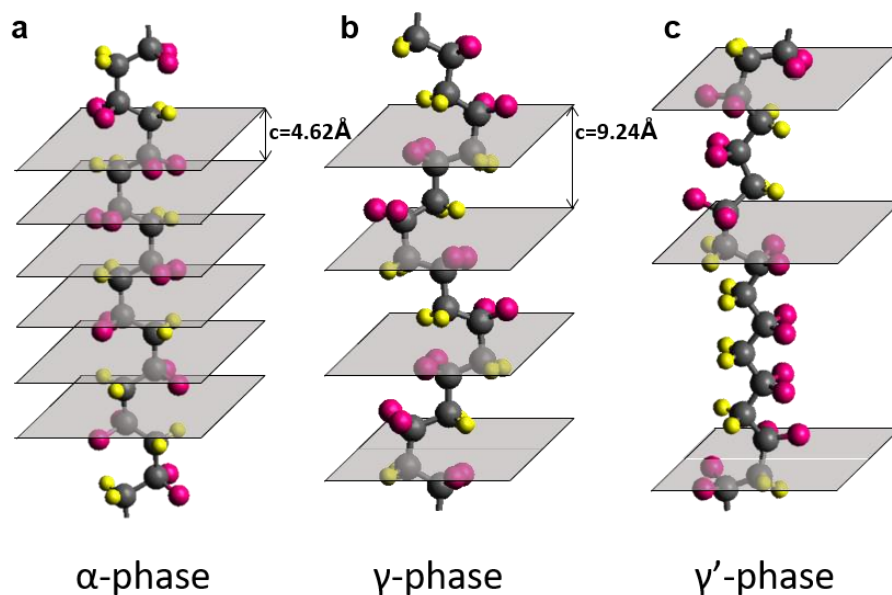


**Figure 5.8.** Crystalline structures of PVDF (a)  $\alpha$ -phase, (b)  $\gamma$ -phase, and (c)  $\gamma'$ -phase.

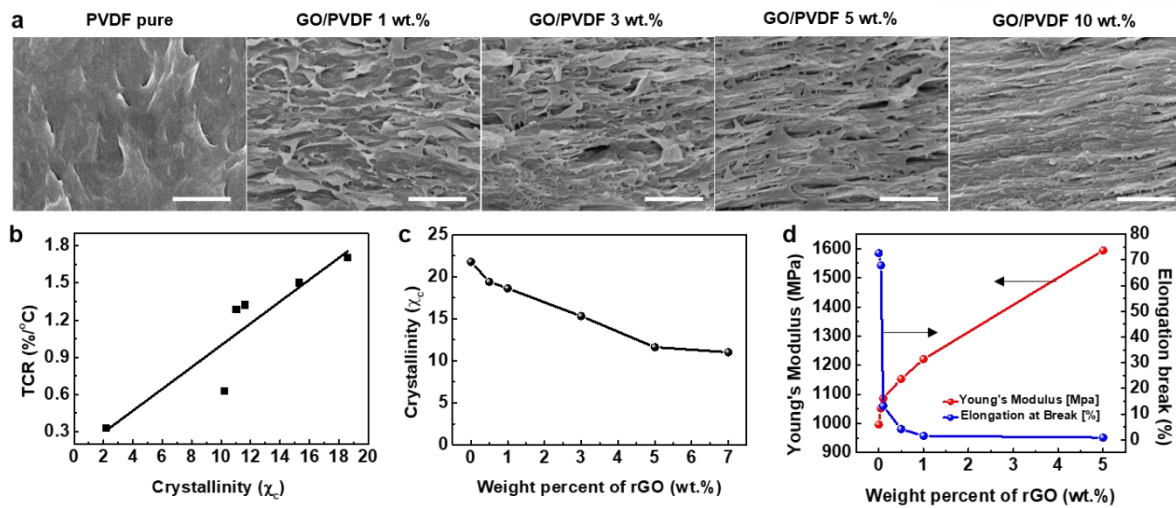


**Figure 5.9.** (a) Cross-sectional SEM images of the rGO/PVDF composite films with various rGO loading concentrations. Scale bar, 1  $\mu\text{m}$ . (b) Relationship between temperature coefficient resistance (TCR) and crystallinity. (c) Crystallinity of the rGO/PVDF composite films with different rGO loading concentrations. (d) Young's modulus and elongation at break of the rGO/PVDF composite films with different rGO loading concentrations.

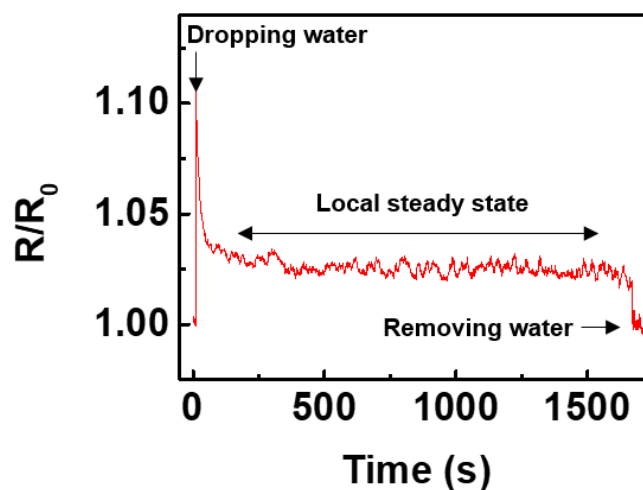


**Figure 5.10.** The time-dependent changes in relative resistance under dropping cold water (19.6  $^{\circ}\text{C}$ ) onto planar-structured rGO/PVDF composite film.

**Simultaneous detection of static pressure and temperature.** The planar composite film is not sensitive to the minute pressure variations induced by the water droplet on the e-skin. The pressure sensitivity can be significantly enhanced by employing an interlocked geometry of microdome arrays in the laminated composite films (Figure 5.11a). In this case, an external stress can induce deformation, which in turn can induce variation in the contact area between the interlocked microdomes, resulting in the pressure-dependent variation of contact resistance. Figure 5.11b confirms that the pressure sensitivity of the interlocked microdome arrays is significantly higher than that of a planar film mainly due to the large change in contact area between neighbouring microdome arrays under external stress.<sup>45</sup>

<sup>46</sup> The contact resistance of interlocked microdome arrays continuously decreases with the increase of pressure up to 49.5 kPa, which indicates the wide dynamic range of pressure detection (Figure 5.12). We also note that a decrease in the loading of rGO in the film improves sensitivity, which can be attributed to the increased softness (Figure 5.9d) and piezoelectric effects associated with the decrease in the rGO content. The e-skins can detect a tiny static pressure (~0.6 Pa) by a human hair pushing or dynamic movements of hair drawing on the e-skin (Figure 5.13a). Furthermore, e-skins enabled the sensitive monitoring of air flow pressure variations ranging from 0.6 to 2.2 Pa (Figure 5.13b). For repetitive cycles (5000 times at 0.3 Hz) of normal force (20 kPa), the e-skin shows no noticeable degradation (Figure 5.14).

The geometry of the interlocked microdome array also results in a higher TCR value (2.93 %/°C) compared to the planar film (1.58 %/°C) (Figure 5.11c). For interlocked microdome structures, in addition to the intrinsic NTC behaviour of the composite films, thermal expansion and softening of the PVDF matrix leads to increased contact area and thus, decreased contact resistance, resulting in enhanced NTC behaviour. The TCR value decreases with increase in the normal pressure on the interlocked microdome arrays (Figure 5.15), indicating the critical role of the initial contact area in modulating the TCR values. Without normal pressure, the initial contact area is very small. However, the contact area can be significantly increased by the thermal expansion of PVDF, resulting in a decrease in the resistance. This effect decreases with increase in the initial contact area with the application of normal pressure. Therefore, the TCR value of 3.15 %/°C under zero pressure significantly decreases to 1.2 %/°C at a normal pressure of 1.2 kPa (Figure 5.15). The TCR values of interlocked microdome arrays are higher than those of film-type thermal sensors, such as carbon nanotube films (1-2.5%/°C at -173~57 °C),<sup>204</sup> multi-walled carbon nanotubes (MWNT)/graphene flakes (0.08%/ °C at 0~30 °C)<sup>205</sup> and graphene nanoplatelets (0.0371 °C at 10~60 °C).<sup>206</sup>

To evaluate the temporal response of interlocked e-skins to continuous temperature and pressure variations at the same time, we analysed the time-dependent variation of e-skin resistance and water temperature immediately after the falling of a water droplet (2 Pa) at various temperatures (Figure 5.11d). The falling of a room-temperature water droplet on the e-skin results in a decrease in the relative

resistance to 0.92, owing to the pressure applied by the water droplet (Figure 5.11e). When warm water droplets at 40 and 60 °C fall on the e-skin, the resistance instantaneously decreases to 0.38 and 0.25, respectively, owing to both pyroelectric and piezoresistive effects, then gradually increase due to the cooling of the warm water droplet over time, and finally reaches the resistance value of 0.92 at thermal equilibrium, which corresponds to the static pressure applied by the water droplet. When the water droplet pressure is changed (Figure 5.11f), the equilibrium value of relative resistance is different for different pressure values. To further demonstrate the discrimination of temperature and pressure variations of different types of objects, we performed loading/unloading cycles of water-filled glass vials with various pressure and temperature values on top of an interlocked e-skin (Figure 5.11g). Compared to the first loading/unloading signals in response to 0.54 kPa pressure at 23 °C without thermal gradient with the e-skin, the gradual resistance change is additionally observed at the moments of loading (Figure 5.11i) and unloading (Figure 5.11h) cycles due to the thermal gradient and the subsequent equilibrium processes. Here, the differences between instantaneous and equilibrated resistance values increases with the increase of temperature, demonstrating the detection of temperature variations. When the pressure is simultaneously varied in addition to temperature variation, the pressure variation can be monitored by the difference between equilibrated resistance values (Figure 5.11i), which can be clearly distinguishable from the instantaneous resistance variation due to the temperature change. These results demonstrate that the interlocked e-skins can simultaneously detect and discern temperature and pressure variations as a result of the piezoresistive and pyroelectric properties of the interlocked ferroelectric e-skins.



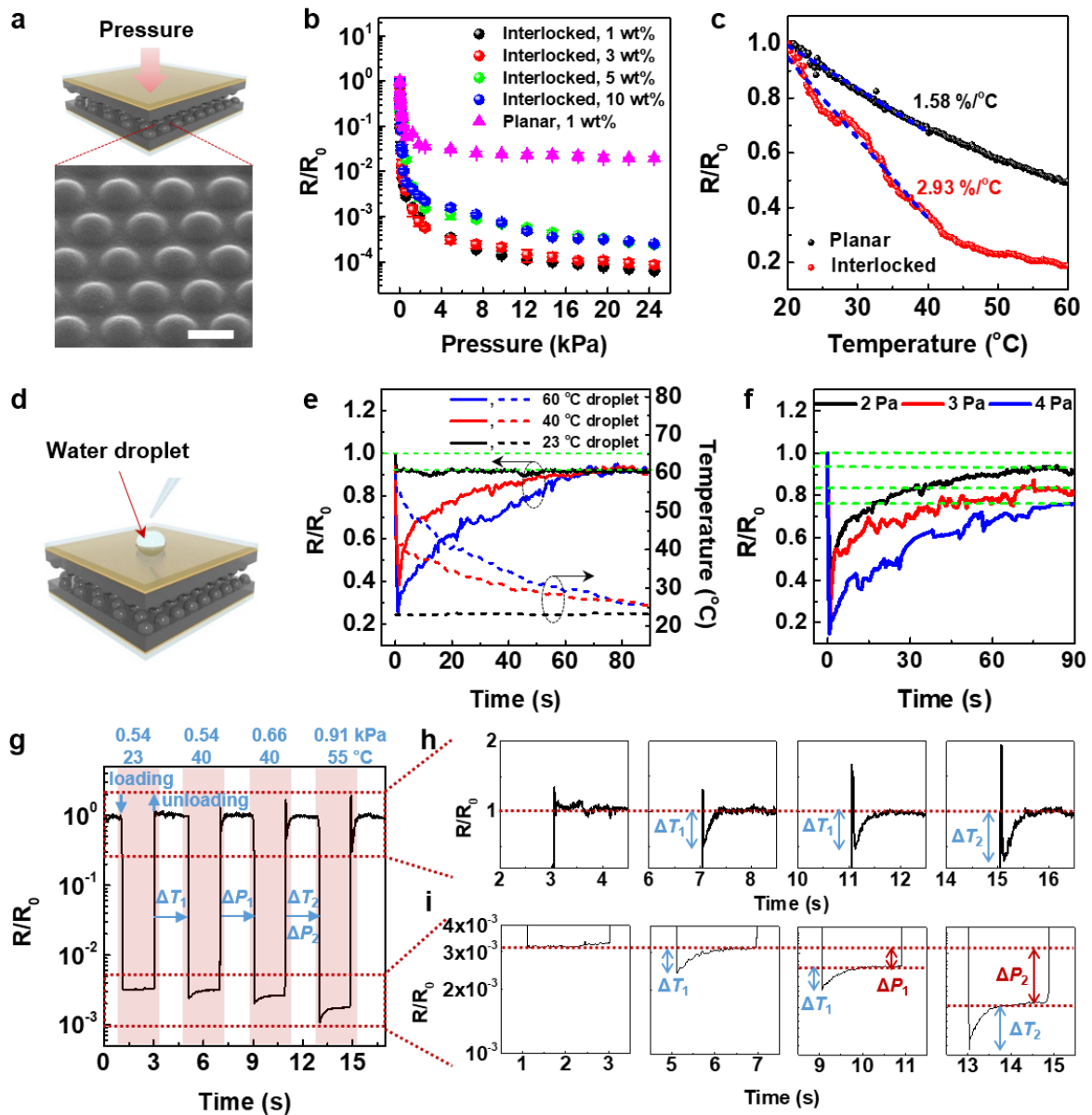


**Figure 5.11.** Piezoresistive e-skin with interlocked microdome arrays for simultaneous detection of static pressure and temperature. (a) Schematic illustration of the e-skin with interlocked microdome array. A tilted SEM image shows the microdome arrays that are 10  $\mu\text{m}$  in diameter, 4  $\mu\text{m}$  in height, and 12  $\mu\text{m}$  in pitch size. Scale bar, 10  $\mu\text{m}$ . (b) Relative resistances of e-skins with interlocked microdome (circle) and single planar (triangle) geometries as a function of applied pressure for different rGO loading concentrations. (c) Relative resistances of e-skins with interlocked microdome (red) and single planar (black) geometries as a function of temperature for 1 wt. % rGO. (d) Schematic illustration of the loading of a water droplet onto the e-skin. (e) and (f) Time-dependent variation of relative resistances and temperature immediately after the loading of the water droplets on the e-skins at (e) different temperatures (droplet pressure: 2 Pa) and (f) different pressures (droplet temperature: 40  $^{\circ}\text{C}$ ). (g) Time-

dependent variation of relative resistances after the loading/unloading cycles of objects with various pressure and temperature values on top of an interlocked e-skin. (h) and (i) Magnified variation of relative resistances at the moment of loading/unloading cycles in (g) showing the detection and discrimination of simultaneous temperature and pressure variations.

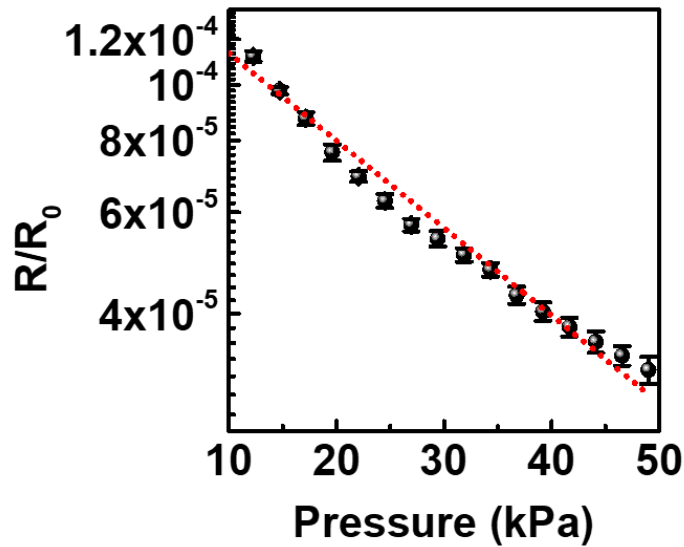


**Figure 5.12.** Relative resistance of e-skin as a function of wide dynamic range of applied pressure from 10 kPa to 49.5 kPa.

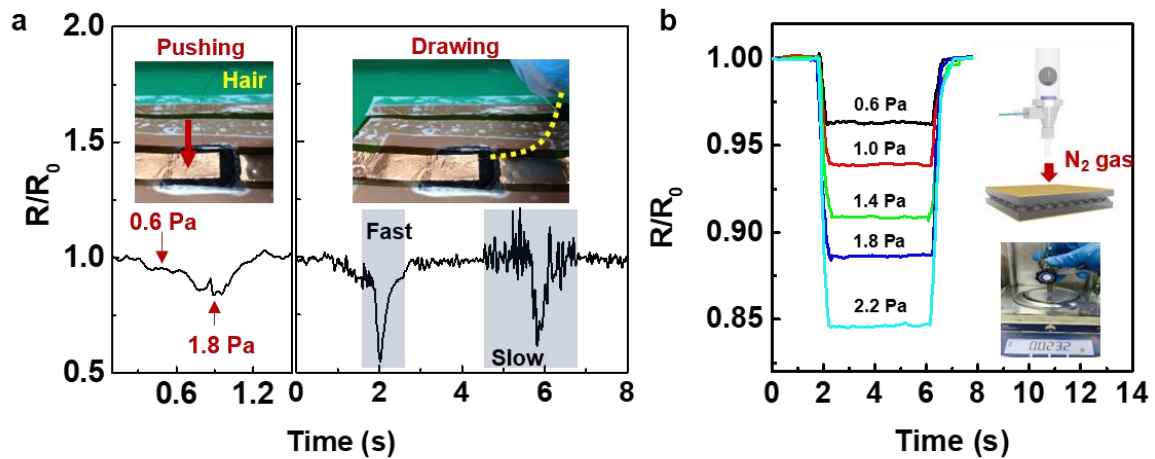


**Figure 5.13.** Minimum pressure detection of ferroelectric e-skins. (a) Electrical resistance changes in response to tiny normal forces generating from static (pushing) or dynamic (drawing) movements of the human hair. The pressure detection level was determined by measuring the hair pushing weight on the e-skin (sample size of 4 cm<sup>2</sup>). (b) Electrical resistance changes in response to weak gas flows with different flow rate from 1.59 to 5.84 m/s. The inset shows a schematic illustration of a setup for the gas flow detection. The photograph shows the weight of gas flow with a flow rate of 1.59 m/s, which corresponds to the pressure of ~0.6 Pa.

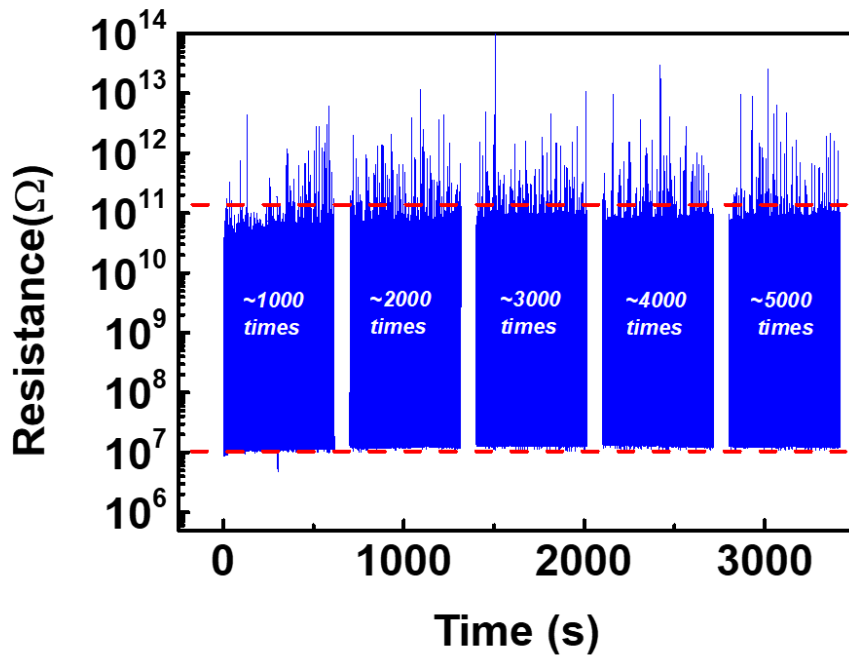


**Figure 5.14.** Stability of the piezoresistive pressure sensor under repetitive application and release of 25.5 kPa of pressure over 5000 cycles.

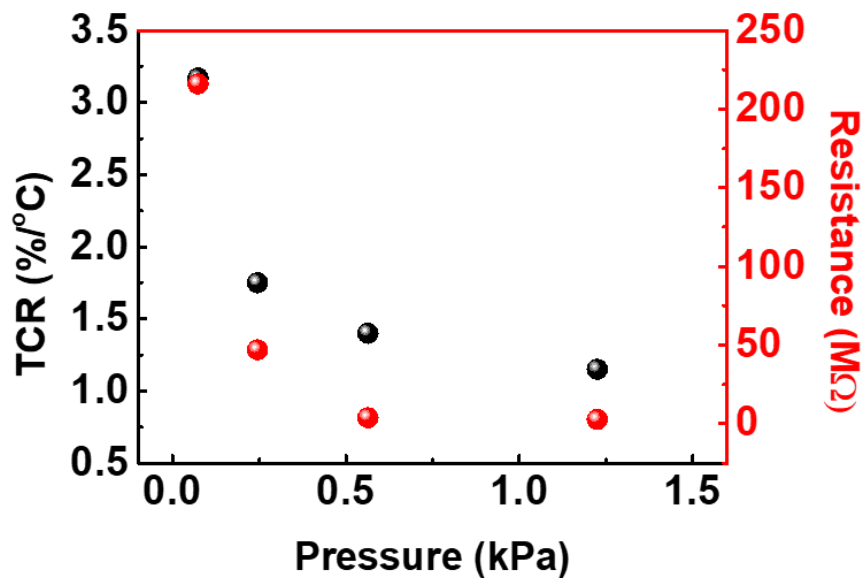


**Figure 5.15.** Changes in the TCR and initial resistance values at different pre-loading weights.

**Simultaneous monitoring of artery pulse pressure and temperature.** The pulse waveform of the radial artery can be used for the real-time and non-invasive diagnosis of cardiovascular problems associated with arteriosclerosis, hypertension, and diabetes.<sup>78</sup> In particular, since the blood pressure is easily influenced by environmental changes, wearable blood pressure monitoring devices are required for the measurement of average daily blood pressure to accurately analyse cardiovascular problems.<sup>207</sup> While capacitive,<sup>18, 208</sup> triboelectric,<sup>209</sup> piezoresistive,<sup>79, 137</sup> and piezoelectric<sup>210</sup> pressure sensors have been introduced as wearable devices for the detection of artery pulse pressure, there have been no reports on the simultaneous detection of artery temperature as well as pressure. Information on the wrist skin temperature during the measurement of artery pulse pressure is critical in the accurate analysis of pulse waveforms because heat and cold stresses affect the vasoconstriction and vasodilation of blood vessels, which results in variation in the arterial stiffness and radial pressure.<sup>211</sup> Our interlocked e-skin enables the simultaneous monitoring of temperature and artery pulse pressure when attached onto the wrist skin (Figure 5.16a). Depending on the skin temperature, the blood vessel undergoes vasodilation or vasoconstriction, which results in a decrease or increase in the pulse pressure, respectively (inset in Figure 5.16a). Figure 5.16b shows the typical piezoresistive read-out of wrist pulse pressure. Three distinguishable peaks ( $P_1$ ,  $P_2$ ,  $P_3$ ) are observed.<sup>179</sup> Here,  $P_1$  (pulse pressure) is due to the blood flow ejected by heart contraction and is the difference between the systolic ( $P_{\text{Sys}}$ ) and diastolic ( $P_{\text{Dia}}$ ) pressures. On the other hand,  $P_2$  and  $P_3$  (reflected wave pressures) are generated by the reflected waves from the peripheral sites (hand for  $P_2$  and lower body for  $P_3$ ).

The shape of the artery pulse wave is variable depending on the arterial stiffness, pulse wave velocity (PWV), and the reflected waves. For individuals with hypertension and for aged persons, the systolic and pulse pressures are augmented, owing to increased arterial stiffness, which causes increased PWV and early return of reflected waves.<sup>179</sup> For the quantitative evaluation of arterial stiffness, the radial artery augmentation index ( $AI_r = P_2/P_1$ ), radial diastolic augmentation ( $DAI = P_3/P_1$ ), and round trip time of reflected wave from the hand periphery ( $T_R$ ) are commonly used.<sup>179, 212</sup> In Figure 5.16c, before physical exercise, the average values (from 5 pulse waves) of  $AI_r$  and  $DAI$  under normal conditions are observed to be 0.45 and 0.31, respectively, which are consistent with the data provided in the literature on healthy 29-year-old males.<sup>179</sup> After physical exercise, the pulse rate increases to 84 beats/min from 72 beats/min under normal conditions and the pulse intensity increases as a result of increased cardiac output to rapidly provide blood to the activated muscles. In addition, owing to vasodilation of the muscular arteries after exercise,  $P_2$  is reduced, resulting in a decrease in the augmentation index ( $AI_r = 0.36$ ,  $DAI = 0.21$ ), indicating decreased arterial stiffness. We also observe that the relative resistance decreases to 0.94, owing to increase in the skin temperature after exercise.

To investigate the skin temperature-dependent variation of pulse pressure of the radial artery, the interlocked e-skin was used to acquire the arterial pulse pressure immediately after immersion of the

hand into a water bath at various temperatures (20–42 °C) for 2 min. With increase in the skin temperature from 20 to 42 °C, the relative resistance of diastolic pressure ( $P_{\text{Dia}}$ ) decreases from 1.40 to 0.65 (Figure 5.16d). In addition, the arterial pulse pressure clearly shows different waveforms depending on the temperature (Figure 5.16e). Here, all the pulse and reflected wave pressures ( $P_1$ ,  $P_2$ , and  $P_3$ ) decrease with increase in the temperature. Detailed analyses of the variations in the pulse waveforms are shown in Figure 5.16f. The relative resistance linearly decreases with increase in the skin temperature, which results in a slope of 3.3 %/°C, which is close to the TCR value (2.93 %/°C) of the interlocked e-skin (Figure 5.11c). This linear relationship between resistance and temperature can be used to directly monitor the skin temperature during the measurement of arterial pulse pressure. With increase in the skin temperature from 20 to 42 °C, the values of  $AI_r$  and  $DAI$  decrease from 0.54 and 0.31 to 0.27 and 0.09, respectively. This phenomenon could be attributed to the cold and heat stress-induced vasoconstriction and vasodilation of blood vessels in the radial artery under normal conditions (skin temperature of 32 °C), which results in an increase (or decrease in the case of heat stress) in arterial stiffness and thus, an increase in the blood pressure, reflection wave, and PWV.<sup>213</sup> In addition,  $T_R$  increases from 142 to 248 ms with increase in the temperature. The increase in the delayed time of the reflective wave with increase in the temperature is attributed to the reduced cardiac output and increased compliance of the blood vessel (arterial stiffness). Compared to traditional arterial tonometry with only pressure sensing functions,<sup>212</sup> the interlocked e-skin, which has both pressure and temperature sensing capabilities, could raise the accuracy of blood pressure monitoring by accounting for the skin temperature.

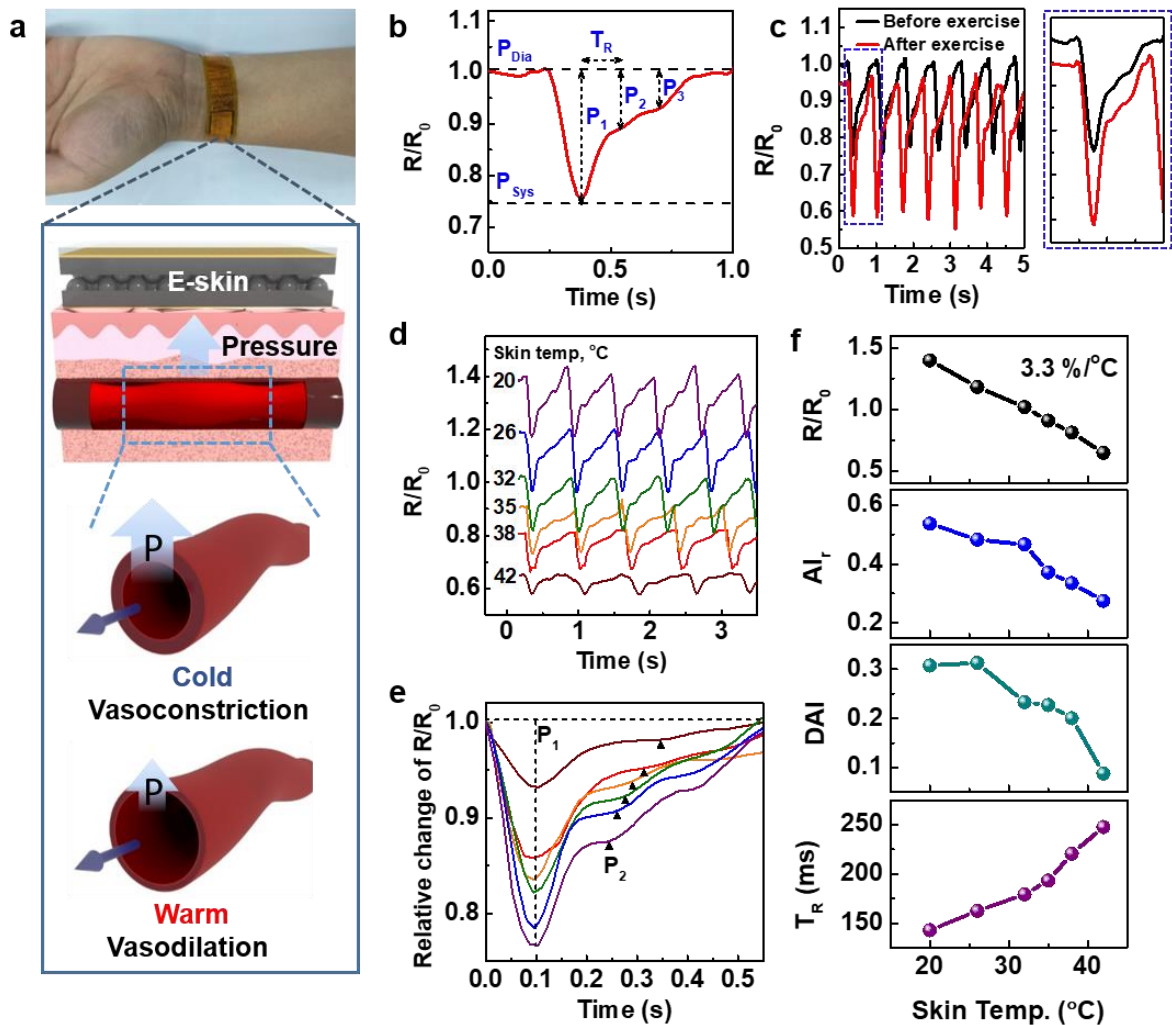


**Figure 5.16.** Piezoresistive e-skin with interlocked microdome array for simultaneous monitoring of artery pulse pressure and temperature. (a) Photograph of a wearable e-skin for the monitoring artery pulse pressure and temperature. The enlarged schematic illustrations indicate the effect of temperature on the constriction (cold) and dilation (warm) of arterial vessels. (b) Relative resistance variations in response to artery pulse pressure. The pulse pressure waveform consists of three peaks corresponding to pulse pressure ( $P_1$ ) and reflected wave pressures from the hand ( $P_2$ ) and lower body ( $P_3$ ).  $P_1$  is the difference between the systolic ( $P_{Sys}$ ) and diastolic ( $P_{Dia}$ ) pressures. (c) Variation of the pulse pressure waveforms before (black) and after (red) physical exercise. (d) Relative resistance change of the artery pulse pressure waveforms as a function of skin temperature (20 - 42 °C). (e) Comparison of the variation of artery pulse pressure waveform at different skin temperatures. The data in (d) is used with the data-offset modification for the comparison. (f) The blood pressure and temperature information acquired from the measurements in (e); variations of relative resistance ( $R/R_0$ ) (black), radial artery augmentation index ( $AI_r = P_2/P_1$ ) (blue), radial diastolic augmentation index (DAI =  $P_3/P_1$ ) (green), and round-trip time for the reflected wave from the hand periphery ( $T_R$ ) (purple) as a function of skin temperature.

**Piezoelectric e-skins for the detection of dynamic touch and acoustic waves.** Our ferroelectric e-skins with interlocked geometry also enable the piezoelectric perception of dynamic tactile stimuli. Compared to planar piezoelectric films, the interlocked e-skin with a larger contact area and stress concentration effects at the small contact spots between the microdomes, can induce a larger deformation and thus a higher piezopotential, resulting in improvements in the piezoelectric performance (Figure 5.17a).<sup>167</sup> For the planar films, the addition of GO into PVDF can enhance the piezoelectricity, but further reduction of GO into rGO decreases the piezoelectricity (Figure 5.17b). We observed that the increase of film conductivity with the increase of rGO reduction time resulted in the decrease of piezoelectric performance (Figure 5.18). This behavior can be attributed to the enhanced screening of piezoelectric polarization with the increase of film conductivity.<sup>214, 215</sup> The piezoelectric current of the interlocked microdome films depends on the applied normal forces with a sensitivity of 35  $\mu\text{A}/\text{Pa}$  below 2.45 kPa and 5  $\mu\text{A}/\text{Pa}$  in the range of 2.45 to 17.15 kPa (Figure 5.17b). The piezoelectric current and voltage gradually increase with increase in the applied impact frequency (0.1 ~ 1.5 Hz) (Figure 5.17c). This behavior can be attributed to the viscoelastic property of PVDF polymers, in which the dynamic modulus increase with the increase of frequency.<sup>216</sup> Because the piezoelectric current and voltage are known to be proportional to elastic modulus of piezoelectric materials,<sup>217</sup> the increase of frequency results in the increase of piezoelectric output. The piezoelectric current is also dependent on the strain rate, which leads to the increase of current with the frequency.<sup>218</sup> In addition, the slow adjustment of the piezoelectric charges to balance the piezoelectric potential can also lead to the frequency dependent piezoelectric output.<sup>218, 219</sup> This frequency-dependent increase in the piezoelectric output could find applications in self-powered systems,<sup>219</sup> accelerometers, and vibrometers.<sup>34</sup> While the piezoelectric e-skins are insensitive to sustained static pressure, the instantaneous generation of piezoelectric current enables the detection of rapid variation in dynamic forces. Figure 5.19 shows piezoelectric and piezoresistive signal variations of the e-skins in response to the applied pressure (8.56 kPa) with different impact frequencies (0.3 – 5.0 Hz). While both the piezoelectric and piezoresistive responses follow dynamic pressure loadings for frequencies below 3.3 Hz, for frequencies over 5 Hz, only the piezoelectric signals properly respond to the dynamic pressure loadings.

The instantaneous deformation and relaxation of interlocked microdome arrays and the subsequent changes in the piezoelectric currents enable the detection of sound waves consisting of high frequency vibrations. To demonstrate the sound detection capabilities, sound waveforms from a speaker were monitored by the interlocked e-skins (Figure 5.17d). The piezoelectric voltage of the interlocked e-skin increases with increase in the sound frequency, reaches a maximum value at 2000 Hz, and then gradually decreases (Figure 5.17e). On the other hand, planar e-skins do not exhibit any noticeable changes in the piezoelectric voltage. Figure 5.17f shows the piezoelectric voltage waveforms observed



in response to the sounds of various alphabets such as S, K, I, and N from a speaker. While the time-dependent variation of the voltage waveforms of the interlocked e-skins precisely match the acoustic waveforms from the speaker, the planar e-skins are unable to monitor the time-dependent variation of the acoustic waveforms. To demonstrate the monitoring of a full sentence of acoustic waveforms, the well-known speech titled “There’s plenty of room at the bottom” by Richard Feynman was played to the interlocked e-skins over a commercial microphone (Figure 5.17g). The time-dependent position and intensity of the piezoelectric voltage waveforms and the corresponding spectrograms agree well with the acoustic waveforms and spectrograms of the acoustic sound of the sentence. A commercial microphone, on the other hand, cannot exactly monitor the time-dependent variation of acoustic waveforms and spectrograms of the sentence.

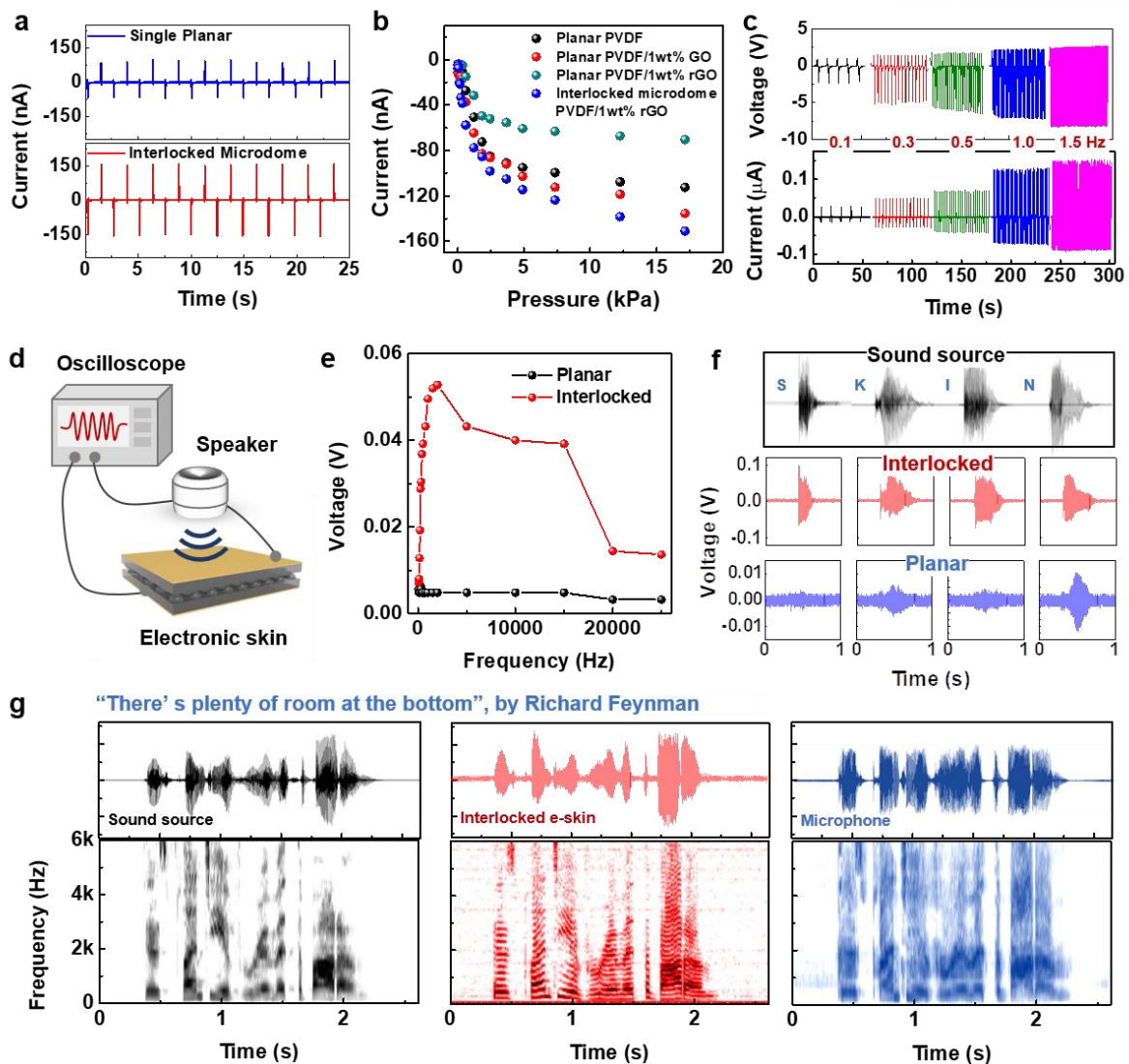


**Figure 5.17.** Piezoelectric e-skin with interlocked microdome array for dynamic touch and acoustic sound detection. (a) Piezoelectric output currents of e-skins with (upper) interlocked microdome array and (bottom) single planar geometries. (b) Piezoelectric pressure sensitivities of the e-skins fabricated with different materials and device structures. (Frequency of loading pressure: 0.5 Hz) (c) Piezoelectric output voltage and current under repetitive impact pressure loadings at different frequencies (0.1-1.5 Hz) for the static normal loading force of 8.56 kPa at a fixed pushing distance of pushing tester. The measurements (d) Schematic illustration of the sound detection tests using the piezoelectric e-skins at the sound intensity of 96.5 dB. The sensor distance from the speaker is 2 cm. (e) Variation of the piezoelectric voltage in response to acoustic waves of different frequencies. (f) The waveforms of acoustic sound for different alphabets ('s', 'k', 'i', and 'n') (black). The read-out voltage signals from the interlocked microdome (red), and planar e-skins (blue). (g) The waveform and short-time Fourier transform (STFT) signals of the original sound ('There's plenty of room at the bottom', black) extracted by the sound wave analyser, read-out signals from the interlocked e-skin (red), and microphone (blue).

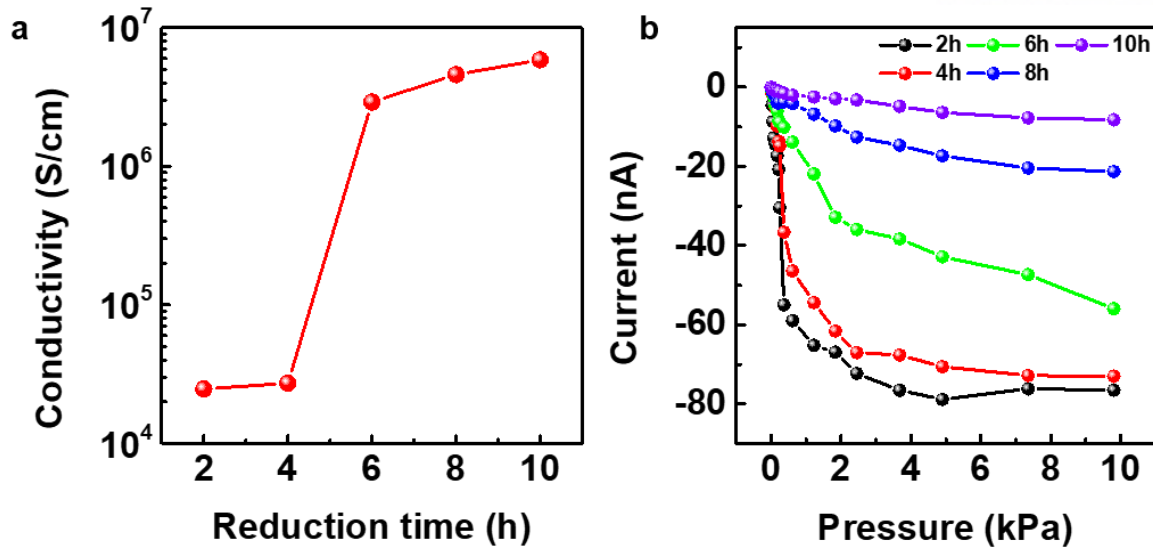


**Figure 5.18.** Effect of conductivity on piezoelectric outputs. (a) Film conductivity as a function of reduction time. (b) Piezoelectric output currents of e-skins with single planar geometry as a function of applied pressure for different film reduction times.

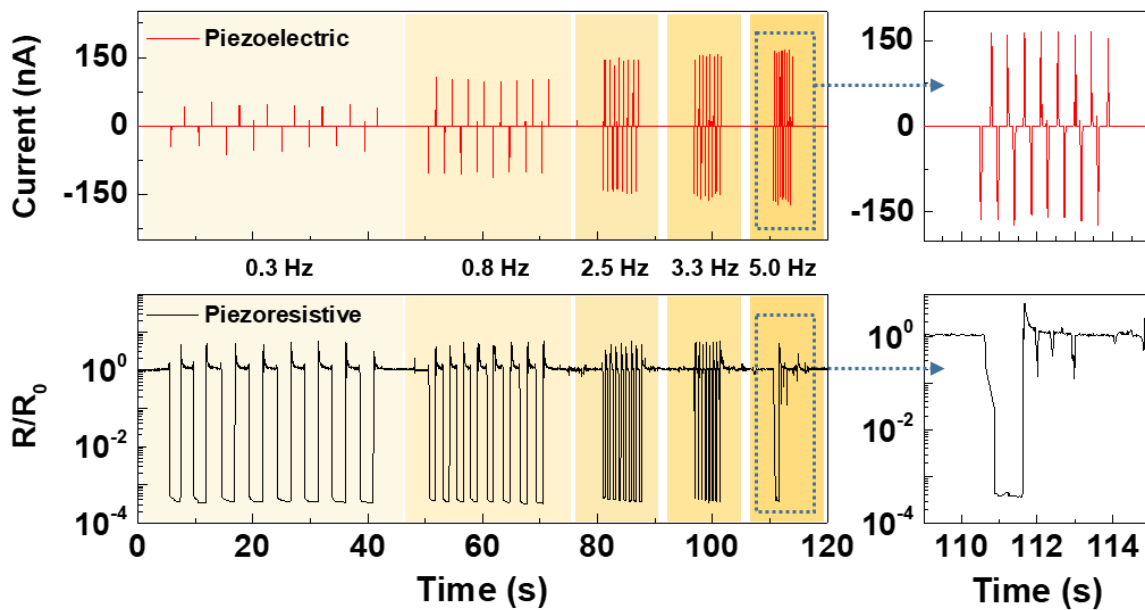


**Figure 5.19.** Comparison of the piezoelectric and piezoresistive signal variations of e-skins in response to applied pressure with different frequencies (0.3 – 5.0 Hz). Applied pressure: 8.56 kPa.

**Piezoelectric e-skins with fingerprint-like patterns for texture perception.** The rapidly adaptive piezoelectric e-skins enable the spatial and temporal encoding of tactile signals, which facilitate the perception of surface textures. For this purpose, e-skins were attached to a microstage (Figure 5.20a, middle) and scanned over a surface texture (Figure 5.20a, bottom) at different scanning speeds. In particular, mimicking the fingerprint patterns on human hands, we employed parallel ridges (pitch: 470  $\mu\text{m}$ , ridge width: 163  $\mu\text{m}$ ) on the surface of the e-skins (Figure 5.20a, top) for the amplification of texture-induced vibrations.<sup>220</sup> Figure 5.20b displays the time-dependent variation of piezoelectric currents when the interlocked e-skin is scanned over a surface texture with parallel line patterns at different scanning speeds (0.25-2.5 mm/s). In addition to the oscillatory piezoelectric currents, periodic spikes (red arrows) in current are observed, owing to the regular topological features on the scanned surface.<sup>74</sup> The intervals between the regular spike peaks decrease with increase in the scanning speed. Fast Fourier transform (FFT) spectra of these piezoelectric current signals indicate that there are fundamental frequencies (arrows) associated with each scanning speed and harmonics with decreasing amplitudes (Figure 5.20c).<sup>221</sup> The fundamental frequency agrees well with the spatial frequency ( $f = v/\lambda$ ) of the line patterns (grating period of 500  $\mu\text{m}$ ), which is determined by the scanning speed ( $v$ ) and the grating period ( $\lambda$ ).<sup>221</sup>

Short-time Fourier transform (STFT) of the current signals further describe the time-dependent variation of the piezoelectric currents (Figure 5.20d). Scanning on the regular surface patterns induce periodic line patterns with respect to time in the frequency range below 30 Hz, the number of which increases with increase in the scanning speed in the same time domain. At frequencies over 100 Hz, a specific frequency is observed for the entire time domain, which can be attributed to the vibrotactile signals induced by the small features on the surface (Figure 5.21). The frequency position increases with increase in the scanning speed. It is worth noting that both the fingerprint-like patterns and interlocked structures are critical in enhancing the perception of surface textures. The regular spike peaks in the piezoelectric currents and the corresponding periodic lines in STFT cannot be observed for the interlocked e-skins without the fingerprint-like patterns (Figure 5.22). While we observe periodic current peaks for the planar e-skins with fingerprint-like patterns, the intensities of the peaks in this case are lower than those for the interlocked geometry. For planar e-skins without fingerprint-like patterns, we do not observe any unique features in the surface texture-dependent frequency variation. When the modulus of regular surface patterns are varied, our e-skins can also discriminate the variation of surface hardness/softness (Figure 5.23). The visibility of periodic line patterns in STFT spectrum attenuates with the decrease of modulus. The interlocked e-skins with fingerprint-like patterns can also detect various surfaces with different roughnesses (Figure 5.20e). Continuous scanning on sandpaper, paper, and glass surfaces results in different STFT features, with the rougher surface (sand paper) exhibiting features with high amplitudes covering all frequencies below 30 Hz and the smoother surface (glass)

not exhibiting any noticeable frequency features. The texture perception capability of the e-skins also enables the perception of different surfaces on our hands (Figure 5.24a). The e-skins can even perceive different surfaces on the hair, facial skin, and whisker regions of our head (Figure 5.24b).

In the tactile perception of human skin, the principal mechanoreceptor involved in the recognition of the surface texture changes depending on the element size of the texture. Slow adapting mechanoreceptors (Merkel Disk) perceive coarse roughness with element size above 100  $\mu\text{m}$ , whereas fast adapting mechanoreceptors (Pacinian Corpuscle) change under fine roughness with element size below 100  $\mu\text{m}$ .<sup>222</sup> To investigate the perception of fine textures, e-skins are scanned (scanning speed of 2.5 mm/s) over silicon substrates with different surface patterns and sizes (line: pitch size (P) = 80  $\mu\text{m}$ , width (W): 10  $\mu\text{m}$ ; square: P = 80  $\mu\text{m}$ , W = 20  $\mu\text{m}$ ; pentagon: P = 90  $\mu\text{m}$ , W = 20  $\mu\text{m}$ ) (Figure 5.20f). Scanning across silicon line patterns in the perpendicular direction (Figure 5.20f, ii) induces periodic output current waves (Figure 5.20f, middle) and exclusive frequency bands near 30 Hz in the STFT spectrogram (Figure 5.20f, bottom), which are clearly recognizable when compared to the smooth silicon surface (Figure 5.20f, i). The 30 Hz frequency band observed at a scanning speed of 2.5 mm/s corresponds to a pitch of 83  $\mu\text{m}$ , which is close to the inter-ridge distance of 80  $\mu\text{m}$ . Scanning over the silicon line pattern in the parallel direction (Figure 5.20f, iii), on the other hand, does not result in a prominent frequency band near 30 Hz. The square pattern (Figure 5.20f, iv) generates frequency bands near 30 Hz, which are similar to the bands observed by perpendicular scanning on the line pattern. On the other hand, scanning on the pentagon pattern (Figure 5.20f, v) without any continuous inter-pattern gaps does not result in any noticeable frequency band near 30 Hz. We also observe a weak frequency band near 10 Hz for all the surfaces, which can be attributed to the stick-slip motions between the PDMS and silicon substrates.<sup>223</sup> This stick-slip frequency near 10 Hz cannot be observed when the scanning speed is increased to 5 mm/s (Figure 5.25). These results indicate that the perception of fine and regular texture is only possible when continuous inter-pattern gaps exist in the scanning direction.

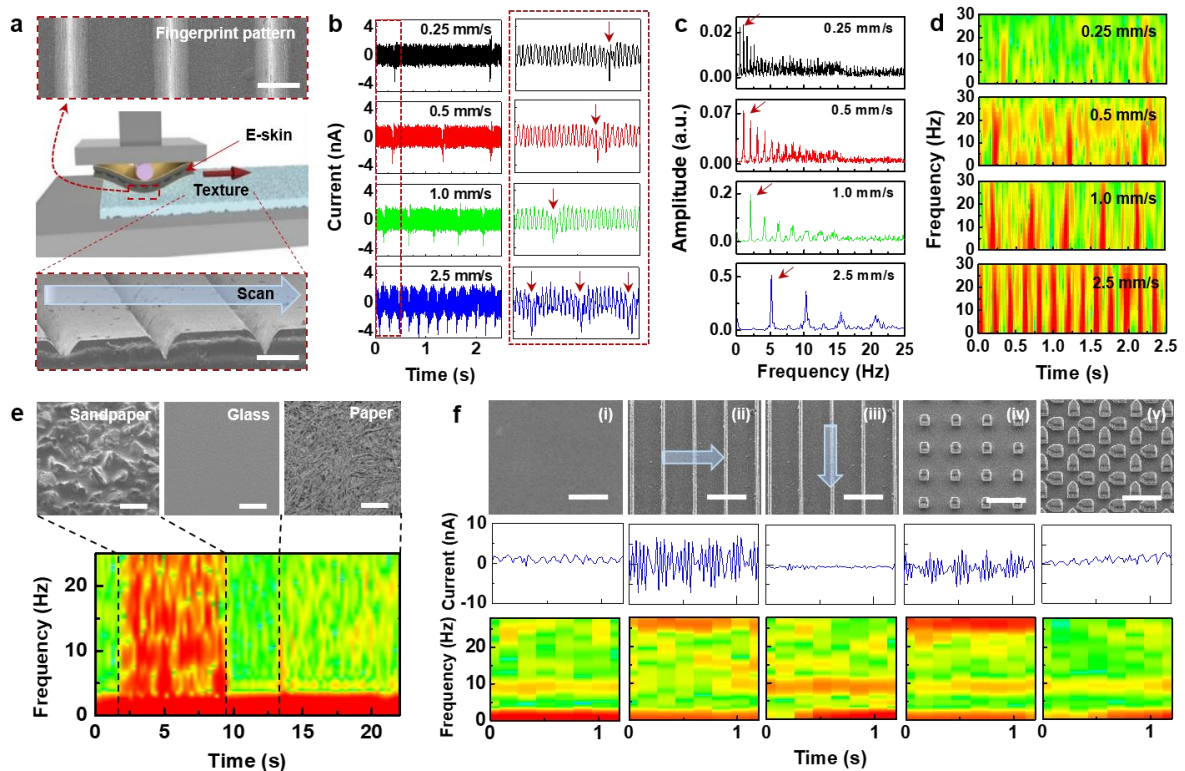


**Figure 5.20.** Piezoelectric e-skin with fingerprint-like patterns for texture perception. (a) Schematic illustration of the texture perception measurements, for which the e-skin is attached to a microstage and scanned over a surface. (top) SEM image of the fingerprint-inspired PDMS pattern. (bottom) SEM image of the PDMS substrate with periodic line-patterns (P: 470  $\mu\text{m}$ , W: 163  $\mu\text{m}$ ). Scale bar, 200  $\mu\text{m}$ . (b) Time-dependent variation of piezoelectric currents when the e-skin is scanned over the patterned surface at different scanning speeds (0.25-2.5 mm/s). (c) FFT spectra of time-dependent piezoelectric current signals in (b). (d) STFT spectrograms of the piezoelectric current signals in (b) for the low frequency range (0-30 Hz). (e) Perception of texture with different roughness. (top) SEM images of the sandpaper, paper, and glass surfaces. (bottom) STFT spectra of the corresponding output currents when the e-skin is scanned at 2.5 mm/s. Scale bar, 200  $\mu\text{m}$ . (f) Perception of fine textures (< 100  $\mu\text{m}$ ). (top) SEM images, (middle) output current signals, and (bottom) STFT spectra of different silicon substrates with (i) planar, (ii) and (iii) line pattern (P: 80  $\mu\text{m}$ , D: 10  $\mu\text{m}$ ), (iv) square pattern (P: 80  $\mu\text{m}$ , D: 20  $\mu\text{m}$ ), and (v) pentagon pattern (P: 90  $\mu\text{m}$ , D: 20  $\mu\text{m}$ ). The arrow indicates the scanning direction. Scale bar, 100  $\mu\text{m}$ .

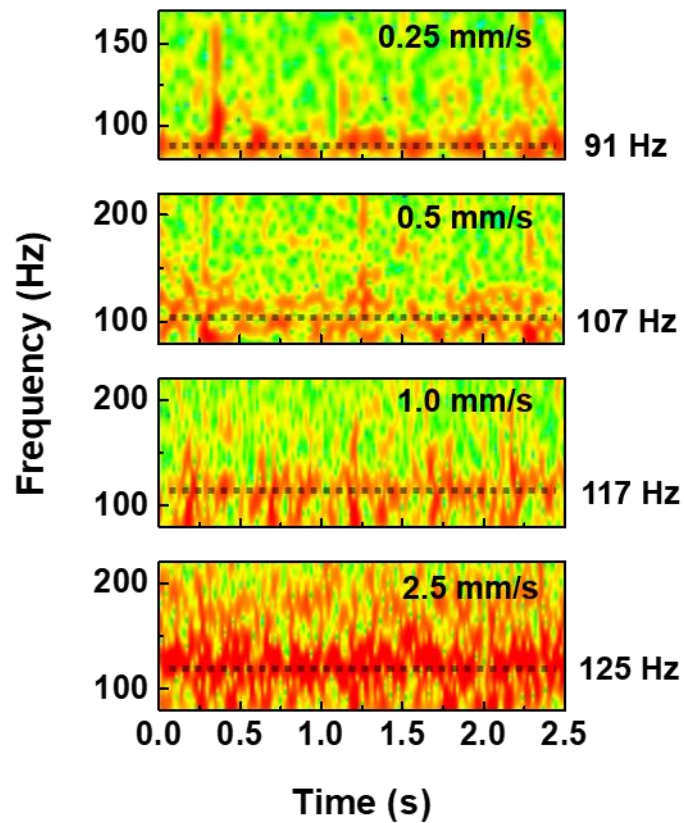


**Figure 5.21.** STFT spectrograms of the piezoelectric current signals for the high frequency range (>80 Hz) obtained by scanning on polydimethylsiloxane (PDMS) films with periodic line patterns as a function of scanning speed.

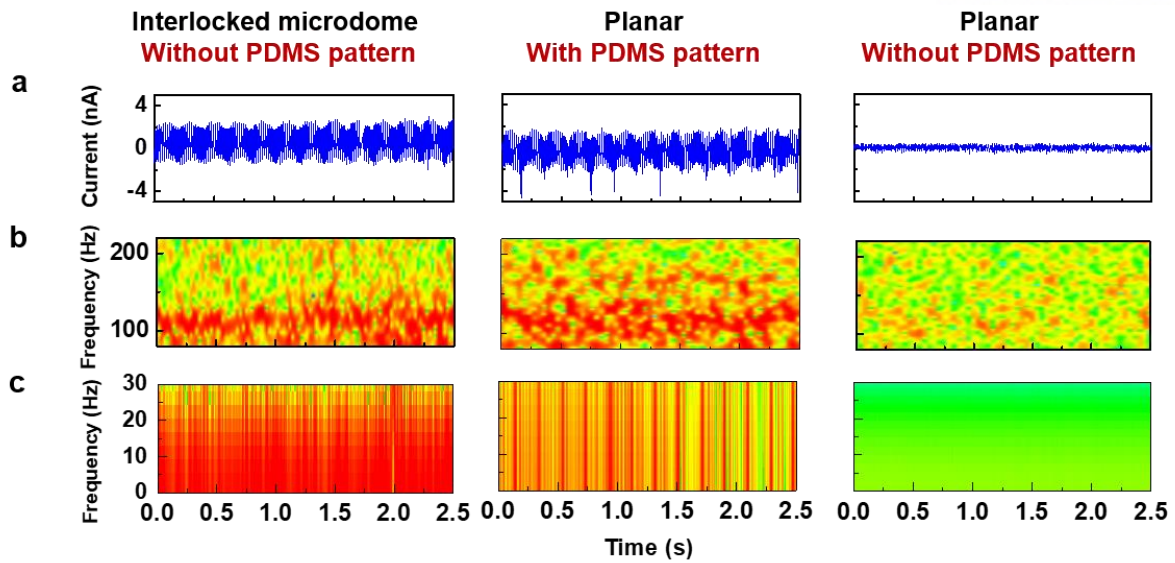


**Figure 5.22.** Effect of e-skin structure and fingerprint patterns for texture perception. (a) Output electrical current, (b) High frequency components of the STFT spectra, and (c) Low frequency components of the STFT spectra obtained from the surface scanning results for various structure and fingerprint patterns.

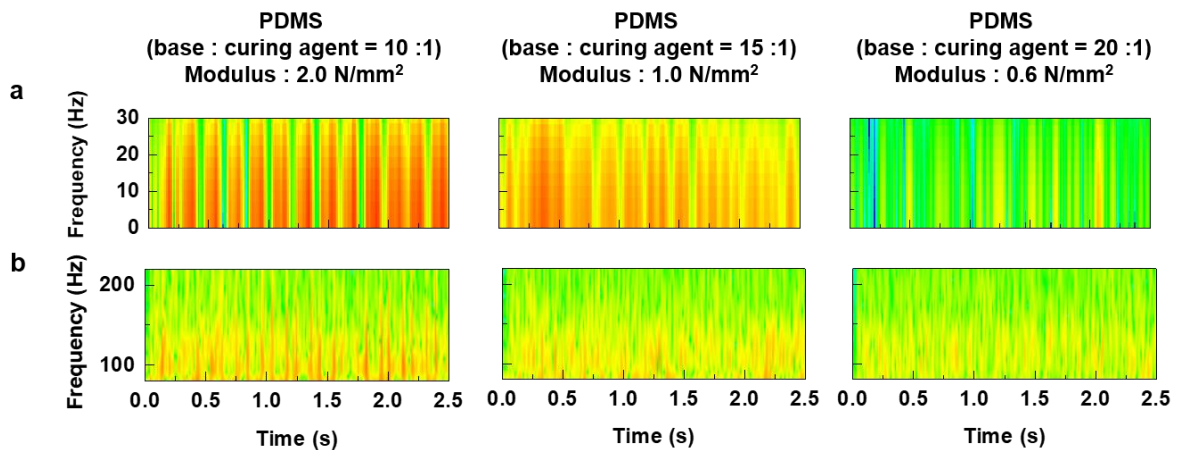


**Figure 5.23.** Perception of hardness/softness of surface. (a) High frequency components of the STFT spectra, and (b) Low frequency components for the STFT spectra resulting from scanning over parallel line patterned-PDMS surfaces with different elastic modulus.



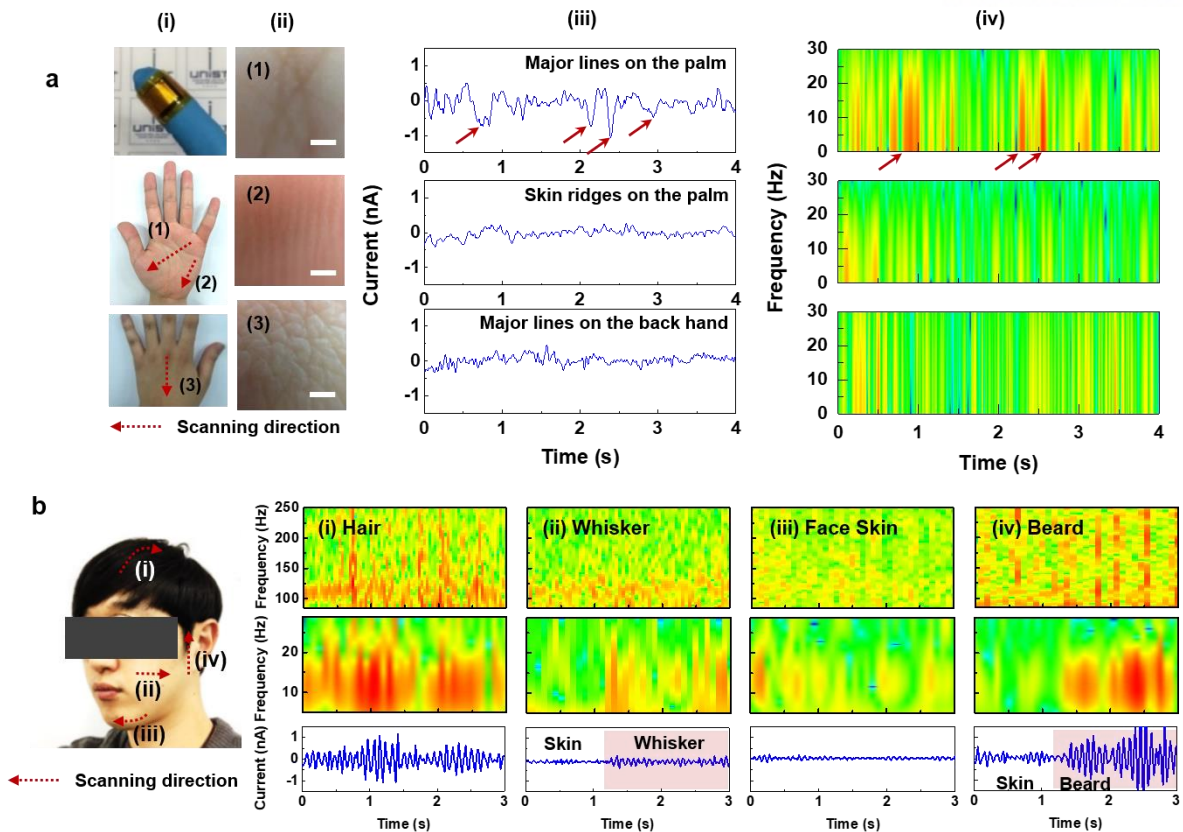


**Figure 5.24.** Wearable e-skins for texture perception. (a) The texture perception capability of different surfaces on our hand. (i) Photographs of flexible and wearable e-skins wrapped onto the human finger and the palm and the back of the human hand with indications of the different scanning directions. (ii) Magnified photographs of the fingerprints on the different sites of human hand skin; (1) centre of palm, (2) side of palm, and (3) back of hand. Scale bar, 500  $\mu\text{m}$ . (iii) Output electrical currents, and (iv) Low frequency components of the STFT spectra obtained by scanning of textural surfaces in different scanning directions. The red arrows in the output electrical currents and STFT spectra indicate the texture signals from major lines on the palm. On the side of palm and back of hand, the strong texture signals are not observed. Instead, random lines with weaker intensities are observed in the STFT spectra due to the skin ridges on the palm and lines on the back hand. (b) Texture perception capability of different surfaces on the hair, facial skin, beard, and whisker regions of the human head. The high intensity red lines in the low frequency STFT spectra are observed when the scanning areas are on top of rough textures.

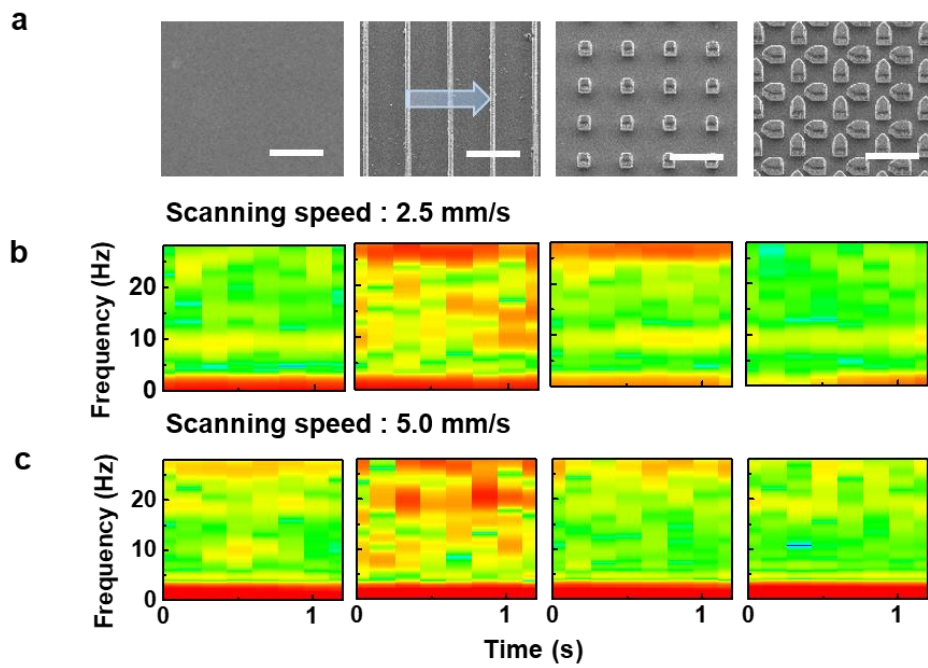


**Figure 5.25.** Perception of fine textures for the low frequency range (< 30 Hz) obtained by scanning on polydimethylsiloxane (PDMS) films with periodic line patterns as a function of scanning speed. (a) SEM images of fine textures, Scale bar, 100 μm. (b) scanning speed of 2.5 mm/s. (c) scanning speed of 5.0 mm/s.

## 5.4 Conclusions

In conclusion, we have demonstrated the functionality of human-skin-inspired multimodal e-skins that enable spatio-temporal recognition of static/dynamic tactile stimuli (pressure, temperature, vibration). The design of our e-skin involves the fabrication of microstructures of ferroelectric rGO/PVDF composite films with interlocked microdome arrays and fingerprint-like microridges on the surface of the films, which enhance the piezoelectric, pyroelectric, and piezoresistive sensing capabilities of the ferroelectric composite films for static and dynamic tactile and thermal signals. Compared to planar ferroelectric films, we have shown that the geometry of the interlocked microdome arrays significantly enhances the tactile sensitivities, enabling the detection of minute variations in temperature, pressure, and acoustic vibration. Furthermore, the employment of fingerprint-like microridges on top of the interlocked e-skins has been shown to significantly enhance the vibrotactile signals when the e-skins are scanned over a textured surface, enabling the perception of surface textures with various roughness and pattern shapes. For proof-of-concept demonstrations, we showed the temperature-dependent pressure monitoring of artery vessels, high-precision acoustic sound detection, and surface texture recognition of various surfaces. All of these capabilities provide a solid platform for the application of the e-skins fabricated in this study in humanoid robotics, flexible sensors, and wearable medical diagnostic systems.

1.

## **Chapter 6. Multilayered ferroelectric electronic skins with ultrahigh pressure sensitivity and linear response over exceptionally broad pressure range**

### **6.1 Introduction**

Rapid advances in physical/chemical sensors, wireless communication, and energy storage systems are driving the interest in wearable electronic devices, such as smartwatches, smartbands, and smartglasses, which enable the monitoring and diagnosis of the personal health status in real-time.<sup>161</sup> Flexible electronic skins (e-skins), which mimic perceptive functions of human skin, have attracted strong research interest as essential components of potential applications in robotics, prostheses, and wearable healthcare monitoring devices. High sensitivity, fast response time, mechanical flexibility, and durability are major requirements for e-skins used for these practical applications and various approaches focused on the improvement of these attributes.<sup>18, 24, 79, 88</sup> Another significant requirement for e-skins with human skin-like tactile sensing properties is the discrimination of spatiotemporal tactile stimuli, including static and dynamic pressure, which allows dexterous manipulation of objects and the perception of vibration and surface textures.<sup>43, 224</sup> In addition, to use e-skins for various applications as a single device, they should have a large dynamic sensing range and linear pressure-sensing capability to constantly maintain their high sensitivity, even in the high-pressure region.<sup>162, 225</sup> E-skins with a high sensitivity over a broad sensing range can perceive, for example, subtle pressure of light breeze and respiration (<1 kPa), medium pressure of pulse pressure and gentle touch (1–10 kPa), and large pressure of plantar foot pressure (>10 kPa). Furthermore, e-skins with linear sensing ability over a large dynamic range do not require additional complex signal processing, which meets the increasing demand for device miniaturization and low power consumption. Although several approaches have been adopted to improve some of the aforementioned requirements of e-skins, the combination of all of these properties in a single e-skin remains a challenge.<sup>6, 47, 162</sup>

As an ideal sensory system, human skin can perceive and differentiate various tactile sensation under different mechanical stimuli.<sup>191</sup> In particular, various sensory receptors are embedded in the human skin, which transduce information from applied stimuli, such as magnitude, distribution, and frequency, into tactile sensation.<sup>121</sup> In addition, the special intermediate ridge structure between dermal and epidermal layers efficiently transmits tactile signals from the skin surface to sensory receptors located in interlocked ridge structures due to the effective stress concentration between dermal and epidermal layers with different moduli.<sup>52, 86, 226</sup> To mimic tactile sensing functions and structures of human skin, various types of e-skins based on different signal transduction modes, including piezoresistivity, capacitance, piezoelectricity, and triboelectricity, have been developed.<sup>11, 34, 72, 90, 92, 93, 137</sup> In particular,

various types of microstructures (e.g., micropyramid, microdome, and micropillar) have attracted much attention with respect to the improvement of sensing characteristics of e-skins such as sensitivity, response time, sensing range, and durability.<sup>161</sup> Recently, Pan et al.<sup>24</sup> demonstrated hollow sphere microstructure-based pressure sensors with a high sensitivity of  $133 \text{ kPa}^{-1}$  and Su et al.<sup>175</sup> designed an irregular microstructure for a mimosa-inspired pressure sensor with a high sensitivity of  $50.17 \text{ kPa}^{-1}$ . However, the high sensitivity is only valid in subtle pressure regions ( $<100 \text{ Pa}$ ) and they can only detect static pressure using the piezoresistive sensing of e-skins. To differentiate spatiotemporal tactile stimuli, interlocked microdome-based e-skins have been suggested.<sup>43</sup> This work showed highly sensitive and multifunctional tactile sensing performance with various transduction modes, but the dynamic pressure-sensing range was still under  $50 \text{ kPa}$  and a linear sensing capability could not be achieved. Therefore, a significant challenge remains in the development of e-skins with new device designs to realize a large dynamic pressure range and linear tactile sensing performances.

In this chapter, we demonstrate a flexible ferroelectric sensor with ultrahigh pressure sensitivity and linear response over an exceptionally broad pressure range based on the ferroelectric composites with a multilayer interlocked microdome geometry. Due to the conductive and ferroelectric nature of polymer composites comprising poly(vinylidene fluoride) (PVDF) and reduced graphene oxide (rGO), our e-skins can perceive and differentiate static and dynamic pressures using piezoresistive and piezoelectric modes. Each layer of e-skins comprises interlocked microdome arrays inspired by interlocked ridge structures between the dermal–epidermal layers, and three interlocked layers are stacked for the fabrication of multilayer e-skins. While previous pressure sensors exhibit nonlinear or narrow range linear sensing, our e-skins can maintain their high sensitivity and linear response over a broad pressure range due to the increased contact area change and efficient stress distribution between stacked layers compared with single-layered e-skins (Figure 6.1a). The multilayer e-skins can constantly maintain an ultrahigh sensitivity of  $47.7 \text{ kPa}^{-1}$  over an exceptionally broad pressure range of  $0.0013 - 353 \text{ kPa}$ . Furthermore, our sensor displayed a fast response time ( $20 \text{ ms}$ ) and high reliability over  $5,000$  repetitive cycles even at extremely high pressure of  $272 \text{ kPa}$ . For proof of concept, our e-skins were used for the monitoring of diverse stimuli from low to high pressure range (Figure 6.1b). For example, our e-skins were used for precise detection of weak gas flow and acoustic sound in a low pressure regime and for monitoring respiration and pulse pressure in a medium pressure regime. In addition, the large dynamic range pressure-sensing capability of e-skins was employed for plantar pressure monitoring in a high pressure regime.

## 6.2 Experimental Details

**Preparation of ferroelectric and conductive composite films:** GO was prepared based on a modified Hummers method.<sup>227, 228</sup> Briefly, graphite powder (SP-1, Bay Carbon),  $K_2S_2O_8$  (Sigma Aldrich), and  $P_2O_5$  (Sigma Aldrich) were dispersed in concentrated  $H_2SO_4$  solution (Sigma Aldrich). The mixture was stirred at 80 °C for 4.5 hours. This solution was then diluted with deionized (DI) water, followed by filtration and DI washing to achieve a neutral pH. The resulting filtrate was dried under 30 °C vacuum conditions overnight. The preoxidized graphite was dispersed in concentrated  $H_2SO_4$ . Subsequently,  $KMnO_4$  (Sigma Aldrich) was slowly added to the solution under vigorous stirring, followed by stirring at 36 °C for 2 hours. The mixture was gradually diluted with DI water, followed by stirring at 36 °C for 2 hours. Subsequently, 30%  $H_2O_2$  (Sigma Aldrich) was added to this mixture, which resulted in a color change to bright yellow with violent bubbling. This mixture was then stirred for 1 hour and centrifuged several times in 10% HCl to remove residual salts. The resulting mixture was subjected to dialysis to adjust the acidity. Finally, the solution was concentrated by drying under 30 °C vacuum conditions and dispersed in dimethylformamide (DMF) solvent by sonication to obtain GO–DMF solution. Prior to blending graphene and PVDF (Sigma Aldrich; molecular weight  $\approx 534,000$ ), PVDF was first dispersed in DMF solvent and the dispersed PVDF–DMF solution (20 wt%) was mixed with GO–DMF solution (10 mg/mL) in the desired mixing ratio. The prepared GO/PVDF was poured on the glass substrate for planar composite films and a microdome-patterned mold (diameter  $\approx 10 \mu m$ ; pitch  $\approx 12 \mu m$ ; height  $\approx 4 \mu m$ ) for microdome composite films. The casted solution was first dried on a heating plate at 50 °C for 12 hours and then annealed in a vacuum oven at 160 °C for 2 hours to reduce GO to rGO and remove residual DMF solvent.

**Multilayer e-skin fabrication:** For the interlocked microdome structure, two microdome-patterned rGO/PVDF composite films with patterned sides face each other. The multilayer structure was fabricated by stacking several layers of interlocked microdome structures with adhesive layers, which had a similar thickness with a single rGO/PVDF composite film. Finally, two copper electrodes were attached to the top and bottom side of the multilayer interlocked microdome composite films using silver paste. To fabricate  $3 \times 3$  and  $4 \times 8$  pixel arrays, the PET supporting layers were coated with a platinum electrode with a mask using sputter coating system (Hitachi, E-1045) and multilayer interlocked microdome rGO/PVDF composite films were sandwiched by patterned electrodes.

*Characterization:* The microstructures and interlocked geometry of rGO/PVDF composites were analyzed by field-emission SEM (S-4800, Hitachi). To check ferroelectric properties, the crystal structures of pure PVDF and PVDF of composite films were measured by XRD spectroscopy (Bruker AXS, D8 ADVANCE) with  $CuK\alpha$  radiation. The pressure-responsive electric properties of e-skins were measured using a semiconductor parameter analyzer (4200-SCS, Keithley) for piezoresistive signals and a sourcemeter (S-2400, Keithley) and oscilloscope (DPO 2022B, Tektronix) for piezoelectric

signals. The static/dynamic normal pressure was applied to e-skins with the pushing tester (JIPT, JUNIL TECH) at different frequencies. For the application of multilayer e-skins, the  $3 \times 3$  and  $4 \times 8$  pixel arrays were measured with a multichannel biosensor test system (OT15-3010D, ONTEST).

**Finite element calculation:** The structural analysis of the interlocked microdome multilayers (single, double, and triple layer) was performed by finite element simulations (ABAQUS software). The contact area and stress between different numbers of interlocked layers were numerically calculated as a function of the applied pressure. All the simulated top and bottom layers comprised rGO/PVDF composite films with interlocked microdome structures ( $10 \mu\text{m}$  in diameter and  $12 \mu\text{m}$  in pitch) and PET-based adhesive layers. The occupied areal ratio of adhesive layer, partly located at the edges of film, is  $\sim 14\%$  in simulated condition, which is almost equal with the experimental values ( $\sim 12\%$ ). The elastic modulus of the rGO/PVDF and PET materials was  $2.5 \text{ GPa}$  and  $1.0 \text{ GPa}$ , respectively, which is consistent with experimental values. We implemented general surface-to-surface contact interaction with linear elastic deformable materials to consider the mechanical contact interaction between the stacked multilayers under the applied pressure.

### 6.3 Results and Discussion

A schematic of interlocked microdome multilayer e-skins for highly sensitive, linear, and large dynamic range pressure sensors is shown in Figure 6.1c. To fabricate conductive and ferroelectric rGO/PVDF composite films, mixtures of graphene oxide (GO) sheets with a PVDF matrix in dimethylformamide (DMF) were cast onto a microdome patterned mold and dried at 50 °C for 12 hours. Subsequently, GO/PVDF films were annealed at 160 °C for 2 hours to completely remove residual DMF and reduce GO to rGO. Figure 6.1d shows the cross-sectional scanning electron microscopy (SEM) image of an rGO/PVDF composite film with interlocked microdome multilayer structures. Figure 6.1e shows a layer with interlocked microdome structures, where the microdome is 10 μm in diameter, 4 μm in height, and 12 μm in pitch size (Figure 6.1f). To check the ferroelectric properties of rGO/PVDF composite films, we performed X-ray diffraction (XRD) spectroscopy analysis on pure PVDF films, GO/PVDF, and rGO/PVDF composite films (Figure 6.2a). Pure PVDF film shows  $2\theta$  diffraction peaks at 18.0 °, 18.7 °, 20.2 °, and 26.9 ° which correspond to the (100), (020), (110), and (021) reflection planes of the nonpolar  $\alpha$ -phase of PVDF.<sup>229</sup> In contrast, PVDF of GO/PVDF composite films has a strong polar  $\beta$ -phase based on the  $2\theta$  diffraction peak at 20.7 ° and a weak  $\gamma$ -phase based on the  $2\theta$  diffraction peaks at 19.0 ° and 20.4 °.<sup>229</sup> The polar  $\beta$ -phase crystal structure can be maintained even after the reduction of GO to rGO under high-temperature annealing. To further investigate the phase transition of PVDF, the crystal structure of PVDF in rGO/PVDF composite films was investigated under different rGO loading concentrations (Figure 6.2b). With an rGO loading over 0.5 wt% of the composite film, all characteristic peaks of the nonpolar  $\alpha$ -phase disappeared and new diffraction peaks due to the polar  $\beta$ -phase of  $2\theta$  at 20.7 °, corresponding to (200/110), and due to the polar  $\gamma$ -phase of  $2\theta$  at 19.0 ° and 20.4 ° occurred. The formation of a polar crystal structure of PVDF in composite films, even without additional electric poling process, can be attributed to the steric effect between rGO sheets and PVDF molecules.<sup>230, 231</sup> In addition to ferroelectric properties, the conductivity of rGO/PVDF composites increased with increasing rGO loading concentration after the reduction of GO to rGO (Figure 6.3). To mimic the interlocked ridge structures between dermal–epidermal layers, rGO/PVDF composite films with interlocked microdome arrays were used in each layer of the multilayer e-skins (Figure 6.1e). Finally, three interlocked layers were stacked for the fabrication of multilayer e-skins with an effective stress concentration (Figure 6.1d).



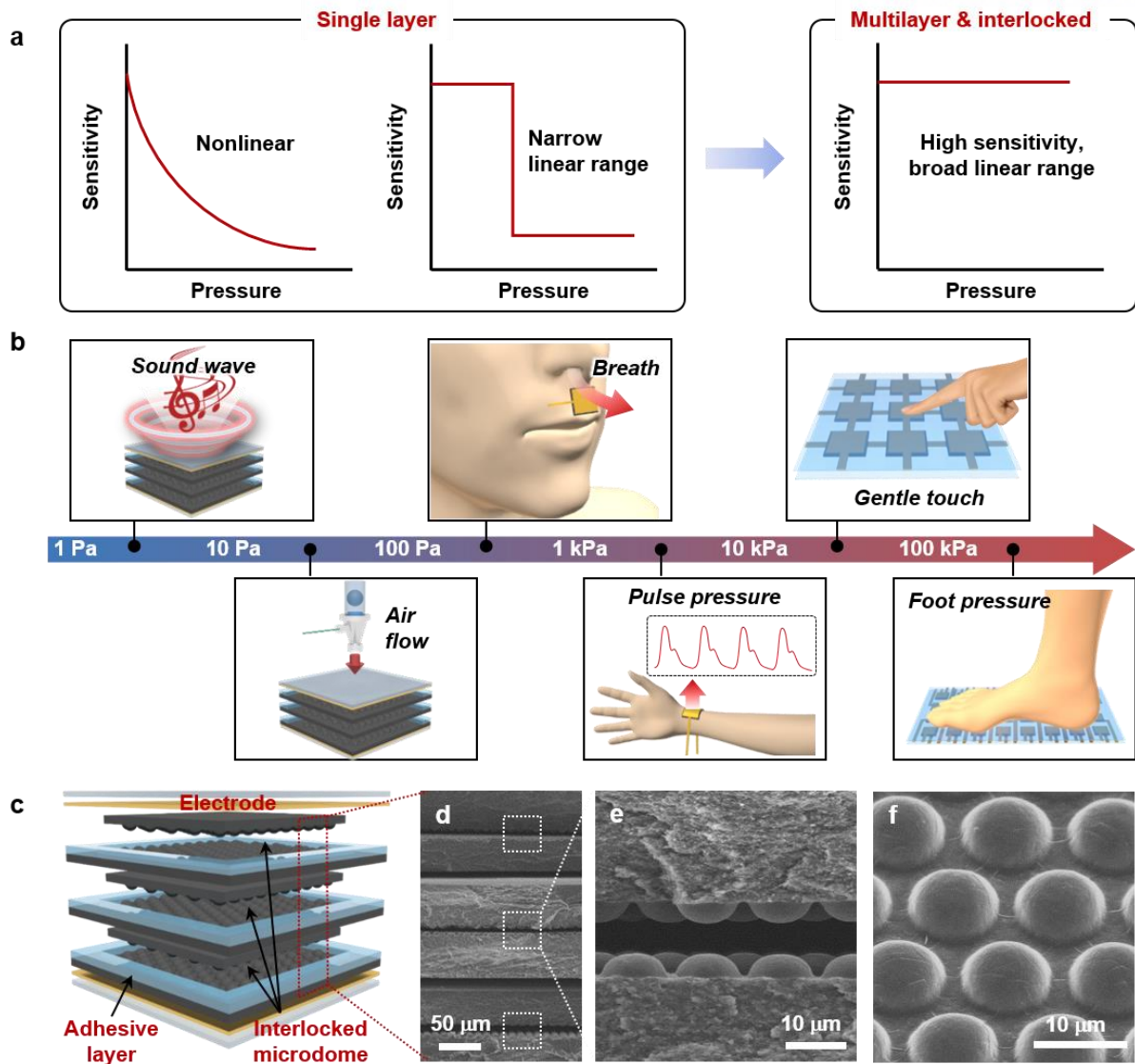


**Figure 6.1.** Applications and schematics of multilayer interlocked microdome e-skins. (a) Schematic showing the different pressure sensing trends between single-layered e-skins and multilayer e-skins. (b) Various applications to show the highly sensitive and large range pressure sensing by multilayer e-skins. (c) Schematic of multilayer e-skins. (d) Cross-sectional scanning electron microscopy (SEM) image of a microdome-patterned rGO/PVDF composite film with multilayer stacked structures. (e) Cross-sectional SEM image of the interlocked microdome geometry of an rGO/PVDF composite film. (f) Tilted SEM image of a microdome array of the rGO/PVDF composite film.

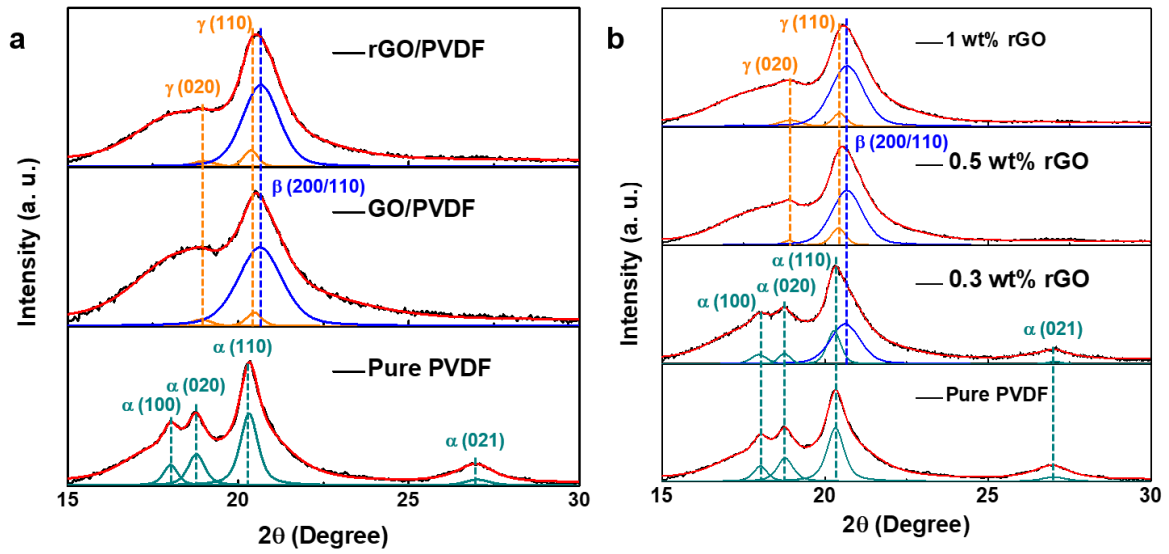


**Figure 6.2.** X-ray diffraction (XRD) spectroscopy of (a) a pure PVDF film, 2 wt% GO/PVDF, and 2 wt% rGO/PVDF composite films; and (b) pure PVDF and 0.3, 0.5, and 1 wt% rGO/PVDF composite films.

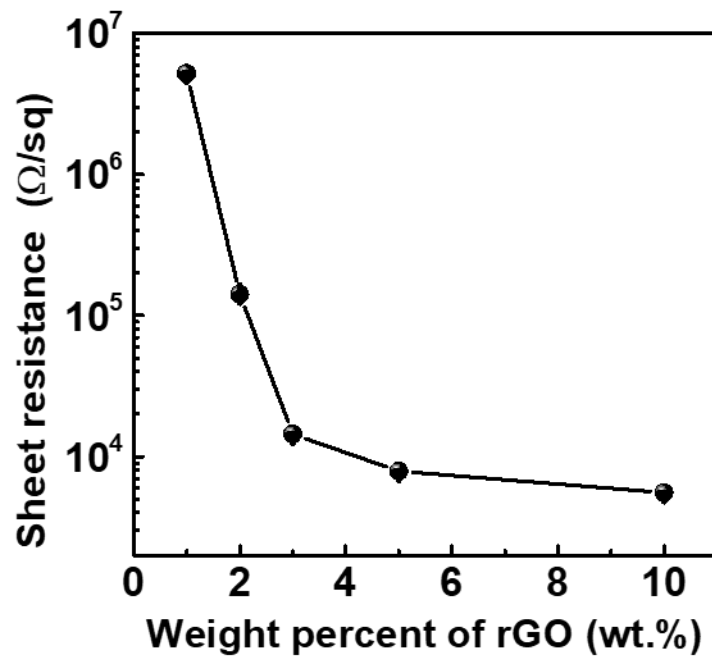


**Figure 6.3.** Sheet resistance of rGO/PVDF composite films as a function of the loading concentration of rGO.

The multilayer structure of interlocked microdome arrays enables e-skins with highly sensitive and linear pressure-sensing capabilities over an exceptionally broad pressure range. The multilayer e-skins are based on conductive composites of interlocked microdome arrays, which can detect static pressure using a piezoresistive sensing mode. Figure 6.5 shows the piezoresistive pressure sensing of multilayer e-skins based on the bulk film resistance ( $R_f$ ) and contact resistance ( $R_c$ ), where large amount of differences in contact resistance is dominant in e-skins with interlocked microstructures.<sup>45</sup> As previously reported, although the small contact area between interlocked microdomes sharply increases due to the stress concentration effects and the subsequent deformation of microdomes, resulting in an extremely high pressure sensitivity, the linear pressure-sensing over a large pressure range is quite limited and the sensitivity significantly decreases when the pressure is over 1 kPa.<sup>45, 46</sup> These issues can be addressed with multilayer structures, which significantly increase the linearity of pressure sensing and maintain the high pressure sensitivity over a range of several hundred kPa. Figure 6.4a shows that interlocked microdome structures can enhance the pressure sensitivity compared with planar structures. Of particular importance, the linearity increases with the increase of interlocked microdome layers, indicating the important role of multilayer structures in enhancing the pressure linearity over large pressure ranges. Figure 6.4b shows the pressure sensitivity of e-skins with different numbers of stacked layers and planar structures. The pressure sensitivity ( $S$ ) can be defined as  $S = (\Delta I/I_0)/\Delta P$ , where  $I$  is the current of the e-skins and  $P$  is the applied pressure. The interlocked microdome e-skins with different stacked layers have a sensitivity of at least four orders higher than that of planar e-skins. Importantly, e-skins with triple-stacked multilayers maintain their high sensitivity of  $47 \text{ kPa}^{-1}$  over an exceptionally broad pressure range (0.0013–353 kPa), demonstrating the linear pressure-sensing capability. In contrast, single- and double-layered e-skins can linearly detect the pressure with a pressure sensitivity of  $20 \text{ kPa}^{-1}$  up to 54 kPa and  $27 \text{ kPa}^{-1}$  up to 190 kPa, respectively. Their high sensitivity gradually decreases beyond the linear detection pressure region. Further increase of the interlocked layers over three layers results in a rather small increase of the sensitivity; i.e., the pressure sensitivity increased from  $47 \text{ kPa}^{-1}$  for three interlocked layers to 52 and  $54 \text{ kPa}^{-1}$  for four and five interlocked layers, respectively (Figure 6.6). In comparison with previous literature, the e-skins with triple multilayer e-skins exhibit a very high sensitivity over an exceptionally broad pressure range (0.0013–353 kPa) with a linear response to pressure (Figure 6.4c and Table 6.1).<sup>9, 20, 21, 44, 47, 137, 156, 162, 165, 232, 233</sup> Most of sensors exhibited a linear range below 60 kPa. Only a few sensors (Figure 6.4c) showed a linear range over 60 kPa, but the sensitivities were below  $0.026 \text{ kPa}^{-1}$ . Although some of previous pressure sensors reported a higher sensitivity than our sensor, they exhibited a nonlinear response<sup>3</sup> or only have been achieved at low pressure range ( $< 100 \text{ Pa}$ ).<sup>175</sup> The simultaneous achievement of linear sensing capability with a high sensitivity of  $47 \text{ kPa}^{-1}$  over a large pressure-sensing range from 1.3 Pa to 353 kPa has not been made in previous works.

To elucidate the structural effect of stacked multilayers on pressure sensitivity and linearity, we performed finite element calculations based on the model system with different numbers of interlocked layers (Figure 6.7a). Figure 6.4d shows the calculated contact area change of three different multilayer e-skins as a function of the applied pressure. The contact area of the interlocked microdome structures rapidly increases from almost zero in the initial unloading state to an extremely high value in the high-pressure loading state, which is attributed to the concentrated and amplified stress at a small spot between interlocked microdomes that greatly deforms the interlocked microdomes, resulting in the significant increase of the contact area (Figure 6.7b). With increasing number of stacked layers, the contact area dramatically increases due to the increased number of contacted microdomes. The contact area changes in Figure 6.4d also indicates that the linearly increasing contact area starts to decrease at a pressure over  $\approx 244$  and 148 kPa for double- and single-interlocked layers, respectively, which matches the trend in Figure 6.4a well. The multilayer geometry can enhance the linearity of pressure sensing because the multilayer interlocked microdomes can distribute the applied stress to each stacked layer (Figure 6.4e). As a result, pressure sensitivity and linearity increase with an increase in the number of layers in multilayer e-skins. We also investigated the effect of the rGO loading concentration on the pressure-sensing performances of multilayer e-skins. Figure 6.8 shows the pressure-sensing performances of single- and multilayer e-skins with different rGO loading concentrations, which indicate that a 2 wt% rGO loading concentration is the best condition for multilayer e-skins (Section S6.1). In addition, the size of microdomes affects to the pressure sensing performances of multilayer e-skins. Figure 6.9 shows the pressure response of multilayer e-skins with different size of microdomes (Section S6.2).

To investigate the real-time pressure-sensing performances of multilayer e-skins, the relative current change of e-skins was measured under incremental pressure (Figure 6.4f). Under a step-by-step increase of pressure from 54 to 326 kPa, e-skins show a fast and linearly increasing current change. In the real-time pressure detection, multilayer e-skins show slight increase of sensor signals under high pressure over 200 kPa, due to the slow response of the bulk film. Although there are some delayed pressure reading at high pressure, those delayed pressure calculated by sensitivity of multilayer e-skins ( $47 \text{ kPa}^{-1}$ ) was only 2-4 % of the applied pressure, which does not affect much on the detected pressure. In addition, the interlocked geometry can provide a fast response and relaxation time due to the immediate deformation and recovery of surface microstructures in response to the applied pressure.<sup>28</sup> At a low pressure of 10 kPa, which corresponds to the pressure of gentle finger touch, multilayer e-skins show a fast response and relaxation time of 40 and 20 ms, respectively (Figure 6.4g), which are comparable to the response time of human skin (30–50 ms).<sup>234</sup> Even at a high pressure of 200 kPa, which can induce significant microdome deformation, e-skins show a fast response/relaxation time of 150/30 ms. Furthermore, during repetitive cycles of high pressure loads of 272 kPa at a frequency of 0.5 Hz, e-

skins show a reliable and uniform pressure-sensing performance up to 5,000 cycles (Figure 6.4h).

### **S6.1 Dependence of rGO loading concentration on pressure-sensing performance of single- and multilayer e-skins**

The static pressure sensing performance of multilayer e-skins was highly affected by the loading concentration of rGO in rGO/PVDF composite films. Figure 6.8a plots pressure-sensing performances of single interlocked microdome e-skins with different loading rGO concentration. In single interlocked structures, e-skins with lower rGO concentration show higher pressure sensitivity, because the modulus of rGO/PVDF composite films increases with increasing rGO concentration, leading to reduced amount of deformation in interlocked microdomes.<sup>43</sup> On the other hand, triple interlocked microdome e-skins show different trends, as e-skins with 2 weight percent (wt%) rGO loading concentration provide higher pressure sensitivity than e-skins with 1 and 3 wt% rGO loading concentrations (Figure 6.8b). This behavior can be attributed to the fact that the initial resistance of multilayer interlocked microdome e-skins is much higher than that of single interlocked microdome e-skins due to the increased contact resistance between multilayer interlocked microdomes (Figure 6.8c). In triple interlocked geometry, the high initial resistance of e-skins with 1 wt% rGO/PVDF composites imposes a too high barrier for the pressure-induced variation of piezoresistive current. On the other hand, e-skins with 3 wt% rGO/PVDF composites are relatively stiff compared to 2 wt% rGO/PVDF composites, resulting in a lower pressure sensitivity.

### **S6.2 Size dependence of microdomes on pressure response of multilayered e-skins**

To investigate the effect of size of microdomes on pressure sensing performances, we fabricated triple multilayer e-skins based on various size of microdome-patterned films (Figure 6.9a-c). Figure 6.9d shows the pressure responses of multilayer e-skins based on microdomes with different pitch size. The microdome arrays with larger pitch size provide smaller surface area and decreased number of contact spots between interlocked microdomes, resulting in lower sensitivity in multilayer e-skins. In addition, due to the diminished stress distribution between decreased number of contacted spots, multilayer e-skins based on microdomes with larger pitch size show linear pressure sensing performances up to lower pressure range (217 kPa) than that of smaller pitch size, resulting in the sensitivity change from 22.8  $\text{kPa}^{-1}$  to 15.8  $\text{kPa}^{-1}$  when the pressure is over 217 kPa. We also investigated the effect of different dome diameter on the performances of multilayer e-skins at the fixed dome diameter to pitch size ratio of 0.833 (Figure 6.9e). We confirmed that the multilayer e-skins based on microdomes with various diameter sizes (10, 25, 50  $\mu\text{m}$ ) show similar pressure sensing performances, which can be attributed to the same ratio between dome diameter and pitch size, resulting in the same total contact area between

interlocked microdome arrays and contact area change in response to applied pressure. However, microdome patterned films with larger diameter will have larger thickness due to increased height of microdomes, which will cause decreased flexibility of e-skins.

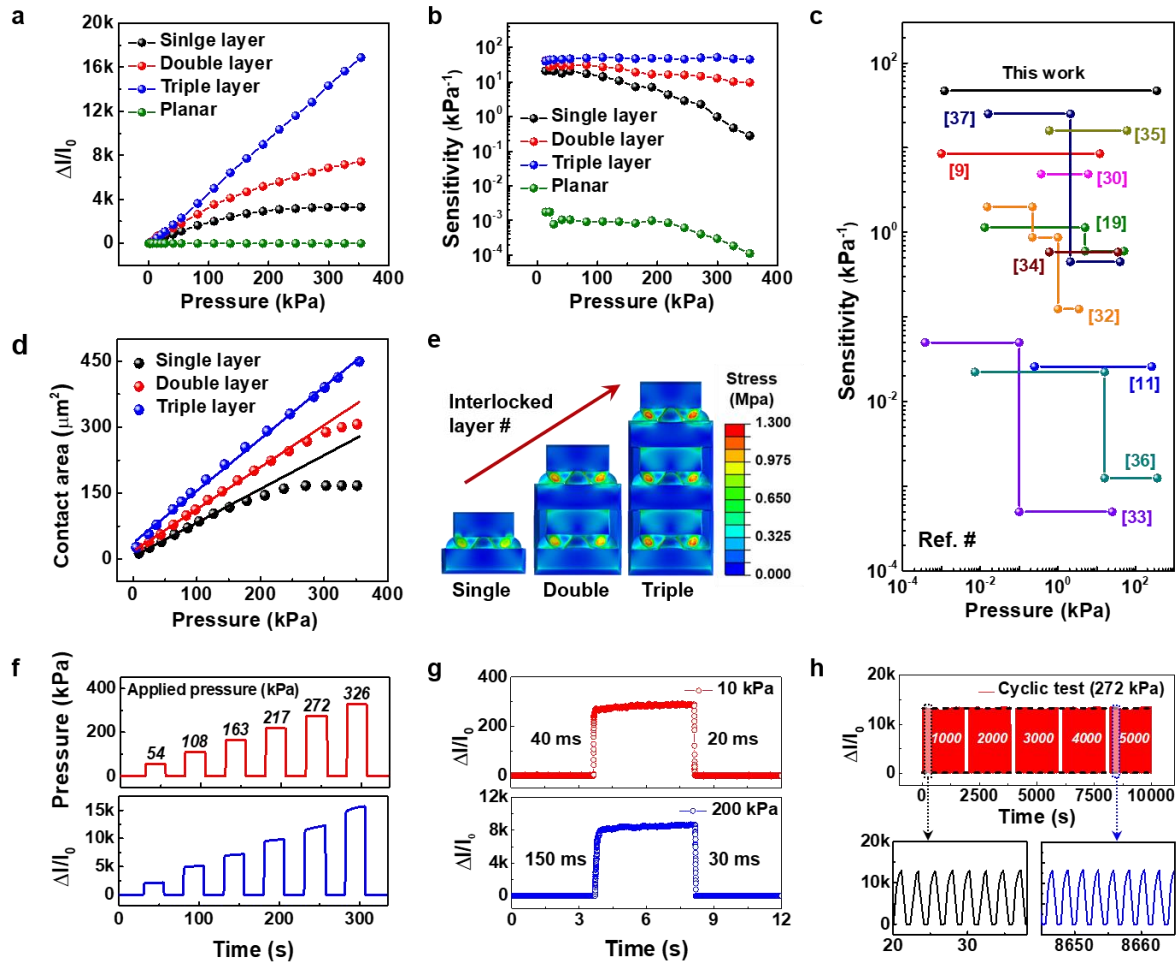


**Figure 6.4.** Piezoresistive static pressure-sensing performances of multilayer interlocked microdome e-skins. (a) Relative current of e-skins with multilayer geometry with different numbers of stacked layers and planar geometry in response to the applied pressure. (b) Pressure sensitivity of e-skins converted from Figure 6.4a. (c) Comparison of the sensitivity and linear sensing performances based on this work and previous reports. (d) Finite element calculation of the contact area change as a function of pressure for different numbers of stacked layers. (e) Finite element calculations of the local stress distribution for different numbers of interlocked layers showing the concentrated and amplified stress at the small spot between interlocked microdomes under a pressure of 355 kPa. (f) Real-time pressure monitoring of e-skins at an applied pressure of 54, 108, 163, 217, 272, and 326 kPa. (g) Response and relaxation times for multilayer e-skins under different pressures of 10 and 200 kPa. (h) Cyclic stability test of multilayer e-skins under repetitive high-pressure loading of 272 kPa at a frequency of 0.5 Hz.

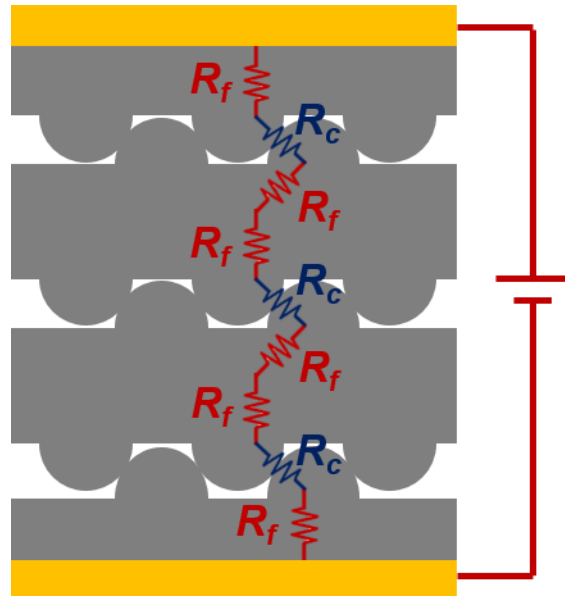


Figure 6.5 Circuit diagram of triple multilayer e-skins.

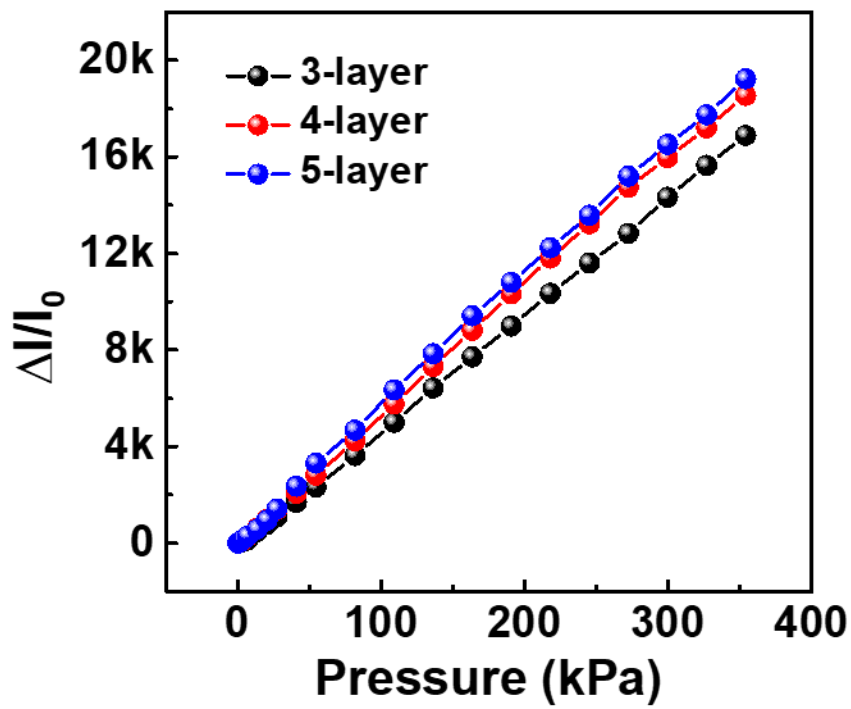
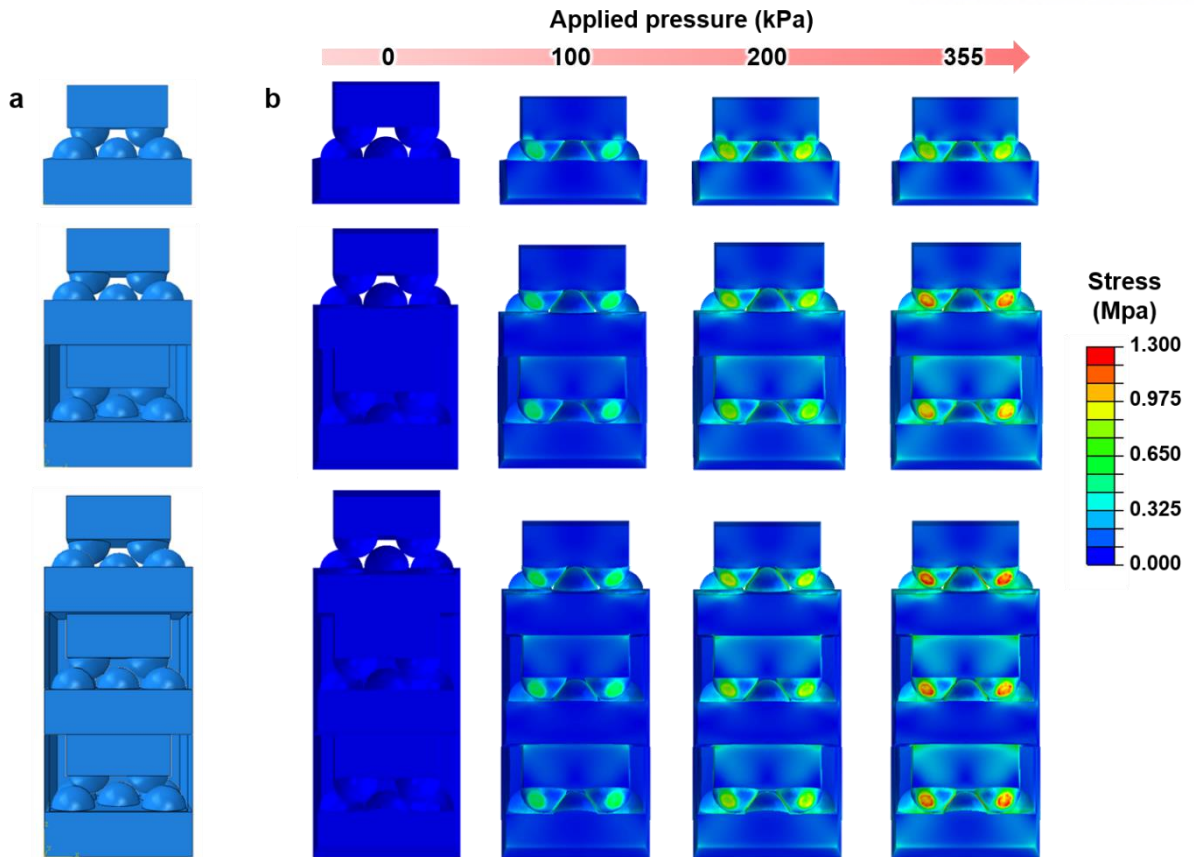
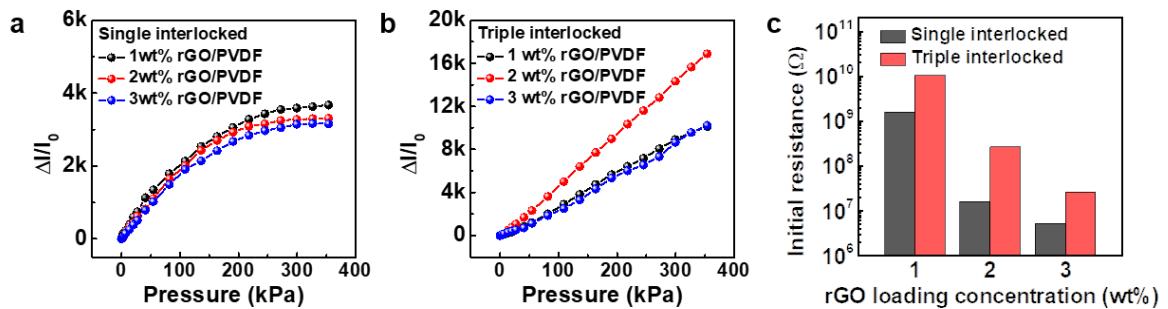


Figure 6.6. Static pressure-sensing performances of multilayer e-skins over three layers.



**Figure 6.7.** Finite-element calculation showing the stress distribution in multilayer e-skins with single, double, and triple layers. (a) Model systems with different number of interlocked layers. (b) Stress distribution of multilayer e-skins with single, double, and triple layers under different applied pressure.



**Figure 6.8.** (a) Static pressure-sensing performances of single-interlocked e-skins with different rGO loading concentrations. (b) Static pressure-sensing performances of triple-interlocked e-skins with different rGO loading concentrations. (c) Initial resistance of single- and triple-interlocked e-skins using 1 and 2 wt% rGO/PVDF composite films.



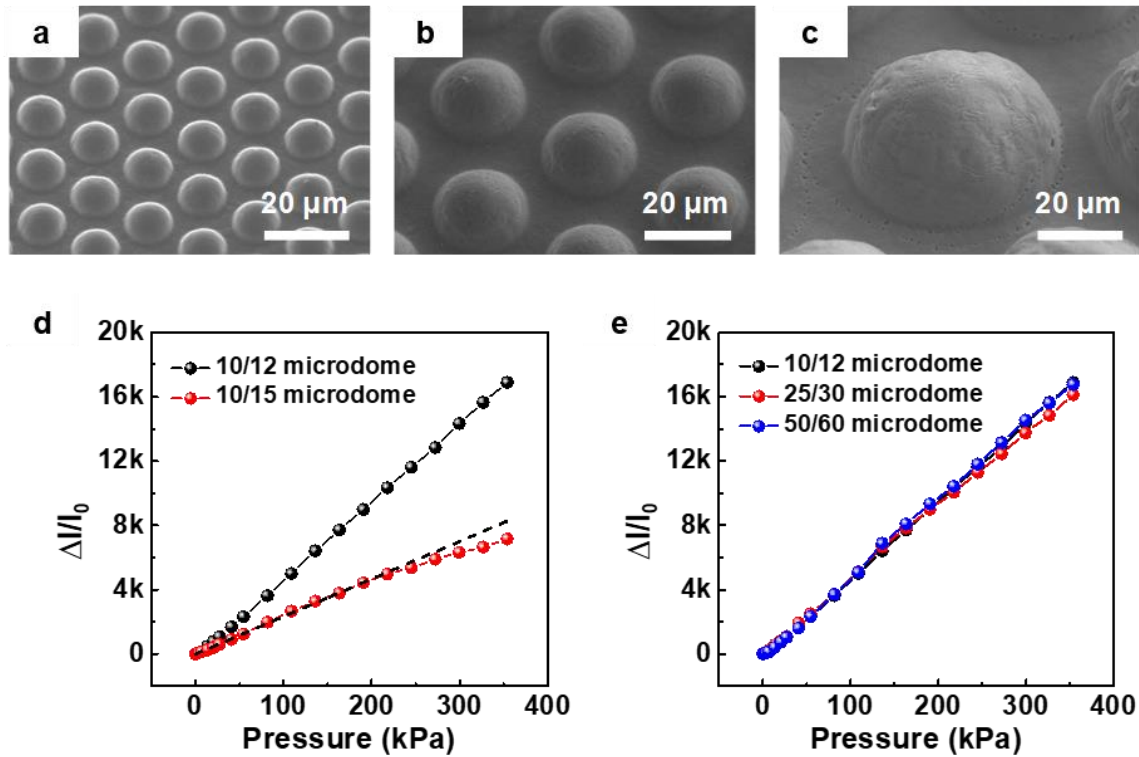


**Figure 6.9.** Pressure-sensing performances of multilayer e-skins based on different size of microdomes. Cross-sectional SEM images of microdome arrays with (a) 10, 15, and 4 μm, (b) 25, 30, and 10 μm, (c) 50, 60, 20 μm in diameter, pitch, and height, respectively. Relative current of multilayer e-skins based on microdomes with (d) different pitch size and (e) different diameter.

**Table 6.1.** Summary of pressure sensors with linear pressure responses and their performances.

NO.	Materials	Type	Range [kPa]	Sensitivity [kPa <sup>-1</sup> ]	Linear range [kPa]	Ref.
1	PEDOT:PSS/PUD micropyramid	Resistive	0.37 – 5.9	4.88	0.37 – 5.9	[44]
2	Porous CNT/PDMS	Resistive	0.25 – 260	0.026	0.25 – 100	[47]
3	Au NWs	Resistive	0.013 – 50	1.14 (<5 kPa) 0.6 (<50 kPa)	0.013 – 5	[137]
4	Single crystal silicon	Resistive	– 200	0.0041	– 200	[20]
5	Polyaniline/Au micropillar	Resistive	0.015 – 3.5	2.0 (< 0.22 kPa) 0.87 (< 1 kPa) 0.12 (< 3.5 kPa)	0.015 – 0.22	[165]
6	CNT microyarn	Capacitive	0.00038 – 25	0.05 (< 0.1 kPa) 0.0005 (> 10 kPa)	0.00038 – 0.1	[9]
7	Graphene/PDMS hierarchical microdome	Resistive	0.001 – 12	8.5	0.001 – 12	[162]
8	Carbon black- coated fabric	Resistive	0.6 – 35	0.585	0.6 – 35	[156]
9	Hollow structured graphene-silicon composite	Resistive	0.6 – 60	15.9	0.6 – 60	[232]
10	Ecoflex dielectric layer with Ag electrode	Capacitive	0.0073 – 360	0.0224 (< 16 kPa) 0.00125 (< 360 kPa)	0.0073 – 16	[21]
11	rGO/PDMS microstructures	Resistive	0.016 – 40	25.1 (<2.6 kPa) 0.45 (<40 kPa)	0.016 – 2.6	[233]
12	<b>rGO/PVDF multilayer interlocked microdome</b>	Resistive	0.0013 – 353	<b>47.7</b>	<b>0.0013 – 353</b>	<b>This work</b>

Multilayer e-skins with high sensitivity, large dynamic pressure-sensing range, and linear detection capabilities can be used in diverse applications requiring a large dynamic pressure range from low to high pressure regimes. To demonstrate the low pressure detection capability of our e-skins, we applied weak gas flow to the surface of multilayer e-skins (Figure 6.10a). Figure 6.10b shows the piezoresistive response of multilayer e-skins under weak gas flow with flow rates ranging from 3 to 15 L/min. The gas flow rate of 3 L/min corresponds to an extremely low static pressure of  $\approx 1.3$  Pa, demonstrating the ultra-low minimum detection limit of our e-skins (Figure 6.11). Even in a very low pressure region, the real-time monitoring of weak gas flow exhibits no significant noise signals, indicating a stable operation of multilayer e-skins. (Figure 6.10c).

In addition to piezoresistive static pressure sensing, multilayer e-skins can be used under dynamic pressure with high frequency due to the piezoelectric properties of rGO/PVDF composites. In this composite, conductive rGO fillers can transform the PVDF phase from the nonpolar  $\alpha$ -phase to the polar  $\beta$ -phase, which can induce high piezoelectric properties.<sup>230, 231</sup> Similar to the piezoresistive sensing mode, interlocked e-skins have higher piezoelectric performances due to the effective stress concentration at the small contact area between microdomes compared with planar structures (Figure 6.10d). The introduction of multilayer geometry in e-skins provides a much higher piezopotential compared with single-interlocked e-skins due to the increased contact area between multilayer-interlocked microdomes. The rGO loading concentration also affects the piezoelectric pressure-sensing performances of multilayer e-skins. Multilayer e-skins with a 2 wt% rGO loading concentration show slightly lower piezoelectric performances than those with a 1 wt% rGO loading concentration (Figure 6.12). This behavior is attributed to the increasing film conductivity with higher rGO loading, which can decrease the piezoelectric polarization of composite films due to the leakage current.<sup>43, 214</sup>

The fast response time of piezoelectric e-skins enables the detection of acoustic sound waves with a wide range of frequencies of up to several tens of kHz (Figure 6.10e). To demonstrate the sound detection performances of e-skins, sound waves were applied to multilayer e-skins using a commercially available microphone. The e-skins with triple-interlocked multilayers show the best sound wave detection performance due to the immediate contact/release of interlocked microdomes in response to vibrations and an increased overall contact area change (Figure 6.10f). The piezoelectric voltage output increases with increasing sound frequency of up to 20 kHz and then slowly decreases. In contrast, single-interlocked microdome e-skins have a slightly decreased piezoelectric voltage due to the reduced contact area and planar e-skins provide a tiny piezoelectric voltage. Figure 6.13 shows the fast Fourier transform (FFT) spectra of the piezoelectric signals of multilayer and planar e-skins after applying a sound wave with a single frequency of 1, 5, 10, and 20 kHz. The multilayer e-skins exhibit a single distinguishable peak according to each sound wave, where the amplitude is 0.006 at 1 kHz and increases with the frequency of the sound wave (Figure 6.13a). On the other hand, the planar

e-skins reveal weak signals with the amplitudes below 0.0005 (Figure 6.13b), indicating a low piezoelectric sensitivity of planar e-skins compared with multilayer e-skins.

The multilayer e-skins can precisely detect time-dependent variation of acoustic sound when the well-known piece “Piano Sonata K.545, 1<sup>st</sup> movement (W.A. Mozart)” was played. Here we chose electric guitar music, which covers a large range of frequencies. Figure 6.10g shows the time-dependent sound waveforms and corresponding spectrograms, which were converted using a short-time Fourier transform (STFT) of the original sound source (black) and recorded piezoelectric signals from multilayer e-skins (red) and planar e-skins (blue). The time-dependent sound waveform and corresponding spectrogram of music recorded by multilayer e-skins accurately match with those of the original sound source covering a large range of frequencies of up to 6 kHz. The enlarged plot of the frequency spectrogram further demonstrates the superior sound wave detection performance of multilayer e-skins (Figure 6.10h). Conversely, planar e-skins with low piezoelectric outputs could not precisely record the waveforms and spectrogram of the original music (Figure 6.10g, blue). The multilayer e-skins also precisely detected the variation of the sound waveform when the same music was played by different musical instruments. Figure 6.14a shows that the waveforms and corresponding spectrograms of the same music differ depending on the musical instruments (piano, guitar, electric guitar). The waveforms and frequency spectrograms recorded from multilayer e-skins in Figure 6.14b indicate that the information from music played by different musical instruments matches well with those of the original sound source.

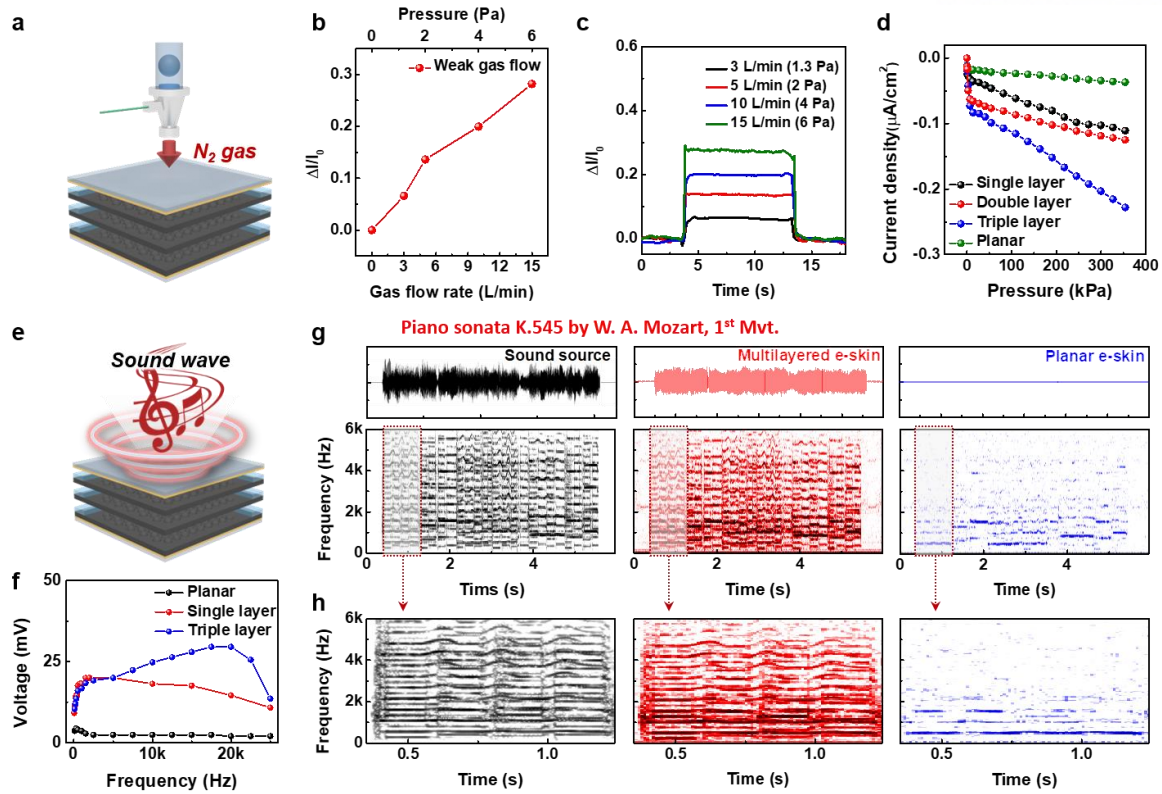


**Figure 6.10.** Application of weak pressure on multilayer e-skins. (a) Schematic illustration showing the detection of weak air flow by multilayer e-skins. (b) Relative current change of multilayer e-skins as a function of gas flow rate. (c) Real-time monitoring of gas flow by multilayer e-skins. (d) Piezoelectric dynamic pressure-sensing performances of e-skins with different multilayer structure geometries with different stacked layers and planar structures. (e) Schematic of sound wave detection by multilayer e-skins. (f) Detection of the sound wave with single frequency for planar, single-interlocked, and multilayer interlocked microdome e-skins. (g) Sound waveforms and corresponding spectrograms converted by STFT from the original sound source (black), signals recorded from multilayer e-skins (red), and planar e-skins (blue). (h) Expanded frequency spectrograms in Figure 6.10g

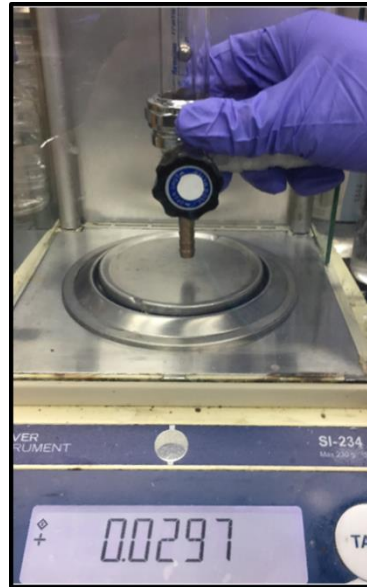


**Figure 6.11.** Applied pressure due to weak gas flow with a flow rate of 3 L/min. Considering the size of the multilayer e-skins, the applied pressure due to gas flow with a flow rate of 3 L/min is  $\approx 1.3$  Pa.

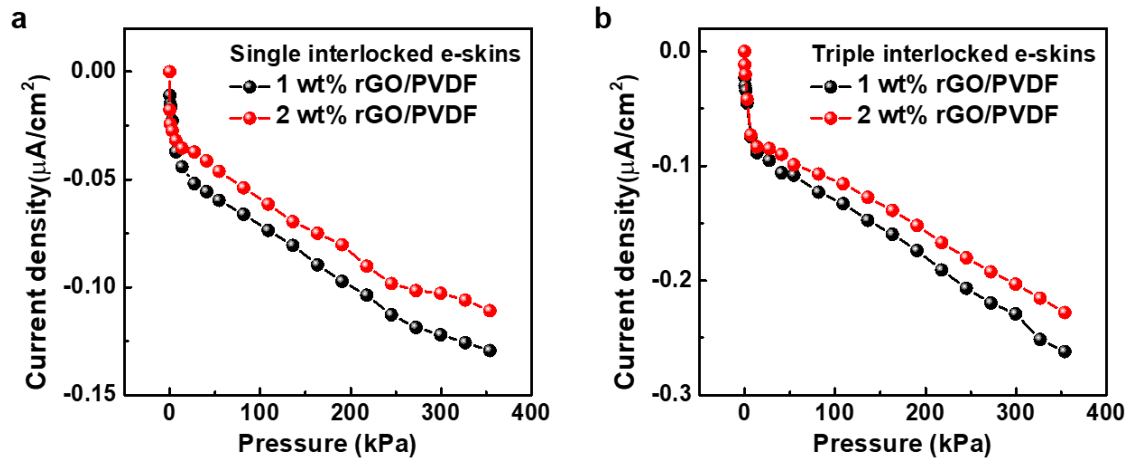


**Figure 6.12.** (a) Dynamic pressure-sensing performances of single-interlocked e-skins with 1 and 2 wt% rGO/PVDF composite films. (b) Dynamic pressure-sensing performances of triple-interlocked e-skins with 1 and 2 wt% rGO/PVDF composite films.

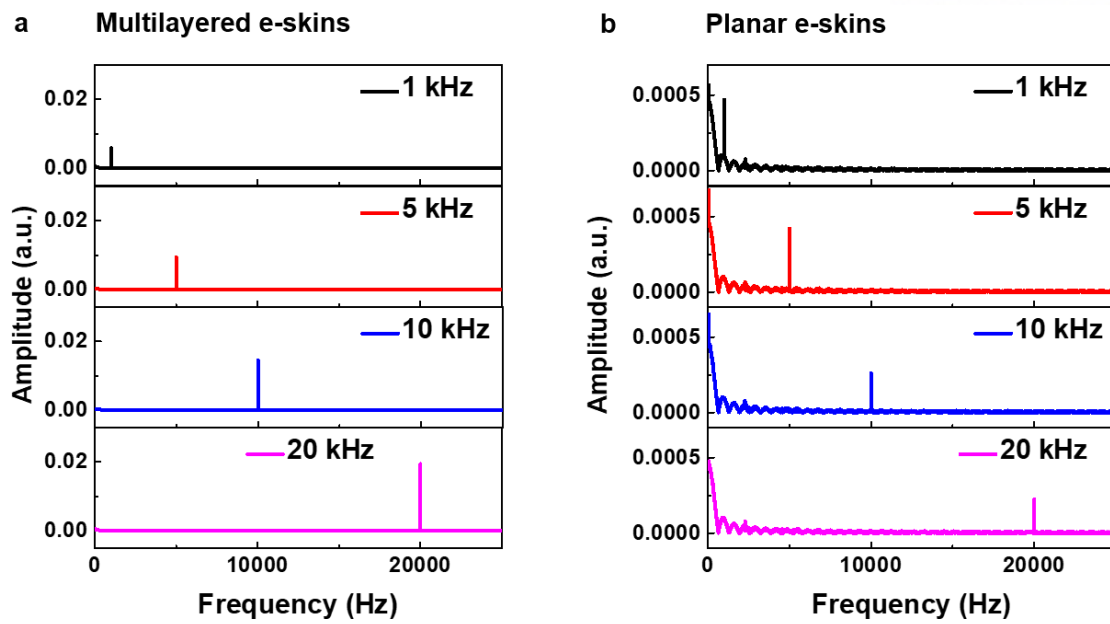


**Figure 6.13.** Piezoelectric single sound frequency detection performances of (a) multilayer e-skins and (b) planar e-skins.

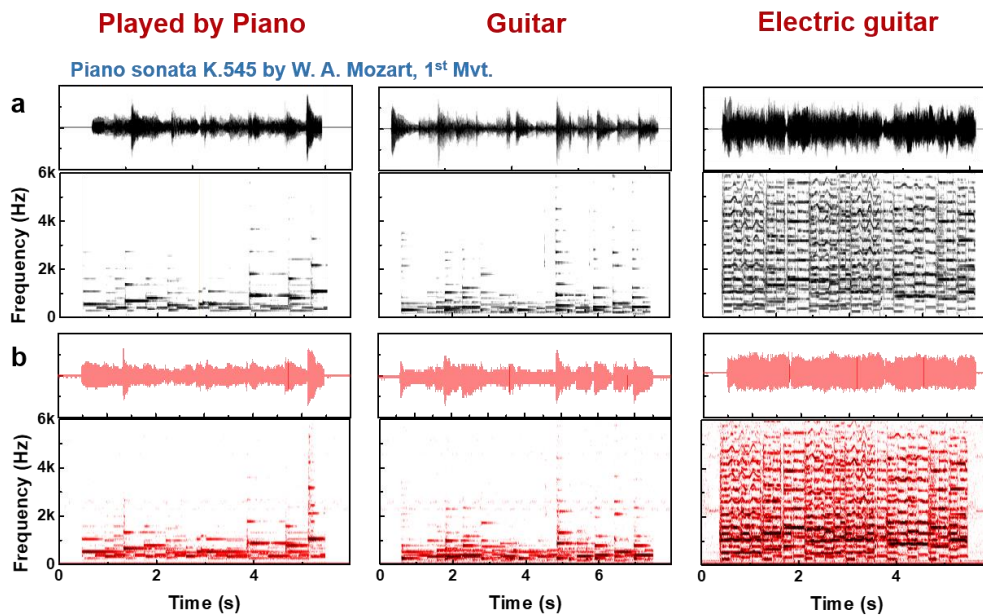


**Figure 6.14.** (a) Sound waveforms and corresponding spectrograms converted by STFT of the original sound from a piano, guitar, and electric guitar (black). (b) Recorded piezoelectric waveforms and corresponding spectrograms from multilayer e-skins, converted by STFT of sound from a piano, guitar, and electric guitar (red).

In addition to low pressure-sensing performances, multilayer e-skins with high sensitivity and large pressure-sensing range with a linear sensing performance can be used for applications requiring the detection of medium pressure (1–20 kPa). For medium pressure sensing applications, highly flexible multilayer e-skins were used as wearable healthcare devices for the monitoring of human breathing and wrist pulses that are considered the four primary vital signs of human life (pulse rate, blood pressure, respiration rate, and temperature).<sup>235</sup> For this purpose, multilayer e-skins were attached to the nostrils (Figure 6.15a). The multilayer e-skins clearly differentiate between weak and deep breathing signals of a volunteer (Figure 6.15b). The monitored weak breathing signals provide a breathing rate of 18 breaths/min, which corresponds to that of healthy adults (12–20 breaths/min).<sup>236</sup> In contrast, intentional deep breathing results in the increase of the signal intensity and decrease of the respiration rate to 12 breaths/min. This capability of breathing detection allows the use of e-skins for applications such as diagnosing the sudden infant death syndrome and monitoring body health state during exercise. As other primary vital signs of human life, the monitoring of pulse signals provides medical information to diagnose and prevent cardiovascular diseases.<sup>179, 237</sup> Figure 6.15c shows multilayer e-skins attached on wrist skin, which provide real-time monitoring of the wrist pulse pressure period and waveform (Figure 6.15d). A pulse frequency of 72 beats/min was recorded, which corresponds to the value of healthy adults.<sup>238</sup> In addition, the pulse waveform contains three distinguishable peaks  $P_1$ ,  $P_2$ , and  $P_3$ , which correspond to incident, tidal, and diastolic waves, respectively.<sup>179</sup> Based on these three peaks, the arterial stiffness of a volunteer can be diagnosed by analyzing the radial augmentation index ( $AI_r = P_2/P_1$ ), diastolic augmentation index ( $DAI_r = P_3/P_1$ ), and digital volume pulse time ( $\Delta T_{DVP} = t_{P2} - t_{P1}$ ), where  $t_{P1}$  and  $t_{P2}$  are the time of the first ( $P_1$ ) and second peak ( $P_2$ ), respectively. The calculated  $AI_r$ ,  $DAI_r$ , and  $\Delta T_{DVP}$  values under relaxed conditions are 0.472, 0.264, and 0.196, respectively, which match the expected values for healthy adults in their mid-twenties.<sup>179</sup>

The multilayer e-skins with pixel array possess the ability to perceive the magnitude and spatial distribution of various tactile stimuli. Figure 6.15e shows the schematic illustration of  $3 \times 3$  pixel arrays of e-skins sandwiched by patterned electrodes. When different shapes of loads in the medium pressure region ( $\approx 2$ –20 kPa) are applied on e-skin arrays (Figures 6.15f–h), the sensor array can differentiate the compressed local regions from other regions, demonstrating the ability of e-skins to perceive the spatial pressure distribution (Figure 6.15f). The linear pressure-sensing capability of multilayer e-skins enables the precise perception of the magnitude and location of the applied pressure. When two different loads, with one load weighing twice than that of the other, are applied to the sensor array, the magnitude and difference of the applied pressure can be visualized by a color map (Figure 6.15g). In addition, for the large load size, the sensor array can differentiate between the center and corner areas of the object based on the color mapping image (Figure 6.15h).



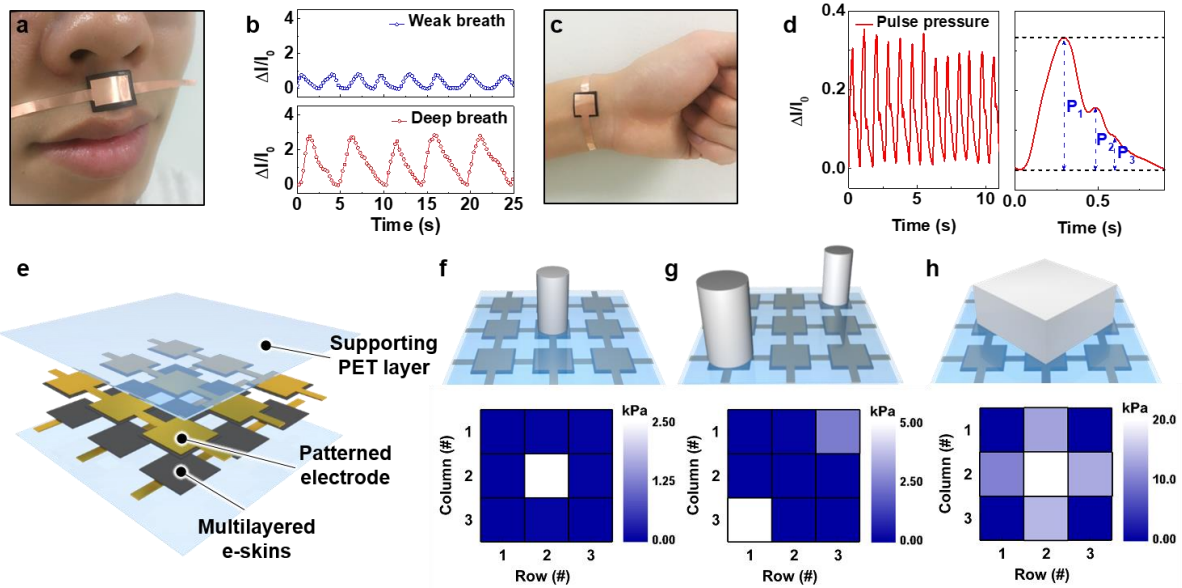


**Figure 6.15.** Application of medium pressure on multilayer e-skins. (a) Photograph showing the detection of human breath by attaching multilayer e-skins to the nostril of a volunteer. (b) Monitored real-time signals of weak and deep breathing detected by multilayer e-skins. (c) Photograph showing the pulse pressure detection after attaching multilayer e-skins to wrist skin. (d) Real-time monitoring of the pulse signals and expanded pulse wave containing three peaks, i.e.,  $P_1$  (incident wave),  $P_2$  (tidal wave), and  $P_3$  (diastolic wave), recorded by multilayer e-skins. (e) Schematic of the  $3 \times 3$  sensor array for the multilayer e-skins with an ability to perceive the magnitude and spatial distribution of the applied pressure. (f–h) Schematics of the detection of applied pressure from different shapes and weights of loads and their corresponding pressure maps.

Monitoring of the foot pressure distribution is considered to be a useful tool in the fields of footwear design, sport biomechanics, and wearable healthcare systems.<sup>239</sup> In particular, abnormal gait patterns and excessive foot pressure in certain areas may cause several diseases such as diabetic foot ulcer.<sup>240</sup> In addition, representative symptom of patients with Parkinson's disease was known as characteristic gait patterns, which are noticeably different with normal gait patterns.<sup>241</sup> Therefore, monitoring of the walker's gait patterns and posture enables the early diagnosis and progress monitoring of those diseases. Pressure sensors with highly sensitive and ultra large range pressure sensing capabilities up to several hundred kPa are required for the precise detection of the foot pressure distribution. In addition, linear pressure sensing is critical for directly comparing the foot pressure distribution of different areas using the contour color maps. Our multilayer e-skins have excellent potential for this purpose due to their high sensitivity ( $47 \text{ kPa}^{-1}$ ) and linear pressure sensing over an exceptionally broad pressure range (0.0013–353 kPa). To fabricate a smart insole for the monitoring of the foot pressure distribution, we designed a sensor array consisting of  $4 \times 8$  pixel e-skin arrays and supporting polyethylene terephthalate (PET) layers (Figure 6.16a). Firstly, to investigate the distribution of the low-pressure detection capability, a petri dish was placed upside down on the sensor array for the application of circular-distributed low pressure below 300 Pa (Figure 6.16b). The corresponding map of the sensor array clearly shows the circular pressure distribution with different colors (Figure 6.16c). Our sensor array was used as a smart insole for the monitoring of the high foot pressure distribution experienced during walking. Figure 6.16d shows the schematics of five different walking motions and the corresponding color maps monitored by a smart insole based on multilayer e-skins. The smart insole precisely detects the foot pressure distribution, where red areas indicate concentrated high stress and blue areas reflect low stress, demonstrating potential applications in wearable medical devices and the sports industry.

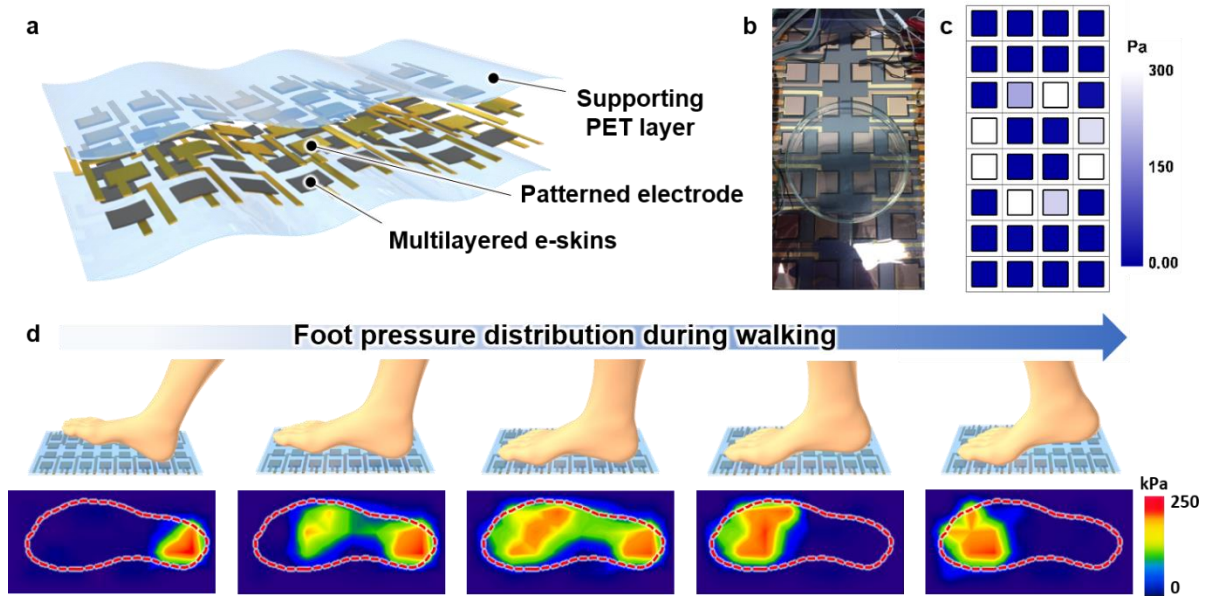


**Figure 6.16.** Application of high pressure to multilayer e-skins. (a) Schematic of the smart insole consisting of  $4 \times 8$  pixel arrays of multilayer e-skins, patterned electrodes, and supporting PET layers. (b) Photograph of  $4 \times 8$  pixel arrays of multilayer e-skins with pressure applied by an upside-down petri dish. (c) Corresponding pressure map. (d) Schematics of five walking motions on the smart insole to monitor the foot pressure distribution and their corresponding pressure maps.

## 6.4 Conclusions

In conclusion, we demonstrated a flexible ferroelectric sensor with high pressure sensitivity and linear response over an exceptionally broad pressure range. The suggested ferroelectric sensor is based on the rGO/PVDF ferroelectric composites with a multilayer interlocked microdome geometry. Our multilayer e-skins showed a simultaneous achievement of linear sensing capability with an ultrahigh sensitivity of  $47 \text{ kPa}^{-1}$  over an exceptionally large pressure-sensing range from 1.3 Pa to 353 kPa. The ultrahigh pressure sensitivity and linear response over an exceptionally broad pressure range can be achieved by the effective stress concentration, increased contact area, and stress distribution between multilayer interlocked microdome arrays, which has been also verified by the theoretical calculations. These sensing capabilities enabled our e-skins to monitor diverse stimuli from low to high pressure range. For example, our e-skins can precisely monitor the weak gas flow and acoustic sound in a low pressure regime, respiration and pulse pressure in a medium pressure regime, and plantar pressure monitoring in a high pressure regime. The suggested e-skins may be useful for diverse sensor applications requiring precise detection of pressure from extremely low to high pressure range such as robotics, prostheses, and wearable healthcare devices.

## Chapter 7. Mechanochromic electronic skins for the visualization of mechanical stimuli

### 7.1 Introduction

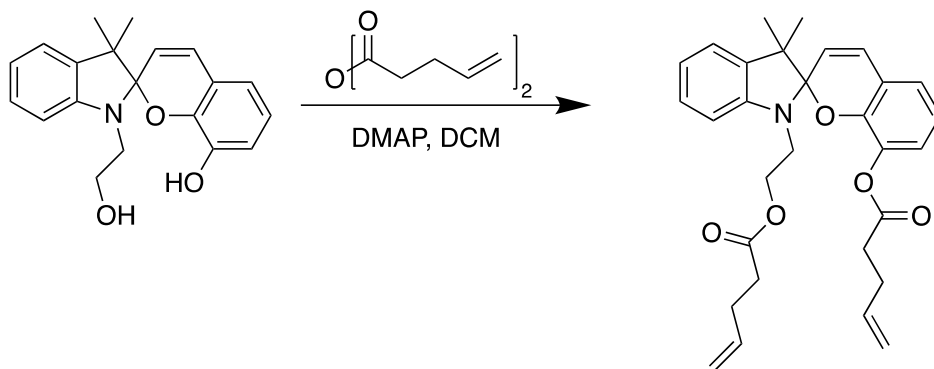
The multi-functional mechanical sensitivity of biological tissues,<sup>121, 242</sup> such as skin, is difficult to reproduce. In polymers that incorporate force-responsive molecules (i.e. mechanophores), mechanical force induces chemical transformations of mechanophores,<sup>243-245</sup> enabling controlled colour/luminescence changes,<sup>246, 247</sup> mechanocatalysis,<sup>248, 249</sup> isomerisation,<sup>250</sup> release of small molecules<sup>250, 251</sup> and self-healing behaviours.<sup>252</sup> Mechanochromic polymers that undergo colour changes in response to mechanical stress can be used to directly visualise the stress distribution and mechanochemical activations within polymers,<sup>246</sup> which is advantageous for application in stress/strain sensing<sup>253-255</sup> and damage monitoring in polymeric materials.<sup>256, 257</sup> To induce stress-driven mechanochemical transformations, efficient transmission of mechanical stress through the polymer matrix and coupling to the mechanophore is critical. Various factors affect the efficiency of mechanochemical activation, including the mechanophore position in the polymer chain,<sup>246</sup> polymer molecular weight,<sup>258</sup> polymer chain alignment<sup>259</sup> and temperature.<sup>260</sup> Mechanochemical activation can also be enhanced by controlling the hard and soft blocks within the polymer. In this approach, soft polymer chains can be aligned parallel to the tensile direction via localised stress at the hard polymer blocks<sup>261, 262</sup> or soft mechanophores and hard ligands enable mechanochemistry even under isotropic compressive force.<sup>263</sup> However, most previously reported mechanochromic polymers exhibit mechanophore activation after irreversible plastic deformation<sup>257</sup> or provide reversible stretchability at the expense of mechanosensitivity.<sup>255, 259, 264, 265</sup> For use in sensing applications, e.g. electronic skins, mechanochromic polymers with high stress sensitivity and reversible stretchability under large strain are needed. Furthermore, conventional mechanochromic polymers cannot detect high-frequency dynamic forces, which is required for multifunctional e-skins.<sup>43, 266, 267</sup> However, mechanochromic materials with all these properties are yet to be demonstrated.

Stress concentration is a phenomenon that is well demonstrated in composite materials wherein stress concentrates at the interface between mechanically dissimilar materials, inducing localised crack and failure.<sup>268</sup> In artificial and biological materials, hierarchical structures can dissipate stress from macroscale to smaller nanoscale structures, thereby enhancing mechanical strength and toughness.<sup>269, 270</sup> Thus, controlling stress concentration in hierarchical structures may enable mechanochromic polymers with high mechanosensitivity and stretchability. Herein, we introduce a hierarchical nanoparticle-in-micropore (NP-MP) architecture in porous mechanochromic composites comprising spiropyran (SP), polydimethylsiloxane (PDMS) and silica nanoparticles (SNPs; Figure. 7.1a) to

enhance force sensitivity and stretchability. In this design, the SP mechanophore undergoes a force-induced reversible ring-opening process from colourless SP to coloured merocyanine (MC).<sup>265</sup> Upon the application of external stress to the mechanochromic composites, the hierarchical NP-MP architecture induces stress concentration near the pore regions decorated with SNPs, significantly enhancing the mechanochromic sensitivity. Our porous mechanochromic composites undergo mechanochromic colour change at lower strain/stress values (tensile strain: 50%; normal force: 1 N) in comparison with composites without the NP-MP architecture (tensile strain: 150%; normal force: 6 N). Furthermore, the failure strain of the hierarchical NP-MP structure (~400%) is larger than that of the planar structure (240%), enabling reversible mechanochromic behaviour at 250% tensile strain in the hierarchical NP-MP composite. In addition, our mechanochromic e-skins are capable of the dual-mode detection of static and dynamic forces without any external power. This property allows the instantaneous visualisation of writing intensity based on colour change, the monitoring of writing speed and the detection of vibrations and acoustic sounds based on changes in triboelectric signal.

## 7.2 Experimental Details

**Fabrication of porous mechanochromic composites:** The mechanophore (SP) was prepared via the chemical reaction shown below. The synthetic procedure and characterisation are detailed in a previously published report.<sup>265, 271</sup> This alkene-functionalized spiropyran can be covalently incorporated into PDMS matrix via platinum-catalyzed hydrosilylation reaction of a PDMS curing agent.<sup>265</sup>



The fabrication of the porous PDMS/SP composites was initiated by adding SP (2 wt%) into a 10:1 mixture of PDMS (Sylgard 184, Dow Corning) and curing agent. Subsequently, hydrophilic solvents (DI water and ethanol) were added into the PDMS/SP precursor, affording PDMS: DI water: ethanol weight ratios of 3:2:0, 3:1.5:0.5 and 3:1:1. The resulting mixtures were mechanically stirred. SNPs (Polysciences) of different sizes (20, 100 and 300 nm) dispersed in DI water (1.07 wt% SNPs) were added to the mixtures of PDMS/SP precursor and solvents. The gel-type mixtures were poured into polyethylene terephthalate (PET) substrates and stored in a desiccator for 1 h to eliminate air bubbles from the PDMS. Subsequently, the prepared mixtures were annealed at 70°C for 2 h to cure the PDMS and eliminate the hydrophilic solvents, generating porous mechanochromic composites. The as-prepared composites were freeze-dried (TFD5503, ilShinBioBase) for 24 h to completely eliminate residual solvent.

**Characterisation of porous mechanochromic composites:** The structures and morphologies of the porous mechanochromic composites were observed using field-emission scanning electron microscopy (S-4800, Hitachi). Mechanical property was measured using a dynamic mechanical analyser (RSA III, TA Instruments) under a stretching velocity of 1 mm/s.

**Evaluation of the colourimetric sensing capability of the e-skins:** The mechanochromic properties of the e-skin were quantitatively evaluated as a function of pressure and strain by analysing the colour gradients ('R', 'G' and 'B') extracted from photographs using both a colour picker program (Color cop) and a spectroradiometer (PR-655, Photo Research, Inc.). Normal pressure was applied using a laboratory-built pushing tester comprised of a push-pull gauge (DFG-10, OPTECH) and a microstage system. Strain was applied using a tensile strain tester (TXA-TM, Yeonjin Corp.). A triboelectric sensor

was constructed by attaching silver nanowire flexible electrodes onto a PET substrate (thickness:  $\sim 1.3$   $\mu\text{m}$ ) on the top of the porous mechanochromic composite. The generated current and voltage outputs were collected using a source meter (S-2450, Keithley) and an oscilloscope (DPO 2022B, Tektronix), respectively. To confirm the dynamic acoustic pressure, a speaker was placed 1 cm from the e-skin and the generated voltage output induced by a sound wave with an intensity of 96.5 dB was recorded.



### 7.3 Results and Discussion

**Porous mechanochromic composites with hierarchical NP-MP architecture.** Porous mechanochromic composites with hierarchical NP-MP architectures were fabricated by mixing SP, PDMS and SNPs in hydrophilic co-solvents (water and ethanol), followed by the evaporation of solvents during the hydrosilylation curing process (Figure 7.2). During this process, spherical pores were formed within the composites as a result of phase separation between the hydrophobic PDMS matrix and hydrophilic solvents following the elimination of trapped solvents.<sup>272</sup> The porous PDMS/SP/SNP composite films were then subjected to a freeze-drying process to eliminate residual solvent (Figure 7.3). The porous PDMS/SP/SNP composite films were light yellow in colour (Figure 7.1b). The scanning electron microscopy (SEM) images in Figure 7.1b show that the porous PDMS/SP/SNP composites contained uniformly distributed pores with SNP-decorated inner pore surfaces, resulting in a hierarchical NP-MP architecture. The pore size was controllable to 5, 10 and 25  $\mu\text{m}$  (referred to as pore-5, pore-10 and pore-25, respectively) by controlling the ratio of water to ethanol (Figure 7.4 and Section S7.1). The porosity remained constant ( $\sim 36\%$ ) at the different pore sizes, whereas the surface area increased with decreasing pore size (Figure 7.5 and Section S7.1). In this study, the SNPs dispersed in hydrophilic water/ethanol droplets within the hydrophobic PDMS matrix were uniformly decorated on the inner pore surfaces during solvent evaporation (Figure 7.6a). SNPs with diameters of 20, 100 and 300 nm (referred to as SNP-20, SNP-100 and SNP-300, respectively) were uniformly decorated on the inner surfaces of the PDMS pores (Figure 7.6b, c).

#### S7.1 Control of pore size and calculation of porosity in porous mechanochromic composite

The pore size can be controlled by controlling the mixing ratio of water and ethanol. Upon increasing the ratio of ethanol in the solvent mixture, the surface tension decreases, resulting in the reduction of the size of solvent droplets in the composite (Figure 7.4a). Figures 7.4b depict the cross-sectional SEM images of the porous PDMS/SP composites with the relative mixing ratio of ethanol increases as PDMS:water:ethanol = 3:2:0, 3:1.5:0.5, and 3:1:1 in weight percent, the average pore size decreases in the order 25, 10, and 5  $\mu\text{m}$ , respectively (Figure 7.4c).

The porosity of the porous mechanochromic composites with different pore size can be calculated as follows

$$\text{Porosity (\%)} = \left(1 - \frac{\rho_m}{\rho_b}\right) \times 100$$

Where  $\rho_m$  is the material density of porous PDMS/SP composite and  $\rho_b$  is the bulk density of PDMS/SP composite taken as  $1.07\text{g/cm}^3$ . The material densities depending on porous structures are estimated by measuring the dimensions (area and thickness) and mass (Figure 7.5a,b). The calculated porosities are approximately constant ( $\sim 36\%$ ) regardless of the pore size, whereas the surface area increases as the pore size decreases (Figure 7.5c).

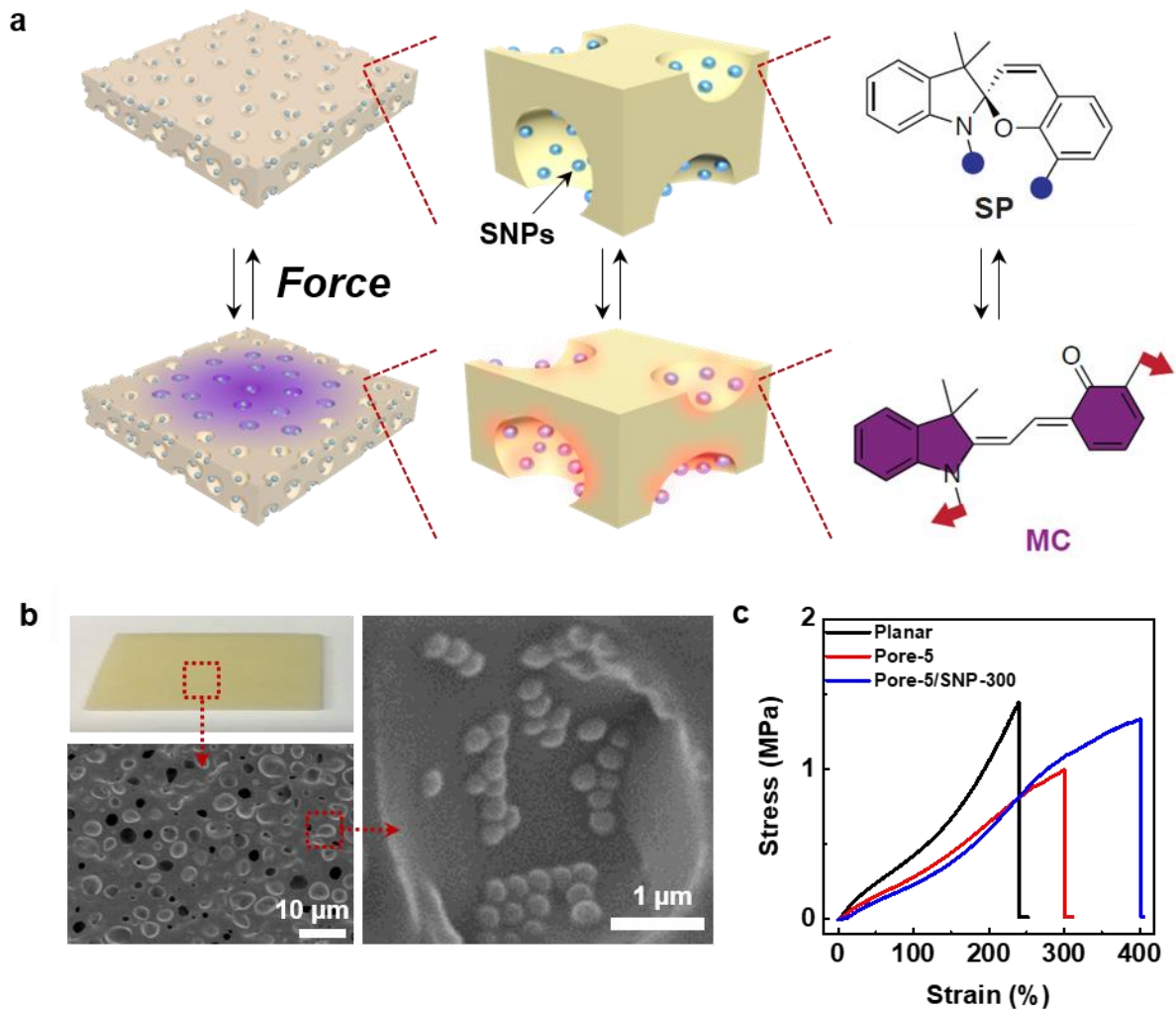


**Figure 7.1.** Hierarchical NP-MP architecture in porous mechanochromic composites. (a) Schematic of the working mechanism of porous mechanochromic composites with hierarchical NP-MP architecture. (b) Photograph and SEM images of porous (pore-5) mechanochromic composites comprising PDMS, SP and 300-nm SNPs (SNP-300). The SEM images show uniform spherical pores and SNPs decorated on the inner pore surfaces. (c) Stress–strain behaviours of the stretchable mechanochromic polymers with planar, porous and SNP-decorated porous structures.

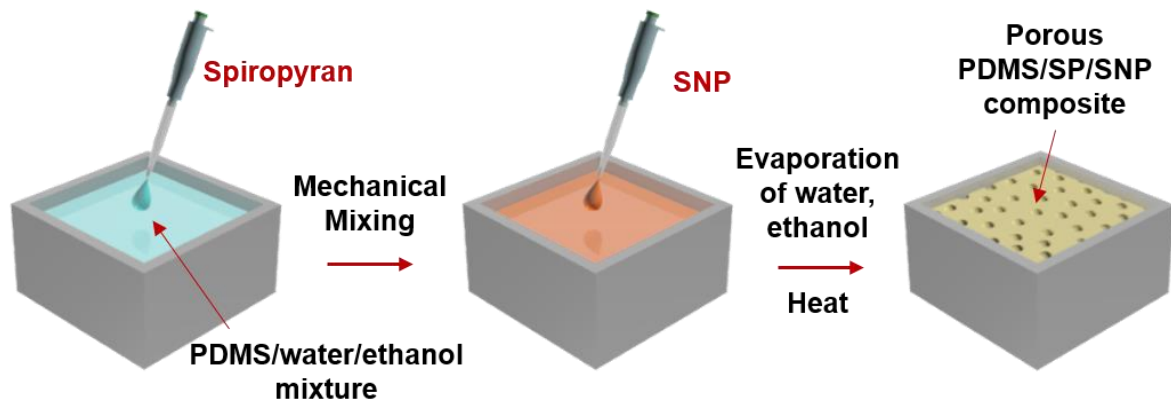


**Figure 7.2.** Schematic of the fabrication procedure for porous mechanochromic composites with PDMS/SP/SNPs. SP, PDMS and SNPs are mixed in hydrophilic co-solvents (water and ethanol) and solvents are evaporated during the hydrosilylation curing process.

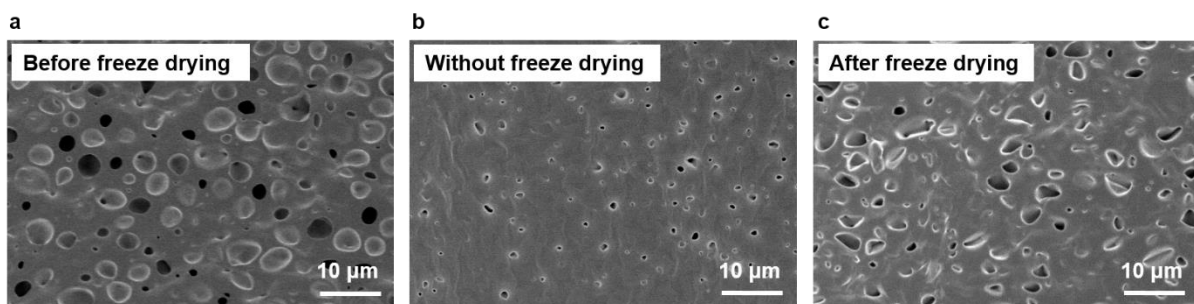


**Figure 7.3.** (a) Scanning electron microscope (SEM) image of a porous mechanochromic composite with an average pore size of 5  $\mu\text{m}$  before freeze-drying. SEM images of a fabricated porous mechanochromic composite after three days before (b) and after (c) freeze-drying. Due to the capillary force-induced pore closure during solvent evaporation, freeze-drying is required to completely evaporate the solvent and obtain uniform pores.

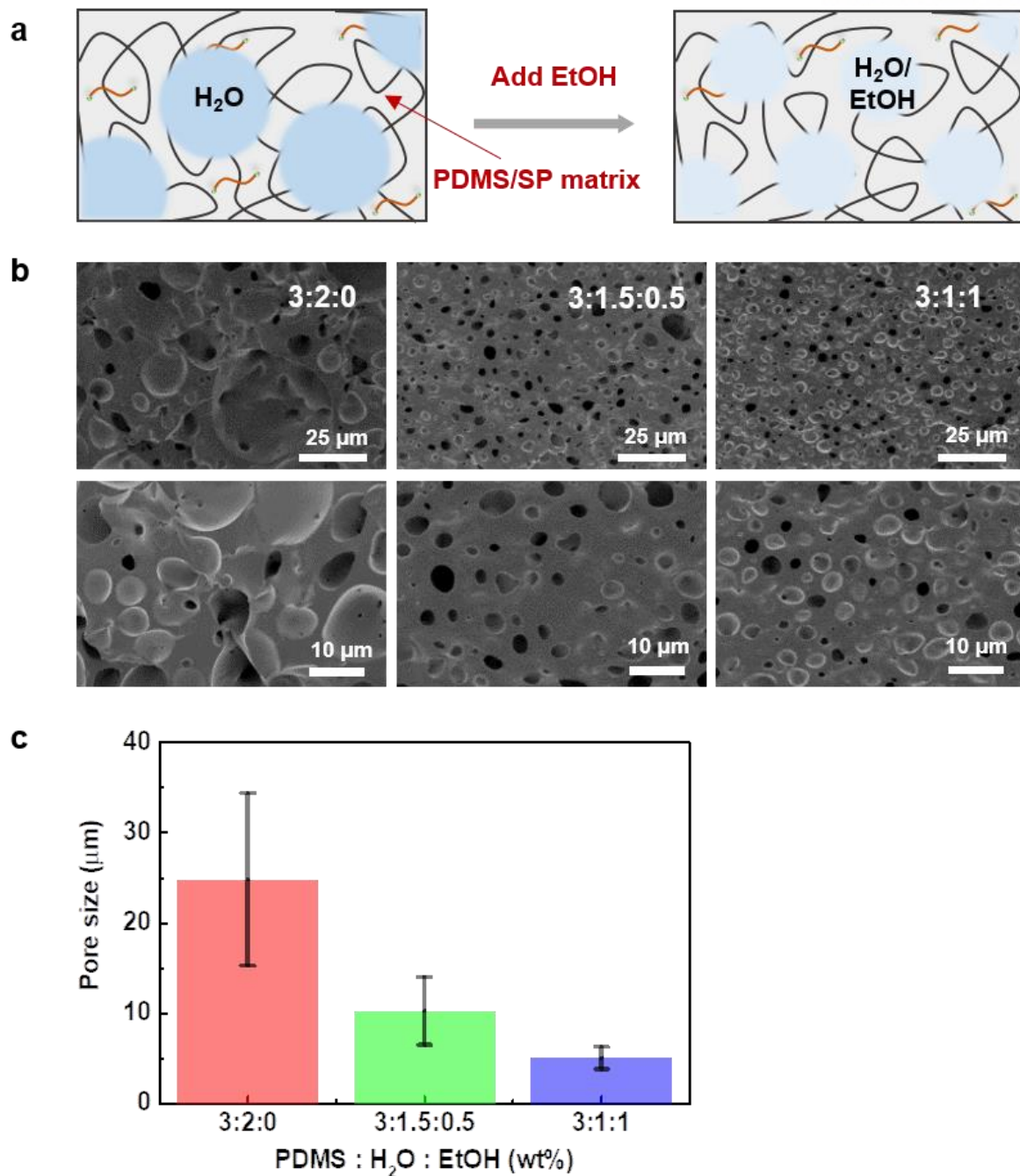


**Figure 7.4.** (a) Schematic of the mechanism of pore formation in composites based on the addition of hydrophilic solvents. (b) Cross-sectional SEM images of porous PDMS/SP composites with different mixed solvent ratios (PDMS:water:ethanol = 3:2:0, 3:1.5:0.5 and 3:1:1). The lower row shows magnified SEM images. (c) Pore size distributions of porous PDMS/SP composites with different mixed solvent ratios.

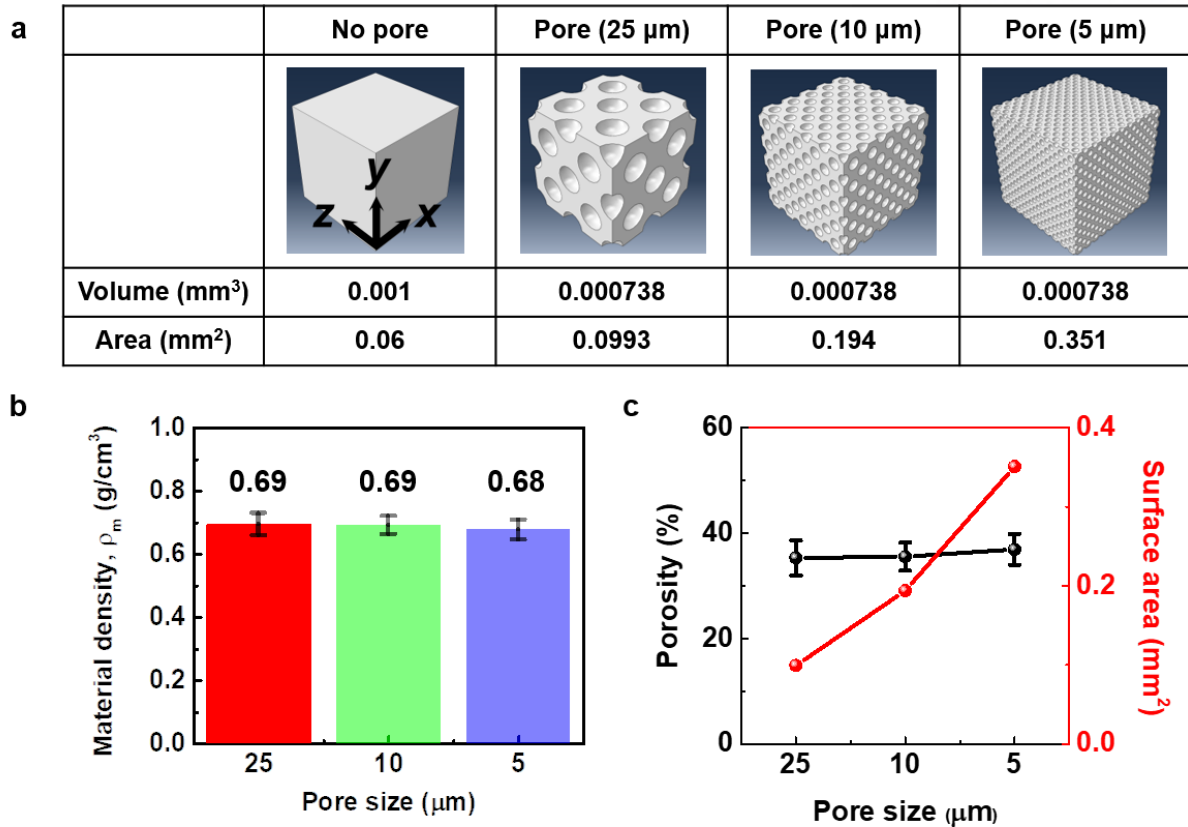


**Figure 7.5.** (a) Simulated surface areas of porous mechanochromic composites with different pore sizes based on face-centered cubic (FCC) unit cell arrays. The porous structures are modelled according to average pore sizes of 25, 10 and 5  $\mu\text{m}$  with the same porosity (26%) based on FCC unit cell arrays. Volume is determined as the total material volume, excluding the pore volume. Area is the total surface area of the porous structure. (b) Material densities of the fabricated porous mechanochromic composites with different pore sizes. (c) Porosity and surface area of porous mechanochromic composites as functions of pore size.

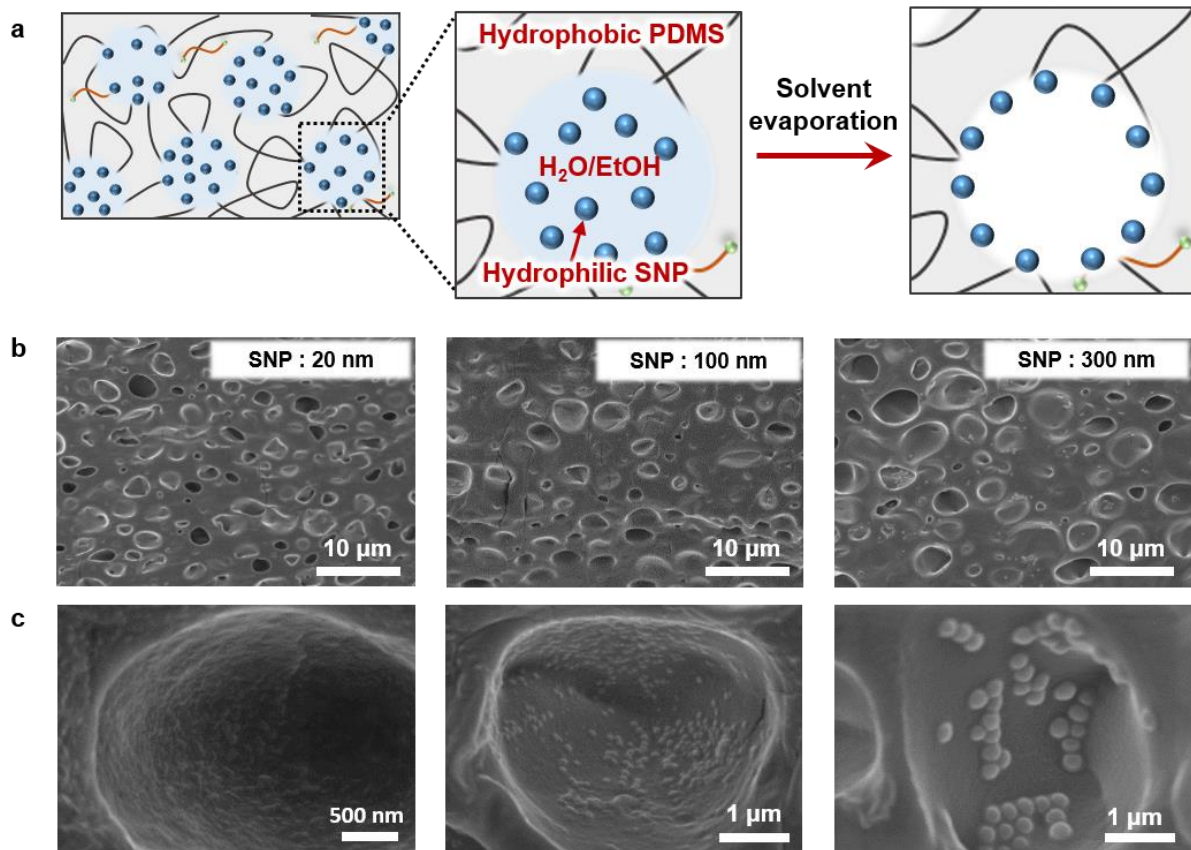


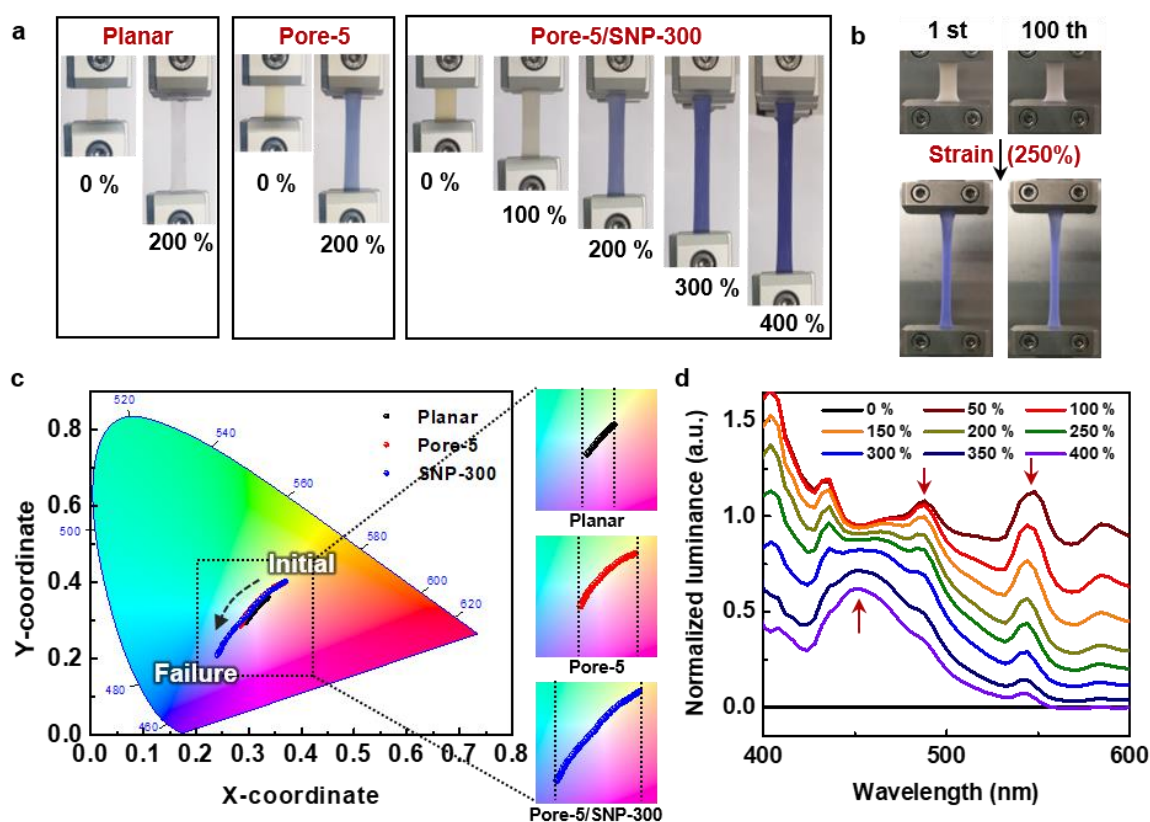
**Figure 7.6.** (a) Schematic of SNP decoration on the inner pore surfaces of a mechanochromic composite during heat-induced solvent evaporation. (b) Cross-sectional SEM images of porous PDMS/SP composites (pore size = 5 μm) with different SNP sizes (20, 100 and 300 nm). (c) Magnified SEM images showing that the SNPs are uniformly decorated on the inner pore surfaces.

**Structure-dependent mechanochromic properties in response to tensile strain.** The hierarchical NP-MP architecture significantly affects the mechanical properties of the mechanochromic composite. Compared to the planar structure, the porous structure enhances the maximum strain and decreases the maximum stress (Figure 7.1c). The decoration of the porous composite with SNPs further increases the stretchability and maximum stress; this effect is attributed to the increase in energy dissipation induced by localised stress in the hierarchical NP-MP architecture.<sup>269, 270, 273</sup> The maximum strain of the porous composite increases with decreasing pore size (Figure 7.8a), which can be attributed to the large number of sites that dissipate mechanical energy via pore–stress interaction.<sup>274</sup> The maximum strain of the porous composite increases with increasing SNP size (Figure 7.8b), which is attributed to the enhanced load-bearing ability with increasing SNP size in hierarchical structures.<sup>269, 275</sup>

We monitored the changes in the colour of mechanochromic polymers under tensile strain using a spectroradiometer (Figure 7.9). Compared to planar PDMS/SP polymers, the porous PDMS/SP/SNP composites undergo a distinct colour change from pale yellow to blue at 200% tensile strain, indicating the mechanochemical ring-opening reaction of SP into MC (Figure 7.7a). As the pore size decreases, the critical strain needed to observe the colour change decreases, while the intensity of the blue colour and stretchability increases (Figure 7.10). For pores decorated with SNPs, a further colour change to a vivid blue colour is observed (Figure 7.11). Amongst the tested composites, the composite with small pores (5  $\mu\text{m}$ ) and large SNPs (300 nm) exhibits the greatest colour change in response to a large range of strain ( $\sim 400\%$ ; Figure 7.7a). The pore-5/SNP-300 composite displays a reversible and highly stable mechanochromic response for up to 100 cycles under a tensile strain of 250% (Figure 7.7b and Figure 7.12).

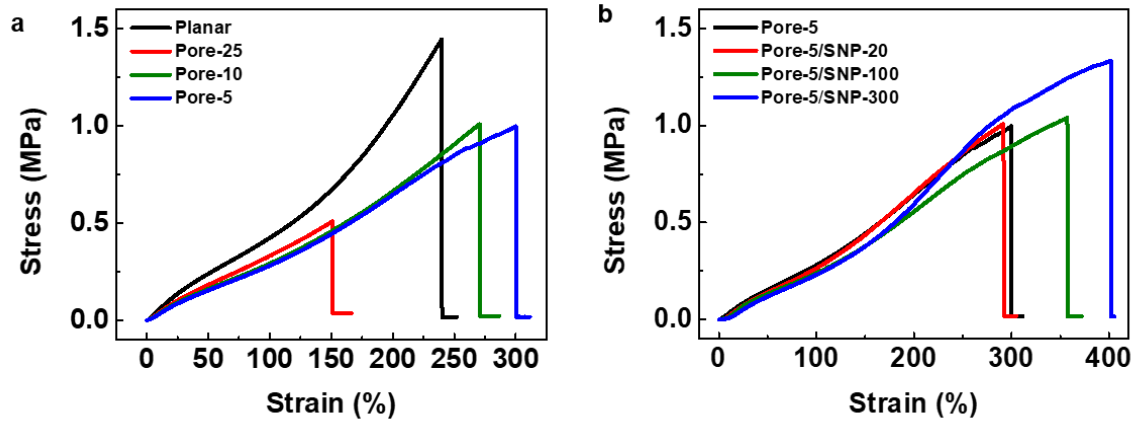
The detailed colour changes of the mechanochromic polymers were further investigated by analysing the changes in the average colour coordinates based on the CIE 1931 colour space diagram (Figure 7.7c). Compared to planar PDMS/SP polymers, porous PDMS/SP polymers exhibit a larger colour transition range, and this range is further increased by decoration with SNPs. This behaviour is ascribed to the effective stress concentration near the hierarchical NP-MP region in the composite by the support of nanoscale hard SNPs at the inner pore surface against the local stress around the microscale pore region. In addition, the improved stretchability increases the colour transition range of the porous composite. The colour transition range increases gradually with decreasing pore size and increasing SNP size (Figure 7.13). For different tensile strains, the porous composites with pore-5/SNP-300 clearly exhibit distinct luminescence spectra in the visible wavelength range in which the peaks in 420–480 nm (blue) significantly increase, whereas those in 500–600 nm are dissipated (Figure 7.7d), supporting the blue colour transition with the tensile strain. The time required for recovery from MC to SP depends on the strain. Figure 7.14a shows that the intensity of the green colour decreases with increasing strain and becomes saturated under fixed strain. Upon releasing the strain, the saturated colour returns to the

original colour after a delay of ~2, 14, and 35 s for the strains of 125%, 150%, and 175%, respectively. Thus, the recovery time decreases with increasing tensile strain. The recovery times of our porous mechanochromic composites compare favourably with those of previous mechanochromic polymers (2–60 min; Table 7.1).<sup>255, 265, 276, 277</sup> Exposing the sample to white light can shorten the recovery time (Figure 7.14b). The ring-closing reaction from MC back to SP can be accelerated by heating or visible-light irradiation.<sup>278</sup>



**Figure 7.7.** Properties of porous mechanochromic composites under tensile strain. (a) Photographs of mechanochromic polymers with different structures exhibiting colour changes in response to tensile strain. (b) Colour change of the pore-5/SNP-300 mechanochromic composite at the first and 100th stretching and releasing cycles. (c) Changes in the average colour coordinates of the mechanochromic polymers with different structures under applied tensile strain. (d) Normalised luminance as a function of wavelength for the pore-5/SNP-300 mechanochromic composite under tensile strains up to 400%.







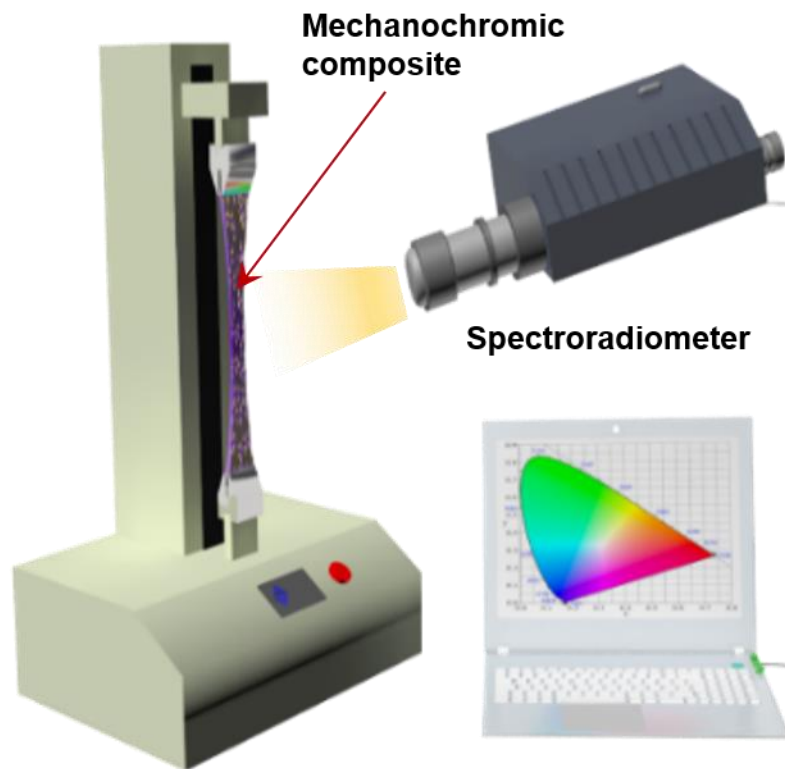















**Figure 7.8.** (a) Strain–stress curves of porous PDMS/SP composites with different pore sizes. (b) S–S curves of porous PDMS/SP composites (pore size = 5  $\mu\text{m}$ ) with different SNP sizes.

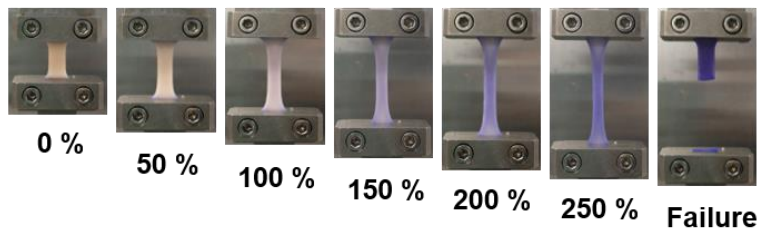


**Figure 7.9.** Schematic of a measurement system using a spectroradiometer for investigating the colour transition properties of porous mechanochromic composites in response to tensile strain.

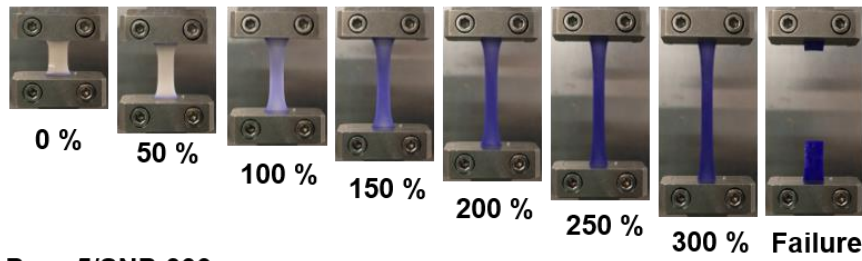
Tensile strain	0 %	50 %	100 %	150 %	200 %	Failure
Porous (25 $\mu\text{m}$ )						
Porous (10 $\mu\text{m}$ )						
Porous (5 $\mu\text{m}$ )						

**Figure 7.10.** Photographs showing the colourimetric strain sensing properties of porous mechanochromic composites with different pore sizes.

**a Pore-5/SNP-20**



**b Pore-5/SNP-100**



**c Pore-5/SNP-300**

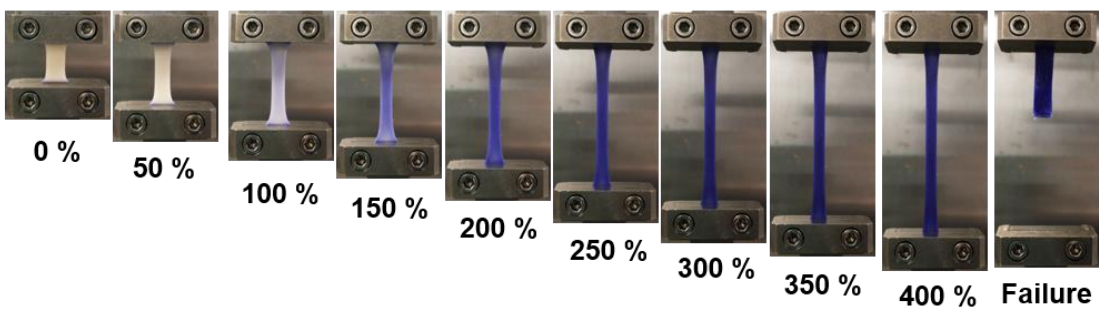


**Figure 7.11.** Photographs showing the colourimetric strain sensing of porous PDMS/SP composites (pore size = 5  $\mu\text{m}$ ) decorated with SNPs with different sizes: (a) 20 nm, (b) 100 nm and (c) 300 nm.

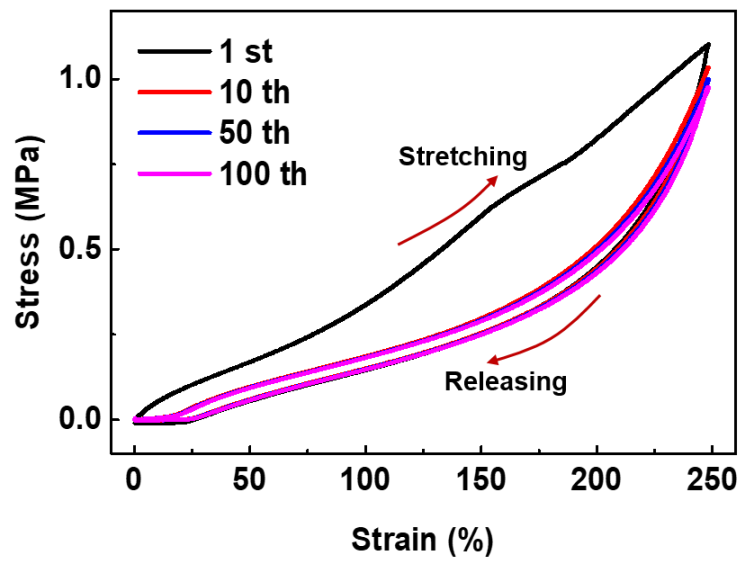


**Figure 7.12.** Strain–stress curves of a porous mechanochromic composite (pore size = 5  $\mu\text{m}$ ; SNP size = 300 nm) under repeated loading/unloading strain of up to 250%.

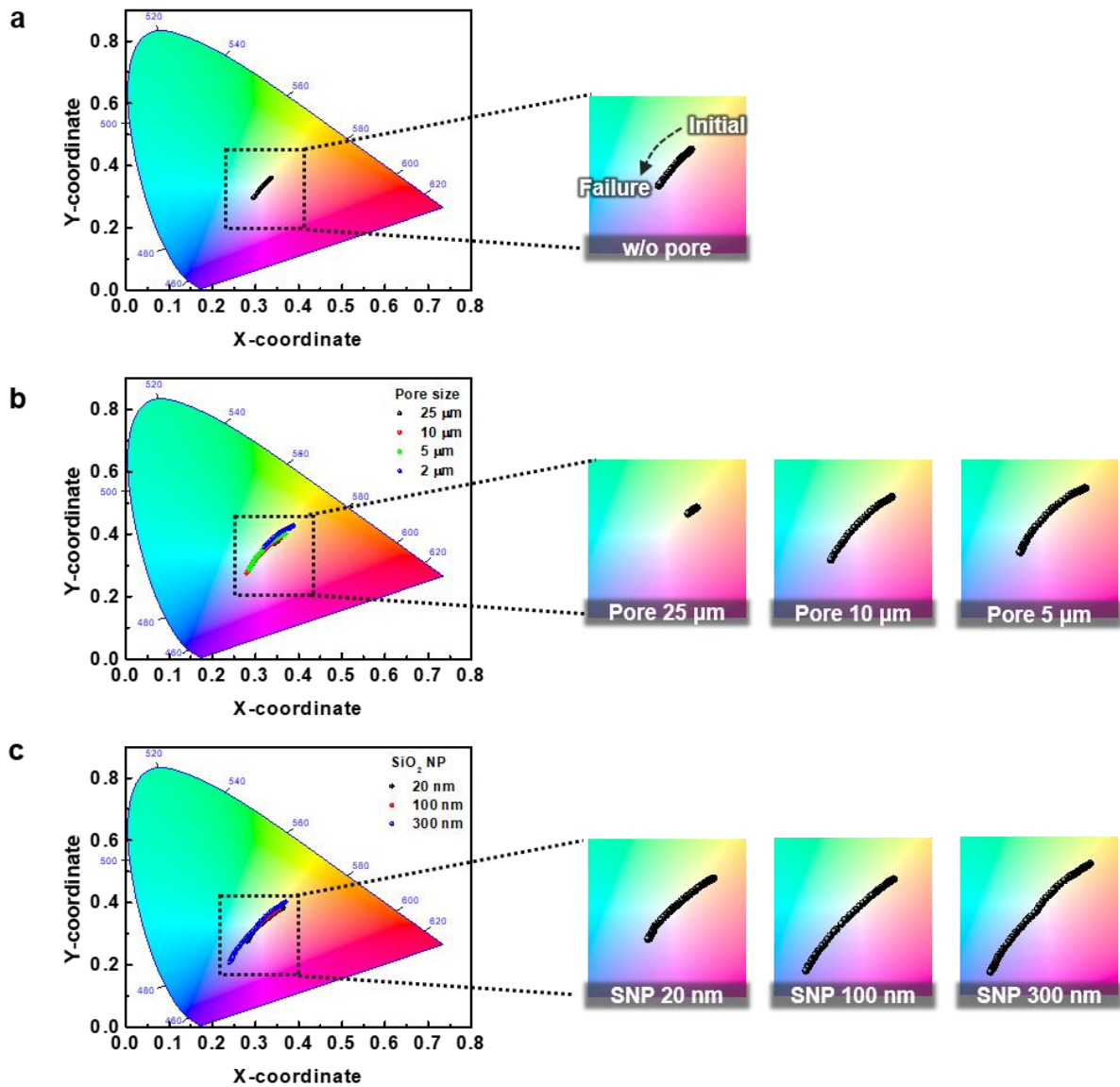


**Figure 7.13.** (a) Average colour coordinates of planar mechanochromic composites under loading tensile strain. (b) Average colour coordinates of porous mechanochromic composites with different pore sizes under loading tensile strain. (c) Average colour coordinates of mechanochromic composites with different SNP sizes under loading tensile strain.

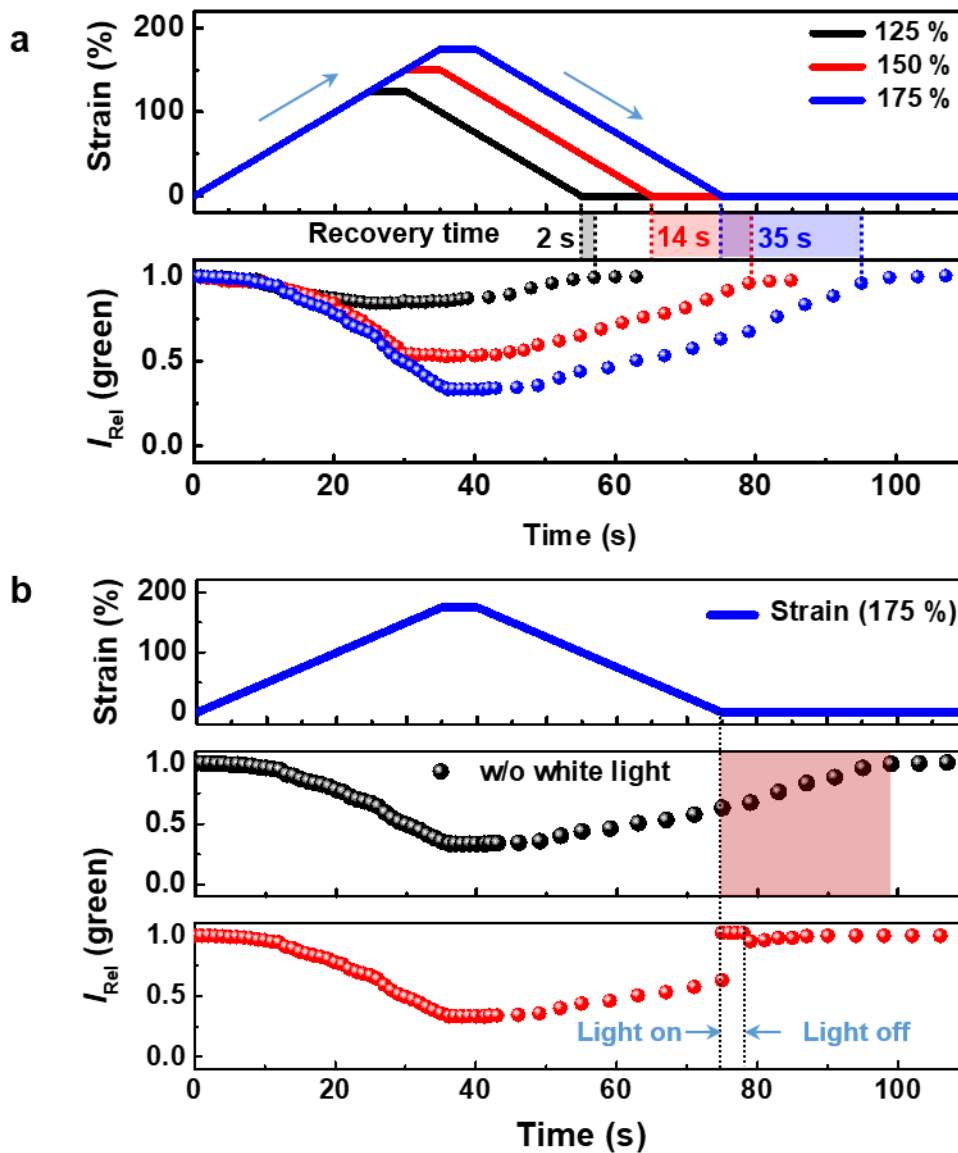


**Figure 7.14.** Recovery time of a porous mechanochromic composite (pore size = 5  $\mu\text{m}$ , SNP size = 300 nm) under different tensile strains. (a) Time-dependent tensile strains of 125%, 150% and 175% (top) and the corresponding change in relative intensity ( $I_{\text{Rel}}$ ) of green colour in response to loading strain (bottom). (b) Relaxation under a loading/unloading strain of 175% depending on exposure to white light.

**Table 7.1.** Summary of recently reported mechanophore systems.

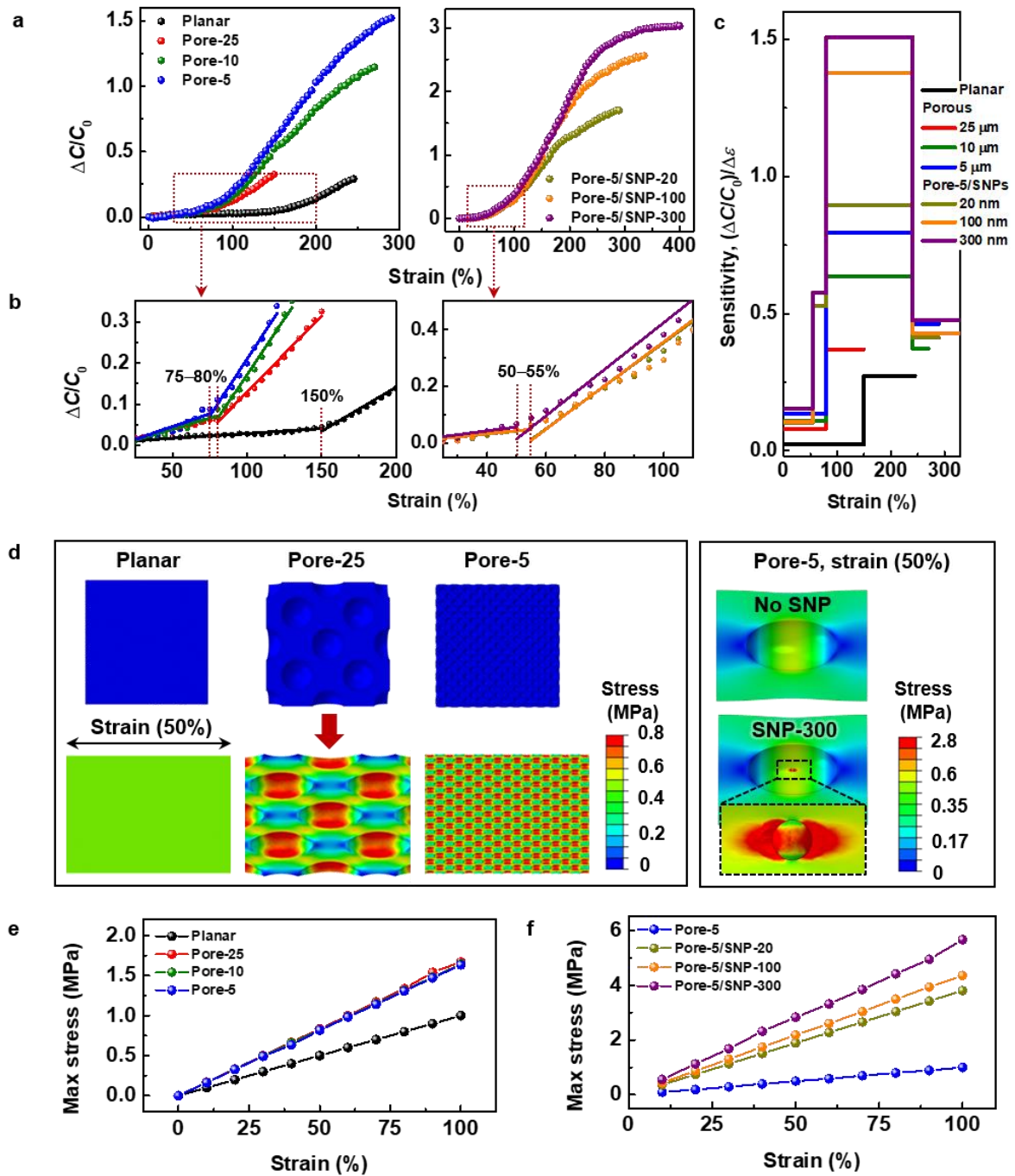
Journal	Materials	Critical strain	Critical pressure	Maximum strain	Recovery time	Ref.
Nature (2009)	SP/PMMA	200%	<50 MPa	1000% (reversible)	-	[246]
ACS Macro Lett. (2014)	SP/PDMS	75%–100%		200% (reversible)	1 h (w/o light); 10 s (with light)	[265]
ACS Macro Lett. (2015)	Diarylbibenzofuranone/ PU	50%		>300% (reversible)	-	[254]
Polymer (2016)	SP/PMA	259%		350% (reversible)	12 min	[276]
ACS Macro Lett. (2013)	SP mechanophore linked triblock copolymers	>600%		>1000% (irreversible)	-	[262]
Macromolecules (2013)	SP-linked segmented PU	200%		>550% (reversible)		[279]
Macromolecules (2014)	Dual crosslinked SP/PU composite	500%		900% (reversible)	-	[264]
ACS Macro Lett. (2014)	SP/ureidopyrimidinone (Supramolecular interaction)	500%		1000% (reversible)	-	[261]
Adv. Mater. (2017)	SP-crosslinked poly(AM-co-MA/SP) hydrogel	>100%		570% (reversible)	30 min (with light)	[255]
Adv. Mater. (2015)	Rhodamine/PU		375 MPa	- (reversible)	-	[280]
Adv. Mater. (2016)	Mechanochromic molecule-epoxy composite	14%		49% (irreversible)		[257]
Adv. Mater. (2018)	P(SP- <i>alt</i> -C <sub>10</sub> ) nanofiber/PDMS	~10%		70% (irreversible)	120 s	[277]
<b>This work</b>	<b>Porous SP/PDMS/SNPs</b>	<b>50%</b>	<b>1 MPa</b>	<b>400% (reversible)</b>	<b>35 s (w/o light); 3 s (with light)</b>	

To quantitatively analyse the strain sensitivity of mechanochromic composites, we monitored the changes in the intensity of red–green–blue (RGB) colour parameters under tensile strain (Figure 7.16). For the accurate investigation of colour change, the relative B/G intensity ratios ( $\Delta C/C_0$ , where  $C$  is the B/G colour intensity ratio) were analysed for mechanochromic polymers with different structures under tensile strain (Figure 7.15a). Compared to the nonporous planar structure, the porous structures exhibit larger colour intensity ratio, indicating a more vivid colour change in the porous structures. The pore-5 structure exhibits the maximum colour intensity ratio of 1.5, which is five times higher than that of the planar structure (0.3). Decorating the pore-5 composite with SNPs further improves the colour intensity ratio to 3.0, which is 10 times higher than that of the planar structure. In addition to the large colour change, the porous structure displays an initial variation in the colour intensity ratio at a critical strain of 75–80%, which is  $\sim 2$  times lower than that of the planar structure (150%; Figure 7.15b). Decorating the pore walls with SNPs further decreases the threshold strain to 50–55%. The critical strain of 50% for the pore-5/SNP-300 composite is significantly lower than those of previous stretchable (stretchability > 200%) mechanochromic polymers based on SP mechanophores (critical strains of 75–500%; Table 7.1).<sup>246, 255, 264, 265, 276, 279</sup> Only the hard mechanochromic polymer with the irreversible stretchability of 70% exhibits a lower critical strain (10%).<sup>277</sup> To quantitatively analyse mechanochromic sensitivity, strain sensitivity ( $S$ ) was calculated as  $S = (\Delta C/C_0)/\Delta\varepsilon$ , where  $\varepsilon$  is the applied strain (Figure 7.15c). For strain of 50–80%, all porous composites with SNPs show higher sensitivities (0.53–0.58) compared to the porous polymers without SNPs (0.08–0.14) and the planar structure (0). In the strain regime of 80%–240%, the pore-5/SNP-300 composite exhibits the highest sensitivity of 1.51, which is  $\sim 4.1$  and  $\sim 5.6$  times higher than those of porous composites without SNPs (0.37–0.8) and the planar composites (0.27), respectively.

To evaluate the stress concentration near the hierarchical NP-MP architecture, which significantly enhances the mechanochromic sensitivity, we further examined the strain–stress relationships by numerical finite-element analysis (FEA). Unlike the planar structure in which stress is homogeneously distributed throughout the matrix, the porous structure has a high stress concentration in the pore region (Figure 7.15d, left). Compared to the planar structure, the porous structures all exhibit higher maximum localised stress at strains up to 100% (Figure 7.15e and Figure 7.17). Furthermore, the porous structure with the smallest pore size amongst the samples possesses the highest PDMS/air surface area, resulting in a greater number of mechanochromic activation sites of concentrated stress near the interface (Figure 7.17). This produced a considerable enhancement in colour change and strain sensitivity, as shown in Figure 7.15a–c. For the porous composites decorated with SNPs, additional stress concentration occurs in the pore region near the SNPs because of the load-bearing support provided by the hard SNPs at the inner surfaces of the soft pores (Figure 7.15d, right). Furthermore, the maximum localised stress near the SNPs gradually increases with SNP size (Figure 7.15f and Figure 7.18), thereby enhancing

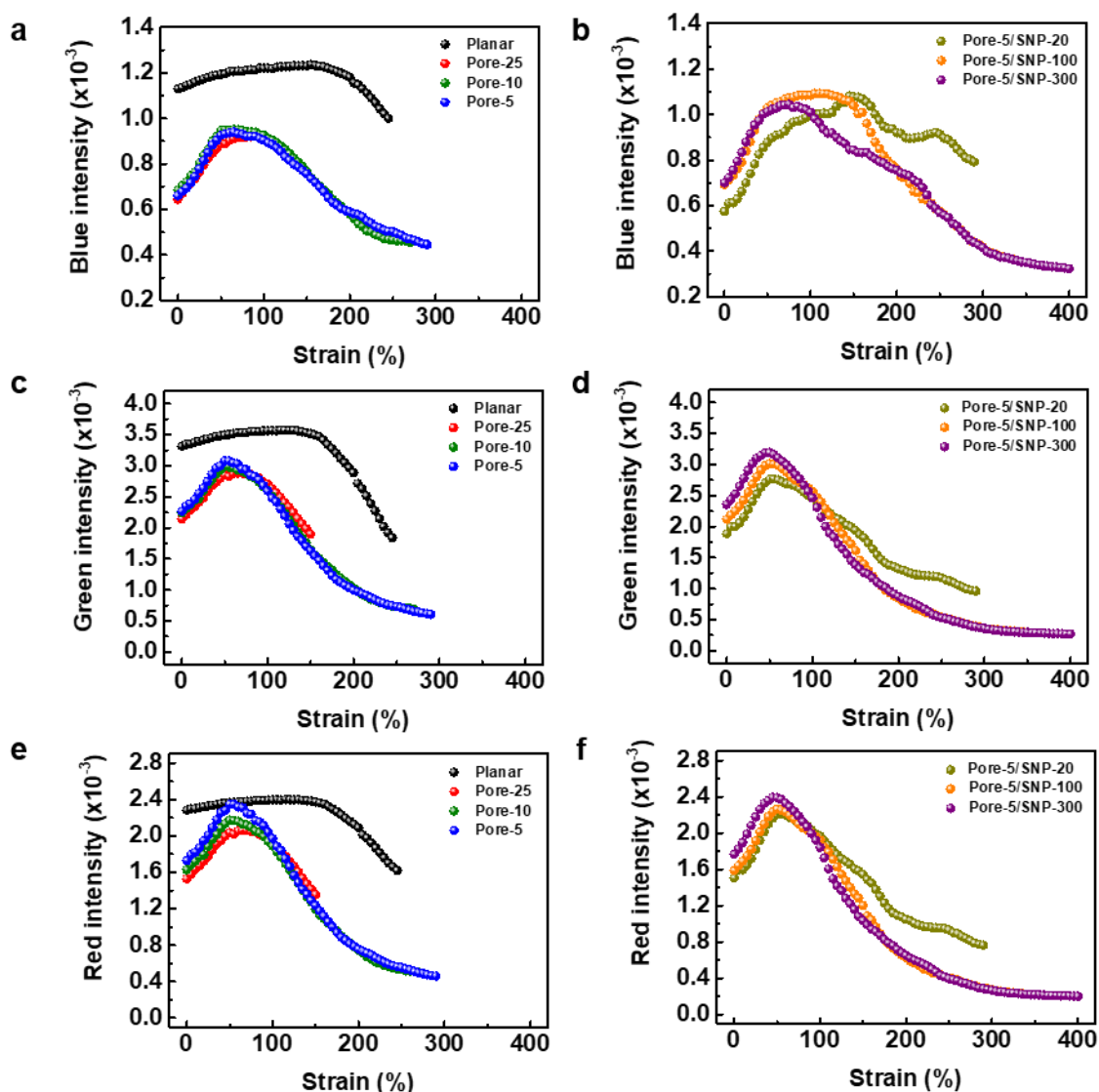


mechromic sensitivity (Figure 7.15a–c). Based on the FEA results, we can conclude that both the amount of activation sites and the maximum stress localised around the pores and SNPs determine the overall mechromic sensing properties (relative colour intensity and strain sensitivity).

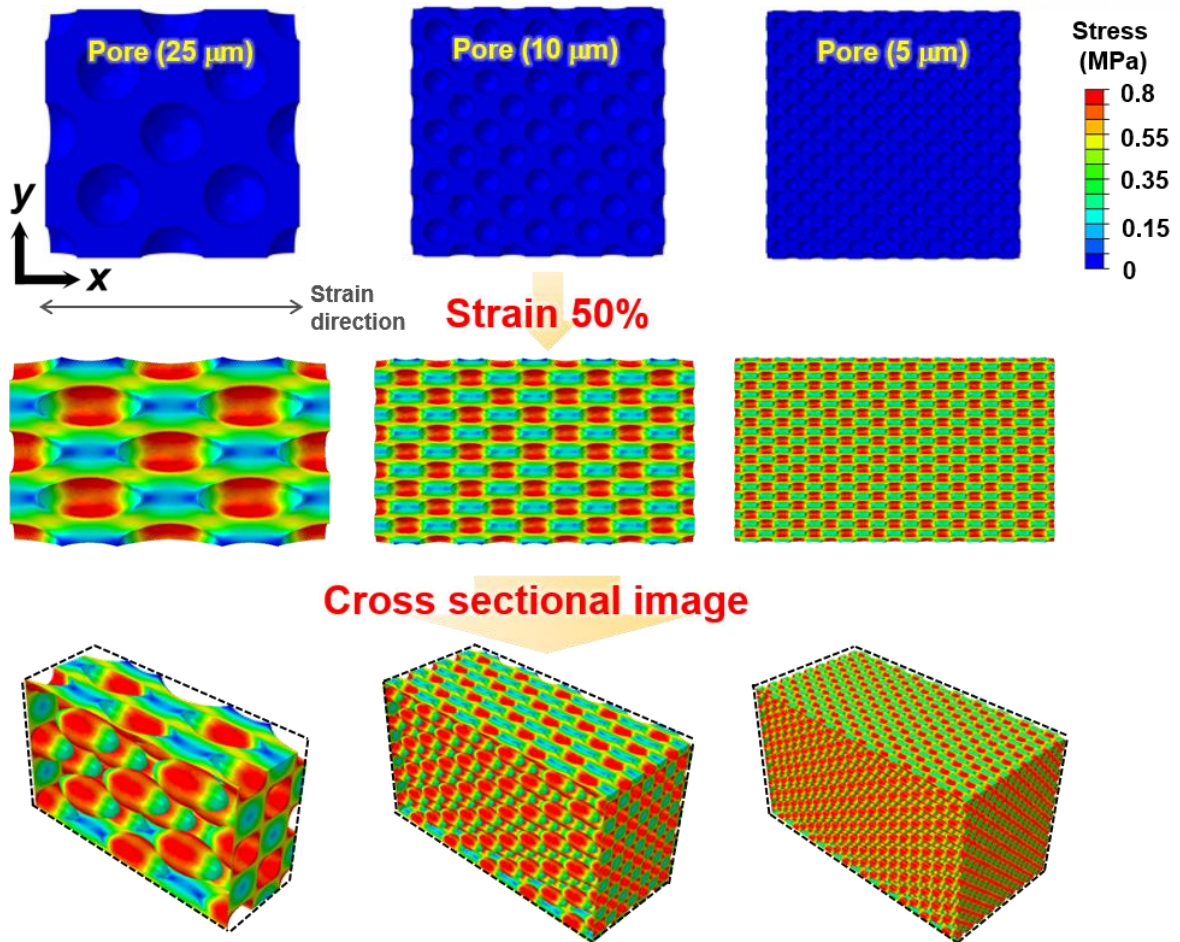


**Figure 7.15.** Structure-dependent strain sensitivity of porous mechanochromic composites. (a) Normalised colour intensity ratio as a function of strain for mechanochromic polymers with different pore sizes (left) and with different SNP sizes at a pore size of 5  $\mu\text{m}$  (right). The colour intensity in response to strain is measured by spectroradiometer. (b) Enlarged plot from (a) in the strain range 20%–100%. (c) Strain sensitivity [ $S = (\Delta C/C_0)/(\Delta \epsilon)$ , where  $C$  is the colour intensity ratio and  $\epsilon$  is the applied strain] of mechanochromic polymers with different structures. Sensitivity is estimated from the plot in (a) for the linear regimes of mechanochromic response. (d) Finite-element analysis (FEA)-determined

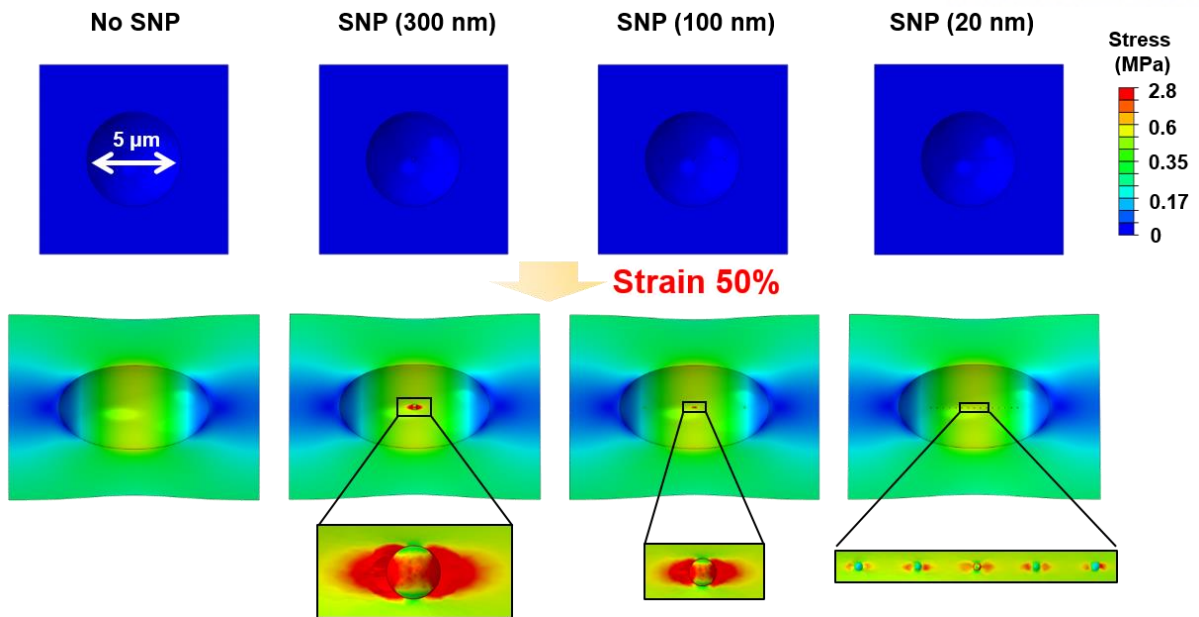
stress distributions of mechanochromic polymers with different pore sizes (left) and with 300-nm SNPs and a 5- $\mu\text{m}$  pore size (right) under a tensile strain of 50%. (e, f) FEA-determined maximum localised stress near the pore surface in porous mechanochromic polymers with (e) different pore sizes and (f) different SNP sizes and a pore size of 5  $\mu\text{m}$  as a function of strain (see Figures 7.17 and 7.18 for additional details).



**Figure 7.16.** Variation in colour component intensities (R, G and B) of porous mechanochromic composites under loading strain at different wavelengths: (a, b) 488 nm, (c, d) 544 nm and (e, f) 612 nm. The intensity of each colour component initially increases because of the decrease in light absorption caused by the concurrent decrease in film thickness. The intensity subsequently decreases because of the colouration of SP.



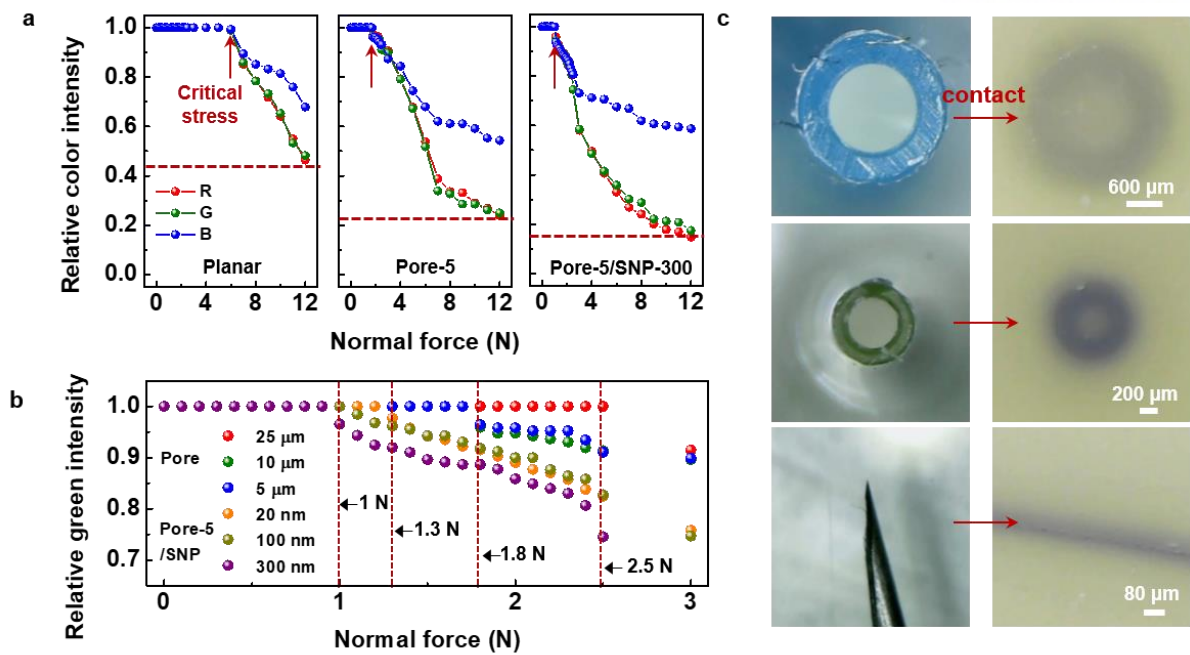
**Figure 7.17.** Stress distributions of porous PDMS/SP composites with different pore sizes (25, 10 and 5  $\mu\text{m}$ ) placed under 50% tensile strain calculated numerically using ABAQUS software. For simplicity, the elastic modulus is set to 1 MPa with the same porosity (26%) for all porous composites (see Figure 7.5 for the initial system configuration).



**Figure 7.18.** Stress distribution of porous PDMS/SP composites (pore size = 5 μm) decorated with SNPs with different sizes (300, 100 and 20 nm) placed under 50% tensile strain calculated numerically using ABAQUS software. For simplicity, to understand the role of the SNPs at the pore walls, the elastic modulus of the porous matrix is set to 0.24 MPa (consistent with the experimental data shown in Figure 7.8). The elastic modulus of the SNPs is set to a general value of 180 GPa for all sizes.

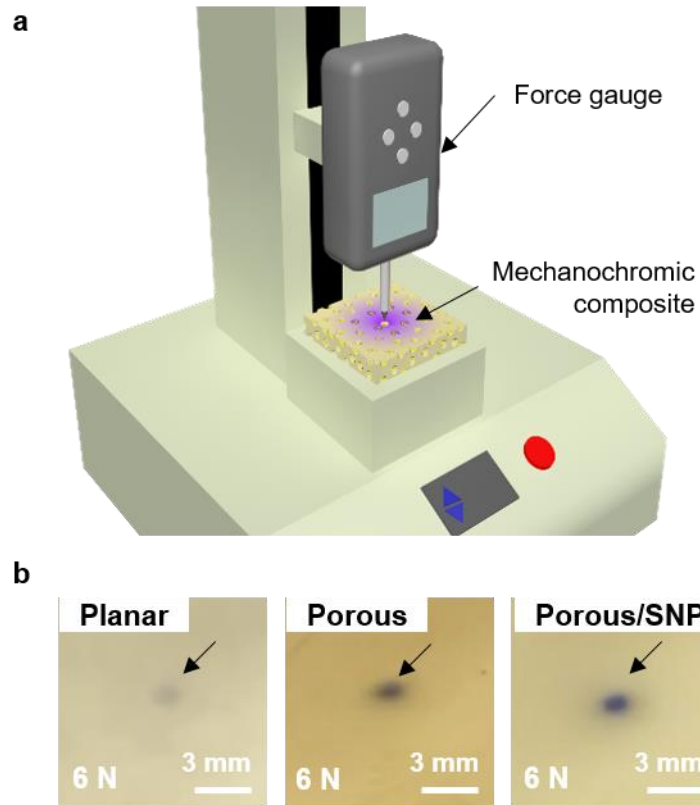
**Structure-dependent mechanochromic property in response to normal force.** The hierarchical NP-MP architecture of the mechanochromic composites also enhances the mechanochromic sensitivity in response to normal force in addition to tensile strain. This property allows the composites to be applied in touch-sensitive mechanochromic e-skins.<sup>281</sup> We evaluated the changes in the RGB colour parameters of the composites in response to normal forces applied using a force gauge (Figure 7.20a). Under a normal force of 6 N, the porous PDMS/SP/SNP composites exhibit more vivid mechanochromic colour than the planar and porous structures (Figure 7.20b). Compared to the planar and porous structures, the changes in the relative red intensities were larger for the hierarchical NP-MP structures, indicating a more vivid colour change (Figure 7.19a). The relative red intensity decreased from 0.42 to 0.24 in conjunction with decreasing pore size (Figure 7.21a). This phenomenon is attributed to the increase in the area of stress concentration with decreasing pore size (Figure 7.21b). Meanwhile, decorating the porous structures with SNPs further increases the dynamic colour transition range to 85% (relative red intensity of 0.15 in Figure 7.19a) over a wide range of force (1–12 N). Amongst the composites with different SNP sizes, the composite with the largest SNPs (300 nm) exhibits the largest colour variation (85%) without saturation (Figure 7.22a).

Figure 7.19b shows the relative changes in the intensity of the green colour under different normal forces in increments of 0.1 N. With decreasing pore size, the critical stress required for the initial colour transition is reduced from 2.5 N (pore-25) to 1.8 N (pore-5). Decorating the pores with 300-nm SNPs further improves the pressure sensitivity, thus enabling detection at a minimum force of 1 N, six times lower than the minimum detection force of planar polymers (6 N). The improvement in mechanochromic sensitivity achieved by the addition of SNPs is attributed to the drastic increase in localised stress near the hard SNPs. The FEA calculations indicate that amongst the tested SNPs, the 300-nm SNPs exhibit the strongest localised stress in response to normal force (Figure 7.22b). The low detection limit (1 N or 1 MPa) represents a significant enhancement (~50 times increase) over previously reported mechanochromic polymers (50 and 375 MPa; Table 7.1).<sup>246, 280</sup> The porous mechanochromic composites reported herein also provide a high lateral resolution for force sensing, enabling the mapping of local pressure distribution without the need for complex sensor array patterns. Figure 7.19c shows the optical mechanochromic pressure maps after contact with various microscale objects. The pressure-induced local colour distribution patterns match the shape and wall thickness of the round microtips. The mechanochromic e-skins exhibit a minimum line width of 80  $\mu\text{m}$  for contact with a needle tip.



**Figure 7.19.** Normal force detection capabilities of porous mechanochromic composites. (a) Relative intensities of the colour components (red, green and blue) of mechanochromic polymers with different structures as functions of normal force. The colour intensity in response to normal force is measured by I-phone camera and colour picker program. (b) Relative green intensity as a function of normal force for mechanochromic polymers with different pore sizes and different SNP sizes with 5-µm pores. (c) Optical images showing the local colour distributions of the porous mechanochromic composites after contact with various objects (microtips and needle).





**Figure 7.20.** (a) Measurement system used to evaluate the colour transition properties of porous mechanochromic composites in response to normal stress. (b) Photographs of the mechanochromic composites with different porous structures under a loading normal stress of 6 N.

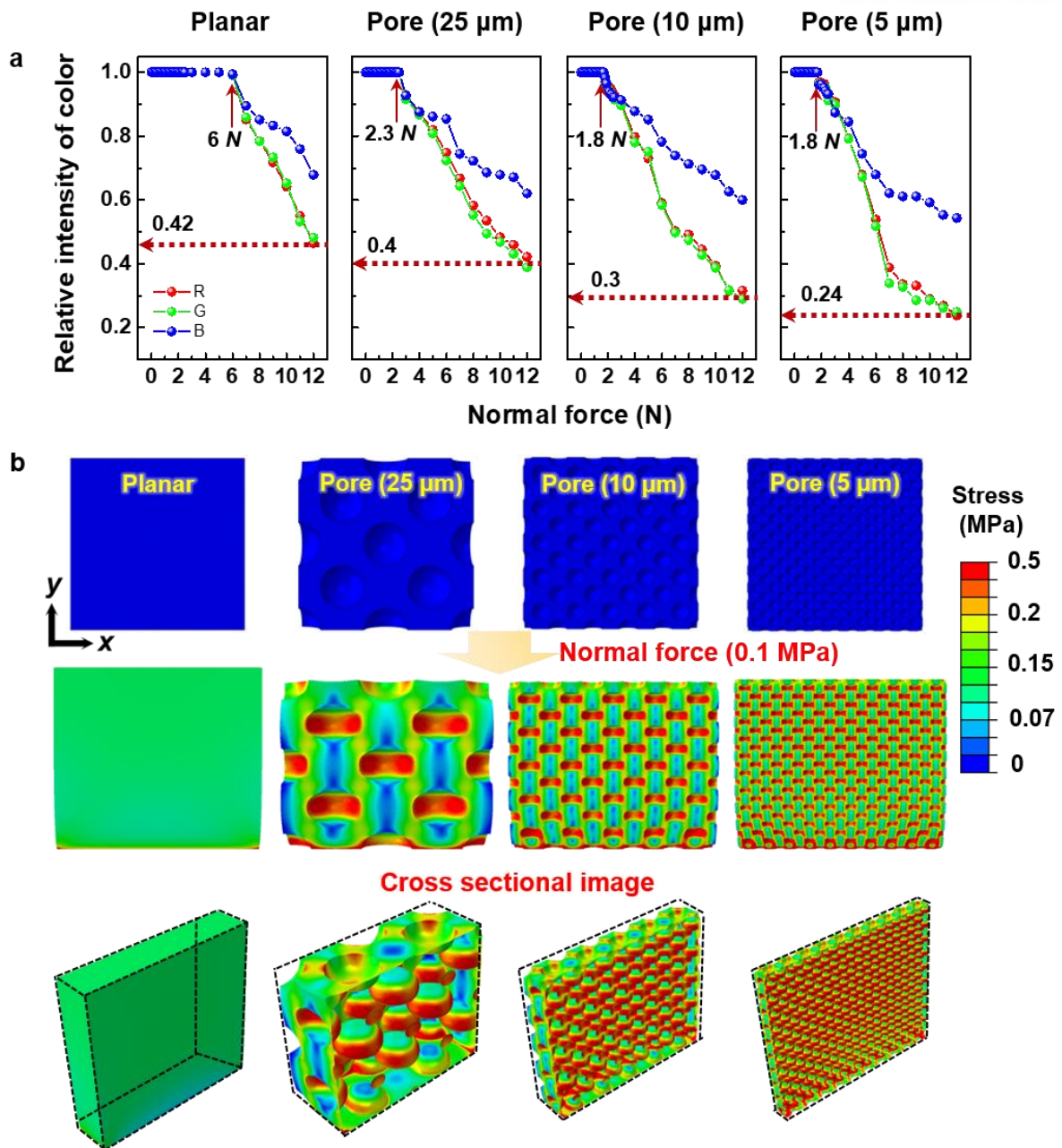


**Figure 7.21.** (a) Relative colour changes of porous PDMS/SP composites with different pore sizes in response to applied normal pressure. (b) Finite-element analysis-determined stress distributions in porous PDMS/SP composites with different pore sizes under applied normal pressure. The simulation conditions are identical to those in Figure 7.17.

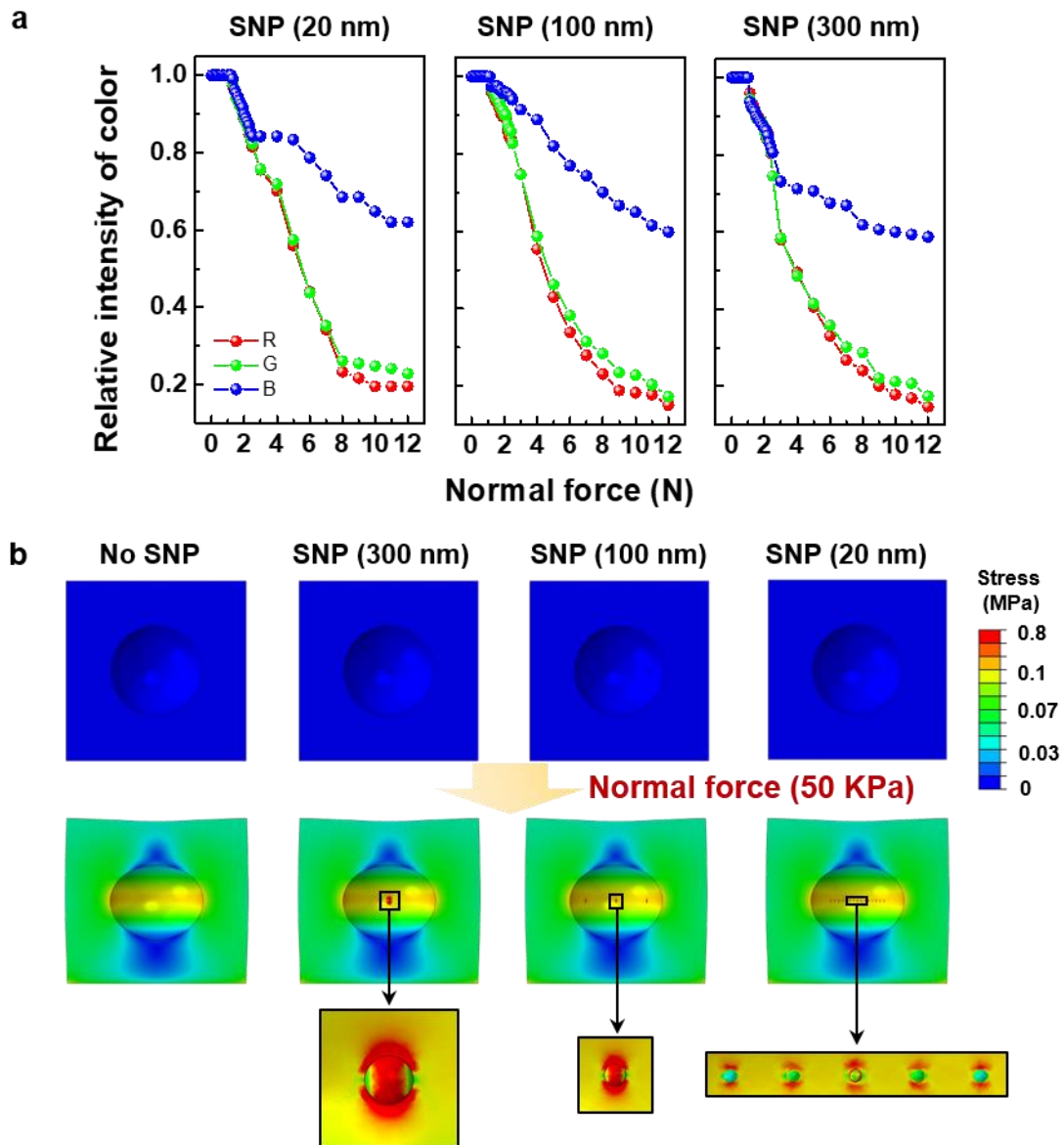


**Figure 7.22.** (A) Relative colour intensities of porous PDMS/SP composites (pore size = 5  $\mu\text{m}$ ) decorated with SNPs of different sizes (20, 100, 300 nm) as functions of pressure. (B) Finite-element analysis-determined stress distributions at the surfaces of pores in porous PDMS/SP composites with SNPs under applied pressure. The simulation conditions are identical to those in Figure 7.18.

**Application of composites in mechanochromic e-skins.** As a proof of concept, we have demonstrated the application of porous mechanochromic composites with hierarchical NP-MP architecture in mechanochromic e-skins. Figure 7.23a shows the colour changes of the mechanochromic e-skins attached to human fingers undergoing different hand motions, including folding/unfolding, rock, scissors and grasping objects. The colour changes enable the real-time detection of the spatial distribution of forces without any complicated monitoring instrument. Thus, the e-skins provide an intuitive perception of local forces according to various hand gestures. While the colour transition of the mechanochromic e-skin is typically limited to static force sensing applications,<sup>281</sup> the present mechanochromic e-skins can be combined with flexible and transparent silver nanowire electrodes for use as triboelectric force sensors. These sensors can be applied in the spatiotemporal detection of both static and high-frequency dynamic forces (Figure 7.23b, left). In this triboelectric force sensor, triboelectrification and electrostatic induction between the porous PDMS (negatively charged) and plastic pen (positively charged) results in spontaneously generated triboelectric current in response to high-frequency dynamic forces (Figure 7.24, Section S7.2).<sup>37, 282, 283</sup> This generated current can be utilised in self-powered dynamic force sensors. In particular, porous structures with large surface areas and high compressibility provide enhanced triboelectric force sensitivity.<sup>267</sup> Figure 7.23b (right) shows a dual-mode mechanochromic e-skin that can simultaneously detect the location and intensity of the writing force based on the mechanochromic colour and the writing speed based on the triboelectric output signals in real time. The triboelectric current and voltage of the mechanochromic e-skin depends on the intensity of the applied normal pressure (Figure 7.25a–b) and the power density also increased up to a maximum of  $4.2 \mu\text{W}/\text{cm}^2$  (Figure 7.25c). Furthermore, the triboelectric output current of the mechanochromic e-skin gradually increases as the frequency of the dynamic impact force increases (Figure 7.25d). This phenomenon can be attributed to the increase in dynamic modulus resulting from the elasticity of the porous mechanochromic composites.<sup>43, 267</sup> To evaluate the ability of our mechanochromic e-skins to detect sound, we monitored the output voltage induced by the acoustic pressure of a speaker (Figure 7.26). When the e-skin is exposed to the sound waves of the words ‘electronic’ and ‘skin’, the generated triboelectric output voltage closely matches the waveform of the sound source (Figure 7.23c, left). The time-dependent frequency obtained by short-time Fourier transformation corresponds to the location and intensity of the recorded frequency, in accordance with the spectrogram of the sound source (Figure 7.23c, right).

### **S7.2 Working mechanism of triboelectric electricity of dual-mode force sensor**

The triboelectric property of dual mode force sensor can be generated by triboelectrification and electrostatic induction between the porous mechanochromic composite and sliding objects (plastic pen).

This triboelectric sensor is operated by single electrode mode, whose working mechanism is schematically depicted in Figure 7.24. When the sensor is initially pressed, friction at the interface between porous PDMS/SP composite and plastic pen is generated, leading to formation of negative charge on one side and positive charge on the other side across the interface by contact electrification. As the pressure is released, the subsequent electrostatic induction promotes current flow from silver nanowire electrodes to ground through external circuit, until the accumulated charge on the electrode is neutralized. Similarly, the current flow is reversed again due to loss of electrostatic equilibrium while the two charged materials are to be closer. From this cyclic contact and separation between two different-charged materials, consequently this triboelectric sensor generates repetitively output current flow back and forth.

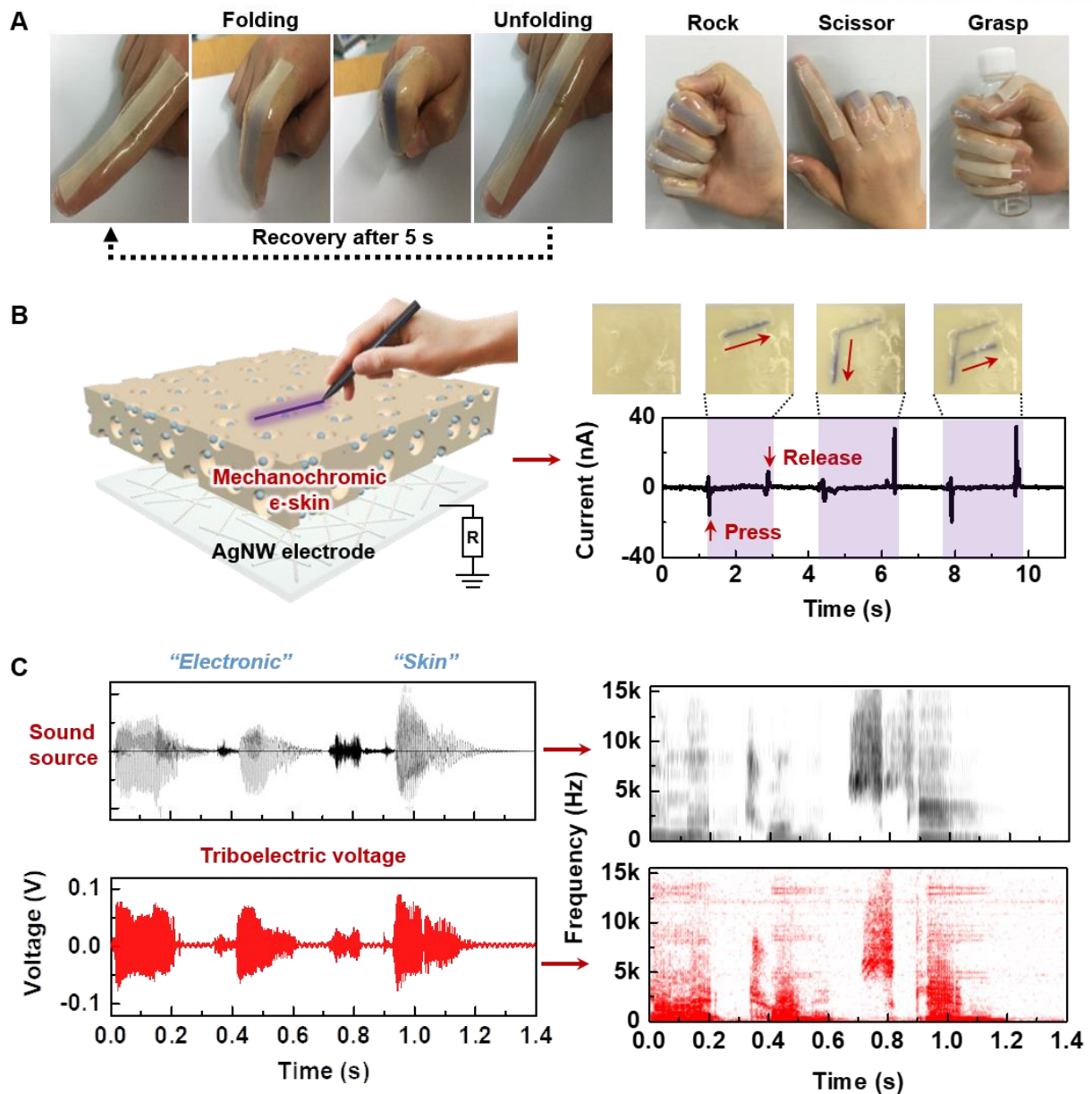


**Figure 7.23.** Applications of porous mechanochromic composites in wearable e-skins and dual-mode static/dynamic touch and audio sensors. (a) Images of wearable mechanochromic e-skins for the detection of various hand gestures (folding/unfolding, rock, scissor and grasp). (b) Schematic of a dual-mode mechanochromic and triboelectric force sensor that enables the spatiotemporal detection of both writing force and speed. (c) Waveforms of the sound sources of the words ‘electronic’ and ‘skin’: waveforms of the detected read-out signals (left) and short-time Fourier transform of the sound source along with the read-out signals from the dynamic force sensor (right). These applications are based on the pore-5/SNP-300 porous mechanochromic composite.

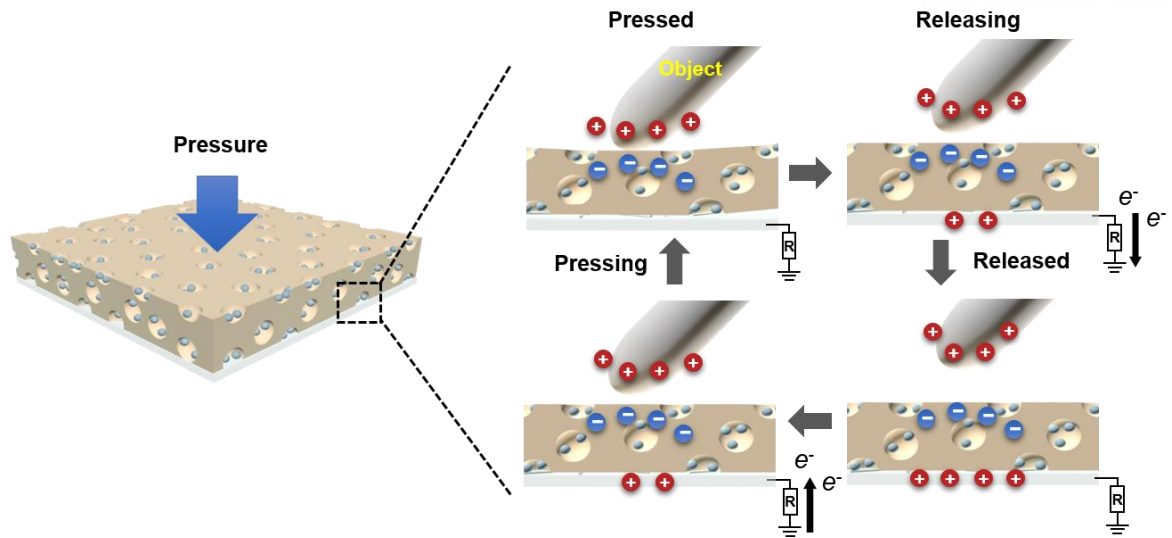


**Figure 7.24.** Schematic of the working mechanism of the single-electrode triboelectric sensor, which comprises a porous mechanochromic composite and silver nanowire-based electrode. Object is the plastic pen in this work.

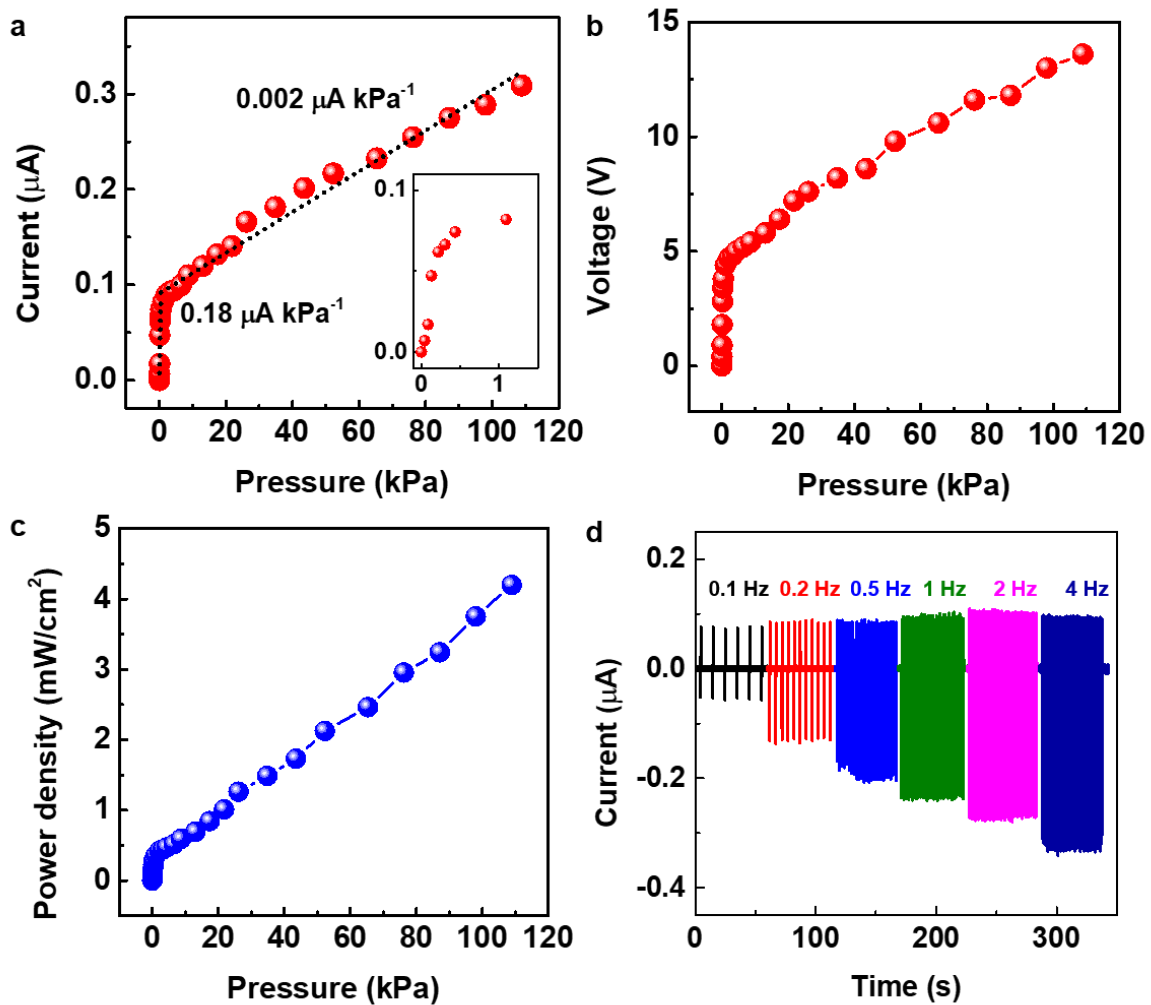


**Figure 7.25.** (a) Output triboelectric current of a mechanochromic composite in response to normal pressure. The sensitivity is  $0.18 \mu\text{A kPa}^{-1}$  below 0.4 kPa and  $0.002 \mu\text{A kPa}^{-1}$  in the range 1–108 kPa. (b) Triboelectric output voltage and (c) power density of porous PDMS/SP composites with 5- $\mu\text{m}$  pores and 300-nm SNPs as functions of applied pressure. (d) Output current of the porous mechanochromic composite in response to dynamic normal pressure with different loading frequencies (0.1–4 Hz).



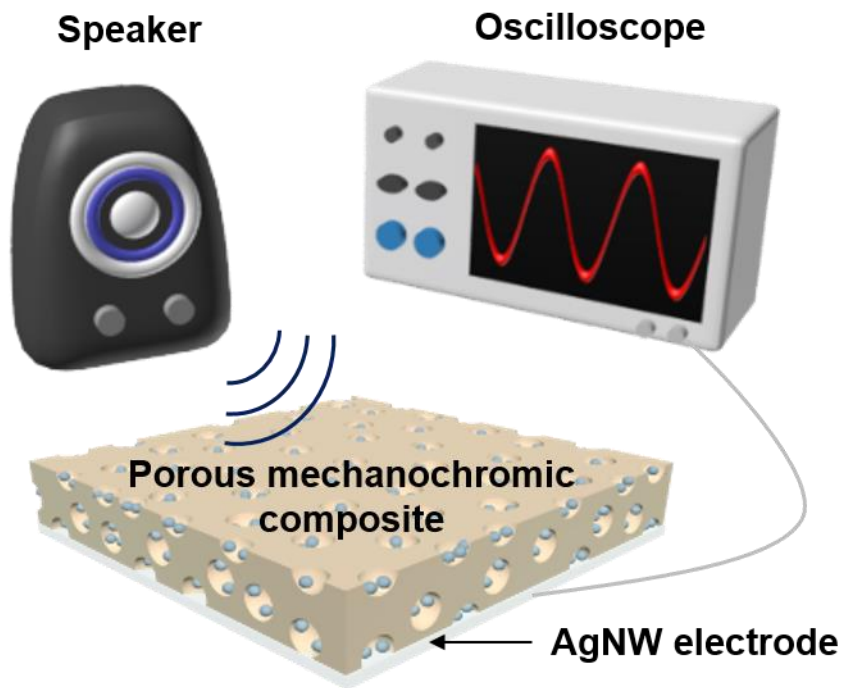


**Figure 7.26.** Schematic showing the setup used to detect dynamic acoustic waves.

## 7.4 Conclusions

This study demonstrates that a hierarchical NP-MP architecture in porous mechanochromic composites can enhance both mechanochromic strain/stress sensitivity and stretchability. The experimentally determined structure–activity relationships and computational modelling results suggest the following general design principle: reducing pore size while increasing SNP size should enhance the mechanochromic sensitivity. Most material modifications that enhance the onset of mechanochromism also reduce extensibility, because mechanochromism is triggered by polymer chains approaching their maximum extension. However, the hierarchical NP-MP architecture of the porous composite structure in this study simultaneously reduces the onset of mechanochromism and enhances the extensibility. As a proof of concept, we fabricated an e-skin based on the composite material and used it as a wearable motion sensor and dual-mode touch audio sensor. The e-skin enabled the detection of static/dynamic force without any external power source. Our hierarchical NP-MP framework is expected to allow the development of multifunctional and multiresponsive mechanochemical materials for user-interactive devices, smart robotics and wearable healthcare/diagnosis applications in future.

## Chapter 8. Summary and Future Perspective

In this thesis, we suggested the high-performance electronic skins with various micro-/nanostructured composite materials and their promising applications including wearable sensors, healthcare monitoring devices, acoustic sensor, and texture perceptions. Firstly, structural modification of device structures into unique micro/nanostructures such as interlocking, porous, and stacking enable to possess great functionalities with high mechanical sensitivity, multidirectional force sensing capability, linear and wide pressure detection, resulting from geometric advantages with large contact area, stress concentration, and anisotropic deformation. Secondly, the demonstration of multifunctional composite materials having piezoresistance, ferroelectricity, and mechanochromism provide the great abilities to detect and discriminate the multiple stimuli (e.g. static/dynamic touches, temperature) and to visualize the mechanical stimuli. Based on the advantages of structural geometry and material characteristic, we can successfully demonstrate the highly sensitive and multifunctional electronic skins and apply our e-skins to future applications.

In chapter 2, we demonstrated an electronic skin consisting of CNT/PDMS composite film that contains interlocked microdome arrays and displays the high pressure sensitivity by the giant tunneling piezoresistance. This design substantially increases the change in contact area upon loading due to stress concentration and enables an extreme resistance-switching behavior ( $R_{OFF}/R_{ON}$  of  $\sim 10^5$ ). This translates into high sensitivity to pressure ( $-15.1 \text{ kPa}^{-1}$ ,  $\sim 0.2 \text{ Pa}$  minimum detection) and rapid response/relaxation times ( $\sim 0.04 \text{ s}$ ), with a minimal dependence on temperature variation. Finally, we showed that our sensors can sensitively monitor human breathing flows and voice vibrations, highlighting their potential use in wearable human-health monitoring systems.

In chapter 3, as further demonstration of e-skin in the chapter 2, we introduced stress-direction-sensitive and stretchable electronic skins with three-axial stress-sensing capabilities. Inspired by the interlocked epidermal-dermal layers in human skin, we employed piezoresistive, interlocked microdome arrays. Similar to the stress concentrating function of interlocked epidermal-dermal ridges which magnify the tactile stimuli, the arrays possess highly sensitive detection capability of various mechanical stimuli including normal, shear, stretching, bending, and twisting. Furthermore, the unique geometry of interlocked microdome arrays enables the differentiation of various mechanical stimuli because the arrays exhibit different levels of deformation depending on the direction of applied forces, thus providing different sensor output patterns. In addition, we showed that the electronic skins attached on human skin in the arm and wrist areas are able to distinguish various mechanical stimuli applied in different directions and can selectively monitor different intensities and directions of air flows and vibrations.

In chapter 4, we presented the piezoresistive e-skins with tunable force sensitivity and selectivity to multidirectional forces through the engineered microstructure geometries (i.e., dome, pyramid, and pillar). Depending on the microstructure geometry, distinct variations in contact area and localized stress distribution are observed under different mechanical forces (i.e., normal, shear, stretching, and bending), which critically affect the force sensitivity, selectivity, response/relaxation time, and mechanical stability of e-skins. Microdome structures present the best force sensitivities for normal, tensile, and bending stresses. In particular, microdome structures exhibit extremely high pressure sensitivities over broad pressure ranges ( $47,062 \text{ kPa}^{-1}$  in the range of  $<1 \text{ kPa}$ ,  $90,657 \text{ kPa}^{-1}$  in the range of  $1\text{--}10 \text{ kPa}$ , and  $30,214 \text{ kPa}^{-1}$  in the range of  $10\text{--}26 \text{ kPa}$ ). On the other hand, for shear stress, micropillar structures exhibit the highest sensitivity. As proof-of-concept applications in healthcare monitoring devices, we showed that our e-skins can precisely monitor acoustic waves, breathing, and human artery/carotid pulse pressures. Unveiling the relationship between the microstructure geometry of e-skins and their sensing capability would provide a significant background for our high-performance e-skins with interlocked microdomes.

In chapter 5, we demonstrated the functionality of human-skin-inspired multimodal e-skins that enable spatio-temporal recognition of static/dynamic tactile stimuli (pressure, temperature, vibration). The design of our e-skin involves the fabrication of microstructures of ferroelectric rGO/PVDF composite films with interlocked microdome arrays and fingerprint-like microridges on the surface of the films, which enhance the piezoelectric, pyroelectric, and piezoresistive sensing capabilities of the ferroelectric composite films for static and dynamic tactile and thermal signals. Compared to planar ferroelectric films, we have shown that the geometry of the interlocked microdome arrays significantly enhances the tactile sensitivities, enabling the detection of minute variations in temperature, pressure, and acoustic vibration. Furthermore, the employment of fingerprint-like microridges on top of the interlocked e-skins has been shown to significantly enhance the vibrotactile signals when the e-skins are scanned over a textured surface, enabling the perception of surface textures with various roughness and pattern shapes. For proof-of-concept demonstrations, we showed the temperature-dependent pressure monitoring of artery vessels, high-precision acoustic sound detection, and surface texture recognition of various surfaces. All of these capabilities provide a solid platform for the application of the e-skins fabricated in this study in humanoid robotics, flexible sensors, and wearable medical diagnostic systems.

In chapter 6, we demonstrated a flexible ferroelectric sensor with ultrahigh pressure sensitivity and linear response over an exceptionally broad pressure range based on the material and structural design of ferroelectric composites with a multilayer interlocked microdome geometry. Due to the stress concentration between interlocked microdome arrays and increased contact area in the multilayer design, the flexible ferroelectric sensors could perceive static/dynamic pressure with high sensitivity ( $47.7 \text{ kPa}$ –

1, 1.3 Pa minimum detection). In addition, efficient stress distribution between stacked multilayers enables linear sensing over exceptionally broad pressure range (0.0013–353 kPa) with fast response time (20 ms) and high reliability over 5000 repetitive cycles even at an extremely high pressure of 272 kPa. Our sensor can be used to monitor diverse stimuli from a low to a high pressure range including weak gas flow, acoustic sound, wrist pulse pressure, respiration, and foot pressure with a single device.

In chapter 7, we reported mechanochromic electronic skins which can visualize the mechanical stimuli enabling user-interactive and intuitive recognition. The mechanochromic e-skin possess a hierarchical nanoparticle-in-micropore (NP-MP) architecture in porous mechanochromic polymers, which can enhance the mechanosensitivity and stretchability of mechanochromic electronic skins. The hierarchical NP-MP structure results in stress concentration-induced mechanochemical activation of mechanophores, significantly improving the mechanochromic sensitivity to both tensile strain and normal force (critical tensile strain: 50% and normal force: 1 N). Furthermore, the porous mechanochromic composites exhibit a reversible mechanochromism under a strain of 250%. This architecture enables a dual-mode mechanochromic e-skin for detecting static/dynamic forces via mechanochromism and triboelectricity. Our hierarchical NP-MP framework is expected to allow the development of multifunctional and multiresponsive mechanochemical materials for user-interactive devices, smart robotics, and wearable healthcare/diagnosis applications in future.

In summary, this thesis presented that various electronic skins with great advantages with giant piezoresistance sensitivity, multidirectional force sensing capabilities, multiple stimuli detection, linear and wide pressure detection, and visualization of mechanical stimuli, resulting from the introduction of uniquely designed micro/nanostructures and functional materials. Moreover, these electronic skins showed a great superiority in terms of additional sensor performances such as response time, durability, and power generations, due to structural advantages of bio-inspired or 2D/3D micro/nanostructures. For the proof-of-concept, we successfully applied our e-skins to various applications including wearable sensors, healthcare monitoring devices, and acoustic and texture sensors. Our electronic skins will provide the powerful platform for next-generation sensor systems in flexible/wearable, stretchable and electronic applications.

## References

1. S. R. Steinhubl, E. D. Muse and E. J. Topol, The emerging field of mobile health, *Sci. Transl. Med.*, **2015**, 7, 283rv283-283rv283.
2. A. Pantelopoulos and N. G. Bourbakis, A survey on wearable sensor-based systems for health monitoring and prognosis, *IEEE Trans. Syst. Man Cybern. Part C-Appl. Rev.*, **2010**, 40, 1-12.
3. S. Patel, H. Park, P. Bonato, L. Chan and M. Rodgers, A review of wearable sensors and systems with application in rehabilitation, *J. Neuroeng. Rehabil.*, **2012**, 9, 21.
4. M. L. Hammock, A. Chortos, B. C. K. Tee, J. B. H. Tok and Z. Bao, 25th anniversary article: the evolution of electronic skin (e-skin): a brief history, design considerations, and recent progress, *Adv. Mater.*, **2013**, 25, 5997-6038.
5. S. Kon, K. Oldham and R. Horowitz, *presented at Sensors and Smart Structures Technologies for Civil Mechanical, and Aerospace Systems*, San Diego, CA, USA, **2007**.
6. M. Ha, S. Lim, J. Park, D. S. Um, Y. Lee and H. Ko, Bioinspired interlocked and hierarchical design of ZnO nanowire arrays for static and dynamic pressure-sensitive electronic skins, *Adv. Funct. Mater.*, **2015**, 25, 2841-2849.
7. K. Kanao, S. Harada, Y. Yamamoto, W. Honda, T. Arie, S. Akita and K. Takei, Highly selective flexible tactile strain and temperature sensors against substrate bending for an artificial skin, *RSC Adv.*, **2015**, 5, 30170-30174.
8. H. Bi, K. Yin, X. Xie, J. Ji, S. Wan, L. Sun, M. Terrones and M. S. Dresselhaus, Ultrahigh humidity sensitivity of graphene oxide, *Sci. Rep.*, **2013**, 3, 2714.
9. S. Y. Kim, S. Park, H. W. Park, D. H. Park, Y. Jeong and D. H. Kim, Highly sensitive and multimodal all-carbon skin sensors capable of simultaneously detecting tactile and biological stimuli, *Adv. Mater.*, **2015**, 27, 4178-4185.
10. E. Snow, F. Perkins, E. Houser, S. Badescu and T. Reinecke, Chemical detection with a single-walled carbon nanotube capacitor, *Science*, **2005**, 307, 1942-1945.
11. K. Takei, T. Takahashi, J. C. Ho, H. Ko, A. G. Gillies, P. W. Leu, R. S. Fearing and A. Javey, Nanowire active-matrix circuitry for low-voltage macroscale artificial skin, *Nat. Mater.*, **2010**, 9, 821.
12. C. Wang, D. Hwang, Z. Yu, K. Takei, J. Park, T. Chen, B. Ma and A. Javey, User-interactive electronic skin for instantaneous pressure visualization, *Nat. Mater.*, **2013**, 12, 899.
13. T. Someya, T. Sekitani, S. Iba, Y. Kato, H. Kawaguchi and T. Sakurai, A large-area, flexible pressure sensor matrix with organic field-effect transistors for artificial skin applications, *Proc. Natl. Acad. Sci.*, **2004**, 101, 9966-9970.
14. N. Lu, C. Lu, S. Yang and J. Rogers, Highly sensitive skin-mountable strain gauges based

- entirely on elastomers, *Adv. Funct. Mater.*, **2012**, *22*, 4044-4050.
15. D.-H. Kim, N. Lu, R. Ghaffari, Y.-S. Kim, S. P. Lee, L. Xu, J. Wu, R.-H. Kim, J. Song and Z. Liu, Materials for multifunctional balloon catheters with capabilities in cardiac electrophysiological mapping and ablation therapy, *Nat. Mater.*, **2011**, *10*, 316.
  16. T. Takahashi, K. Takei, A. G. Gillies, R. S. Fearing and A. Javey, Carbon nanotube active-matrix backplanes for conformal electronics and sensors, *Nano Lett.*, **2011**, *11*, 5408-5413.
  17. T. Sekitani, Y. Noguchi, K. Hata, T. Fukushima, T. Aida and T. Someya, A rubberlike stretchable active matrix using elastic conductors, *Science*, **2008**, *321*, 1468-1472.
  18. G. Schwartz, B. C.-K. Tee, J. Mei, A. L. Appleton, D. H. Kim, H. Wang and Z. Bao, Flexible polymer transistors with high pressure sensitivity for application in electronic skin and health monitoring, *Nat. Commun.*, **2013**, *4*, 1859.
  19. C. Pang, G.-Y. Lee, T.-i. Kim, S. M. Kim, H. N. Kim, S.-H. Ahn and K.-Y. Suh, A flexible and highly sensitive strain-gauge sensor using reversible interlocking of nanofibres, *Nat. Mater.*, **2012**, *11*, 795.
  20. J. Kim, M. Lee, H. J. Shim, R. Ghaffari, H. R. Cho, D. Son, Y. H. Jung, M. Soh, C. Choi and S. Jung, Stretchable silicon nanoribbon electronics for skin prosthesis, *Nat. Commun.*, **2014**, *5*, 5747.
  21. Q. Hua, J. Sun, H. Liu, R. Bao, R. Yu, J. Zhai, C. Pan and Z. L. Wang, Skin-inspired highly stretchable and conformable matrix networks for multifunctional sensing, *Nat. Commun.*, **2018**, *9*, 244.
  22. T. W. Tomblor, C. Zhou, L. Alexseyev, J. Kong, H. Dai, L. Liu, C. Jayanthi, M. Tang and S.-Y. Wu, Reversible electromechanical characteristics of carbon nanotubes under local-probe manipulation, *Nature*, **2000**, *405*, 769.
  23. T. Toriyama and S. Sugiyama, Analysis of piezoresistance in p-type silicon for mechanical sensors, *J. Microelectromech. Syst.*, **2002**, *11*, 598-604.
  24. L. Pan, A. Chortos, G. Yu, Y. Wang, S. Isaacson, R. Allen, Y. Shi, R. Dauskardt and Z. Bao, An ultra-sensitive resistive pressure sensor based on hollow-sphere microstructure induced elasticity in conducting polymer film, *Nat. Commun.*, **2014**, *5*, 3002.
  25. M. Park, H. Kim and J. P. Youngblood, Strain-dependent electrical resistance of multi-walled carbon nanotube/polymer composite films, *Nanotechnology*, **2008**, *19*, 055705.
  26. R. King-Smith and D. Vanderbilt, Theory of polarization of crystalline solids, *Phys. Rev. B*, **1993**, *47*, 1651.
  27. S. R. Anton and H. A. Sodano, A review of power harvesting using piezoelectric materials (2003–2006), *Smart Mater. Struct.*, **2007**, *16*, R1.
  28. Z. L. Wang and J. Song, Piezoelectric nanogenerators based on zinc oxide nanowire arrays,

- Science*, **2006**, *312*, 242-246.
29. H.-B. Fang, J.-Q. Liu, Z.-Y. Xu, L. Dong, L. Wang, D. Chen, B.-C. Cai and Y. Liu, Fabrication and performance of MEMS-based piezoelectric power generator for vibration energy harvesting, *Microelectron. J.*, **2006**, *37*, 1280-1284.
  30. M.-H. Zhao, Z.-L. Wang and S. X. Mao, Piezoelectric characterization of individual zinc oxide nanobelt probed by piezoresponse force microscope, *Nano Lett.*, **2004**, *4*, 587-590.
  31. R. C. Luo and C. S. Tsai, Thin film PZT pressure/temperature sensory arrays for on-line monitoring of injection molding, *Proc. IEEE. IECON*, **2001**, *1*, 375-380.
  32. K.-I. Park, S. Xu, Y. Liu, G.-T. Hwang, S.-J. L. Kang, Z. L. Wang and K. J. Lee, Piezoelectric BaTiO<sub>3</sub> thin film nanogenerator on plastic substrates, *Nano Lett.*, **2010**, *10*, 4939-4943.
  33. J. Dargahi, M. Parameswaran and S. Payandeh, A micromachined piezoelectric tactile sensor for an endoscopic grasper-theory, fabrication and experiments, *J. Microelectromech. Syst.*, **2000**, *9*, 329-335.
  34. L. Persano, C. Dagdeviren, Y. Su, Y. Zhang, S. Girardo, D. Pisignano, Y. Huang and J. A. Rogers, High performance piezoelectric devices based on aligned arrays of nanofibers of poly (vinylidene fluoride-co-trifluoroethylene), *Nat. Commun.*, **2013**, *4*, 1633.
  35. S.-H. Shin, Y.-H. Kim, M. H. Lee, J.-Y. Jung and J. Nah, Hemispherically aggregated BaTiO<sub>3</sub> nanoparticle composite thin film for high-performance flexible piezoelectric nanogenerator, *ACS Nano*, **2014**, *8*, 2766-2773.
  36. Z. L. Wang, Triboelectric nanogenerators as new energy technology for self-powered systems and as active mechanical and chemical sensors, *ACS Nano*, **2013**, *7*, 9533-9557.
  37. M. Ha, J. Park, Y. Lee and H. Ko, Triboelectric generators and sensors for self-powered wearable electronics, *ACS Nano*, **2015**, *9*, 3421-3427.
  38. L. Lin, Y. Xie, S. Wang, W. Wu, S. Niu, X. Wen and Z. L. Wang, Triboelectric active sensor array for self-powered static and dynamic pressure detection and tactile imaging, *ACS Nano*, **2013**, *7*, 8266-8274.
  39. J. Chen, G. Zhu, W. Yang, Q. Jing, P. Bai, Y. Yang, T. C. Hou and Z. L. Wang, Harmonic-resonator-based triboelectric nanogenerator as a sustainable power source and a self-powered active vibration sensor, *Adv. Mater.*, **2013**, *25*, 6094-6099.
  40. D. Kang, P. V. Pikhitsa, Y. W. Choi, C. Lee, S. S. Shin, L. Piao, B. Park, K.-Y. Suh, T.-i. Kim and M. Choi, Ultrasensitive mechanical crack-based sensor inspired by the spider sensory system, *Nature*, **2014**, *516*, 222.
  41. Y. Yang, K. C. Pradel, Q. Jing, J. M. Wu, F. Zhang, Y. Zhou, Y. Zhang and Z. L. Wang, Thermoelectric nanogenerators based on single Sb-doped ZnO micro/nanobelts, *ACS Nano*, **2012**, *6*, 6984-6989.



42. K. Takei, Z. Yu, M. Zheng, H. Ota, T. Takahashi and A. Javey, Highly sensitive electronic whiskers based on patterned carbon nanotube and silver nanoparticle composite films, *Proc. Natl. Acad. Sci.*, **2014**, *111*, 1703-1707.
43. J. Park, M. Kim, Y. Lee, H. S. Lee and H. Ko, Fingertip skin-inspired microstructured ferroelectric skins discriminate static/dynamic pressure and temperature stimuli, *Sci. Adv.*, **2015**, *1*, e1500661.
44. C. L. Choong, M. B. Shim, B. S. Lee, S. Jeon, D. S. Ko, T. H. Kang, J. Bae, S. H. Lee, K. E. Byun and J. Im, Highly stretchable resistive pressure sensors using a conductive elastomeric composite on a micropillar array, *Adv. Mater.*, **2014**, *26*, 3451-3458.
45. J. Park, Y. Lee, J. Hong, M. Ha, Y.-D. Jung, H. Lim, S. Y. Kim and H. Ko, Giant tunneling piezoresistance of composite elastomers with interlocked microdome arrays for ultrasensitive and multimodal electronic skins, *ACS Nano*, **2014**, *8*, 4689-4697.
46. J. Park, Y. Lee, J. Hong, Y. Lee, M. Ha, Y. Jung, H. Lim, S. Y. Kim and H. Ko, Tactile-direction-sensitive and stretchable electronic skins based on human-skin-inspired interlocked microstructures, *ACS Nano*, **2014**, *8*, 12020-12029.
47. S. Jung, J. H. Kim, J. Kim, S. Choi, J. Lee, I. Park, T. Hyeon and D. H. Kim, Reverse-micelle-induced porous pressure-sensitive rubber for wearable human-machine interfaces, *Adv. Mater.*, **2014**, *26*, 4825-4830.
48. Y. R. Jeong, H. Park, S. W. Jin, S. Y. Hong, S. S. Lee and J. S. Ha, Highly stretchable and sensitive strain sensors using fragmented graphene foam, *Adv. Funct. Mater.*, **2015**, *25*, 4228-4236.
49. D.-Y. Khang, H. Jiang, Y. Huang and J. A. Rogers, A stretchable form of single-crystal silicon for high-performance electronics on rubber substrates, *Science*, **2006**, *311*, 208-212.
50. K. K. Kim, S. Hong, H. M. Cho, J. Lee, Y. D. Suh, J. Ham and S. H. Ko, Highly sensitive and stretchable multidimensional strain sensor with prestrained anisotropic metal nanowire percolation networks, *Nano Lett.*, **2015**, *15*, 5240-5247.
51. D.-H. Kim, N. Lu, R. Ma, Y.-S. Kim, R.-H. Kim, S. Wang, J. Wu, S. M. Won, H. Tao and A. Islam, Epidermal electronics, *Science*, **2011**, *333*, 838-843.
52. N. Cauna, Nature and functions of the papillary ridges of the digital skin, *Anat. Rec.*, **1954**, *119*, 449-468.
53. A. Farooq, G. Evreinov, R. Raisamo and A. A. Majeed, Haptic user interface enhancement system for touchscreen based interaction. *International Conference on Open Source Systems and Technologies (ICOSST)*, **2014**.
54. C. Pang, T. i. Kim, W. G. Bae, D. Kang, S. M. Kim and K. Y. Suh, Bioinspired Reversible Interlocker Using Regularly Arrayed High Aspect-Ratio Polymer Fibers, *Adv. Mater.*, **2012**, *24*,

- 475-479.
55. S. N. Gorb, R. G. Beutel, E. V. Gorb, Y. Jiao, V. Kastner, S. Niederegger, V. L. Popov, M. Scherge, U. Schwarz and W. Vötsch, Structural design and biomechanics of friction-based releasable attachment devices in insects, *Integr. Comp. Biol.*, **2002**, *42*, 1127-1139.
  56. R. A. Grant, B. Mitchinson, C. W. Fox and T. J. Prescott, Active touch sensing in the rat: anticipatory and regulatory control of whisker movements during surface exploration, *J. Neurophysiol.*, **2009**, *101*, 862-874.
  57. D. J. Krupa, M. S. Matell, A. J. Brisben, L. M. Oliveira and M. A. Nicolelis, Behavioral properties of the trigeminal somatosensory system in rats performing whisker-dependent tactile discriminations, *J. Neurophysiol.*, **2001**, *21*, 5752-5763.
  58. Y. Mao, P. Zhao, G. McConohy, H. Yang, Y. Tong and X. Wang, Sponge-like piezoelectric polymer films for scalable and integratable nanogenerators and self-powered electronic systems, *Adv. Energy Mater.*, **2014**, *4*, 1301624.
  59. J. Yang, J. Chen, Y. Su, Q. Jing, Z. Li, F. Yi, X. Wen, Z. Wang and Z. L. Wang, Eardrum-inspired active sensors for self-powered cardiovascular system characterization and throat-attached anti-interference voice recognition, *Adv. Mater.*, **2015**, *27*, 1316-1326.
  60. J. Chen, G. Zhu, J. Yang, Q. Jing, P. Bai, W. Yang, X. Qi, Y. Su and Z. L. Wang, Personalized keystroke dynamics for self-powered human-machine interfacing, *ACS Nano*, **2015**, *9*, 105-116.
  61. P. Bai, G. Zhu, Q. Jing, J. Yang, J. Chen, Y. Su, J. Ma, G. Zhang and Z. L. Wang, Membrane-based self-powered triboelectric sensors for pressure change detection and its uses in security surveillance and healthcare monitoring, *Adv. Funct. Mater.*, **2014**, *24*, 5807-5813.
  62. Q. Zheng, B. Shi, F. Fan, X. Wang, L. Yan, W. Yuan, S. Wang, H. Liu, Z. Li and Z. L. Wang, In vivo powering of pacemaker by breathing-driven implanted triboelectric nanogenerator, *Adv. Mater.*, **2014**, *26*, 5851-5856.
  63. Y. Jie, N. Wang, X. Cao, Y. Xu, T. Li, X. Zhang and Z. L. Wang, Self-powered triboelectric nanosensor with poly (tetrafluoroethylene) nanoparticle arrays for dopamine detection, *ACS Nano*, **2015**, *9*, 8376-8383.
  64. W. Seung, M. K. Gupta, K. Y. Lee, K.-S. Shin, J.-H. Lee, T. Y. Kim, S. Kim, J. Lin, J. H. Kim and S.-W. Kim, Nanopatterned textile-based wearable triboelectric nanogenerator, *ACS Nano*, **2015**, *9*, 3501-3509.
  65. X. Wang, H. Zhang, R. Yu, L. Dong, D. Peng, A. Zhang, Y. Zhang, H. Liu, C. Pan and Z. L. Wang, Dynamic pressure mapping of personalized handwriting by a flexible sensor matrix based on the mechanoluminescence process, *Adv. Mater.*, **2015**, *27*, 2324-2331.
  66. M.-H. Yeh, L. Lin, P.-K. Yang and Z. L. Wang, Motion-driven electrochromic reactions for self-

- powered smart window system, *ACS Nano*, **2015**, *9*, 4757-4765.
67. H. S. Lee, J. Chung, G. T. Hwang, C. K. Jeong, Y. Jung, J. H. Kwak, H. Kang, M. Byun, W. D. Kim and S. Hur, Flexible inorganic piezoelectric acoustic nanosensors for biomimetic artificial hair cells, *Adv. Funct. Mater.*, **2014**, *24*, 6914-6921.
  68. F. Yi, L. Lin, S. Niu, J. Yang, W. Wu, S. Wang, Q. Liao, Y. Zhang and Z. L. Wang, Self-powered trajectory, velocity, and acceleration tracking of a moving object/body using a triboelectric sensor, *Adv. Funct. Mater.*, **2014**, *24*, 7488-7494.
  69. Q. Shao, Z. Niu, M. Hirtz, L. Jiang, Y. Liu, Z. Wang and X. Chen, High-performance and tailorable pressure sensor based on ultrathin conductive polymer film, *Small*, **2014**, *10*, 1466-1472.
  70. Z.-H. Lin, Y. Xie, Y. Yang, S. Wang, G. Zhu and Z. L. Wang, Enhanced triboelectric nanogenerators and triboelectric nanosensor using chemically modified TiO<sub>2</sub> nanomaterials, *ACS Nano*, **2013**, *7*, 4554-4560.
  71. A. P. Gerratt, H. O. Michaud and S. P. Lacour, Elastomeric electronic skin for prosthetic tactile sensation, *Adv. Funct. Mater.*, **2015**, *25*, 2287-2295.
  72. B. C. Tee, C. Wang, R. Allen and Z. Bao, An electrically and mechanically self-healing composite with pressure-and flexion-sensitive properties for electronic skin applications, *Nat. Nanotechnol.*, **2012**, *7*, 825.
  73. X. Li, M. Chen, R. Yu, T. Zhang, D. Song, R. Liang, Q. Zhang, S. Cheng, L. Dong and A. Pan, Enhancing Light Emission of ZnO-Nanofilm/Si-Micropillar Heterostructure Arrays by Piezo-Phototronic Effect, *Adv. Mater.*, **2015**, *27*, 4447-4453.
  74. J. Scheibert, S. Leurent, A. Prevost and G. Debrégeas, The role of fingerprints in the coding of tactile information probed with a biomimetic sensor, *Science*, **2009**, *323*, 1503-1506.
  75. T. Yoshioka, B. Gibb, A. K. Dorsch, S. S. Hsiao and K. O. Johnson, Neural coding mechanisms underlying perceived roughness of finely textured surfaces, *J. Neurosci.*, **2001**, *21*, 6905-6916.
  76. Y. Cao, T. Li, Y. Gu, H. Luo, S. Wang and T. Zhang, Fingerprint-Inspired Flexible Tactile Sensor for Accurately Discerning Surface Texture, *Small*, **2018**, *14*, 1703902.
  77. D. Hughes and N. Correll, Texture recognition and localization in amorphous robotic skin, *Bioinspiration Biomimetics*, **2015**, *10*, 055002.
  78. J. N. Cohn, S. Finkelstein, G. McVeigh, D. Morgan, L. LeMay, J. Robinson and J. Mock, Noninvasive pulse wave analysis for the early detection of vascular disease, *Hypertension*, **1995**, *26*, 503-508.
  79. X. Wang, Y. Gu, Z. Xiong, Z. Cui and T. Zhang, Silk-molded flexible, ultrasensitive, and highly stable electronic skin for monitoring human physiological signals, *Adv. Mater.*, **2014**, *26*, 1336-1342.

80. R. Parkes, Rate of respiration: the forgotten vital sign, *Emerg. Nurse*, **2011**, 19.
81. N. Douglas, D. White, C. K. Pickett, J. Weil and C. Zwillich, Respiration during sleep in normal man, *Thorax*, **1982**, 37, 840-844.
82. B.-U. Hwang, J.-H. Lee, T. Q. Trung, E. Roh, D.-I. Kim, S.-W. Kim and N.-E. Lee, Transparent stretchable self-powered patchable sensor platform with ultrasensitive recognition of human activities, *ACS Nano*, **2015**, 9, 8801-8810.
83. D.-H. Kim, J. Viventi, J. J. Amsden, J. Xiao, L. Vigeland, Y.-S. Kim, J. A. Blanco, B. Panilaitis, E. S. Frechette and D. Contreras, Dissolvable films of silk fibroin for ultrathin conformal bio-integrated electronics, *Nat. Mater.*, **2010**, 9, 511.
84. E. A. Lumpkin and M. J. Caterina, Mechanisms of sensory transduction in the skin, *Nature*, **2007**, 445, 858.
85. V. Maheshwari and R. Saraf, Tactile devices to sense touch on a par with a human finger, *Angew. Chem. Int. Ed.*, **2008**, 47, 7808-7826.
86. R. S. Dahiya, G. Metta, M. Valle and G. Sandini, Tactile sensing—from humans to humanoids, *IEEE Trans. Robot.*, **2010**, 26, 1-20.
87. T. Sekitani, T. Yokota, U. Zschieschang, H. Klauk, S. Bauer, K. Takeuchi, M. Takamiya, T. Sakurai and T. Someya, Organic nonvolatile memory transistors for flexible sensor arrays, *Science*, **2009**, 326, 1516-1519.
88. S. C. Mannsfeld, B. C. Tee, R. M. Stoltenberg, C. V. H. Chen, S. Barman, B. V. Muir, A. N. Sokolov, C. Reese and Z. Bao, Highly sensitive flexible pressure sensors with microstructured rubber dielectric layers, *Nat. Mater.*, **2010**, 9, 859.
89. T. Yamada, Y. Hayamizu, Y. Yamamoto, Y. Yomogida, A. Izadi-Najafabadi, D. N. Futaba and K. Hata, A stretchable carbon nanotube strain sensor for human-motion detection, *Nat. Nanotechnol.*, **2011**, 6, 296.
90. D. J. Lipomi, M. Vosgueritchian, B. C. Tee, S. L. Hellstrom, J. A. Lee, C. H. Fox and Z. Bao, Skin-like pressure and strain sensors based on transparent elastic films of carbon nanotubes, *Nat. Nanotechnol.*, **2011**, 6, 788.
91. R. C. Webb, A. P. Bonifas, A. Behnaz, Y. Zhang, K. J. Yu, H. Cheng, M. Shi, Z. Bian, Z. Liu and Y.-S. Kim, Ultrathin conformal devices for precise and continuous thermal characterization of human skin, *Nat. Mater.*, **2013**, 12, 938.
92. W. Wu, X. Wen and Z. L. Wang, Taxel-addressable matrix of vertical-nanowire piezotronic transistors for active/adaptive tactile imaging, *Science*, **2013**, 1234855.
93. F.-R. Fan, L. Lin, G. Zhu, W. Wu, R. Zhang and Z. L. Wang, Transparent triboelectric nanogenerators and self-powered pressure sensors based on micropatterned plastic films, *Nano Lett.*, **2012**, 12, 3109-3114.

94. G. Ruschau, S. Yoshikawa and R. Newnham, Resistivities of conductive composites, *J. Appl. Phys.*, **1992**, 72, 953-959.
95. N. Hu, Y. Karube, C. Yan, Z. Masuda and H. Fukunaga, Tunneling effect in a polymer/carbon nanotube nanocomposite strain sensor, *Acta Mater.*, **2008**, 56, 2929-2936.
96. D. Bloor, K. Donnelly, P. Hands, P. Laughlin and D. Lussey, A metal–polymer composite with unusual properties, *J. Phys. D-Appl. Phys.*, **2005**, 38, 2851.
97. W. E. Mahmoud, A. El-Lawindy, M. El Eraki and H. Hassan, Butadiene acrylonitrile rubber loaded fast extrusion furnace black as a compressive strain and pressure sensors, *Sens. Actuator A-Phys.*, **2007**, 136, 229-233.
98. J. Zhang, S. Zhang, S. Feng and Z. Jiang, The correlativity of positive temperature coefficient effects in conductive silicone rubber, *Polym. Int.*, **2005**, 54, 1175-1179.
99. N. Hu, H. Fukunaga, S. Atobe, Y. Liu and J. Li, Piezoresistive strain sensors made from carbon nanotubes based polymer nanocomposites, *Sensors*, **2011**, 11, 10691-10723.
100. S. Stassi and G. Canavese, Spiky nanostructured metal particles as filler of polymeric composites showing tunable electrical conductivity, *J. Polym. Sci. Pt. B-Polym. Phys.*, **2012**, 50, 984-992.
101. M. Copel, M. Kuroda, M. Gordon, X.-H. Liu, S. Mahajan, G. Martyna, N. Moumen, C. Armstrong, S. Rossnagel and T. Shaw, Giant piezoresistive On/Off ratios in rare-earth chalcogenide thin films enabling nanomechanical switching, *Nano Lett.*, **2013**, 13, 4650-4653.
102. H. B. Yao, J. Ge, C. F. Wang, X. Wang, W. Hu, Z. J. Zheng, Y. Ni and S. H. Yu, A flexible and highly pressure-sensitive graphene–polyurethane sponge based on fractured microstructure design, *Adv. Mater.*, **2013**, 25, 6692-6698.
103. R. S. Johansson and J. R. Flanagan, Coding and use of tactile signals from the fingertips in object manipulation tasks, *Nat. Rev. Neurosci.*, **2009**, 10, 345.
104. M. Ramuz, B. C. K. Tee, J. B. H. Tok and Z. Bao, Transparent, optical, pressure-sensitive artificial skin for large-area stretchable electronics, *Adv. Mater.*, **2012**, 24, 3223-3227.
105. J. G. Simmons, Generalized formula for the electric tunnel effect between similar electrodes separated by a thin insulating film, *J. Appl. Phys.*, **1963**, 34, 1793-1803.
106. J. Archard, Elastic deformation and the laws of friction, *Proc. R. Soc. Lond. A*, **1957**, 243, 190-205.
107. M. Shiraiishi and M. Ata, Work function of carbon nanotubes, *MRS Online Proceedings Library Archive*, **2000**, 633.
108. N. Pan, Analytical characterization of the anisotropy and local heterogeneity of short fiber composites: Fiber fraction as a variable, *J. Compos Mater.*, **1994**, 28, 1500-1531.
109. J. Sandler, J. Kirk, I. Kinloch, M. Shaffer and A. Windle, Ultra-low electrical percolation

- threshold in carbon-nanotube-epoxy composites, *Polymer*, **2003**, *44*, 5893-5899.
110. L. Hu, D. Hecht and G. Grüner, Percolation in transparent and conducting carbon nanotube networks, *Nano Lett.*, **2004**, *4*, 2513-2517.
  111. P. X. Braun, C. F. Gmachl and R. A. Dweik, Bridging the collaborative gap: Realizing the clinical potential of breath analysis for disease diagnosis and monitoring—tutorial, *IEEE Sens. J.*, **2012**, *12*, 3258-3270.
  112. F. Hedrich, K. Kliche, M. Storz, S. Billat, M. Ashauer and R. Zengerle, Thermal flow sensors for MEMS spirometric devices, *Sens. Actuator A-Phys.*, **2010**, *162*, 373-378.
  113. N. Andre, S. Druart, P. Gerard, R. Pampin, L. Moreno-Hagelsieb, T. Kezai, L. A. Francis, D. Flandre and J.-P. Raskin, Miniaturized wireless sensing system for real-time breath activity recording, *IEEE Sens. J.*, **2010**, *10*, 178-184.
  114. A. R. Aiyar, C. Song, S.-H. Kim and M. G. Allen, An all-polymer airflow sensor using a piezoresistive composite elastomer, *Smart Mater. Struct.*, **2009**, *18*, 115002.
  115. Q. Zhang, W. Ruan, H. Wang, Y. Zhou, Z. Wang and L. Liu, A self-bended piezoresistive microcantilever flow sensor for low flow rate measurement, *Sens. Actuator A-Phys.*, **2010**, *158*, 273-279.
  116. S. Zhang, L. Lou and C. Lee, Piezoresistive silicon nanowire based nanoelectromechanical system cantilever air flow sensor, *Appl. Phys. Lett.*, **2012**, *100*, 023111.
  117. D. D. Mehta, M. Zanartu, S. W. Feng, H. A. Cheyne II and R. E. Hillman, Mobile voice health monitoring using a wearable accelerometer sensor and a smartphone platform, *IEEE Trans. Biomed. Eng.*, **2012**, *59*, 3090-3096.
  118. M. Nolan, B. Madden and E. Burke, Accelerometer based measurement for the mapping of neck surface vibrations during vocalized speech, **2009**.
  119. D. M. Newns, B. G. Elmegeen, X. H. Liu and G. J. Martyna, High response piezoelectric and piezoresistive materials for fast, low voltage switching: simulation and theory of transduction physics at the nanometer-scale, *Adv. Mater.*, **2012**, *24*, 3672-3677.
  120. W. Han, Y. Zhou, Y. Zhang, C.-Y. Chen, L. Lin, X. Wang, S. Wang and Z. L. Wang, Strain-gated piezotronic transistors based on vertical zinc oxide nanowires, *ACS Nano*, **2012**, *6*, 3760-3766.
  121. P. Delmas, J. Hao and L. Rodat-Despoix, Molecular mechanisms of mechanotransduction in mammalian sensory neurons, *Nat. Rev. Neurosci.*, **2011**, *12*, 139.
  122. B. B. Edin and N. Johansson, Skin strain patterns provide kinaesthetic information to the human central nervous system, *The Journal of physiology*, **1995**, *487*, 243-251.
  123. I. Birznieks, P. Jenmalm, A. W. Goodwin and R. S. Johansson, Encoding of direction of fingertip forces by human tactile afferents, *J. Neurosci.*, **2001**, *21*, 8222-8237.
  124. J. A. Dobrzynska and M. Gijs, Polymer-based flexible capacitive sensor for three-axial force

- measurements, *J. Micromech. Microeng.*, **2012**, *23*, 015009.
125. H.-K. Lee, J. Chung, S.-I. Chang and E. Yoon, Real-time measurement of the three-axis contact force distribution using a flexible capacitive polymer tactile sensor, *J. Micromech. Microeng.*, **2011**, *21*, 035010.
  126. R. Surapaneni, Q. Guo, Y. Xie, D. Young and C. Mastrangelo, A three-axis high-resolution capacitive tactile imager system based on floating comb electrodes, *J. Micromech. Microeng.*, **2013**, *23*, 075004.
  127. D. J. Cohen, D. Mitra, K. Peterson and M. M. Maharbiz, A highly elastic, capacitive strain gauge based on percolating nanotube networks, *Nano Lett.*, **2012**, *12*, 1821-1825.
  128. X.-S. Zhang, M.-D. Han, R.-X. Wang, F.-Y. Zhu, Z.-H. Li, W. Wang and H.-X. Zhang, Frequency-multiplication high-output triboelectric nanogenerator for sustainably powering biomedical microsystems, *Nano Lett.*, **2013**, *13*, 1168-1172.
  129. W. H. Yeo, Y. S. Kim, J. Lee, A. Ameen, L. Shi, M. Li, S. Wang, R. Ma, S. H. Jin and Z. Kang, Multifunctional epidermal electronics printed directly onto the skin, *Adv. Mater.*, **2013**, *25*, 2773-2778.
  130. D. Son, J. Lee, S. Qiao, R. Ghaffari, J. Kim, J. E. Lee, C. Song, S. J. Kim, D. J. Lee and S. W. Jun, Multifunctional wearable devices for diagnosis and therapy of movement disorders, *Nat. Nanotechnol.*, **2014**, *9*, 397.
  131. L. Xu, S. R. Gutbrod, A. P. Bonifas, Y. Su, M. S. Sulkin, N. Lu, H.-J. Chung, K.-I. Jang, Z. Liu and M. Ying, 3D multifunctional integumentary membranes for spatiotemporal cardiac measurements and stimulation across the entire epicardium, *Nat. Commun.*, **2014**, *5*, ncomms4329.
  132. S. Harada, W. Honda, T. Arie, S. Akita and K. Takei, Fully printed, highly sensitive multifunctional artificial electronic whisker arrays integrated with strain and temperature sensors, *ACS Nano*, **2014**, *8*, 3921-3927.
  133. C. Hou, H. Wang, Q. Zhang, Y. Li and M. Zhu, Highly Conductive, Flexible, and Compressible All-Graphene Passive Electronic Skin for Sensing Human Touch, *Adv. Mater.*, **2014**, *26*, 5018-5024.
  134. N. T. Tien, S. Jeon, D. I. Kim, T. Q. Trung, M. Jang, B. U. Hwang, K. E. Byun, J. Bae, E. Lee and J. B. H. Tok, A flexible bimodal sensor array for simultaneous sensing of pressure and temperature, *Adv. Mater.*, **2014**, *26*, 796-804.
  135. D. M. Vogt, Y.-L. Park and R. J. Wood, Design and characterization of a soft multi-axis force sensor using embedded microfluidic channels, *IEEE Sens. J.*, **2013**, *13*, 4056-4064.
  136. L. Viry, A. Levi, M. Totaro, A. Mondini, V. Mattoli, B. Mazzolai and L. Beccai, Flexible three-axial force sensor for soft and highly sensitive artificial touch, *Adv. Mater.*, **2014**, *26*, 2659-

- 2664.
137. S. Gong, W. Schwalb, Y. Wang, Y. Chen, Y. Tang, J. Si, B. Shirinzadeh and W. Cheng, A wearable and highly sensitive pressure sensor with ultrathin gold nanowires, *Nat. Commun.*, **2014**, *5*, 3132.
  138. G. J. Gerling and G. W. Thomas, Proc. First Joint Euro-haptics Conf. Symp. Haptic Interfaces Virtual Environ. Teleoperator Syst., **2005**, 63-72.
  139. H. Ko, J. Lee, B. E. Schubert, Y.-L. Chueh, P. W. Leu, R. S. Fearing and A. Javey, Hybrid core-shell nanowire forests as self-selective chemical connectors, *Nano Lett.*, **2009**, *9*, 2054-2058.
  140. H. Ko, Z. Zhang, Y. L. Chueh, J. C. Ho, J. Lee, R. S. Fearing and A. Javey, Wet and Dry Adhesion Properties of Self-Selective Nanowire Connectors, *Adv. Funct. Mater.*, **2009**, *19*, 3098-3102.
  141. D. F. Collins, K. M. Refshauge, G. Todd and S. C. Gandevia, Cutaneous receptors contribute to kinesthesia at the index finger, elbow, and knee, *J. Neurophysiol.*, **2005**, *94*, 1699-1706.
  142. M. Amjadi, A. Pichitpajongkit, S. Lee, S. Ryu and I. Park, Highly stretchable and sensitive strain sensor based on silver nanowire-elastomer nanocomposite, *ACS Nano*, **2014**, *8*, 5154-5163.
  143. C. Yan, J. Wang, W. Kang, M. Cui, X. Wang, C. Y. Foo, K. J. Chee and P. S. Lee, Highly stretchable piezoresistive graphene-nanocellulose nanopaper for strain sensors, *Adv. Mater.*, **2014**, *26*, 2022-2027.
  144. X. Xiao, L. Yuan, J. Zhong, T. Ding, Y. Liu, Z. Cai, Y. Rong, H. Han, J. Zhou and Z. L. Wang, High-strain sensors based on ZnO nanowire/polystyrene hybridized flexible films, *Adv. Mater.*, **2011**, *23*, 5440-5444.
  145. J. Zhou, Y. Gu, P. Fei, W. Mai, Y. Gao, R. Yang, G. Bao and Z. L. Wang, Flexible piezotronic strain sensor, *Nano Lett.*, **2008**, *8*, 3035-3040.
  146. J. Cao, Q. Wang and H. Dai, Electromechanical properties of metallic, quasimetallic, and semiconducting carbon nanotubes under stretching, *Phys. Rev. Lett.*, **2003**, *90*, 157601.
  147. X. Li, R. Zhang, W. Yu, K. Wang, J. Wei, D. Wu, A. Cao, Z. Li, Y. Cheng and Q. Zheng, Stretchable and highly sensitive graphene-on-polymer strain sensors, *Sci. Rep.*, **2012**, *2*, 870.
  148. C.-X. Liu and J.-W. Choi, Strain-dependent resistance of PDMS and carbon nanotubes composite microstructures, *IEEE Trans. Nanotechnol.*, **2010**, *9*, 590-595.
  149. Y. Yang, W. Guo, J. Qi and Y. Zhang, Flexible piezoresistive strain sensor based on single Sb-doped ZnO nanobelts, *Appl. Phys. Lett.*, **2010**, *97*, 223107.
  150. H.-K. Lee, J. Chung, S.-I. Chang and E. Yoon, Normal and shear force measurement using a flexible polymer tactile sensor with embedded multiple capacitors, *J. Microelectromech. Syst.*, **2008**, *17*, 934-942.



151. S. Teshigawara, S. Shimizu, K. Tadakuma, M. Aiguo, M. Shimojo and M. Ishikawa, High sensitivity slip sensor using pressure conductive rubber, *IEEE Sensors 2009 Conf.*, **2009**, 988-991.
152. M. Vatani, E. D. Engeberg and J.-W. Choi, Force and slip detection with direct-write compliant tactile sensors using multi-walled carbon nanotube/polymer composites, *Sens. Actuator A-Phys.*, **2013**, *195*, 90-97.
153. B. T. Gleeson, S. K. Horschel and W. R. Provancher, Design of a fingertip-mounted tactile display with tangential skin displacement feedback, *IEEE Trans. Haptics*, **2010**, *3*, 297-301.
154. C. Pang, J. H. Koo, A. Nguyen, J. M. Caves, M. G. Kim, A. Chortos, K. Kim, P. J. Wang, J. B. H. Tok and Z. Bao, Highly skin-conformal microhairy sensor for pulse signal amplification, *Adv. Mater.*, **2015**, *27*, 634-640.
155. C. M. Boutry, A. Nguyen, Q. O. Lawal, A. Chortos, S. Rondeau-Gagné and Z. Bao, A sensitive and biodegradable pressure sensor array for cardiovascular monitoring, *Adv. Mater.*, **2015**, *27*, 6954-6961.
156. N. Luo, W. Dai, C. Li, Z. Zhou, L. Lu, C. C. Poon, S. C. Chen, Y. Zhang and N. Zhao, Flexible piezoresistive sensor patch enabling ultralow power cuffless blood pressure measurement, *Adv. Funct. Mater.*, **2016**, *26*, 1178-1187.
157. J. W. Jeong, M. K. Kim, H. Cheng, W. H. Yeo, X. Huang, Y. Liu, Y. Zhang, Y. Huang and J. A. Rogers, Capacitive epidermal electronics for electrically safe, long-term electrophysiological measurements, *Adv. Healthc. Mater.*, **2014**, *3*, 642-648.
158. C. M. Lochner, Y. Khan, A. Pierre and A. C. Arias, All-organic optoelectronic sensor for pulse oximetry, *Nat. Commun.*, **2014**, *5*, 5745.
159. X. Liao, Q. Liao, X. Yan, Q. Liang, H. Si, M. Li, H. Wu, S. Cao and Y. Zhang, Flexible and highly sensitive strain sensors fabricated by pencil drawn for wearable monitor, *Adv. Funct. Mater.*, **2015**, *25*, 2395-2401.
160. X. Liao, Q. Liao, Z. Zhang, X. Yan, Q. Liang, Q. Wang, M. Li and Y. Zhang, A Highly Stretchable ZnO@ Fiber-Based Multifunctional Nanosensor for Strain/Temperature/UV Detection, *Adv. Funct. Mater.*, **2016**, *26*, 3074-3081.
161. J. Park, Y. Lee, M. Ha, S. Cho and H. Ko, Micro/nanostructured surfaces for self-powered and multifunctional electronic skins, *J. Mater. Chem. B*, **2016**, *4*, 2999-3018.
162. G. Y. Bae, S. W. Pak, D. Kim, G. Lee, D. H. Kim, Y. Chung and K. Cho, Linearly and Highly Pressure-Sensitive Electronic Skin Based on a Bioinspired Hierarchical Structural Array, *Adv. Mater.*, **2016**, *28*, 5300-5306.
163. K. Y. Lee, H. J. Yoon, T. Jiang, X. Wen, W. Seung, S. W. Kim and Z. L. Wang, Fully Packaged Self-Powered Triboelectric Pressure Sensor Using Hemispheres-Array, *Adv. Energy Mater.*,

- 2016**, 6, 1502566.
164. B. C. K. Tee, A. Chortos, R. R. Dunn, G. Schwartz, E. Eason and Z. Bao, Tunable flexible pressure sensors using microstructured elastomer geometries for intuitive electronics, *Adv. Funct. Mater.*, **2014**, 24, 5427-5434.
  165. H. Park, Y. R. Jeong, J. Yun, S. Y. Hong, S. Jin, S.-J. Lee, G. Zi and J. S. Ha, Stretchable array of highly sensitive pressure sensors consisting of polyaniline nanofibers and Au-coated polydimethylsiloxane micropillars, *ACS Nano*, **2015**, 9, 9974-9985.
  166. M. R. Maschmann, G. J. Ehlert, B. T. Dickinson, D. M. Phillips, C. W. Ray, G. W. Reich and J. W. Baur, Bioinspired Carbon Nanotube Fuzzy Fiber Hair Sensor for Air-Flow Detection, *Adv. Mater.*, **2014**, 26, 3230-3234.
  167. M.-L. Seol, H. Im, D.-I. Moon, J.-H. Woo, D. Kim, S.-J. Choi and Y.-K. Choi, Design strategy for a piezoelectric nanogenerator with a well-ordered nanoshell array, *ACS Nano*, **2013**, 7, 10773-10779.
  168. H.-H. Chou, A. Nguyen, A. Chortos, J. W. To, C. Lu, J. Mei, T. Kurosawa, W.-G. Bae, J. B.-H. Tok and Z. Bao, A chameleon-inspired stretchable electronic skin with interactive colour changing controlled by tactile sensing, *Nat. Commun.*, **2015**, 6, 8011.
  169. D. Jang, Y. Kim, T. Y. Kim, K. Koh, U. Jeong and J. Cho, Force-assembled triboelectric nanogenerator with high-humidity-resistant electricity generation using hierarchical surface morphology, *Nano Energy*, **2016**, 20, 283-293.
  170. J. H. Lee, H. J. Yoon, T. Y. Kim, M. K. Gupta, J. H. Lee, W. Seung, H. Ryu and S. W. Kim, Micropatterned P (VDF-TrFE) Film-Based Piezoelectric Nanogenerators for Highly Sensitive Self-Powered Pressure Sensors, *Adv. Funct. Mater.*, **2015**, 25, 3203-3209.
  171. W. Deng, X. Huang, W. Chu, Y. Chen, L. Mao, Q. Tang and W. Yang, Microstructure-based interfacial tuning mechanism of capacitive pressure sensors for electronic skin, *J. Sens.*, **2016**, 2016.
  172. J. Park, Y. Lee, S. Lim, Y. Lee, Y. Jung, H. Lim and H. Ko, Ultrasensitive piezoresistive pressure sensors based on interlocked micropillar arrays, *BioNanoSci.*, **2014**, 4, 349-355.
  173. J. Fisher and I. Giaever, Tunneling through thin insulating layers, *J. Appl. Phys.*, **1961**, 32, 172-177.
  174. Z. Huang, M. Gao, Z. Yan, T. Pan, S. A. Khan, Y. Zhang, H. Zhang and Y. Lin, Pyramid microstructure with single walled carbon nanotubes for flexible and transparent micro-pressure sensor with ultra-high sensitivity, *Sens. Actuator A-Phys.*, **2017**, 266, 345-351.
  175. B. Su, S. Gong, Z. Ma, L. W. Yap and W. Cheng, Mimosa-inspired design of a flexible pressure sensor with touch sensitivity, *Small*, **2015**, 11, 1886-1891.
  176. Y. Zang, F. Zhang, D. Huang, X. Gao, C.-a. Di and D. Zhu, Flexible suspended gate organic

- thin-film transistors for ultra-sensitive pressure detection, *Nat. Commun.*, **2015**, *6*, 6269.
177. Y. Zang, F. Zhang, C.-a. Di and D. Zhu, Advances of flexible pressure sensors toward artificial intelligence and health care applications, *Mater. Horiz.*, **2015**, *2*, 140-156.
178. J. A. Vita, R. S. Vasan, D. Levy, G. F. Mitchell, H. Parise, E. J. Benjamin, M. G. Larson and M. J. Keyes, Changes in Arterial Stiffness and Wave Reflection With Advancing Age in Healthy Men and Women The Framingham Heart Study, *Hypertension*, **2004**, *43*, 1239-1245.
179. W. W. Nichols, Clinical measurement of arterial stiffness obtained from noninvasive pressure waveforms, *Am. J. Hypertens*, **2005**, *18*, 3S-10S.
180. K. Hirata, T. Yaginuma, M. F. O'rourke and M. Kawakami, Age-related changes in carotid artery flow and pressure pulses: possible implications for cerebral microvascular disease, *Stroke*, **2006**, *37*, 2552-2556.
181. C. Lang, J. Fang, H. Shao, X. Ding and T. Lin, High-sensitivity acoustic sensors from nanofibre webs, *Nat. Commun.*, **2016**, *7*, 11108.
182. S. N. Cha, J. S. Seo, S. M. Kim, H. J. Kim, Y. J. Park, S. W. Kim and J. M. Kim, Sound-driven piezoelectric nanowire-based nanogenerators, *Adv. Mater.*, **2010**, *22*, 4726-4730.
183. J. Yang, J. Chen, Y. Liu, W. Yang, Y. Su and Z. L. Wang, Triboelectrification-based organic film nanogenerator for acoustic energy harvesting and self-powered active acoustic sensing, *ACS Nano*, **2014**, *8*, 2649-2657.
184. N. Cui, L. Gu, J. Liu, S. Bai, J. Qiu, J. Fu, X. Kou, H. Liu, Y. Qin and Z. L. Wang, High performance sound driven triboelectric nanogenerator for harvesting noise energy, *Nano Energy*, **2015**, *15*, 321-328.
185. Y. Gu, X. Wang, W. Gu, Y. Wu, T. Li and T. Zhang, Flexible electronic eardrum, *Nano Res.*, **2017**, *10*, 2683-2691.
186. T. Someya, Y. Kato, T. Sekitani, S. Iba, Y. Noguchi, Y. Murase, H. Kawaguchi and T. Sakurai, Conformable, flexible, large-area networks of pressure and thermal sensors with organic transistor active matrixes, *Proc. Natl. Acad. Sci.*, **2005**, *102*, 12321-12325.
187. M. Kaltenbrunner, T. Sekitani, J. Reeder, T. Yokota, K. Kuribara, T. Tokuhara, M. Drack, R. Schwödlaier, I. Graz and S. Bauer-Gogonea, An ultra-lightweight design for imperceptible plastic electronics, *Nature*, **2013**, *499*, 458.
188. S. Bauer, S. Bauer-Gogonea, I. Graz, M. Kaltenbrunner, C. Keplinger and R. Schwödlaier, 25th anniversary article: a soft future: from robots and sensor skin to energy harvesters, *Adv. Mater.*, **2014**, *26*, 149-162.
189. I. Graz, M. Krause, S. Bauer-Gogonea, S. Bauer, S. P. Lacour, B. Ploss, M. Zirkl, B. Stadlober and S. Wagner, Flexible active-matrix cells with selectively poled bifunctional polymer-ceramic nanocomposite for pressure and temperature sensing skin, *J. Appl. Phys.*, **2009**, *106*,

- 034503.
190. R. D. Howe and M. R. Cutkosky, Dynamic tactile sensing: Perception of fine surface features with stress rate sensing, *IEEE Trans. Robot. Autom.*, **1993**, *9*, 140-151.
  191. J. Dargahi and S. Najarian, Human tactile perception as a standard for artificial tactile sensing—a review, *Int. J. Med. Robot. Comp.*, **2004**, *1*, 23-35.
  192. R. Fagiani, F. Massi, E. Chatelet, Y. Berthier and A. Akay, Tactile perception by friction induced vibrations, *Tribol. Int.*, **2011**, *44*, 1100-1110.
  193. E. Wandersman, R. Candelier, G. Debrégeas and A. Prevost, Texture-induced modulations of friction force: the fingerprint effect, *Phys. Rev. Lett.*, **2011**, *107*, 164301.
  194. H. Athenstaedt, Permanent longitudinal electric polarization and pyroelectric behaviour of collagenous structures and nervous tissue in man and other vertebrates, *Nature*, **1970**, *228*, 830.
  195. H. Athenstaedt, H. Claussen and D. Schaper, Epidermis of human skin: pyroelectric and piezoelectric sensor layer, *Science*, **1982**, *216*, 1018-1020.
  196. D. De Rossi, A. Nannini and C. Domenici, Artificial sensing skin mimicking mechano-electrical conversion properties of human dermis, *IEEE Trans. Biomed. Eng.*, **1988**, *35*, 83-92.
  197. D.-S. Um, S. Lim, Y. Lee, H. Lee, H.-j. Kim, W.-C. Yen, Y.-L. Chueh and H. Ko, Vacuum-induced wrinkle arrays of InGaAs semiconductor nanomembranes on polydimethylsiloxane microwell arrays, *ACS Nano*, **2014**, *8*, 3080-3087.
  198. V. Sencadas, S. Lanceros-Méndez and J. Mano, Characterization of poled and non-poled  $\beta$ -PVDF films using thermal analysis techniques, *Thermochim. Acta*, **2004**, *424*, 201-207.
  199. X. He, J. Du, Z. Ying, H. Cheng and X. He, Positive temperature coefficient effect in multiwalled carbon nanotube/high-density polyethylene composites, *Appl. Phys. Lett.*, **2005**, *86*, 062112.
  200. J. Meyer, Stability of polymer composites as positive-temperature-coefficient resistors, *Polym. Eng. Sci.*, **1974**, *14*, 706-716.
  201. H. Pang, Y.-C. Zhang, T. Chen, B.-Q. Zeng and Z.-M. Li, Tunable positive temperature coefficient of resistivity in an electrically conducting polymer/graphene composite, *Appl. Phys. Lett.*, **2010**, *96*, 251907.
  202. S. Ansari and E. P. Giannelis, Functionalized graphene sheet—Poly (vinylidene fluoride) conductive nanocomposites, *J. Polym. Sci. Pt. B Polym. Phys.*, **2009**, *47*, 888-897.
  203. I. Jung, D. A. Dikin, R. D. Piner and R. S. Ruoff, Tunable electrical conductivity of individual graphene oxide sheets reduced at “low” temperatures, *Nano Lett.*, **2008**, *8*, 4283-4287.
  204. M. E. Itkis, F. Borondics, A. Yu and R. C. Haddon, Bolometric infrared photoresponse of suspended single-walled carbon nanotube films, *Science*, **2006**, *312*, 413-416.
  205. R. Lu, C. Christianson, B. Weintrub and J. Z. Wu, High photoresponse in hybrid graphene—

- carbon nanotube infrared detectors, *ACS Appl. Mater. Interfaces*, **2013**, *5*, 11703-11707.
206. M. Tian, Y. Huang, W. Wang, R. Li, P. Liu, C. Liu and Y. Zhang, Temperature-dependent electrical properties of graphene nanoplatelets film dropped on flexible substrates, *J. Mater. Res.*, **2014**, *29*, 1288-1294.
207. W. B. White, L. Wolfson, C. Guttman, N. Moscufo, D. Wakefield, R. Kaplan and G. Pearlson, Average daily blood pressure, not office blood pressure, determines the progression of cerebrovascular disease and functional decline in older persons, *J. Am. Coll. Cardiol.*, **2011**, *57*, E490.
208. L. Y. Chen, B. C.-K. Tee, A. L. Chortos, G. Schwartz, V. Tse, D. J. Lipomi, H.-S. P. Wong, M. V. McConnell and Z. Bao, Continuous wireless pressure monitoring and mapping with ultra-small passive sensors for health monitoring and critical care, *Nat. Commun.*, **2014**, *5*, 5028.
209. Z. Li and Z. L. Wang, Air/Liquid-Pressure and Heartbeat-Driven Flexible Fiber Nanogenerators as a Micro/Nano-Power Source or Diagnostic Sensor, *Adv. Mater.*, **2011**, *23*, 84-89.
210. C. Dagdeviren, Y. Su, P. Joe, R. Yona, Y. Liu, Y.-S. Kim, Y. Huang, A. R. Damadoran, J. Xia and L. W. Martin, Conformable amplified lead zirconate titanate sensors with enhanced piezoelectric response for cutaneous pressure monitoring, *Nat. Commun.*, **2014**, *5*, 4496.
211. C.-M. Huang, H.-C. Chang, S.-T. Kao, T.-C. Li, C.-C. Wei, C. Chen, Y.-T. Liao and F.-J. Chen, Radial pressure pulse and heart rate variability in heat-and cold-stressed humans, *Evid. Based Complement. Alternat. Med.*, **2011**, *2011*.
212. S. Munir, B. Jiang, A. Guilcher, S. Brett, S. Redwood, M. Marber and P. Chowienczyk, Exercise reduces arterial pressure augmentation through vasodilation of muscular arteries in humans, *Am. J. Physiol Heart Circ. Physiol.*, **2008**, *294*, H1645-H1650.
213. J. O. Godden, G. M. Roth, E. A. Hines and J. F. Schlegel, The changes in the intra-arterial pressure during immersion of the hand in ice-cold water, *Circulation*, **1955**, *12*, 963-973.
214. H. Yu, T. Huang, M. Lu, M. Mao, Q. Zhang and H. Wang, Enhanced power output of an electrospun PVDF/MWCNTs-based nanogenerator by tuning its conductivity, *Nanotechnology*, **2013**, *24*, 405401.
215. L. Huang, C. Lu, F. Wang and L. Wang, Preparation of PVDF/graphene ferroelectric composite films by in situ reduction with hydrobromic acids and their properties, *RSC Adv.*, **2014**, *4*, 45220-45229.
216. M. El Achaby, F. Arrakhiz, S. Vaudreuil, E. Essassi, A. Qaiss and M. Bousmina, Preparation and characterization of melt-blended graphene nanosheets-poly (vinylidene fluoride) nanocomposites with enhanced properties, *J. Appl. Polym. Sci.*, **2013**, *127*, 4697-4707.
217. J. Sirohi and I. Chopra, Fundamental understanding of piezoelectric strain sensors, *J. Intell. Mater. Syst. Struct.*, **2000**, *11*, 246-257.

218. C. Chang, V. H. Tran, J. Wang, Y.-K. Fuh and L. Lin, Direct-write piezoelectric polymeric nanogenerator with high energy conversion efficiency, *Nano Lett.*, **2010**, *10*, 726-731.
219. L. Gu, N. Cui, L. Cheng, Q. Xu, S. Bai, M. Yuan, W. Wu, J. Liu, Y. Zhao and F. Ma, Flexible fiber nanogenerator with 209 V output voltage directly powers a light-emitting diode, *Nano Lett.*, **2012**, *13*, 91-94.
220. A. Prevost, J. Scheibert and G. Debrégeas, Effect of fingerprints orientation on skin vibrations during tactile exploration of textured surfaces, *Commun. Integr. Biol.*, **2009**, *2*, 422-424.
221. M. Wiertlewski, C. Hudin and V. Hayward, On the 1/f noise and non-integer harmonic decay of the interaction of a finger sliding on flat and sinusoidal surfaces, in *2011 World Haptics Conference*, **2011**, 25-30.
222. S. J. Bensmaïa and M. Hollins, The vibrations of texture, *Somatosens. Mot. Res.*, **2003**, *20*, 33-43.
223. M. Audry, C. Frétiigny, A. Chateauminois, J. Teissere and E. Barthel, Slip dynamics at a patterned rubber/glass interface during stick-slip motions, *Eur. Phys. J. E*, **2012**, *35*, 83.
224. A. Vallbo and R. S. Johansson, Properties of cutaneous mechanoreceptors in the human hand related to touch sensation, *Hum Neurobiol*, **1984**, *3*, 3-14.
225. X. Wang, M. Que, M. Chen, X. Han, X. Li, C. Pan and Z. L. Wang, Full Dynamic-Range Pressure Sensor Matrix Based on Optical and Electrical Dual-Mode Sensing, *Adv. Mater.*, **2017**, *29*, 1605817.
226. T. Maeno, K. Kobayashi and N. Yamazaki, Relationship between the structure of human finger tissue and the location of tactile receptors, *JSME Int. J. Ser. C*, **1998**, *41*, 94-100.
227. W. S. Hummers Jr and R. E. Offeman, Preparation of graphitic oxide, *J. Amer. Chem. Soc.*, **1958**, *80*, 1339-1339.
228. D. Kang, Y. E. Shin, H. J. Jo, H. Ko and H. S. Shin, Mechanical Properties of Poly (dopamine)-Coated Graphene Oxide and Poly (vinyl alcohol) Composite Fibers Coated with Reduced Graphene Oxide and Their Use for Piezoresistive Sensing, *Part. Par. Synt. Char.*, **2017**, *34*, 1600382.
229. P. Martins, A. Lopes and S. Lanceros-Mendez, Electroactive phases of poly (vinylidene fluoride): determination, processing and applications, *Progress in polymer science*, **2014**, *39*, 683-706.
230. S. K. Karan, R. Bera, S. Paria, A. K. Das, S. Maiti, A. Maitra and B. B. Khatua, An Approach to Design Highly Durable Piezoelectric Nanogenerator Based on Self-Poled PVDF/AIO-rGO Flexible Nanocomposite with High Power Density and Energy Conversion Efficiency, *Adv. Energy Mater.*, **2016**, *6*, 1601016.
231. X.-J. Zhang, G.-S. Wang, W.-Q. Cao, Y.-Z. Wei, M.-S. Cao and L. Guo, Fabrication of multi-

- functional PVDF/RGO composites via a simple thermal reduction process and their enhanced electromagnetic wave absorption and dielectric properties, *RSC Adv.*, **2014**, *4*, 19594-19601.
232. N. Luo, Y. Huang, J. Liu, S. C. Chen, C. P. Wong and N. Zhao, Hollow-Structured Graphene–Silicone-Composite-Based Piezoresistive Sensors: Decoupled Property Tuning and Bending Reliability, *Adv. Mater.*, **2017**, *29*, 1702675.
233. Y. Pang, K. Zhang, Z. Yang, S. Jiang, Z. Ju, Y. Li, X. Wang, D. Wang, M. Jian and Y. Zhang, Epidermis Microstructure Inspired Graphene Pressure Sensor with Random Distributed Spinosum for High Sensitivity and Large Linearity, *ACS Nano*, **2018**, *12*, 2346-2354.
234. A. Chortos and Z. Bao, Skin-inspired electronic devices, *Mater. Today*, **2014**, *17*, 321-331.
235. M. A. Cretikos, R. Bellomo, K. Hillman, J. Chen, S. Finfer and A. Flabouris, Respiratory rate: the neglected vital sign, *Med. J. Aust.*, **2008**, *188*, 657.
236. P. B. Lovett, J. M. Buchwald, K. Stürmann and P. Bijur, The vexatious vital: neither clinical measurements by nurses nor an electronic monitor provides accurate measurements of respiratory rate in triage, *Ann. Emerg. Med.*, **2005**, *45*, 68-76.
237. J. Blacher, R. Asmar, S. Djane, G. M. London and M. E. Safar, Aortic pulse wave velocity as a marker of cardiovascular risk in hypertensive patients, *Hypertension*, **1999**, *33*, 1111-1117.
238. D. H. Spodick, Survey of selected cardiologists for an operational definition of normal sinus heart rate, *Am. J. Cardiol.*, **1993**, *72*, 487-488.
239. A. Razak, A. Hadi, A. Zayegh, R. K. Begg and Y. Wahab, Foot plantar pressure measurement system: A review, *Sensors*, **2012**, *12*, 9884-9912.
240. T. A. Bacarin, I. C. Sacco and E. M. Hennig, Plantar pressure distribution patterns during gait in diabetic neuropathy patients with a history of foot ulcers, *Clinics*, **2009**, *64*, 113-120.
241. S. Kimmeskamp and E. M. Hennig, Heel to toe motion characteristics in Parkinson patients during free walking, *Clin. Biomech.*, **2001**, *16*, 806-812.
242. P. G. Gillespie and R. G. Walker, Molecular basis of mechanosensory transduction, *Nature*, **2001**, *413*, 194.
243. C. R. Hickenboth, J. S. Moore, S. R. White, N. R. Sottos, J. Baudry and S. R. Wilson, Biasing reaction pathways with mechanical force, *Nature*, **2007**, *446*, 423.
244. M. M. Caruso, D. A. Davis, Q. Shen, S. A. Odom, N. R. Sottos, S. R. White and J. S. Moore, Mechanically-induced chemical changes in polymeric materials, *Chem. Rev.*, **2009**, *109*, 5755-5798.
245. J. Li, C. Nagamani and J. S. Moore, Polymer mechanochemistry: from destructive to productive, *Acc. Chem. Res.*, **2015**, *48*, 2181-2190.
246. D. A. Davis, A. Hamilton, J. Yang, L. D. Cremar, D. Van Gough, S. L. Potisek, M. T. Ong, P. V. Braun, T. J. Martínez and S. R. White, Force-induced activation of covalent bonds in

- mechanoresponsive polymeric materials, *Nature*, **2009**, *459*, 68.
247. Y. Chen, A. Spiering, S. Karthikeyan, G. W. Peters, E. Meijer and R. P. Sijbesma, Mechanically induced chemiluminescence from polymers incorporating a 1, 2-dioxetane unit in the main chain, *Nat. Chem.*, **2012**, *4*, 559.
248. A. Piermattei, S. Karthikeyan and R. P. Sijbesma, Activating catalysts with mechanical force, *Nat. Chem.*, **2009**, *1*, 133-137.
249. C. E. Diesendruck, B. D. Steinberg, N. Sugai, M. N. Silberstein, N. R. Sottos, S. R. White, P. V. Braun and J. S. Moore, Proton-coupled mechanochemical transduction: a mechanogenerated acid, *J. Am. Chem. Soc.*, **2012**, *134*, 12446-12449.
250. J. M. Lenhardt, M. T. Ong, R. Choe, C. R. Evenhuis, T. J. Martinez and S. L. Craig, Trapping a diradical transition state by mechanochemical polymer extension, *Science*, **2010**, *329*, 1057-1060.
251. M. B. Larsen and A. J. Boydston, Successive mechanochemical activation and small molecule release in an elastomeric material, *J. Am. Chem. Soc.*, **2014**, *136*, 1276-1279.
252. G. Hong, H. Zhang, Y. Lin, Y. Chen, Y. Xu, W. Weng and H. Xia, Mechanoresponsive healable metallosupramolecular polymers, *Macromolecules*, **2013**, *46*, 8649-8656.
253. C. K. Lee, D. A. Davis, S. R. White, J. S. Moore, N. R. Sottos and P. V. Braun, Force-induced redistribution of a chemical equilibrium, *J. Am. Chem. Soc.*, **2010**, *132*, 16107-16111.
254. K. Imato, T. Kanehara, T. Ohishi, M. Nishihara, H. Yajima, M. Ito, A. Takahara and H. Otsuka, Mechanochromic dynamic covalent elastomers: quantitative stress evaluation and autonomous recovery, *ACS Macro Lett.*, **2015**, *4*, 1307-1311.
255. H. Chen, F. Yang, Q. Chen and J. Zheng, A Novel Design of Multi-Mechanoresponsive and Mechanically Strong Hydrogels, *Adv. Mater.*, **2017**, *29*, 1606900.
256. O. Rifaie-Graham, E. A. Apebende, L. K. Bast and N. Bruns, Self-Reporting Fiber-Reinforced Composites That Mimic the Ability of Biological Materials to Sense and Report Damage, *Adv. Mater.*, **2018**, *30*, 1705483.
257. Z. a. Li, R. Toivola, F. Ding, J. Yang, P. N. Lai, T. Howie, G. Georgeson, S. H. Jang, X. Li and B. D. Flinn, Highly sensitive built-in strain sensors for polymer composites: Fluorescence turn-on response through mechanochemical activation, *Adv. Mater.*, **2016**, *28*, 6592-6597.
258. M. J. Kryger, A. M. Munaretto and J. S. Moore, Structure–mechanochemical activity relationships for cyclobutane mechanophores, *J. Am. Chem. Soc.*, **2011**, *133*, 18992-18998.
259. B. A. Beiermann, S. L. Kramer, P. A. May, J. S. Moore, S. R. White and N. R. Sottos, The Effect of Polymer Chain Alignment and Relaxation on Force-Induced Chemical Reactions in an Elastomer, *Adv. Funct. Mater.*, **2014**, *24*, 1529-1537.
260. B. A. Beiermann, D. A. Davis, S. L. Kramer, J. S. Moore, N. R. Sottos and S. R. White,



- Environmental effects on mechanochemical activation of spiropyran in linear PMMA, *J. Mater. Chem.*, **2011**, *21*, 8443-8447.
261. Y. Chen, H. Zhang, X. Fang, Y. Lin, Y. Xu and W. Weng, Mechanical activation of mechanophore enhanced by strong hydrogen bonding interactions, *ACS Macro Lett.*, **2014**, *3*, 141-145.
262. S. Jiang, L. Zhang, T. Xie, Y. Lin, H. Zhang, Y. Xu, W. Weng and L. Dai, Mechanoresponsive PS-PnBA-PS triblock copolymers via covalently embedding mechanophore, *ACS Macro Lett.*, **2013**, *2*, 705-709.
263. H. Yan, F. Yang, D. Pan, Y. Lin, J. N. Hohman, D. Solis-Ibarra, F. H. Li, J. E. Dahl, R. M. Carlson and B. A. Tkachenko, Sterically controlled mechanochemistry under hydrostatic pressure, *Nature*, **2018**, *554*, 505.
264. H. Zhang, Y. Chen, Y. Lin, X. Fang, Y. Xu, Y. Ruan and W. Weng, Spiropyran as a mechanochromic probe in dual cross-linked elastomers, *Macromolecules*, **2014**, *47*, 6783-6790.
265. G. R. Gossweiler, G. B. Hewage, G. Soriano, Q. Wang, G. W. Welshofer, X. Zhao and S. L. Craig, Mechanochemical activation of covalent bonds in polymers with full and repeatable macroscopic shape recovery, *ACS Macro Lett.*, **2014**, *3*, 216-219.
266. Y. Lee, J. Park, S. Cho, Y.-E. Shin, H. Lee, J. Kim, J. Myoung, S. Cho, S. Kang and C. Baig, Flexible Ferroelectric Sensors with Ultrahigh Pressure Sensitivity and Linear Response over Exceptionally Broad Pressure Range, *ACS Nano*, **2018**, *12*, 4045-4054.
267. M. Ha, S. Lim, S. Cho, Y. Lee, S. Na, C. Baig and H. Ko, Skin-Inspired Hierarchical Polymer Architectures with Gradient Stiffness for Spacer-Free, Ultrathin, and Highly Sensitive Triboelectric Sensors, *ACS Nano*, **2018**, *12*, 3964-3974.
268. F. Berto and P. Lazzarin, Recent developments in brittle and quasi-brittle failure assessment of engineering materials by means of local approaches, *Mater. Sci. Eng. R Rep*, **2014**, *75*, 1-48.
269. H. Gao, B. Ji, I. L. Jäger, E. Arzt and P. Fratzl, Materials become insensitive to flaws at nanoscale: lessons from nature, *Proc. Natl. Acad. Sci.*, **2003**, *100*, 5597-5600.
270. R. Lakes, Materials with structural hierarchy, *Nature*, **1993**, *361*, 511.
271. M. H. Barbee, K. Mondal, J. Z. Deng, V. Bharambe, T. V. Neumann, J. J. Adams, N. Boechler, M. D. Dickey and S. L. Craig, Mechanochromic Stretchable Electronics, *ACS Appl. Mater. Interfaces*, **2018**, *10*, 29918-29924.
272. J. Chun, J. W. Kim, W.-s. Jung, C.-Y. Kang, S.-W. Kim, Z. L. Wang and J. M. Baik, Mesoporous pores impregnated with Au nanoparticles as effective dielectrics for enhancing triboelectric nanogenerator performance in harsh environments, *Energ. Environ. Sci.*, **2015**, *8*, 3006-3012.
273. N. Kazem, M. D. Bartlett and C. Majidi, Extreme Toughening of Soft Materials with Liquid Metal, *Adv. Mater.*, **2018**, *30*, 1706594.

274. R. Rice, Limitations of pore-stress concentrations on the mechanical properties of porous materials, *J. Mater. Sci.*, **1997**, *32*, 4731-4736.
275. D. Sen and M. J. Buehler, Structural hierarchies define toughness and defect-tolerance despite simple and mechanically inferior brittle building blocks, *Sci. Rep.*, **2011**, *1*, 35.
276. M. Li, Q. Zhang and S. Zhu, Photo-inactive divinyl spiropyran mechanophore cross-linker for real-time stress sensing, *Polymer*, **2016**, *99*, 521-528.
277. M. Raisch, D. Genovese, N. Zaccheroni, S. B. Schmidt, M. L. Focarete, M. Sommer and C. Gualandi, Highly Sensitive, Anisotropic, and Reversible Stress/Strain-Sensors from Mechanochromic Nanofiber Composites, *Adv. Mater.*, **2018**, *30*, 1802813.
278. M. Dübner, N. D. Spencer and C. Padeste, Light-responsive polymer surfaces via postpolymerization modification of grafted polymer-brush structures, *Langmuir*, **2014**, *30*, 14971-14981.
279. C. K. Lee, B. A. Beiermann, M. N. Silberstein, J. Wang, J. S. Moore, N. R. Sottos and P. V. Braun, Exploiting force sensitive spiropyrans as molecular level probes, *Macromolecules*, **2013**, *46*, 3746-3752.
280. Z. Wang, Z. Ma, Y. Wang, Z. Xu, Y. Luo, Y. Wei and X. Jia, A novel mechanochromic and photochromic polymer film: when rhodamine joins polyurethane, *Adv. Mater.*, **2015**, *27*, 6469-6474.
281. S. Cho, S. Kang, A. Pandya, R. Shanker, Z. Khan, Y. Lee, J. Park, S. L. Craig and H. Ko, Large-area cross-aligned silver nanowire electrodes for flexible, transparent, and force-sensitive mechanochromic touch screens, *ACS Nano*, **2017**, *11*, 4346-4357.
282. S. Kang, S. Cho, R. Shanker, H. Lee, J. Park, D.-S. Um, Y. Lee and H. Ko, Transparent and conductive nanomembranes with orthogonal silver nanowire arrays for skin-attachable loudspeakers and microphones, *Sci. Adv.*, **2018**, *4*, eaas8772.
283. S. W. Chen, X. Cao, N. Wang, L. Ma, H. R. Zhu, M. Willander, Y. Jie and Z. L. Wang, An ultrathin flexible single-electrode triboelectric-nanogenerator for mechanical energy harvesting and instantaneous force sensing, *Adv. Energy Mater.*, **2017**, *7*, 1601255.

\*Chapter 2 is reproduced in part with permission of “Giant tunneling piezoresistance of composite elastomers with interlocked microdome array for ultrasensitive and multimodal electronic skins, *ACS Nano*, 2014, *8*, 4689-4697”. Copyright 2014, American Chemical Society

\*Chapter 3 is reproduced in part with permission of “Tactile-Direction-Sensitive and Stretchable Electronic Skins Based on Human-Skin-Inspired Interlocked Microstructures, *ACS Nano*, 2014, *8*, 12020-12029”. Copyright 2014, American Chemical Society

\*Chapter 4 is reproduced in part with permission of “Tailoring Force Sensitivity and Selectivity by Microstructure Engineering of Multidirectional Electronic Skins, *NPG. Asia Mater.* 2018, *10*, 163-176.”. Copyright 2018, Nature Publishing Group

\*Chapter 5 is reproduced in part with permission of “Fingertip skin-inspired microstructured ferroelectric skins discriminate static/dynamic pressure and temperature stimuli, *Science Advances*, 2015, *1*, e1500661”. Copyright 2015, American Association for the Advancement of Science

\*Chapter 6 is reproduced in part with permission of “Flexible Ferroelectric Sensors with Ultrahigh Pressure Sensitivity and Linear Response over Exceptionally Broad Pressure Range, *ACS Nano*, 2018, *12*, 4045-4054”. Copyright 2018 American Chemical Society

## Appendix A: List of Achievements

The results of this dissertation have been published in: (†: equal contribution)

1. **Jonghwa Park**, Youngoh Lee, Jaehyung Hong, Minjeong Ha, Young-Do Jung, Hyuneui Lim, Sung Youb Kim, and Hyunhyub Ko, Giant tunneling piezoresistance of composite elastomers with interlocked microdome array for ultrasensitive and multimodal electronic skins, *ACS Nano*, **2014**, *8*, 4689-4697
2. **Jonghwa Park**†, Youngoh Lee†, Jaehyung Hong, Youngsu Lee, Minjeong Ha, Youngdo Jung, Hyuneui Lim, Sung Youb Kim, and Hyunhyub Ko, Tactile-Direction-Sensitive and Stretchable Electronic Skins Based on Human-Skin-Inspired Interlocked Microstructures, *ACS Nano*, **2014**, *8*, 12020-12029
3. **Jonghwa Park**†, Jinyoung Kim†, Jaehyung Hong, Hochan Lee, Youngoh Lee, Seungse Cho, Sung Youb Kim, and Hyunhyub Ko, Tailoring Force Sensitivity and Selectivity by Microstructure Engineering of Multidirectional Electronic Skins, *NPG. Asia Mater.* **2018**, *10*, 163-176
4. **Jonghwa Park**†, Marie Kim†, Youngoh Lee, Heon-Sang Lee, and Hyunhyub Ko, Fingertip skin-inspired microstructured ferroelectric skins discriminate static/dynamic pressure and temperature stimuli, *Science Advances*, **2015**, *1*, e1500661
5. Youngoh Lee†, **Jonghwa Park**† (co-first author), Soo won Cho, Young-Eun Shin, Hochan Lee, Jinyoung Kim, Jinyoung Myoung, Seungse Cho, Saewon Kang, Chunggi Baig, and Hyunhyub Ko, Flexible Ferroelectric Sensors with Ultrahigh Pressure Sensitivity and Linear Response over Exceptionally Broad Pressure Range, *ACS Nano*, **2018**, *12*, 4045-4054
6. **Jonghwa Park**, Youngoh Lee, Minjeong Ha, Seungse Cho, and Hyunhyub Ko, Micro/nanostructured surfaces for self-powered and multifunctional electronic skins, *J. Mater. Chem. B*, **2016**, Advance Article
7. **Jonghwa Park**, Youngoh Lee, Seongdong Lim, Youngsu Lee, Youngdo Jung, Hyuneui Lim, and Hyunhyub Ko, Ultrasensitive piezoresistive pressure sensors based on interlocked micropillar arrays, *BioNanoSci.*, **2014**, *4*, 349-355

**The other related results have been published in:**

1. Minjeong Ha, **Jonghwa Park**, Youngoh Lee, and Hyunhyub Ko, Triboelectric Generators and Sensors for Self-Powered Wearable Electronics, *ACS Nano*, **2015**, *9*, 3421-3427.
2. Saewon Kang, Seungse Cho, Ravi Shanker, Hochan Lee, **Jonghwa Park**, Doo-Seung Um, Youngoh Lee, Hyunhyub Ko, Transparent and conductive nanomembranes with orthogonal silver nanowire arrays for skin-attachable loudspeakers and microphones, *Science Advances*, **2018**, *4*, eaas8772
3. Minsoo P. Kim, Youngoh Lee, Yoon Hyung Hur, **Jonghwa Park**, Jinyoung Kim, Youngsu Lee, Chang Won Ahn, Seung Won Song, Yeon Sik Jung, Hyunhyub Ko, Molecular structure engineering of dielectric fluorinated polymers for enhanced performances of triboelectric nanogenerators, *Nano Energy*, **2018**, *53*, 37-45
4. Minjeong Ha, Seongdong Lim, **Jonghwa Park**, Doo-Seung Um, Youngoh Lee, and Hyunhyub Ko, Bioinspired Interlocked and Hierarchical Design of ZnO Nanowire Arrays for Static and Dynamic Pressure-Sensitive Electronic Skins, *Adv. Funct. Mater.*, **2015**, *25*, 2841-2849.
5. Sehee Ahn, Ayoung Choe, **Jonghwa Park**, Heesuk Kim, Jeong Gon Son, Sang-Soo Lee, Min Park, and Hyunhyub Ko, Directed self-assembly of rhombic carbon nanotube nanomesh films for transparent and stretchable electrodes, *J. Mater. Chem. C*, **2015**, *3*, 2319-2325.
6. Youngdo Jung, Duck-Gyu Lee, **Jonghwa Park**, Hyunhyub Ko, and Hyuneui Lim, Piezoresistive Tactile Sensor Discriminating Multidirectional Forces, *Sensors*, **2015**, *15*, 25463-25473.
7. Youngoh Lee, Jiwon Lee, Tae Kyung Lee, **Jonghwa Park**, Minjung Ha, Sang Kyu Kwak, and Hyunhyub Ko, Particle-on-Film Gap Plasmons on Antireflective ZnO Nanocone Arrays for Molecular-Level Surface-Enhanced Raman Scattering Sensors, *ACS Appl. Mater. Interfaces*, **2015**, *7*, 26421-26429.
8. Doo-Seung Um, Youngsu Lee, Seongdong Lim, **Jonghwa Park**, Wen-Chun Yen, Yu-Lun Chueh, Hyung-jun Kim, and Hyunhyub Ko, InGaAs Nanomembrane/Si van der Waals Heterjunction Photodiodes with Broadband and High Photoresponsivity, *ACS Appl. Mater. Interfaces*, **2016**, *8*, 26105-26111.
9. **Jonghwa Park**, Minjeong Ha, Youngoh Lee, and Hyunhyub Ko, Polymer-Based Electronic Skins and Wearable Sensors, *Polymer Science and Technology (Korea)*, **2015**, *26*, 274-281
10. Seungse Cho, Saewon Kang, Ashish Pandya, Ravi Shanker, Ziyauddin Khan, Youngsu Lee, **Jonghwa Park**, Stephen L Craig, Hyunhyub Ko, Large-Area Cross-Aligned Silver Nanowire

Electrodes for Flexible, Transparent, and Force-Sensitive Mechanochromic Touch Screens, *ACS Nano*, **2017**, *11*, 4346-4357

11. Sung-Woo Kim, Youngoh Lee, **Jonghwa Park**, Seungmok Kim, Heeyoung Chae, Hyunhyub Ko, Jae Joon Kim, A Triple-Mode Flexible E-Skin Sensor Interface for Multi-Purpose Wearable Applications, *Sensors*, **2018**, *18*, 78.
12. **Jonghwa Park**, Sehee Ahn, Hyunhyub Ko, Nanomaterials, Polymers and Devices: Materials Functionalization and Device Fabrication [Chapter 15. Nanostructured Conductors for Flexible Electronics], **2015**, John Wiley & Sons

#### Conference Presentation:

1. **Jonghwa Park**, Jinyoung Kim, Jaehyung Hong, Hochan Lee, Youngoh Lee, Seungse Cho, Sung-Woo Kim, Jae Joon Kim, Sung Youb Kim, and Hyunhyub Ko, “Tailoring Force Sensitivity and Selectivity of Microstructured Electronic Skins”, *International Conference on Electronic Materials and Nanotechnology for Green Environment (ENGE) 2018*, Korea
2. **Jonghwa Park**, Jinyoung Kim, Jaehyung Hong, Hochan Lee, Youngoh Lee, Seungse Cho, Sung-Woo Kim, Jae Joon Kim, Sung Youb Kim, and Hyunhyub Ko, “Microstructural Engineering of Multidirectional Electronic Skins with Tailoring Force Sensitivity and Selectivity”, *The Polymer Society of Korea 2018*, Korea
3. **Jonghwa Park**, Jinyoung Kim, Jaehyung Hong, Hochan Lee, Youngoh Lee, Seungse Cho, Sung-Woo Kim, Jae Joon Kim, Sung Youb Kim, and Hyunhyub Ko, “Tailoring Force Sensitivity and Selectivity by the Microstructural Engineering of Multidirectional Electronic skins”, *International Union of Materials Research Society-International Conference on Electronic Materials (IUMRS-ICEM) 2018*, Korea
4. **Jonghwa Park**, Jinyoung Kim, Jaehyung Hong, Hochan Lee, Youngoh Lee, Seungse Cho, Sung Youb Kim, and Hyunhyub Ko, “Multidirectional Electronic Skins Tunable Force Sensitivity and Selectivity by Microstructure Engineering”, *The polymer Society of Korea 2017*, Korea
5. **Jonghwa Park**, Youngoh Lee, Heon Sang Lee, and Hyunhyub Ko, “Fingertip skin-inspired Multimodal Ferroelectric Skins Discriminating Static/Dynamic Pressure and Temperature Stimuli”, *International Symposium on Nature-inspired Technology 2016*, Korea
6. **Jonghwa Park**, Youngoh Lee, Heon Sang Lee, and Hyunhyub Ko, “Fingertip Skin-Inspired Multimodal Electronic Skins Discriminating Temperature, Static and Dynamic Touch”, *Fall MRS Meeting 2016*, Boston, USA (selected nominee of best poster award)
7. **Jonghwa Park**, Youngoh Lee, Heon Sang Lee, and Hyunhyub Ko, “Fingertip Skin-inspired

- Microstructured Electronic Skins Discriminating Multidirectional Static/Dynamic Touches and Temperature”, *Korea Carbon Society 2015*, Korea
8. **Jonghwa Park**, Youngoh Lee, Heon Sang Lee, and Hyunhyub Ko, “Human skin-inspired Multimodal Electronic Skins Differentiating Temperature, Static and Dynamic Touch”, *The 15th international meeting on information display 2015*, Korea
  9. **Jonghwa Park**, Youngoh Lee, Jaehyung Hong, Minjeong Ha, Young-Do Jung, Hyuneui Lim, Sung Youb Kim, Hyunhyub Ko, “Interlocked piezoresistive composite elastomers with micro-patterns for ultra-sensitive and multimodal electronic skins”, *The Korea institute of Chemical Engineering 2014*, Korea
  10. **Jonghwa Park**, Youngoh Lee, Jaehyung Hong, Minjeong Ha, Young-Do Jung, Hyuneui Lim, Sung Youb Kim, Hyunhyub Ko, “Ultra-sensitive electronic skin based on composite elastomers with giant tunneling piezoresistance”, *The Polymer Society of Korea 2014*, Korea
  11. **Jonghwa Park**, Youngoh Lee, Jaehyung Hong, Minjeong Ha, Young-Do Jung, Hyuneui Lim, Sung Youb Kim, Hyunhyub Ko, “Micro-patterned piezoresistive composite elastomers for ultra-sensitive and multimodal electronic skins”, *Fall MRS Meeting 2014*, Boston, USA
  12. **Jonghwa Park**, Youngoh Lee, MinJeong Ha, SeungYoung Park, and Hyunhyub Ko, “Microstructured Carbon Nanotube Elastic Conductors for Electronic Skins”, *International Symposium on Nature-inspired Technology 2014*, Japan
  13. **Jonghwa Park**, Youngoh Lee, and Hyunhyub Ko, “Micropatterned Carbon Nanotube Elastic Conductors for Flexible Tactile Sensors”, *The international Conference on Flexible and Printed Electronics 2013*, Korea

#### **Honors and Awards:**

1. ENE Graduate student of the year for outstanding achievement in research, Ulsan National Institute of Science and Technology, 2014
2. The 21th SAMSUNG Human Tech paper award, Gold prize, 2015
3. The 23th SAMSUNG Human Tech paper award, Bronze prize, 2017
4. Best poster Award, Korea Carbon Society, 2015
5. Best poster Award, The Polymer Society of Korea, 2014
6. Best poster Award, The Korea institute of Chemical Engineering, 2014
7. UNIST BK 21 Plus 2nd International Symposium Materials on Demand for Energy, Grand prize, 2014
8. Nanoscience & Engineering Fair hosted by GIST, Grand prize, 2010

## Acknowledgements

First of all, I would like to express a great appreciation to Prof. Hyunhyub Ko who is my principal investigator during my doctoral course. Since I met my professor, I have learned a lot of things from him for my research, my state of mind, and my life. Due to great concerns and supports of him, successfully I have done my ph. D course and have obtained a lot of achievements. Without his help, I might not be able to do this. So, I would like to say to my professor again, “It is great honor to meet you in my life, thank you”

And, I would like to thank my committee members, Prof. Jae Joon Kim, Prof. Chunggi Baig, Prof. Chang Young Lee and Prof. Jiseok Lee, *Ulsan National Institute of Science and Technology (UNIST)*, for their kind encouragement and constructive reviews. Furthermore, I feel a great appreciation for Prof. Stephen L. Craig who is research adviser during my visiting scholar in Duke University. With his kind assistance, I could do a research comfortably and gain different perspectives for my researches.

In addition, I would like to thank all lab leaders, my previous colleagues Dr. Jiwon Lee, Dr. Doo-Seung Um, Dr. Saewon Kang, Sehee Ahn, Dr. Ziyauddin Khan, Dr. Ravi Shanker and Current members Dr. Minsoo Kim, Young-Eun Shin, Young-Ryul Kim, Seongdong Lim, Minjeong Ha, Hochan Lee, Youngsu Lee, Youngoh Lee, Ayoung Choe, Seungse Cho, Jeonghee Yeom, Jinyoung Kim, Jinyoung Myoung, Yoojeong Park, Sangyun Na, and Donghee Kang. Due to my lab member, my ph.D course have been always happy and meaningful. Especially, I feel special thanks to our team members, Youngoh Lee, *my first baby and great supporter*, and Jinyoung Kim, *my second baby and fighting*, Jinyoung Myeong, *baby of baby*, for their devoted help and efforts. In addition, I wanna appreciate to my meaningful brothers and sisters, Jiwon, *high purity*, Doo-Seung, *my mentor*, Saewon, *mimi*, Sehee, *strict teacher*, Hochan, *sick finger*, Seungse, *chatty guy*, Youngsu, *x-boyfriend*, Young-Ryul, *solo*, Ayoung, *cutie* Yoojeong, *lovely* and Donghee, *pizza boy* for having a fun with too much drinking and chatter. I cannot forget that moment forever.

Lastly, I would like to appreciate my parents, brother and cousin for continuous encouragement and long waiting. I will remember a great love given by my family and I will make a return for their love.

Thanks



